Current Sensorless Control Strategies for an Automotive Electric Powertrain

Adrien Corne

UNIVERSITÉ DE LORRAINE

Université de Lorraine : GREEN
Ecole Doctorale : Informatique Automatique Electrotechnique Electronique Mathématiques
Commission de mention : Electrotechnique Electronique

Thèse

présentée en vue de l'obtention du titre de

Docteur de l'Université de Lorraine

Spécialité : Génie électrique

par **Adrien CORNE**

Current Sensorless Control Strategies for an Automotive Electric Powertrain

Soutenue publiquement le 16/12/2019 devant la commission d'examen composée de

Rapporteurs :	Prof. Franck Betin	Univ. de Picardie Jules Verne, LTI
	Dir. Rech. Alexandre De Bernardinis	IFSTTAR
Examinateurs :	Prof. Xuefang Lin-Shi	INSA Lyon, AMPERE
	Prof. Babak Nahid-Mobarakeh	Univ. de Lorraine, GREEN
	Dr. Jean-Philippe Martin	Univ. de Lorraine, LEMTA
Invités :	Prof. Serge Pierfederici	Univ. de Lorraine, LEMTA
	François-Xavier Bernard	Valeo Créteil

Groupe de Recherche en Electrotechnique et Electronique de Nancy
Ecole Nationale Supérieure d'Electricité et de Mécanique - TSA 60604 - 54518 Vandoeuvre-lès-Nancy

Mis en page avec la classe Phdlasl

Remerciements

Les travaux réalisés dans cette thèse ont été réalisés au sein du laboratoire du GREEN Nancy à l'Université de Lorraine sous la direction de Babak Nahid-Mobarakeh, professeur au GREEN, Université de Lorraine, et de Jean-philippe Martin, maître de conférence au LEMTA, Université de Lorraine, en partanariat avec l'entreprise Valeo dans le cadre du projet LowCO2Motion+.

Je tiens tout d'abord à remercier M. Bernard Davat, directeur du GREEN à mon arrivée en thèse, de m'avoir accueilli au sein du laboratoire, ainsi que M. Noureddine Takorabet, son successeur en tant que directeur du laboratoire du GREEN, pour sa disponibilité et son aide administrative précieuse.

Je souhaite également vivement remercier M. Serge Pierfederici, qui m'a accordé sa confiance en m'encourageant à poursuivre mes études d'ingénieur par une thèse. Ses précieuses idées et conseils ont également été d'une aide considérable à l'obtention des résultats présentés dans ce mémoire.

Je remercie évidemment mes directeurs de thèse, M. Babak Nahid-Mobarakeh et M. Jean-Philippe Martin pour leur implication et leur accompagnement tout au long de ces années de thèse. Les connaissances, conseils et savoirs-faire qu'ils m'ont transmis ont été essentiels à l'élaboration des résulats obtenus dans le manuscrit que vous allez parcourir.

J'aimerais également exprimer ma vive reconnaissance à M. Franck Betin, professeur à l'Université de Picardie Jules Verne et M. Alexandre De Bernardinis, directeur de recherche à l'IFSTTAR, de s'être intéressés à mes travaux et d'avoir accepté de rapporter ma thèse. Mes sincères remerciements vont également à Mme Xuefang Lin-Shi, professeur à l'INSA Lyon, et à M. François-Xavier Bernard, ingénieur de recherche à Valéo, d'avoir pris part au jury de ma soutenance de thèse.

Je remercie aussi sincèrement M. Denis Netter, professeur au GREEN, et M. Julien Fontchastagner, maître de conférence au GREEN, pour leur soutien, leur bonne humeur et le partage de leurs connaissances en électrotechnique, ainsi que M. Farid Meibody, professeur au LEMTA, pour son expérience et ses conseils en matière de modélisation de machine électrique.

Le banc expérimental présenté dans ce manuscrit n'auraient pu être réalisé sans l'aide et le savoir-faire de M. Fadi Sharif, ingénieur d'étude au GREEN, Mme Sophie Guichard, assistante ingénieure, M. Fabrice Tesson et Mme Isabelle Schwenker, technicien et technicienne au GREEN. Un grand merci à eux pour leurs enseignements et le temps qu'ils ont consacré à la fabrication et aux réparations sur le banc. Je souhaite également remercier chaleureusement Mme Sylvie Colinet, secrétaire au GREEN, pour son aide administrative indispensable et pour les petits chocolats toujours offerts dans son bureau.

Ces années de recherche auraient été bien ternes sans la présence des collègues doctorant.e.s, post-doctorant.e.s et stagiaires du GREEN. Je pense bien sûr à Davide, dont je ne suis que l'humble *creatura*, qui m'a tant appris en (baby)foot, en cuisine de l'Italie du sud et en rudiments

du dialecte napolitain. Je lui aurai au moins transmis le doux et chatoyant accent franc-comtois lors de son apprentissage du français. Je pense également à Thibaud, mon voisin de bureau et compagnon de cordée, qui m'a fait redécouvrir l'escalade et a partagé mes hauts et mes bas au labo pendant tout ce temps. Je remercie tous les "anciens" du GREEN, Geoffrey, Marc, Ivano, Jérémy et Najla, pour nos longues parties de baby endiablées et nos sorties chez Nénette, Mikey boy, Hamid, Blaise, Sara et Hugues. Je salue également les "jeunes" du GREEN, Pang, Dom, Abdou, pour les grandes parties de foot à la sap, Baptiste, JB et François le trio du bad du mercredi midi, Saed, Peyman et Mathieu. Je remercie aussi les doctorants du LEMTA, Max, Quentin et Thomas, ainsi que ceux du CRAN, Tommaso, Daniele, Prisca et Harry. Je souhaite bonne continuation dans la vie à toutes celles et ceux qui ont terminé leur thèse et bon courage pour la fin de thèse aux autres.

Je souhaite également en ces quelques lignes remercier mes amis de toujours qui m'ont soutenu de loin en me prodiguant leurs conseils et en me transmettant leur bonne humeur, David, Florent, Eleonore, Etienne, bb Gatien, Chalu, Ludo, Cardes, Olivier, Ioul, Houles, ainsi que les copains d'apéro de Nancy.

Enfin mes dernières pensées vont évidemment à ma famille, mes parents et ma soeur, qui m'ont toujours encouragé dans mes choix et qui ont été d'un soutien considérable durant ces années de thèse, ainsi qu'à Elodie, qui a été en première ligne ces trois dernières années pour me supporter et qui m'a aidé à garder le cap dans les moments difficiles.

Resumé en français

L'industrie automobile a considérablement évolué tout au long de son histoire, suivant les transformations technologiques ainsi que les politiques économiques et fiscales. Le tournant majeur de ces dernières années dans le secteur de la technologie du transport est lié à l'augmentation de la part de l'électrique dans la motorisation, tendance motivée par par la diminution de la consommation de carburant qui résulte de l'électrification des véhicules. Cette volonté de réduire la consommation de carburant fossile chez les constructeurs automombiles trouve son origine dans plusieurs facteurs, notamment l'impact d'un produit présenté comme plus écologique auprès des consommateurs, la chute du prix des batteries, ainsi que la nécessité de se conformer aux quotas d'émissions de gazs à effet de serre imposés par la législation européenne.

Différents degrés d'électrification de véhicule automobile existent. Le plus bas, le Stop-Start, est une solution hybride aujourd'hui équipée sur la plupart des véhicules neufs et dont l'action du moteur électrique se limite au redémarrage du moteur thermique. Le mild-hybrid, ou hybridation douce, est une évolution du système Stop-Start où la chaîne de traction électrique est active et apporte du couple au moteur thermique à chaque appel de puissance du véhicule, lors du démarrage ou d'une accélération. La technologie full-hybrid est la technologie hybride dont le degré d'éléctrification est le plus élevé, avec une chaîne de traction capable d'assurer seule la motorisation du véhicule en alternance avec le moteur thermique. En parallèle des technologies hybrides, les véhicules tout électriques se sont également largement développés, atteignants la barre du million de véhicules tout électriques neufs vendus dans le monde en 2018. Le scénario d'évolution du nombre de véhicules électriques dans le monde développé par l'Agence Internationale de l'Energie et basé sur les politiques mondiales actuelles en matière de transition énergétique prévoie même de dépasser les 100 millions de véhicules tout électriques ou full-hybrid d'ici l'horizon 2030.

Dans ce contexte d'électrification de l'automobile, le besoin d'optimiser les coûts de production chez les constructeurs automobiles reste grand, le secteur étant extrêmement concurrentiel. Une des solutions à la disposition des fabricants pour réduire les coûts de production d'un véhicule et de chercher à s'affranchir de certains éléments d'un système. En suivant cette logique, pour Valeo et son système mild-hybrid i-StARS, composé d'une machine synchrone à rotor bobiné à griffes et doté d'un stator double, la suppression des capteurs de courant permet de réduire les coûts liés à la fabrication du système de manière non négligeable. En effet, sur cette chaîne de traction destinée à être alimentée par une batterie de 12V, les courants statoriques de la machine sont élevés, avec des pics pouvant aller à 300A. Avec ses deux stators, un minimum de 4 capteurs de courant pour fort ampérage sont nécessaires.

L'alimentation de la machine en boucle ouverte permet d'éviter l'utilisation de capteurs de courant, mais le système n'est dans ce cas pas contrôlé et est sujet à des pics de courants risquant d'endommager le système. Afin de garantir le contrôle vectoriel de la machine, permettant de contrôler le couple mécanique en optimisant le vecteur tension de commande, tout en s'affranchissant des capteurs de courant statorique, il est necessaire de mettre au point une stratégie de commande sans capteur de courant de la machine. C'est cette problématique qui a fait l'objet de l'étude présentée dans cette thèse.

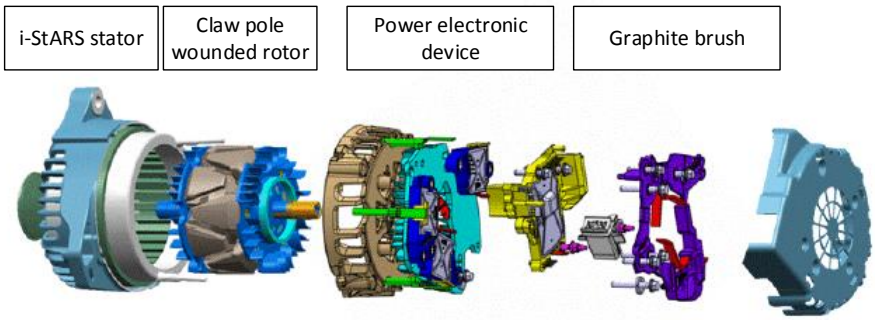

Vue éclatée du système i-StARS

Le projet LowCO2Motion+ dans lequel s'inscrivent ces travaux a été inité par de l'entreprise Valeo. Le but de ce projet mené en partenariat avec de nombreux acteurs industriels et laboratoire, dont le GREEN, est d'augmenter le niveau d'électrification du système i-StARS d'une application Stop-Start vers une application mild-hybrid, permettant ainsi de proposer rapidement un produit mild-hybrid aux constructeurs automobiles sans changer l'architecture hybride existante. Comme annoncé plus tôt, le rôle de l'étude confiée au GREEN qui a fait l'objet de cette thèse est de proposer une stratégie de commande sans capteur de courant d'une machine synchrone à rotor bobiné afin d'éviter l'utilisation de capteur de courant dans le système final commercialisé et ainsi réduire le coût de production de l'i-StARS.

Dans la littérature scientifique, la commande sans capteur mécanique est bien connue et souvent référencée simplement par l'appelation "commande sans capteur". C'est la stratégie de commande sans capteur la plus répandue, dû au fait que les capteurs de position mécanique sont encombrants et leur intégration sur la machine est relativement longue à cause du réglage nécessaire de décalage de l'angle électrique du stator par rapport au rotor. Plusieurs solutions de commande sans capteur existent, notamment basée sur l'estimation de la force contre électromotrice de la machine. Si les méthodes développées pour la commande sans capteur mécanique ne peuvent pas être appliquées directement dans le cadre de la commande sans capteur de courant, elles ont néanmoins été une source d'inspiration, en particulier celle basée sur l'utilisation d'estimateur non linéaire pour estimer la variable d'état de la vitesse de la machine. Des solutions de commande sans capteur de courant existent également dans la littérature mais dans des cas particuliers. En effet, les solutions proposées suppriment les capteurs de courant au niveau du stator mais utilisent un capteur de courant au niveau du bus DC de l'onduleur. La connaissance du courant du bus DC de l'onduleur ainsi que de l'état des interrupteurs de l'onduleur permet de reconstruire les courants dans le stator de la machine. Cette solution présente néanmoins des inconvéniants majeurs qui la rend inadaptée à l'application décrite par le projet LowCO2Motion+. En effet, les gradiants de courant du bus DC étant très grands dû aux commutations des semi-conducteurs, le capteur de courant DC doit être précis et avoir une large bande passante afin de mesurer les variations du courant DC. L'ajout d'un tel capteur annule donc le bénéfice sur le coût de production qu'occasionne la suppression des capteurs DC. En outre, un capteur à effet Hall sur un bus barre d'onduleur est encombrant, ce qui est indésirable dans le cadre d'une application embarquée.

Il a donc été choisi de mettre au point une solution de commande sans capteur de courant

qui ne nécessite pas de modifier le matériel existant. Le système i-StARS étudié est composé d'une batterie 12V, d'un filtre d'entrée composé d'un condensateur de 6mF, d'un onduleur 2x3 bras de MOSFETs et de la machine synchrone à rotor bobiné i-StARS. Le schéma du système est présenté ci-dessous.

Les mesures disponibles sur le système sont constituées du courant de batterie, de la tension d'entrée de l'onduleur, du courant d'excitation ainsi que de la position et la vitesse mécanique du rotor. Le système i-StARS étant un produit industriel, il n'était pas possible de travailler directement dessus, l'onduleur étant difficilement accessible car imbriqué sur la carcasse du moteur. Un banc d'essai présentant les mêmes caractéristiques que le système i-StARS a donc été mis au point au laboratoire. Sur le banc développé, la machine d'étude est la même MSRB que celle de l'i-StARS. Une autre MSRB fournie par Valéo a été utilisée comme machine de charge. Les MOSFETs de l'onduleur élaboré ont été choisis de manière à obtenir les même comportements que ceux utilisés sur le système i-StARS.

S'affranchir de la mesure des courants statorique n'est pas sans poser plusieurs problématiques. En effet le couple moteur est lié aux courants dans le stator, et le contrôle optimal du couple passe par une bonne connaissance des courants. Si les courants ne sont pas mesurés, il doivent donc être estimés en se basant sur un modèle du système. Cependant, un modèle ne peut représenter fidèlement la complexité d'un système réel, notamment lors des phasess transitoires de la machine où des phénomènes subtransitoires peuvent avoir lieu. De plus, l'usure des différents composants de la machine et de l'onduleur due aux contraintes mécaniques (températures, poussières ou humidité) et éléctriques (pics de courrants, forts gradiants de tension) peut changer les valeurs de ces composants. Il a donc été décidé de dresser, dans un premier temps de cette étude, un modèle du système à la fois simple et suffisamment précis pour être utile à l'estimation des courants statoriques.

Ainsi, un modèle électrique classique de machine synchrone a été élaboré, sans tenir compte du phénomène de damping dans les phases transitoires ni des phases sub-transitoires, qui alourdissent la synthèse du modèle sans apporter de précisions significatives. En revanche il a été décidé d'ajouter au modèle une cartographie de paramètres de la machine en régime permanent, ceux-ci étant sujets aux variations des points de fonctionnement de la machine. Une étude de sensibilité a donc été effectuée afin de déterminer quels paramètres électriques de la machine sont les plus sensibles. Le paramètre M correspondant à la mutuelle entre le rotor et le stator étant

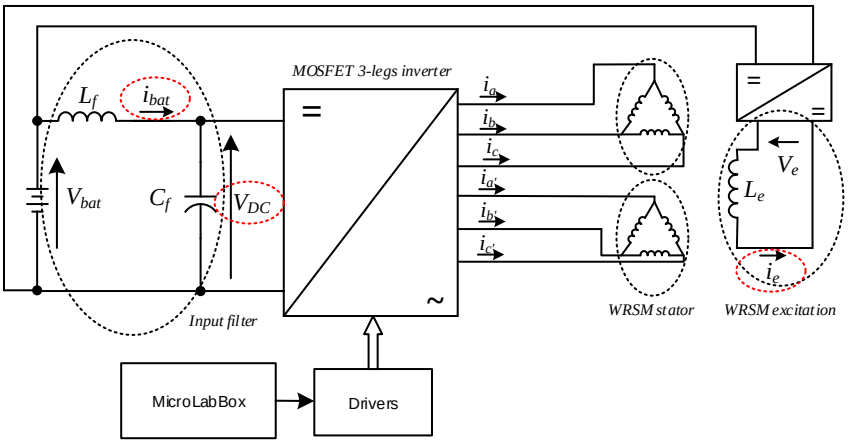

Schéma électrique du banc expérimental

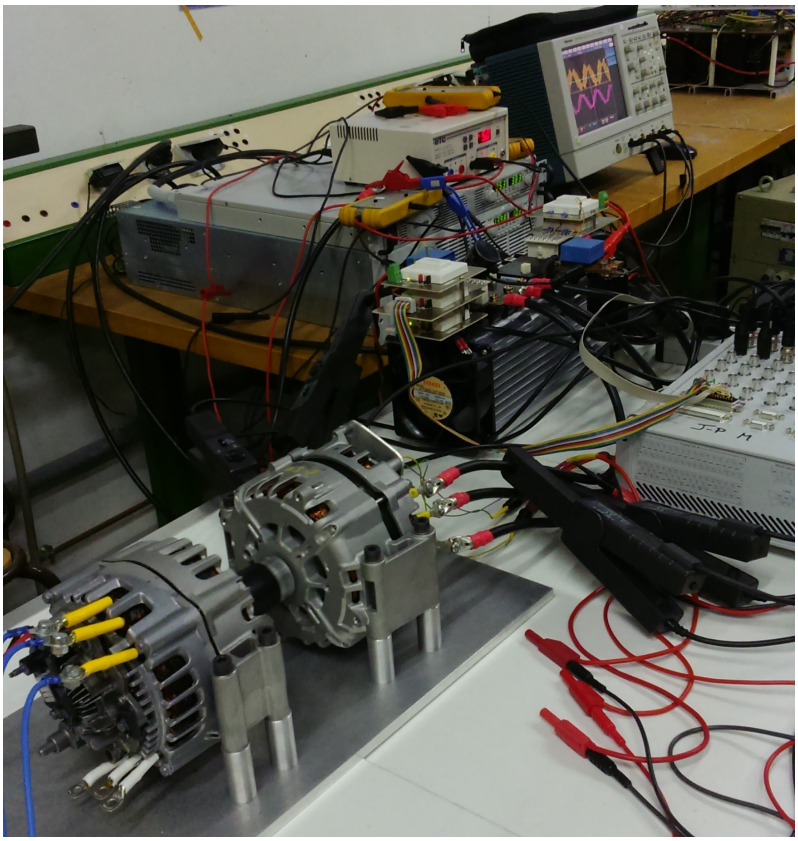

Photo du banc moteur avec au centre la machine i-StARS

le plus sensible, c'est sur ce paramètre uniquement que la cartographie s'est concentrée. Afin d'inclure les erreurs de modèle pouvant survenir sur les autres paramètres, un paramètre μ_M a été introduit sur l'équation du courant statorique d'axe q.

A l'aide d'un observateur, le paramètre introduit μ_M a donc été cartographié en fonction de plusieurs points de fonctionnement en régime permanent. Ces points de fonctionnements ont été définis en fonction de trois variables : la vitesse mécanique, le courant d'excitation et la charge mécanique de la machine. Lors de cette étape, la présence de capteurs de courants est nécessaire, car la mesure du courant d'axe q est utilisée dans la syntaxe de l'observateur du paramètre introduit μ_M. Le schéma électrique représentant l'étape de cartographie de μ_M est donné ci-après.

Afin de cartographier μ_M sur l'ensemble des points de fonctionnements en régime permanent de la MSRB, un procédé algorithmique a été élaboré. Dans un premier temps, les trois variables de point de fonctionnement sont initialisées à leur valeurs minimales. Le courant d'excitation est ensuite incrémenté d'une valeur définie selon les besoins en précision de la cartographie, dans notre étude un incrément de 2A a été sélectionné. Quand le régime permanent est atteint, la valeur de μ_M est enregistrée. Lorsque que le courant d'excitation maximal a été atteint, il est réinitialisé à sa valeur initiale et la vitesse de la machine est incrémentée. Le courant d'excitation est alors de nouveau balayé. Lorsque que la vitesse atteint sa valeur maximale, elle est également réinitialisée et la charge mécanique est incrémentée. Le procédé est alors recommencé jusqu'à ce que la valeur de charge maximale soit atteinte.

La cartographie de μ_M telle qu'elle a été réalisée à l'issue du procédé algorithmique est utilisable en l'état. Néanmoins, en fonction des incréments utilisés dans la cartographie, un phénomène de frontière de case risque d'apparaitre et de dégrader la précision de la valeur de μ_M. Afin d'éviter ce phénomène indésirable, l'extrapolation des données de μ_M en fonction de

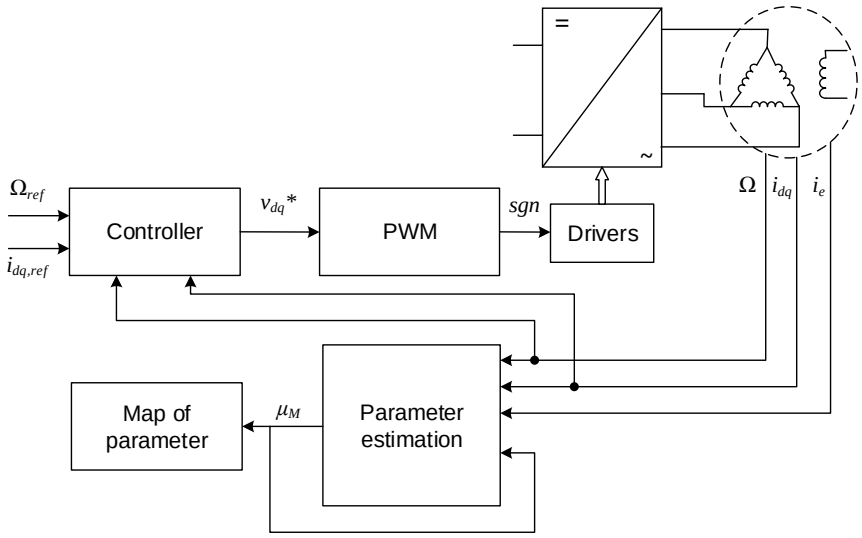

Schéma bloc de la stratégie de cartographie

la vitesse a été réalisée. L'extrapolation en fonction de la vitesse plutôt que la charge ou le courant d'excitation a été privilégiée car dans le système étudié, c'est la vitesse qui varie le plus fréquemment. La cartographie finale se présente donc sous la forme de fonctions de μ_M par rapport à la vitesse de la machine, réparties en sections de courant d'excitation de charge de la machine, comme explicité sur la figure suivante.

Seul, le modèle de la machine agrémenté de la cartographie du paramètre μ_M ne peut suffire à la reconstruction des courants, dû au fait que de nombreux phénomènes ne sont pas pris en

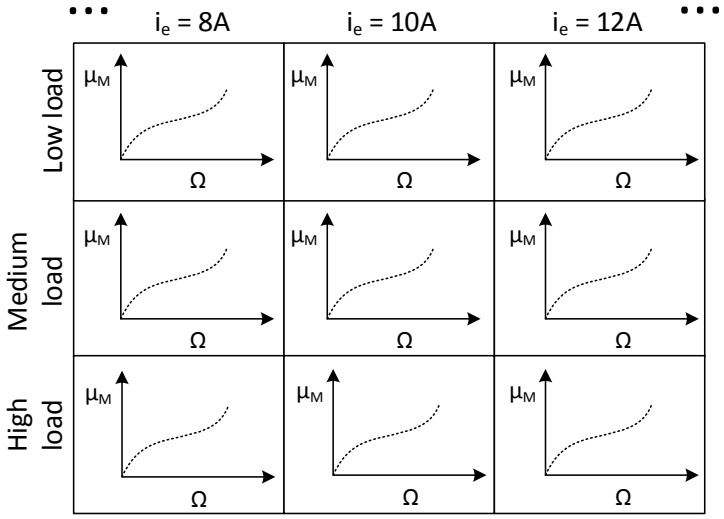

Schéma montrant la cartographie de μ_M par section de charge et de courant d'excitation en utilisant une fonction interpolée sur la vitesse de rotation.

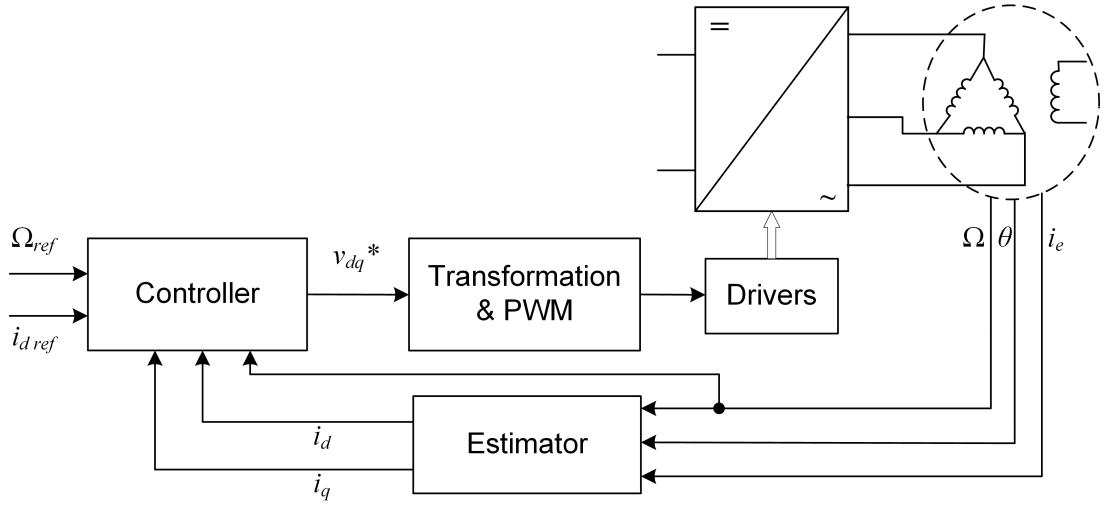

Schéma bloc du contrôle sans capteur de courant en utilisant un observateur.

compte. Pour cette raison, l'utilisation d'un observateur d'état a été étudiée afin d'estimer les courants statoriques à partir des mesures accessibles sur la machine. Ainsi, comme montré sur la figure ci-dessus, la commande en boucle fermée des courants statoriques se fait par l'intermédiaire d'un observateur d'état, les courants n'étant pas directement accessibles.

L'observabilité du système en utilisant les courants statoriques en sortie et les mesures de courants d'excitation et de vitesse en entrée est garantie par une démonstration basée sur les dérivées de Lie du système d'équations d'état. Plusieurs synthèses d'observateurs d'état ont alors été testés. Dans un premier temps, le filtre de Kalman étendu (EKF) a été testé. L'EKF est un observateur d'état bien connu des automaticiens et largement utilisé pour le filtrage de mesures et l'observation de variables d'état de systèmes non linéaires. Le principe de fonctionnement du filtre peut se décomposer en deux étapes : une première étape de prédiction, où le modèle d'état est utilisé pour calculer les courants à l'itération suivante, et une deuxième étape de mise à jour, où une prédiction d'erreur est calculée et sert à ajuster la prédiction des courants faite en première étape. Les résultats de simulation sans erreur sur les paramètres dans le modèle montre que les courants sont estimés avec précision.

Un autre estimateur d'état, dérivé d'un estimateur mis au point au laboratoire du GREEN pour l'estimation de paramètre mais modifié pour estimer des variables d'état dans cette thèse, a été réalisé et testé. Cet estimateur proposé est basé sur la convergence de fonctions de Lyapunov. L'avantage de cet estimateur est que la convergence exponentielle de l'estimation est garantie sur l'ensemble de la plage de fonctionnement de la machine. Sans ajout d'erreur de paramètres dans le modèle de l'estimateur, les performances de cet estimateur en simulation sont comparables au résultats d'estimation donné par l'EKF. En revanche, en présence d'erreurs de paramètre, l'EKF et l'estimateur proposé convergent vers des valeurs différentes des courants statoriques réels. Pour réduire la sensibilité de l'estimation des courants vis à vis des erreurs paramétriques, la définition de l'estimateur proposé a été légerement modifié. En plus d'estimer les variables d'état correspondant aux courants statoriques de la machine, deux paramètres sont introduits dans les équations d'états et estimés, un paramètre appelé Δ_Γ sur l'équation de la vitesse pour absorber les erreurs de nature mécanique et un paramètre appelé I_p sur l'équation de la tension DC pour absorber les erreurs de nature électrique. L'observateur proposé étendu estime donc à la fois les courants statoriques et ces deux paramètres introduits. Si les résultats de simulations en présence d'erreurs sur les paramètres électriques ne montrent pas d'amélioration par rapport aux estimateurs précédents, les résultats de cet estimateur en présence d'erreurs sur les paramètres

mécaniques sont précis et les estimations convergent vers les valeurs attendues. Au regard des résultats de simulation, cet estimateur a été privilégié lors des essais sur le banc expérimental.

Une autre stratégie d'estimation a été élaborée lors de ces travaux. Cette stratégie baptisée contrôle sans capteur de courant avec observateur proposé étendu (CSC-EO) propose de réaliser en parallèle l'observation des courants statoriques avec l'observateur proposé étendu et la génération du vecteur de tension de contrôle. Cette stratégie permet d'accélérer la dynamique de contrôle sans être limité par la dynamique de l'observateur. Les résultats de simulation montrent de bonnes performances dynamiques mais cette stratégie reste sensible aux erreurs de paramètres électriques.

Sur le banc expérimental, l'observateur proposé étendu a été intégré et couplé à la cartographie de μ_M décrite précédemment afin de bénéficier des améliorations de précisions apportées par les deux études. Ainsi la cartographie a été intégrée à l'observateur, et les changements du point de fonctionnement de la machine modifie la valeur du μ_M dans le modèle de l'observateur. Le schéma de contrôle utilisé sur le banc est présenté sur la figure suivante.

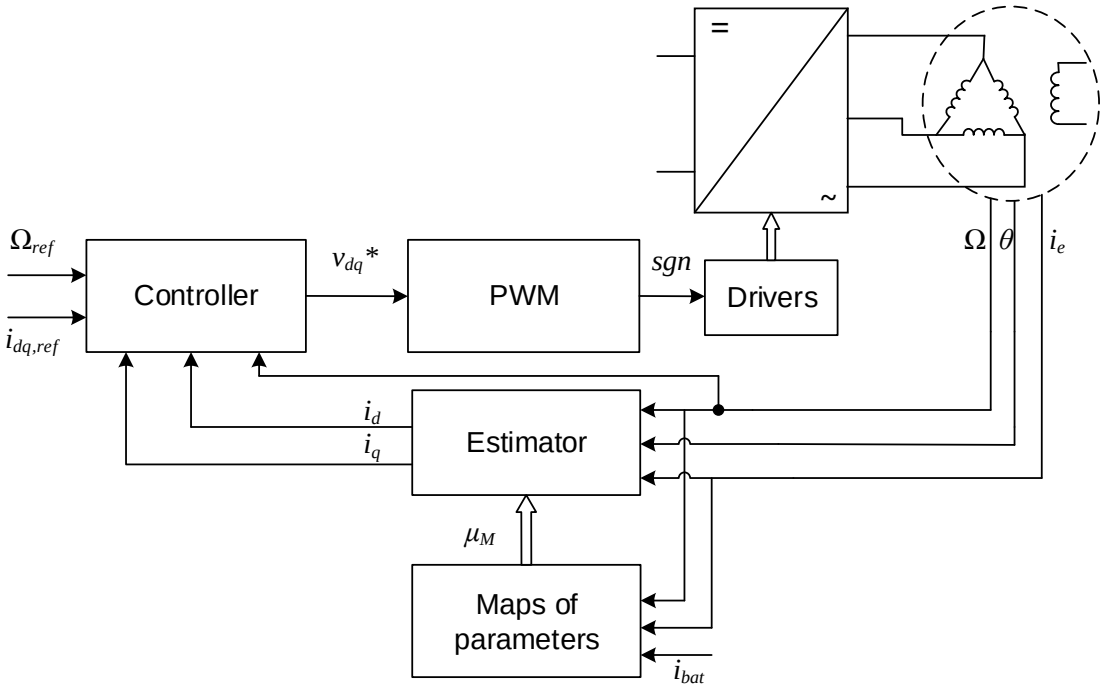

Schéma bloc du contrôle sans capteur de courant avec cartographie de μ_M intégrée.

Les premiers résultats expérimentaux de l'estimation des courants ont été obtenus lors d'un fonctionnement hors-ligne, lorsque l'estimation se fait en dehors de la boucle de contrôle (les courants mesurés sont contrôlés lors des tests dits hors-ligne). Comme le montrent les figures suivantes, les résultats en régime permanents présentent une bonne pécision avec des erreurs totales de moins de 10%.

Les résultats obtenus lors de régimes transitoires montrent que les points de fonctionnement en régime permanents au départ et la convergence du régime transitoire sont bien estimés. En revanche, plus les courants réels évoluent rapidement, plus l'erreur d'estimation sur les courants est grande. L'ajout de rampe sur les références de courant permet de réduire significativement les erreurs d'estimation comme les montre la figure ci-après.

En réalisant un test d'échelon de charge ou d'échelon de courant d'excitation, l'évolution

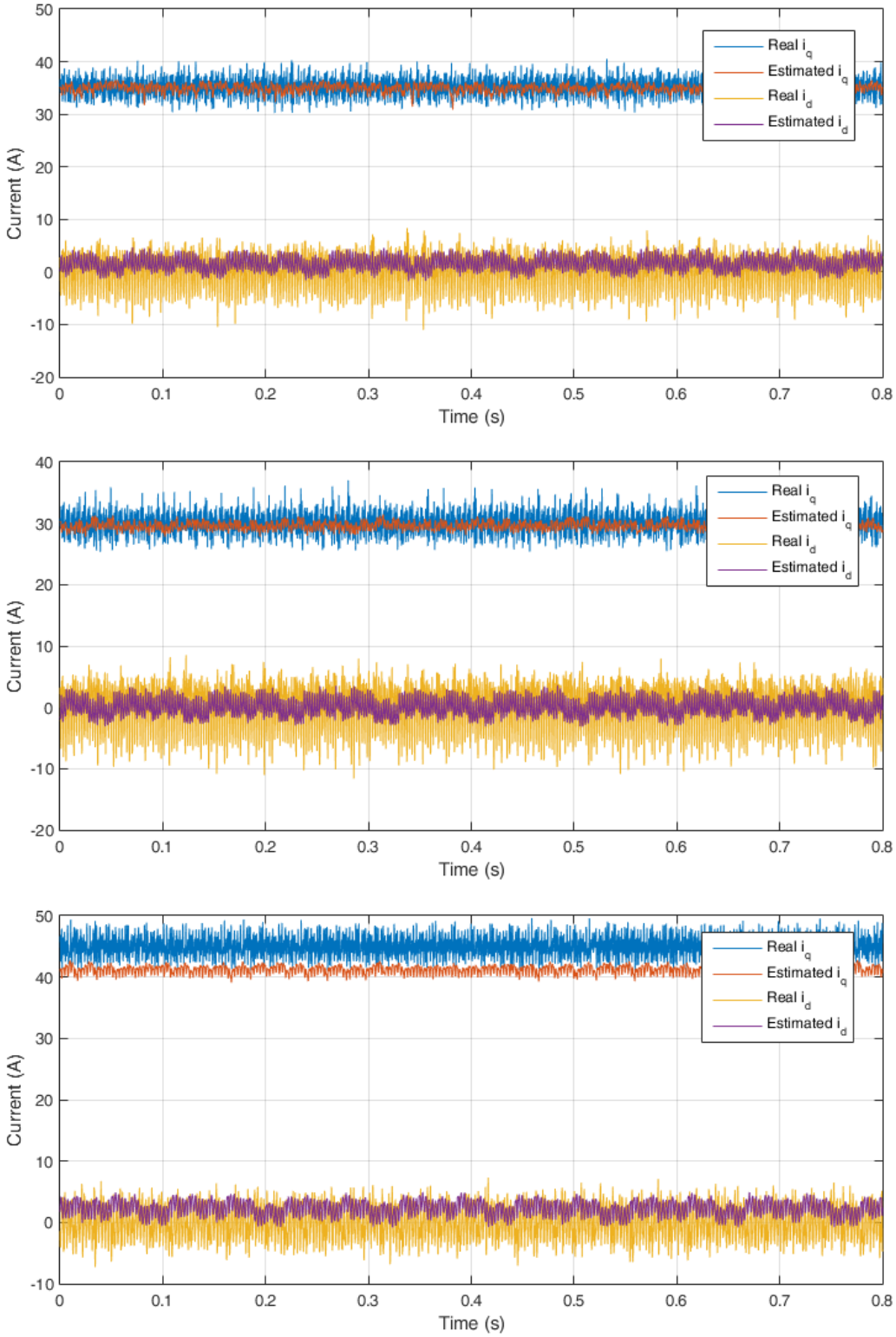

Observation des courants statoriques en régime permanent pour trois points de charge différents.

du μ_M cartographié permet d'obtenir une estimation qui reste précise lorsque le point de fonctionnement change, ce qui rend l'estimation robuste vis à vis des changements de points de

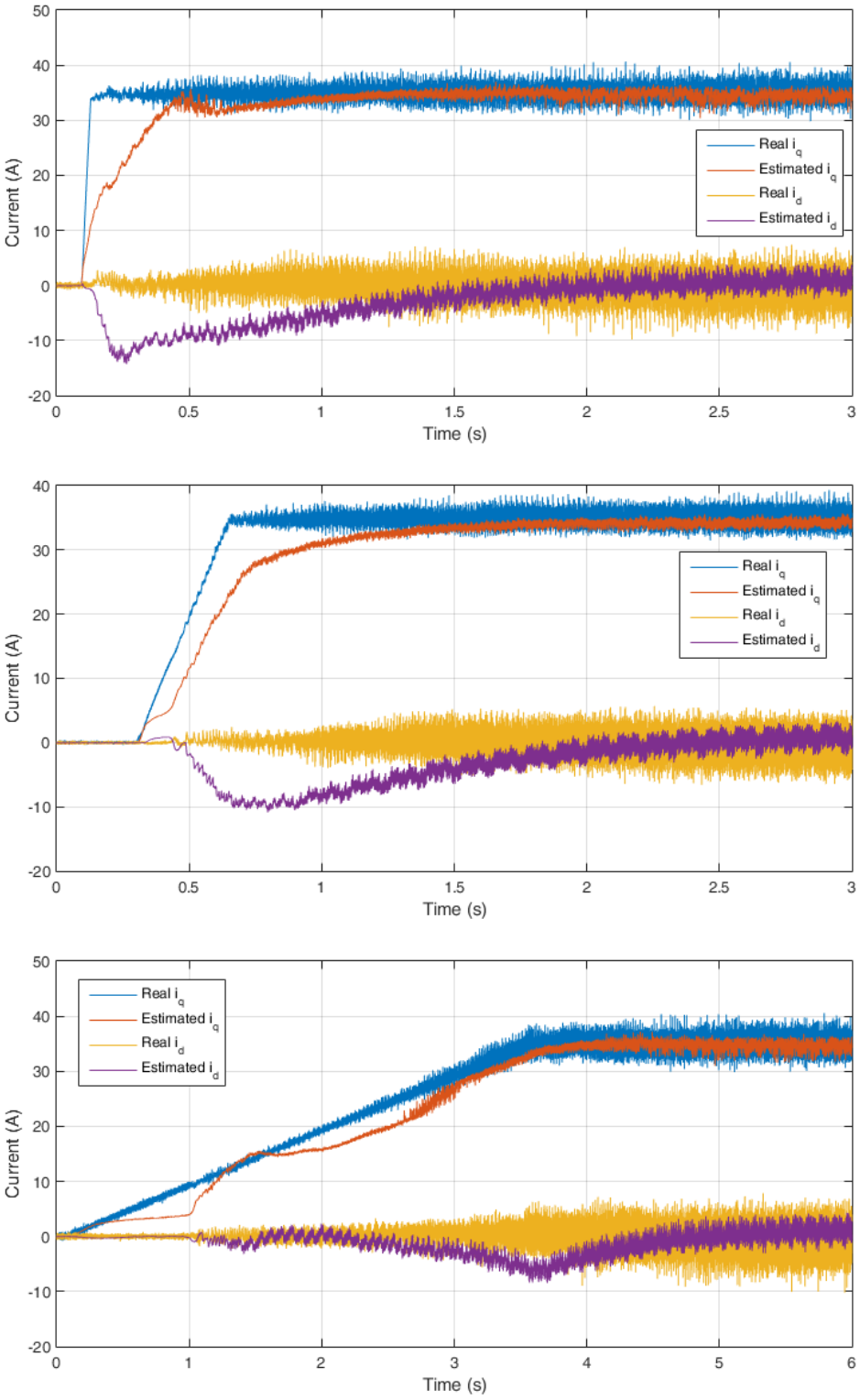

Observation des courants en régimes transitoires avec trois rampes de valeurs différentes sur les références de courants (haut : $1000A.s^{-1}$, milieu : $100A.s^{-1}$ et bas : $10A.s^{-1}$.

fonctionnement.

Des tests en ligne, c'est-à-dire que cette fois les courants estimés sont injectés dans la boucle

de contrôle ce qui correspond à une commande sans capteur de courant, ont ensuite été réalisés. Les résultats lors des régimes permanents testés donnent les mêmes résultats que lors des tests hors-ligne, avec une erreur totale maximale de 10% entre les courants estimés et les courants réels dans la machine. Les résultats en régime transitoire en revanche sont sujets à de forts pics de courant dans la machine. Cette différence entre la précision de l'estimation en régime permanent et en régime transitoire s'explique notamment par le fait que la cartographie de μ_M a été réalisée sur des régimes permanents de la machine i-StARS. Ces erreurs d'estimation ne sont néanmoins pas problématique d'un point de vue énergétique. En effet, un test comparatif entre l'énergie consommée lorsque la machine est contrôlée avec capteur et sans capteur montre que la sur-consommation énergétique avec le contrôle sans capteur de courant est très faible, même lors des régimes transitoires.

Contents

Introduction

In its history, the automotive industry has incredibly evolved, following the latest trends and economical policies. Nowadays one of the most significant shift in the automotive area, as well as all the means of transportation that rely on fossil fuels, is the increase of the share of electrification on vehicles' powertrain. This upward trend is motivated by the reduction of fuel consumption of the vehicles. This leads to a more environmental friendly product by decreasing the greenhouse emissions, bringing not only to a positive impact on potential consumers but also enabling automotive manufacturers to reach the CO_2 emission quotas.

Different degrees of electrification have been developed in the last decade. The most frequently found on vehicles is the Stop-Start solution. This is the lowest type of hybridization, the electric actuator activates only for the restarting of the fuel engine, which is stopped every time the vehicles is stationary. Mild-hybrid solution includes this feature and extends the role of the electric powertrain by activating it each time the vehicle needs a power boost, for example during accelerations phases or to pass a steep slope. Full hybrid solutions constitute the highest degree of electric hybridization and the electric powertrain can be used alone to drive the vehicle, allowing to completely turn off the main engine.

This thesis is included in the LowCO2Motion+ project, a european project involving several companies and led by Valeo. The aim of LowCO2Motion+ is to develop and extend the use of mild hybrid solutions for the automotive industry by improving the starter alternators structures and control strategies. The viability of this large project arises from european legislation, which has constantly lowered the CO_2 emissions quotas on the one hand, and hardened the penalties when those quotas are overstepped. In order to be able to meet these quotas, one possible technical solution for car manufacturers is to increase the use of electric actuators in the powertrain and reduce the part of the combustion engine that emits the unwanted greenhouse gases (GHG). In addition, the positive impact of a reduction of GHG emissions on customers is also a motivating factor which encourages manufacturers to use more electric cars and advertise on it. The technical solutions proposed by Valeo within the LowCO2Motion+ project aspire to meet the needs of car manufacturers and help them to reach the european quotas in a short time frame.

To do so, developing mild hybrid solutions have been Valeo first choice. As it has been stated before, mild hybridization is an upgraded technology compared to Stop-Start hybridization, which means the part of the electric powertrain in a driving cycle is more important. The technical solution proposed within the LowCO2Motion+ project has been to develop a starter alternator adapted to the mild hybrid functioning, the "i-StARS" (integrated Starter Alternator Reversible System). The topology chosen for the i-StARS machine is a doubly-fed claw pole wired rotor synchronous machine (WRSM). WRSM are sometimes also called electrically excited synchronous machine (EESM) in the scientific and technical literature. In order to optimize this kind of machine for mild hybrid application, a first study has been realized in the GREEN laboratory to enhance the finite elements modeling of a claw pole WRSM within Dr. Devornique's thesis work.

Competition between automotive suppliers being tough, reducing the overall costs of the products is an important issue for Valeo. The optimization of the machine topology allowed by

the finite element modeling of the machine is a good asset to limit the production costs, but an optimization on the electronic part of the system has also been considered. Therefore, among the possibilities to reduce the manufacturing costs linked to the electronic part of the system, the removal of the current sensors for the control of the WRSM is one of the most appealing. Indeed, on a doubly-fed machine, at least 4 current sensors are required to control the electric powertrain. As it will be detailed in chapter one, the system operates under low voltage (12 V) and the currents in the stator are high (up to 150 A) and the current sensors capable of measuring such large currents are rather expensive. Thus, the benefits of removing those sensors on the manufacturing costs are clear.

The work that will be presented in this thesis aims to realize a current sensorless control of the WRSM, which means to control the machine without using the stator currents feedbacks. Usually manufacturers prefer to remove the mechanical sensor because of its cost and the constraints linked to its assembly on the motor. In that sense, scientific literature on current sensorless control is scarce, leaving a large choice in the strategies to achieve the expectations. The main issue induced by current sensorless control is, as its name suggests, the lack of the stator currents measurements. Indeed the stator currents measures are essential for the control of the machine: they carry a lot of information useful for a feedback control or for the diagnosis of a machine. In addition, the model of the WRSM, as it will be demonstrated later, is difficult to know with precision, and the parameters of the passive components in the system may vary with the saturation, the temperature or the wear of the system. The control of the machine without the current sensors is not the only constraint imposed: as a matter of fact, the battery current draws during the transient phases of the machine need to be limited to guarantee a satisfying efficiency of the system.

The strategy of sensorless control that has been chosen to answer those issues and that will be detailed in this thesis, relies on the use of a state observer to estimate the stator currents using the available measures, and the injection of these estimated currents in a closed loop controller. This configuration has been favored mainly because of the fact that it is easy to implement on an existing control loop. Indeed, this solution enables to only add the current estimator in the control loop and use the existing measures to retrieve the phase currents.

To present the work that has been done on the current sensorless control, this thesis has been divided in four chapters, each one focusing on a different aspect of the study. The first chapter will present with more details the context of this study. To do so, mild hybrid technology will be explained with more details, and examples of existing systems will be given. A general overview of the machine control in the automotive industry will be conducted before focusing on sensorless control: an overview on the different existing techniques will be given for any kind of sensorless control (mechanical sensorless and special configurations of current sensorless). Finally specifications on the system the study is based on will be given, and the related issues that oriented the study will be listed.

The second chapter will be dedicated to the modeling of the system, consisting in a claw-pole WRSM, an inverter, an input filter and a 12V battery. First a modeling based on finite elements analysis (FEA) based on the work of Geoffrey Devornique will be briefly introduced. Then an electric approach of the modeling will be presented more specifically for a WRSM. The machine of the test bench developed in the laboratory will be experimentally identified in order to access the different parameters of the system. A study of sensitivity of the state model towards parameter errors will then be conducted, showing that the mutual inductance between the rotor and the stator of the machine can be problematic when errors on the identification of this parameter occurs. An online identification of an introduced parameter will then be conducted in order to realize a map of this parameter and reduce the developed model sensitivity towards parametric

errors.

The third chapter will be focused on the strategies of current sensorless control. As stated before, the choice has been made to use state observers to retrieve the stator currents of the machine. Descriptions of the state observers used, such as the Extended Kalman Filter (EKF) or another proposed state observer will be presented. These state observers will be tested and compared in simulations with and without model errors. Other strategies of current sensorless control that could be investigated in future work will also be evoked.

Finally the fourth and last chapter of this thesis will present the experimental results of the current sensorless control using a state observer designed in the third chapter connected with the map of parameter realized in chapter 2. First, the estimation will be performed off-loop: this means the controlled currents are the real ones and the estimated currents are only displayed to study their experimental behavior. Then a true current sensorless control will be shown, the estimation being performed in-loop. As it will be shown, the estimation results are very positive in steady-state, the estimations and the real currents showing few errors. The transient phases however are still subject to errors. A comparison between a control with and without the current sensors has also been conducted. This comparison will be based on the energy consumed by the different techniques on a characteristic load profile. This will allow to quantify the loss of efficiency induced by current sensorless control.

Chapter 1

General presentation of hybrid electric vehicles technologies and sensorless control

Contents

Introduction

The last three decades have been a major watershed for the automotive industry. Technology improvements are partly responsible for the constant mutation of what can be considered as one of the most competitive sector of the industry in the world, but another decisive factor is the governmental policies at the national or even international scale. In the past years, international NGOs recommendations for environmental actions have brought about the creation of COP, leading to the ratification of agreements on the reduction of greenhouse gas (GHG) emissions. The evolution of environmental taxes within the EU is presented in the 2016 eurostat report [1] and summarized in figure 1.1, showing that since 2009 the taxes on transportation have not ceased to increase. The decisions ratified in a COP are then meant to be applied by different authorities at the scale of a state or an association of states such as the European Union. Consequently to COP agreements, the EU have voted laws providing the creation of taxes on the emissions of GHG for the industries within european countries.

These taxes on GHG had a wide impact on the automotive industries. Since most of the vehicles running today are still powered by internal combustion engines (ICE), the transportation industry is responsible for an estimated 25% to 30% of the global greenhouse effect gas emission according to the International Energy Agency in its last Global EV Outlook [2] and [3]. Combined with the impact of environmental considerations on the consumers, these factors steered the automotive manufacturers towards the increase of the electrification of vehicles' motorization. Figure 1.2 illustrates this will to reduce CO_2 emissions of vehicles for different regions of the world, displaying the evolution of the CO_2 emissions prior to 2015, and the aimed evolution up to 2025 regarding the New European Driving Cycle (NEDC). NEDC was designed to reproduce the average driving conditions on the european roads, and most of the GHG and other particulates emissions of a vehicle were measured with the NEDC standard in Europe. It has however very recently been replaced by the Worldwide Harmonized Light Vehicles Test Procedure (WLTP). The two driving cycles are presented on figure 1.3. Battery Electric Vehicles (BEVs), also sometimes called full electric vehicles, benefit from a very positive impact on the consumers with regard to the eco-friendly factor, but suffers from the lack of infrastructure for battery recharging and the low autonomy compared to gas driven vehicles. In order to match

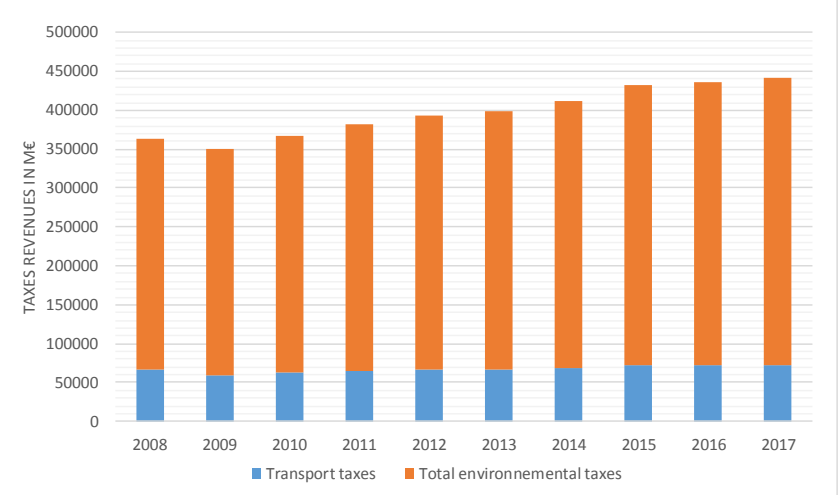

Figure 1.1. Evolution of environmental taxes revenue within UE from 2008 to 2017 (data sources [1].

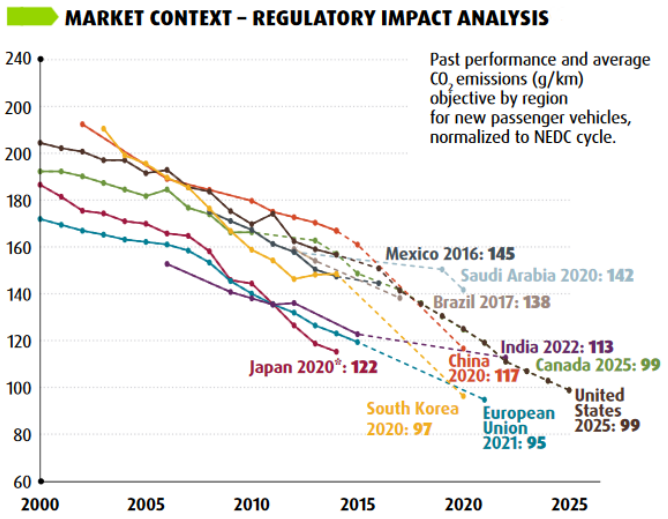

Figure 1.2. Evolution and expected evolution of the CO_2 emissions normalized to the NEDC cycle for a set of countries [4].

the EU gas emission quotas and the consumers needs, hybrid solutions have tend to emerge in the past few years.

The term "hybrid" in an automotive context is used when there is more than one type of motorization. Most of the time, the powertrain in a vehicles features a combustion engine (ICE) or an electric machine [6], and that is the hybridization of those two types of motors we will focus on for the rest of the study. Different levels of hybridization exist. The lowest is the "Stop-Start": the electric motor activates and apply torque to ICE only for the start of the main

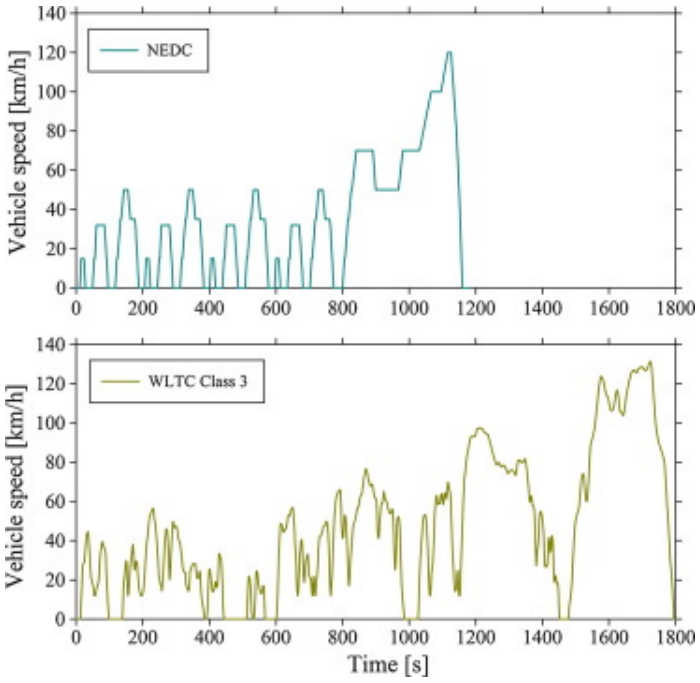

Figure 1.3. NEDC driving cycle (top) and WLTP's worldwide harmonized light-duty vehicles test cycles (WLTC) class 3b driving cycle (bottom) [5].

engine. The most advanced hybrid technologies are called full hybrid, where the motorization of the vehicle switches between the fuel driven powertrain and the electric powertrain. Plug-in Hybrid vehicles (PHEV), Extended Range Electric Vehicles (EREV) are examples of full hybrids and their functioning will be described later. An intermediate hybridization exists and is usually referred to using the term "mild-hybrid". These solutions propose to assist the main powertrain with an electric powertrain during transient phases of the vehicle, such as accelerations of the vehicle or anytime a peak of power is needed. This kind of hybridization is the one that constitutes the framework of this study. In addition with the different levels of hybridization, hybrid strategies decline in different architectures according to the type of connection between the ICE and the electric machine [6]. On the top of that, a large choice of different electric machines can be used in an HEV and a comparative study has been performed in [6]. This leads to a very large panel of hybridization solutions and a rigorous study is required when designing a HEV to combine the different elements of an electric powertrain to optimize the whole system.

The firm Valeo proposes a wide range of products related to automotive manufacturing. In this context, Valeo also manufactures and sells hybrid related products to the automotive main firms with a will to make their hybrid solutions adaptable to all light vehicles through their program Hybrid4all [7]. Among other products, Valeo has developed a mild-hybrid system to be supplied by a 12V-battery, called the i-StARS, within the LowCO2Motion+ project. This system is composed of an AC motor, a doubly fed Wound Rotor Synchronous Machine (WRSM), supplied by two 3-leg inverters and connected to the 12V battery when mounted on a vehicle. A full and detailed description of this system, constituting the electric powertrain, is made in chapter 2. More recently Valeo also oriented their research on 48V-battery supplied mild-hybrid systems.

Because of the very competitive nature of the automotive industry, Valeo puts constant efforts in the reduction of manufacturing costs. This traduces in optimization studies in order to cut on the costs in every step of the manufacturing of a product, from the design to the industrial production. For the i-StARS system, Valeo set the objective to propose good performances for a reduced cost. With that aim in mind, Valeo proposed to remove the current sensors on the phases of the i-StARS machine. In order to keep good performances, the study realized within the frame of this thesis proposes to use state observers to retrieve the non measured phase currents. The goal is to use vector based controllers with the observed phases currents as feedback, instead of the measures of the currents.

This chapter will first give details about the context of this study. A presentation of the different types of thermal/electrical hybridization will be realized, before focusing on the mild-hybrid solution and more specifically the LowCO2Motion+ project, that set the frames of the work realized. In a second part, the existing solutions for the control of mild-hybrid electric powertrain will be introduced, more specifically the classic vector based controllers and the six-step controller. In a last section, an overview of the different existing solution of non measured variables observation will be proposed, especially those developed for mechanical sensorless control, and a current sensorless control realized in a specific configuration.

1.1 Context of the study

As stated in introduction, the need for Valeo to remain competitive in the automotive industry led the firm to optimize every possible costs on a product. Valeo started to propose hybrid solutions in 2004 with Stop-Start systems, and extended their hybrid solution product range to mild-hybrid in 2010. In a process of manufacturing costs reduction, Valeo proposed two studies in link with each other to the GREEN laboratory within the framework of the LowCO2Motion+ project: one focusing on the architecture optimization of the WRSM and one (resulting in this thesis) aiming to remove the current sensors of the stator of the WRSM. In this section, the

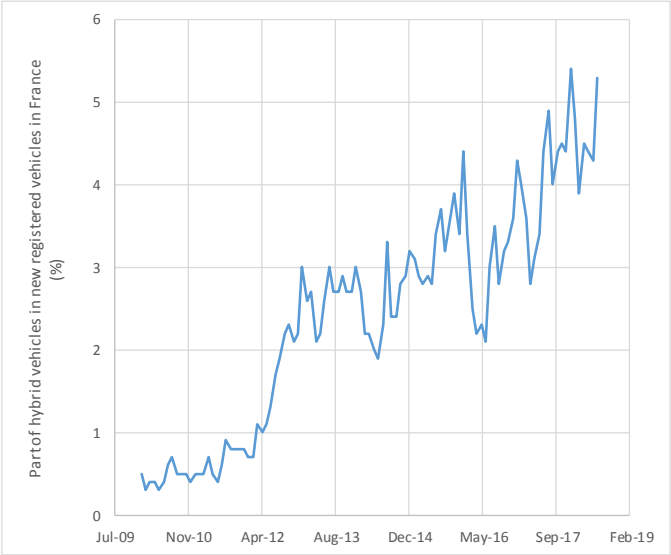

Figure 1.4. Evolution of the part of hybrid vehicles registered in France from 2010 to 2018 [8].

general context of the study developed in this thesis will be detailed by giving an overview of the different level of ICE/electric hybridization for automotive applications before developing the mild-hybrid strategy. More specifically, the LowCO2Motion+ project will be presented in order to grasp the motivations that resulted in the proposition of this study.

1.1.a Presentation of electrification solutions for automotive application

Electrification of vehicles is a trend that has been continuously growing in the automotive industry since the last three decades. Historically the first electric vehicles where developed in the 1830's, in parallel with the ICEs and expended continuously to reach a selling peak in the beginning of the 1900's, capturing up to 28% of the US market [9]. The EV market then dramatically depleted in the first half of the 20th century due to the sharp decrease of the oil prices and an aggressive commercial strategy performed by the US oil industry and the ICE vehicles manufacturers. A renewed interest in the EV technology occurred in the mid 1970's due to the OPEC oil embargo that lead to a large oil price increase, but the first hybrid car that has been widely commercialized and that truly experienced a great popularity is the Toyota Prius, released in 1997. The part of hybrid vehicles among the worldwide car fleet has increased with regularity since then.

Figure 1.4 shows the evolution of the number of registered cars featuring hybrid technology from 2009 to 2018 in France, showing that HEV have experienced a regular growth since 2010. The worldwide sales of full electric cars have also been constantly increasing since 2010, as it can be seen from the graph on figure 1.5. This trend reflects both the continuous decrease of the EV prices and the growth of environmental considerations from the consumers and their will to reduce their greenhouse gas effect emissions, electricity being usually pictured as a "green" energy. In figure 1.6, the graph presents the predicted evolution of the worldwide number of EV on the road from 2017 to 2030 according to two different scenarios. The first scenario, the "New Policies Scenario" takes into account the existing policies and measures that governments around the world and the future ones that have been officially announced. The second scenario "EV30@30 Scenario" is based on the projections if the different countries in the world follow

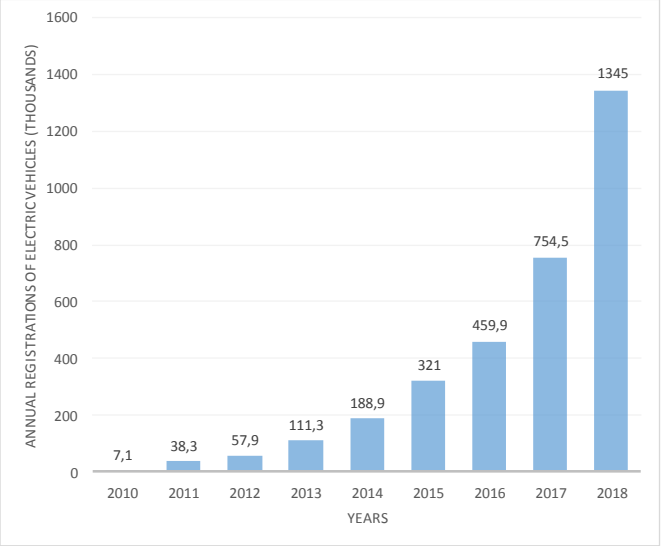

Figure 1.5. Evolution of the annual worldwide new BEV registrations between 2010 and 2018 [10].

the recommendations made by the Paris Agreements in 2016. Both of the trend forecasts a significant growth of the EV market, all technologies included, reaching by 2030 more than 120 million vehicles for the "New Policies Scenario" and up to 220 million vehicles for the "EV30@30 Scenario", making vehicle electrification unmissable in the automotive industry.

There is however a large amount of different hybridization. A comprehensive study of the different hybrid strategies is presented in [6]. This study presents the different architectures of HEV, it also introduces different electric machine topologies' strong and weak points for a hybrid application. As it will also be presented, the levels of hybridization, which correspond to the power rate of the electric powertrain compared to the ICE powertrain, can differ.

Full electric vehicles or Battery Electric Vehicles (BEV) do not belong to the hybrid category since they only have one electric powertrain. They constitute nonetheless the highest level of electrification in a vehicle. Figure 1.5 shows that the sales of electric vehicles has known a

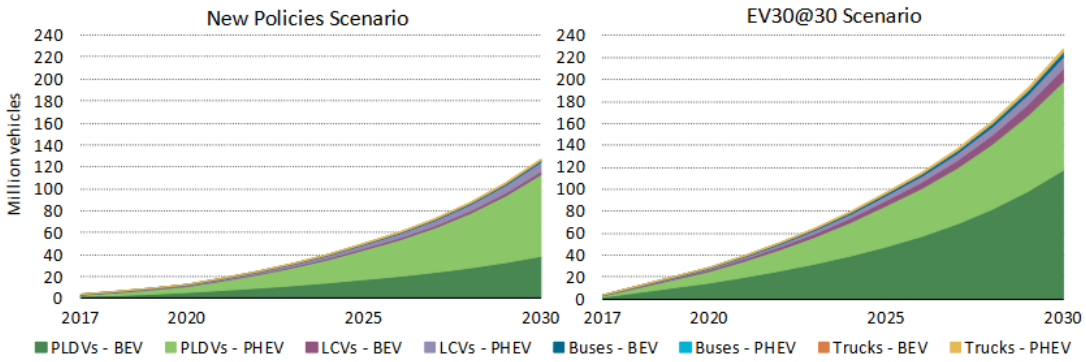

Figure 1.6. Global EV stock by scenario [2]. PLDV: Passenger light duty vehicle; LCV: light commercial vehicle; BEV: Battery Electric Vehicle; PHEV: Plug-in Hybrid Electric Vehicle.

considerable growth between 2010 and 2018, the number of new registrations being multiplied by a hundred and exceeding the million in 2018. Most of the recently designed BEVs are supplied by Lithium-ion and lithium polymer batteries since they have a high energy density compared to their weight, but other technologies are common, especially lead-acid, NiCd and nickel-metal hybrid batteries [11].

One of the main deadlock with full electric vehicles for customers is that the prices of those cars increase with the kilometer range. To be more precise, the price increases with the energy storage capacity of the battery pack, and the distance that can be traveled depends directly on the energy storage capacity of the battery pack for a given weight. In 2016, the Nissan Leaf could travel 250 km with a battery pack of 30 kWh while the Tesla S P100D has an operating range of 600 km for a 100 kWh battery pack [12]. According to Bloomberg New Energy Finance in [13], the average part of the price of the battery pack in the total price of a BEV reached 48% in 2016. However the latest trends seem to suggest that the Li-ions battery price per kWh is decreasing. Indeed from figure 1.7, the average cost of a battery in 2010 was \$1000/kWh and it dropped at \$300/kWh in 2016. A more precise estimation on the future costs of Li-ions batteries applied to EV applications is shown on figure 1.8 and detailed in [14]. The estimations based on economic models predict the battery costs to continue its decrease to reach less than a \$100/kWh, allowing the electric vehicles of all nature to absorb the price gap with the ICE powered vehicles.

In spite of this decrease of the battery cost per kWh, the spread of the BEV is held back by scarce charging stations in most of the world regions. Based on International Energy Agency figures, Forbes magazine [15] claims that there are great disparities between the countries: France for example has an average of 1.5 charging stations per 100 km on its territory, while it raises to 19.3 charging stations per 100 km in the Netherlands, and even though the United States have seen the number of EV sold increase sharply in the past few years, there are still only an average of 0.9 charging stations per 100 km in this country. To sum up, one of the main levee to increase the EV industry is the development of charging stations amount and efficiency. The time needed for a full battery charge also need to be reduced to be appealing for customers.

In parallel of BEVs, hybrid vehicles also feature an electric powertrain but it is mounted in association with an ICE. The advantage of hybrid vehicles compared to BEVs is that they do not need to have their battery packs electrically recharged in a charging station, except for the Plug-in Hybrid Electric Vehicles (PHEVs). Indeed the charging of the car battery is performed

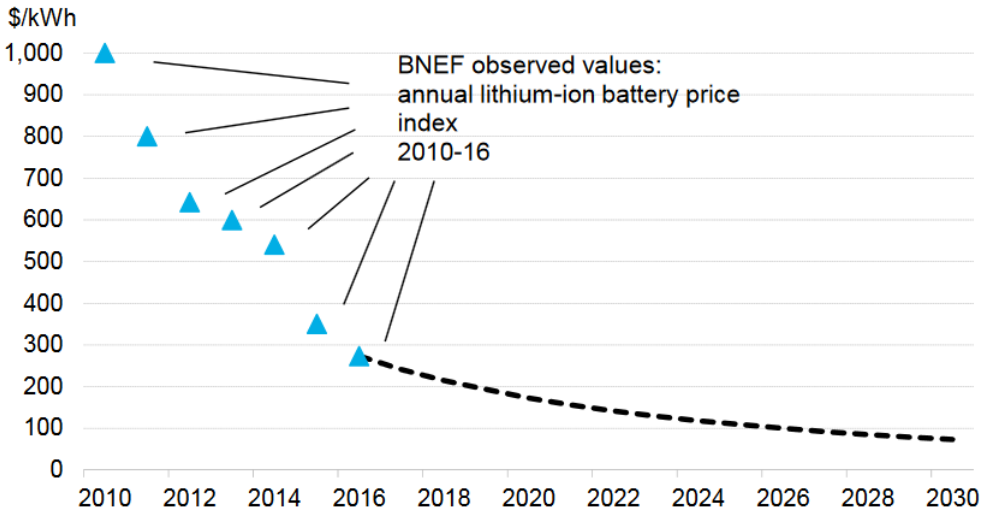

Figure 1.7. Evolution of the Li-ions battery pack cost/kWh from 2010 to 2016 and the expected tendency until 2030 (dot line) (BNEF = Bloomeberg New Energy Finance) [13].

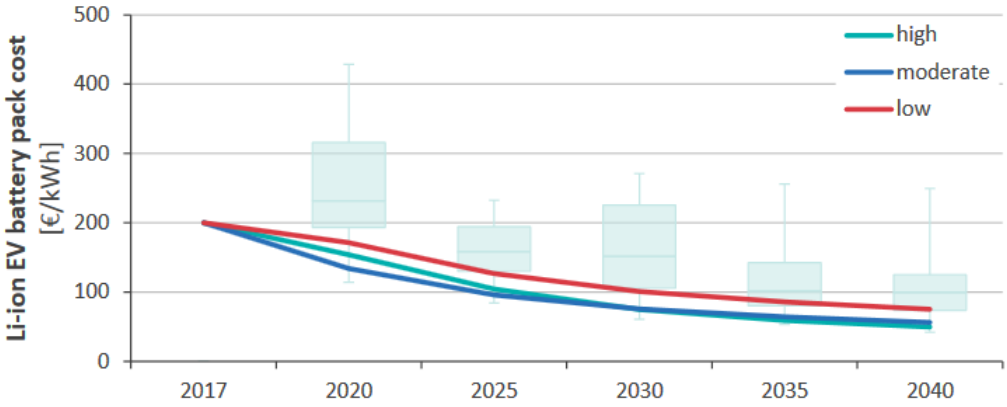

Figure 1.8. Evolution of the Li-ions battery pack cost/kWh for EV application after 2017 according to three models: high predicting the highest price drop, moderate and low predicting the lowest price drop [14].

when the electric powertrain is not in a motor mode but in a generator mode.

The lowest level of ICE/electric hybridization is the Stop-Start hybridization. Valeo started developing and commercializing its Start-Stop technology solution in 2004. This hybrid system is designed to completely stop the combustion engine each time the speed of the vehicle is null, and restart it with the electric motor (called "starter-alternator" by Valeo) when the driver press the accelerator pedal. This solution is efficient to reduce the CO_2 emissions for city trips for example, or any journey where the vehicle stops often. For its Stop-Start system with the i-StARS starter-alternator, Valeo claims a reduction of fuel consumption of 6% based on the WLTP profile (see figure 1.3, and up to 15% on a dense urban traffic drive. This kind of hybridization has been first developed in the early 80s, but it has been used widely only since the end of the 2000s, boosted by EU regulations on CO_2 emissions (see figure 1.1).

On the other extremity of the hybridization spectrum lies the full hybridization. This is the kind of hybridization that is the most well known to consumers. This solution is available in many forms, but the principle is the same: the vehicle alternates phases where the combustion engine drives the car and recharges the battery pack through the electric machine (in alternator mode) with phases where the combustion engines is stopped and the vehicle is driven by the electric powertrain. Among full hybrid cars, the most famous example is the Toyota Prius, which were very successful: more than 1.2 million of units have been sold worldwide between 2003 and 2009. The battery pack being charged during ICE cycles, those cars do not need to be plugged on a charging station, which is a strong asset for the customers in regions where charging stations are scarce.

More recently, a new trend of hybrid has emerged on the market, the Plug-in Hybrid Electric Vehicle (PHEV). This hybrid technology gives an even more increased role to the electric powertrain. The principle of PHEV is to drive the vehicle with the electric powertrain only, and charging the battery through an external source (charging station). The combustion engine's role in PHEV is either to serve as a backup solution if the battery is empty to power the wheels, according to the architecture. In Extended Range Electric vehicles (EREV), the principle is almost the same than PHEV, but the combustion engine is undersized and only used to charge the battery pack, it cannot be used to drive the vehicle.

Between stop-start hybridization and full hybrid technologies lies the mild-hybrid solutions. This type of hybridization will be described with more details in the next paragraph, since it is the application of the LowCO2Motion+ project led by Valeo.

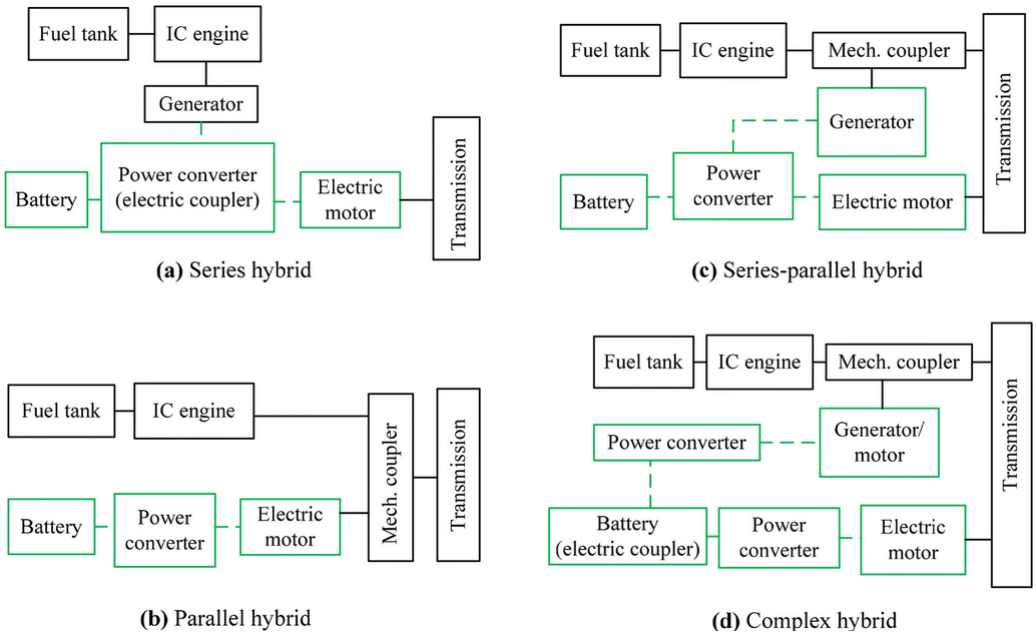

Figure 1.9. Four different possible coupling between the ICE and the electric powertrain [6].

All the different level of hybridization presented above can be designed differently according to how the electric powertrain is connected to the ICE. Figure 1.9 from [6] illustrates the four main existing architectures. Series hybrid architectures use the electric motor only for the traction. The ICE is connected to a generator to produce electric energy then used for traction or to recharge the batteries. This architecture allows the ICE to be operating at all time at its optimal operating point, since it is disconnected from the wheels, resulting in an increased overall efficiency of the ICE powertrain.

In parallel hybrid architectures, the only connection between the ICE and the electric powertrain is through a mechanical coupler. The HEV can be driven by each one of the powertrain alone or together, depending on the strategy and the level of hybridization of the vehicle. This is the most commonly found architecture in HEV nowadays due to the facts that it can be applied to all level of hybridization and it needs only one electric motor for traction power and battery charging through the ICE or regenerative braking, where two are needed in the series HEVs [16].

The series-parallel hybrid, as its name suggests, is the combination of the series hybrid and the parallel hybrid. The power from the ICE to the wheels can either be mechanical (when connected directly to the transmission) or electrical (when connected to the generator to supply the electric powertrain). This architecture combines the advantages of both the series and parallel architecture, it is however usually more difficult to design. The well known Toyota Prius features a series-parallel architecture. The complex hybrid architecture is similar to the series-parallel, except that the electric power flow between the ICE and the electric motor is bidirectional, meaning that torque can be supplied by the electric machine to the mechanical coupler. This architecture is more rare due to its complexity. Table 1.1 sums up the different architectures characteristics and the usual associated type of HEV.

1.1.b Details on Mild-hybrid systems

A lot of hybrid solutions exist and are currently commercialized and mounted on vehicles. A level of hybridization exists between full hybrid and Stop-Start solutions presented in the previous section, subsequently called "mild-hybrid" solutions.

Architecture	Efficiency [6]	Complexity	Size of components	Type of HEV
Series	1	1	4	Full HEV, PHEV
Parallel	2	2	3	Stop-start, mild, full HEV
Series-Parallel	3	3	2	Full HEV, PHEV
Complex	4	4	2	Full HEV, PHEV

Table 1.1. HEV architectures characteristics. '1' = low, '2' = average, '3' = high and '4' = very high.

"Mild-hybrid" is generic term used for the category of hybrid vehicles that are always driven by the combustion engine (unlike full hybrids) but where the electric powertrain is more often used than only for the start of the vehicle in Stop-Start technologies. Nevertheless the principle of the mild-hybrid solutions developed by Valeo is an extension of the Stop-Start: use the alternator of a vehicle and use it as a motor when required. If the Stop-Start only use the starter-alternator during the ignition of the combustion engine, mild-hybrid applications extend the role of the starter-alternator to other phases of the functioning of a vehicle.

Indeed, mild-hybrid technology proposes to increase the number of conditions where the starter-alternator is used as a motor to any phases where a torque draw is required. To illustrate this with an example applied to a personal vehicle, in a mild-hybrid application the electric powertrain would be activated any time the driver needs a torque boost: the start of the combustion engine, a sudden acceleration or to pass a steep road. To sum up, the role of the electric powertrain in mild-hybrid applications is to reduce the peaks of fuel consumption of the main engine during the phases when torque boosts are needed by providing the torque needed to the main engine.

The purpose of this technology is to extend the reduction of CO_2 emissions from 6% (for the Stop-Start technology) up to 12% on the NEDC cycle [17]. This is a very attractive achievement for the automotive companies in the context of increased taxes on GHG emissions described in the beginning of this chapter. In addition, the mild-hybrid solution proposed by Valeo is convenient and requires few modifications from the Stop-Start hybridization: the machine is the same (the i-StARS), the voltage used to feed the inverter is 12V which is the usual battery voltage in a vehicle and the connection between the ICE and the electric powertrains is made through a belt as it is represented on figure 1.10. On this figure, the transmission belt performing the connection between the ICE and the electric powertrain can be seen, as well as the battery pack.

However a new trend has emerged about mild-hybrid technology: the 48V mild-hybrid. The principle is the same, it is still a mild hybridization, but the electric powertrain is supplied with a DC voltage of 48V instead of the usual 12V. The 12V battery is not replaced and it is still used for the on-board network and a 48V battery linked to the powertrain is added on the vehicle, and connected to the 12V grid through a DC/DC boost converter. This is a conveniant solution since it can be easily be mounted on an existing vehicle without modifying all the on-board network. 48V mild-hybrid is appealing for an automotive supplier such as Valeo, because it allows increasing the power the machine can deliver for the same current values in the machine and consequently it allows to increase the role of the electric powertrain and increase the fuel consumption reduction to 12-15% for light cars [18].

Table 1.2 sums up and compares the different level of hybridization presented in this chapter. The Hybridization Factor (HF) defined in [19] used in the table is described by the following

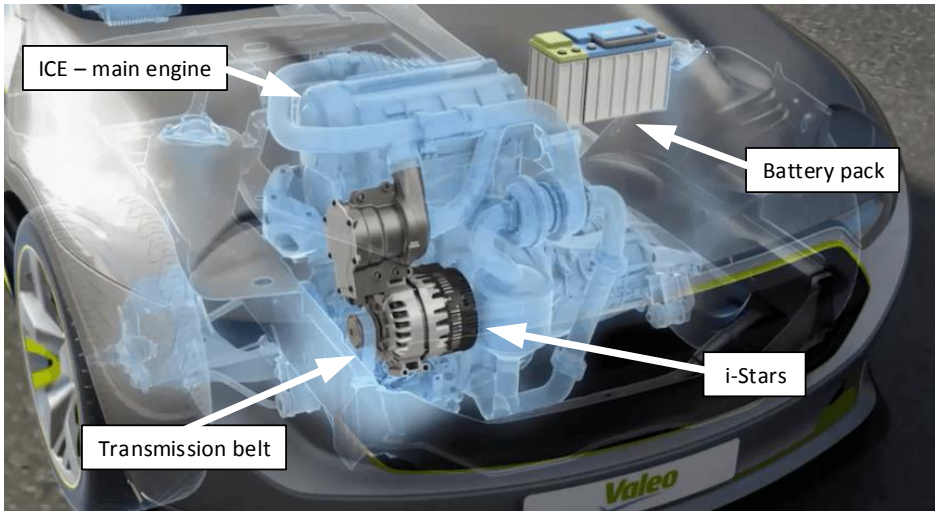

Figure 1.10. Valeo's mild-hybrid powertrain representation: battery pack (top right) and WRSM connected to the ICE with a transmission belt (source: Valeo).

equation:

$$HF = \frac{P_{EM}}{P_{EM} + P_{ICE}} \tag{1.1}$$

With P_{EM} the maximum power of the electric machine and P_{ICE} the maximum power of the ICE, the maximum total traction power of the vehicle being defined by $P_{vehicle} = P_{EM} + P_{ICE}$. Note also that the GHG emissions depend on a lot of variables. If the production of electricity is taken in account, the GHG emissions linked to the production of electricity will depend on the technology on which relies the electric production: nuclear plants, coal or renewable energy won't have the same impact on GHG emissions. This topic is well described in [20].

Now that the concept of "mild-hybrid" has been clarified, the next paragraph will focus on the description of the overall mild-hybrid project initiated by Valeo in which the current sensorless study presented in this thesis belongs.

1.1.c The LowCO2Motion+ project

As stated before, the i-StARS starter-alternator was originally designed for Stop-Start application but was later redesigned to reach mild-hybrid performances within the LowCO2Motion+ project. This large project, initiated by Valeo, gathered several actors of the automotive and power electronic industry and research laboratories. It was financed by french government through the "Banque Publique d'Investissement" (BPI) and the "Agence de l'Innovation Industrielle" (AII). The main goal of this project was to propose an appealing mild-hybrid solution for the automotive manufacturers with an already existing system, the i-StARS, which can be seen on the exploded view of figure 1.11.

The advantages of reusing an existing system are obvious for Valeo. There is indeed no need to start a design from scratch: the machine already exists and is already produced industrially. This saves a lot of time and design costs to Valeo. In addition, Valeo can easily propose the solution to automotive manufacturers that already use the i-StARS, since the upgrade to the mild-hybrid performance does not require to change the electric powertrain design and size.

Type of electrified vehicles	Level of electrification (Hybridization Factor HF)* [19]	Ability of charging from external source	GHG emissions reduction compared to ICE [20]
Stop-Start	<10%	no	1
Mild-hybrid	10-30%	no	2
Full hybrid	>30%	yes	3
BEV	100%	yes	4

Table 1.2. Level of electrification comparison. '1' = low, '2' = average, '3' = high and '4' = very high.

This allowed Valeo to rapidly develop its mild-hybrid technology with the i-StARS. In parallel different studies have been conducted by Valeo or ordered to other firms and research laboratories in order to stay competitive. Among those studies, the "i-StARS Evolutions" (a part of the LowCO2Motion+ project) main challenges were to optimize the i-StARS system for mild-hybrid application by reducing the Electromagnetic compatibility (EMC) constraints, the bulk of the system, the voltage drop at the start of the machine and the costs of production. It also aimed to extend the mild-hybrid range of the system. The firms and research laboratories in links with the i-StARS evolution project are Eolane for the electronic micro-assembly of the control unit, the GREEN laboratory worked on the control laws and the architecture optimization of the i-StARS, TEMPO laboratory worked on the thermal modeling of the system and IFPEN studied the pulse width modulation (PWM) signal generation for the controller.

1.2 Existing control solutions for mild-hybrid

As it has been seen in the previous section, the control laws and the modulation solution have been subjects to studies and researches within the LowCO2Motion+ project in order to improve

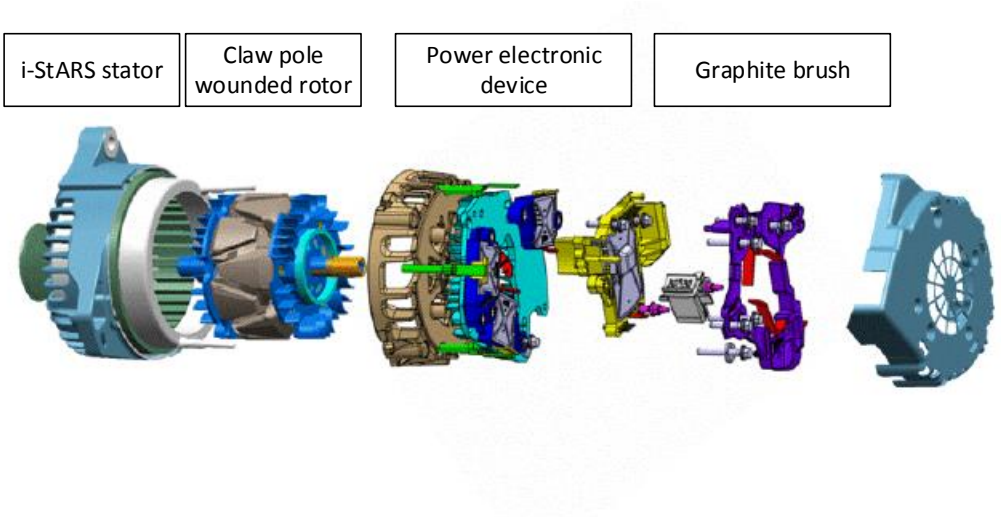

Figure 1.11. Exploded view of the i-StARS system (source: Valeo).

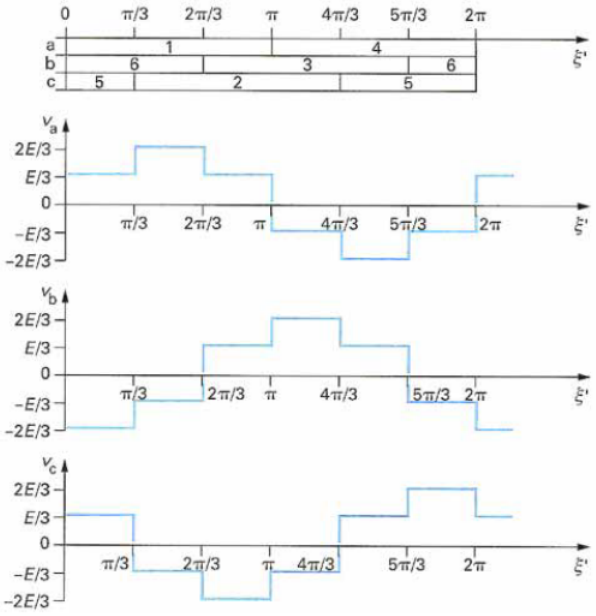

Figure 1.12. Switching pattern and line voltages of the six-step controller [21].

and extend the existing system. Control strategies using PWM have been investigated for the project since it is a very commonly used modulation strategy for machine control but other types of signal generation techniques exist for machine control, such as the six-step controller or the Space Vector PWM (SVPWM). In this section the PWM principle will be explained and the six-step controller technique will be briefly introduced as well, since it could also be used for HEV application.

A valuable description of the six-step controller is made in [21]. This is an easy solution for machine control that is appealing for automotive application such as Start-Stop technology or mild-hybrid vehicles mainly because it is easy to implement and it does not require an expensive micro-controller unit, since, for a stator, only six switches are performed during a whole cycle.

The six-step controller is usually used for AC machines that have a well known steady state functioning, and that usually operates at this steady state, since this is an open-loop control strategy. In a cycle of six-step control strategy, the switches of the inverter are open one half of a cycle and closed the other half.

For a six-step control strategy, the three phases of the inverter are controlled with a phase shift of 120°. The command pattern is shown on 1.12. As it can be seen on this timing diagram, the switching states of the three inverter legs are shifted by 120°, leading to the line voltage displayed on figure 1.12.

This control strategy's main asset, besides its simplicity, is the low switching frequency. Indeed, with this kind of controller, there are only six commutations per cycle for the whole inverter, allowing to avoid the inherent switching losses of the components to be too high (see the paragraph associated to figure 1.15 on switching losses). However, as it will be shown in the next paragraph, the waveform of the currents presents a higher total harmonic distortion leading to increased copper and iron losses as well as torque ripples [22], [23]. This leads to the necessity to use over-sized power electronic devices and a passive filter in input of the inverter. In addition, only the frequency of the output voltage can be controlled, its amplitude depending only on the value of the input DC voltage. Another drawback is that this solution does not allow the vector control of the torque (described in the next section 1.3).

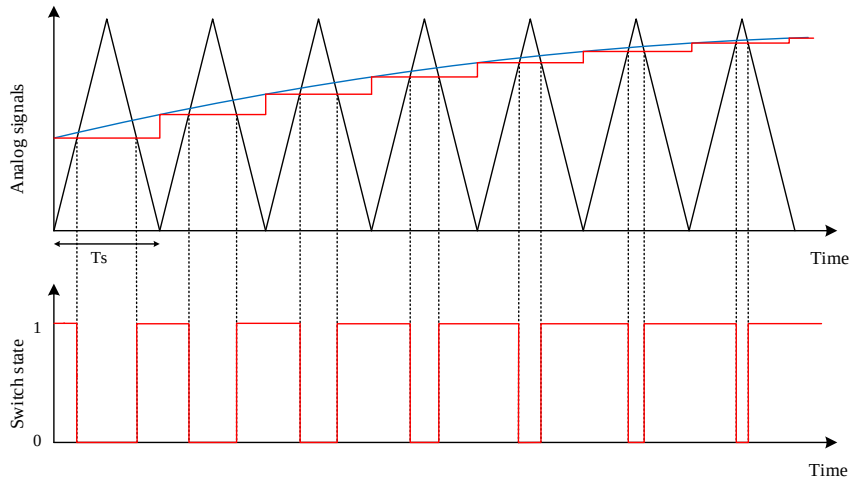

Figure 1.13. Simplified diagram of PWM signal generation with T_s the sample time. Top graph: blue line corresponds to the analog modulation signal, red line corresponds to the sampled modulation signal and black line corresponds to the carrier).

When a higher switching frequency can be used, the pulse width modulation (PWM) is preferred to the six-step controller, because it allows modifying both the frequency and the amplitude of the output voltage of the inverter [24]. This type of signal generation is widely used in the control of electric machines applied to transport. The principle of PWM will be briefly explained in this paragraph, since it is commonly used for electric vehicles in the automotive industry.

The principle of PWM is the discretization of a reference signal through the switching of the inverter's semi-conductors. For the classic intersective method, the reference voltage signal is compared to a modulation waveform (usually a sawtooth or a triangle waveform). When the reference signal has a higher value than the modulation waveform, the associated inverter leg's top switch is set in the high state and the bottom switch in the low state and vice versa when the reference signal has a lower value than the modulation waveform. Figure 1.13 illustrates the principle of the PWM described above.

This kind of switching signal generation is perfectly adapted to electric machines control. Indeed, when an inductive load is connected to the output of the inverter, the currents in the phases' inductances subjected to a voltage step due to a semi-conductor's switch evolve as a first order waveform. In light of this fact, the higher the switching frequency compared to the reference signal's frequency, the smallest the rise or fall time of a phase current's first order response. Consequently a high switching frequency increases the quality of the output current regarding its THD. Figure 1.14 compares the current outputs of an inverter with a given RL-load and signal reference for two different switching frequencies. It is obvious from this figure that the higher the switching frequency the lower the current ripple, enhancing the THD and thus decreasing the power losses.

However, a high switching frequency will lead to excessive switching losses. Those losses occur during each switching sequence of a semi-conductor. When a MOSFET switches off, the voltage between the drain and the source drops, and the current rises before it reaches 0V as it is shown on figure 1.15. This figure illustrates the evolution of the collector voltage V_{CE} and current I_C, the gate voltage V_{GE} and the relative power loss p of an IGBT, whose behavior is similar to a power MOSFET, during the switch on and off. As it can be seen on this figure, during the

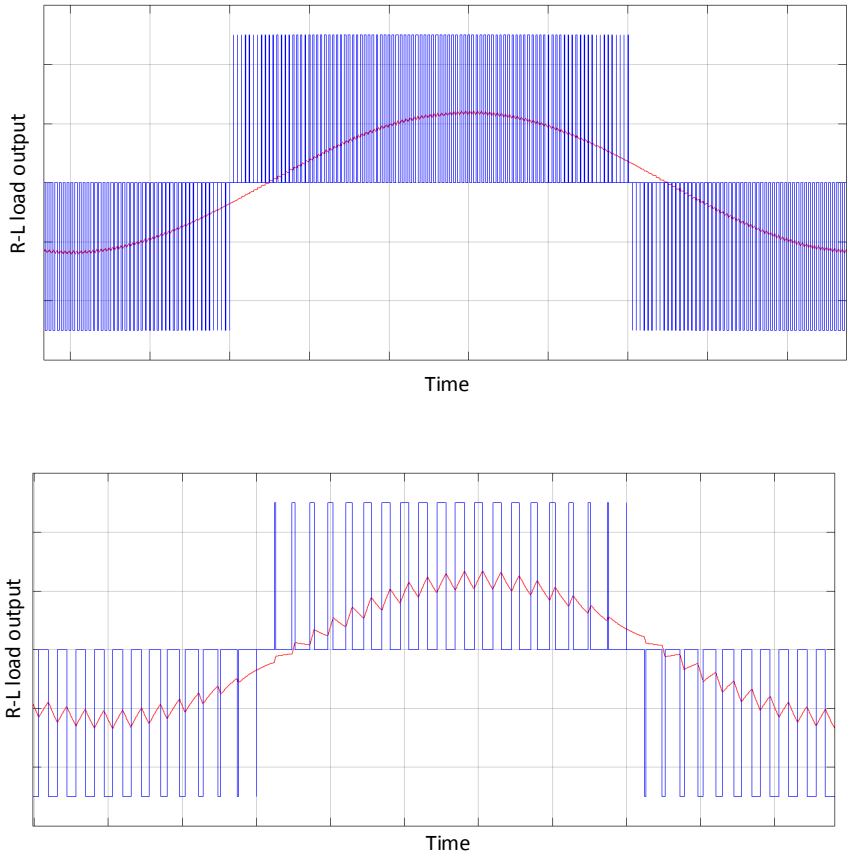

Figure 1.14. Comparison of the current output (in red) in a RL-load for two different switching frequencies.

switching sequences the power $p(t) = V_{CE}(t).I_C(t)$ is non null, leading to an energy dissipation $E(t) = \int p(t).dt$. This means that the higher the switching frequency, the higher the switching losses in the system. This can be avoided using snubbers on each semi-conductor but this extends the switching period and makes the system bulkier [25]. The power associated to switching losses then dissipates as heat through the heat sink. Thus the higher the switching frequency, the bulkier the design of the heat sink and the heavier the whole inverter. To summarize, a proper optimization needs to be carried out when designing an inverter with PWM, with a switching frequency not too high to avoid excessive switching losses, but not too low in order to keep a satisfying THD on the output current. Usually, the ratio between the switching frequency and the reference signal frequency should be at least 20 for an acceptable output current ripple [26].

Another common modulation technique used for machine control is the Space-Vector Pulse Width Modulation (SVPWM). SVPWM is similar to PWM except the reference signal is computed with a specific algorithm that determines which commutation vectors (corresponding to the top switches states) to apply and for how much time. This allows to choose the commutation pattern, as long as the times computed from the algorithm are respected, and thus reduce the number of switching during a cycle, reducing the switching losses. In addition, this modulation technique allows a better use of the DC voltage. For further information on the SVPWM, a general presentation is realized in [26] and comprehensive studies can be found in [27] and [28].

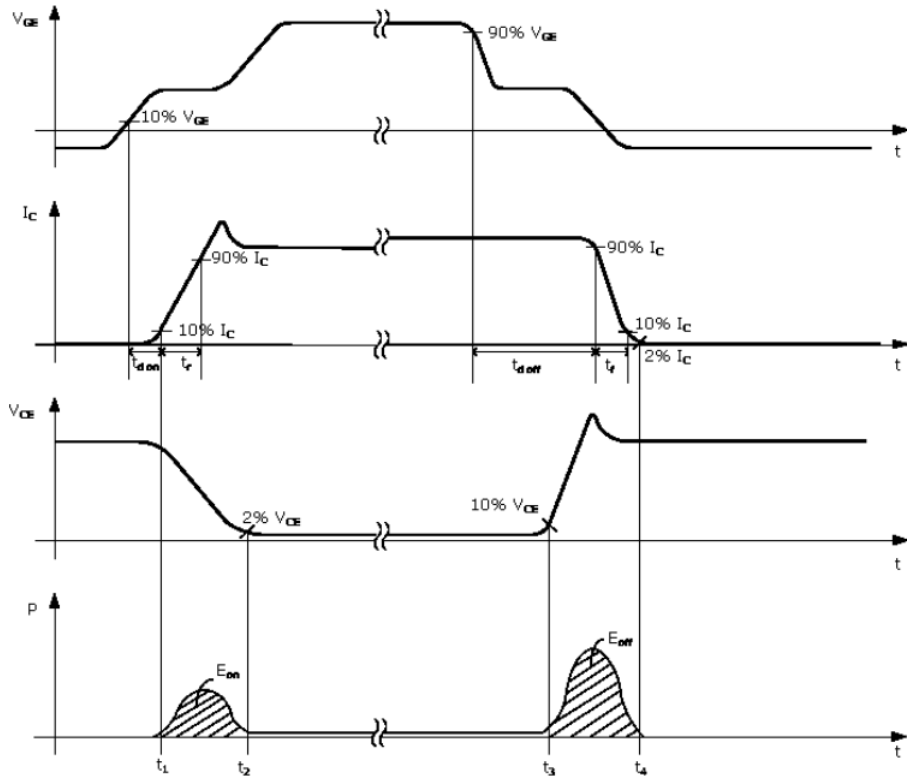

Figure 1.15. Simplified switch on and switch off of an IGBT and related energy losses [29].

1.3 Vector control

In general, the torque of an electric machine is controlled. It depends on two state variables, the dq-axis currents i_d and i_q according to the following equation 1.2 of the torque T_{em} for a WRSM [24]:

$$T_{em} = p.\left((M.i_e + (L_d - L_q).i_d)\right).i_q \tag{1.2}$$

With p the number of pair of poles of the machine, M the mutual inductance between the rotor and the stator, L_d and L_q respectively the d and q axis inductances of the stator and i_e the excitation current. This equation will be detailed and demonstrated in the case of a WRSM in chapter 2, section 2.2.b.

The role of the vector control is to control the torque of the machine through the state currents in an optimal way according to a chosen criteria. In general, the bulkiness of the stator of a machine makes it sensitive to critical temperatures, hence the criteria chosen is usually the minimization of the Joule heating for a given torque. This optimization problem is also called "Maximum Torque Per Ampere" (MTPA) control [30]. Since the Joule heating is proportional to the total RMS current, this means minimizing the value $i_d^2 + i_q^2$ for a given torque. This leads to the coupled control of i_d and i_q. For a non-salient pole machine, the d axis current is usually controlled to 0A, since $L_d = L_q$ thus regarding to equation 1.2 i_d does not participate to the torque and $T_{em} = p.M.i_e.i_q$. The torque of the machine is then proportional to i_q only.

1.3.a Principle of vector control

The vector control consists then in controlling two variables i_d and i_q by acting on the dq-axis voltages v_d and v_q through the inverter with a signal generation technique such as the PWM

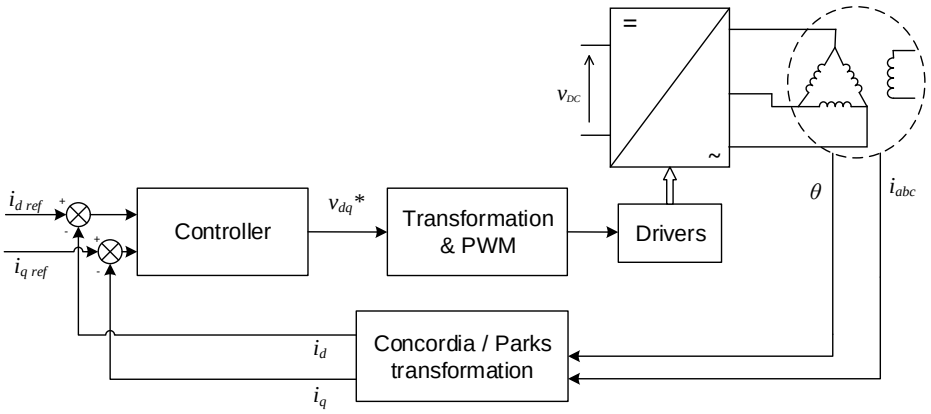

Figure 1.16. Block diagram of the vector control of a WRSM.

presented in the previous section. With the help of feedback loops, it is possible to obtain the voltages needed to maintain the dq axis currents in the neighborhood of the reference values fixed by the user i_{dref} and i_{qref}. Let's note that the control is made on the mean values of i_d and i_q on a switching period, and the output voltages are mean values as well, representing a duty cycle for the semiconductors.

As a control signal generation solution, PWM can be used with any controller. PI controller are widely used in the industry, since it is a simple and robust controller. However, other control strategies seem to have useful characteristics for a sensorless application. This is the case of the flatness-based controller, that will be presented in the next paragraph. Sliding mode controller is a robust nonlinear controller can also be used for machine control since it shows good dynamic performances [31]. More recently, passivity based controllers (PBC) have been studied for machine control application, especially for EV and HEV applications since it is robust and presents a good behavior towards disturbances rejection [32], [33].

Figure 1.16 shows a block diagram representing the vector control strategy applied to a WRSM. The Concordia/Park transformation is detailed in chapter 2 section 2.

1.3.b Flatness-based controller

The flatness-based controller (FBC) is a controller based on a mathematical property, the differential flatness of a system. It was first mathematically described by Fliess *and al.* in [34]. The main advantage of this control strategy is that it is possible to define a precise trajectory for the controlled state variables. The only yet restrictive condition is that the considered system of equation needs to be "differentially flat". A precise definition of "differential flatness" has been given in [34] and [35], and detailed for electric machine control in [36], [37] and [38].

By definition, a state system x, with $x \in \mathbb{R}^n$, defined by $\dot{x} = f(x, u)$, $u \in \mathbb{R}^m$ the input vector, is considered flat if there is a flat output $y \in \mathbb{R}^m$ that can be written $y = g(x, u, \dot{u}, \ddot{u}, ..., u^{(q)})$ and if x and u can be written as function of solely the flat output y and its derivatives, such as $x = h_1(y, \dot{y}, ..., y^{(r)})$ and $u = h_2(y, \dot{y}, ..., y^{(r+1)})$, where the functions g, h_1 and h_2 are regular functions. The mathematical proof showing that the state system describing the WRSM is differentially flat is presented in appendix, with the flat outputs being the machine speed Ω and the excitation current of the rotor i_e.

As stated before, the main advantage of this controller is the fact that the flat output vector trajectory can be configured according to the user's needs. By definition, the trajectories chosen

for the state variables of the flat vector y have to be differentiable at least to the $r+1$ order. Due to this constraint, the trajectories usually used are polynomial since those functions are infinitely differentiable and can be easily tuned. In the configuration described in appendix, a particular trajectory can be applied to the mechanical speed and the rotor current, allowing to reach a particular speed with a selected dynamic and to generate a magnetic flux in the rotor more or less according to the operating cycle of the WRSM. For example when the machine starts, the rotor current is increased in order to increase the mechanical torque that can be delivered by the WRSM, and the final speed can be reached within a specific time frame.

This kind of controller can be of great use for an automotive application such as mild-hybrid, where the machine has to be started at any operating point of the vehicle. In addition of the fact that the dynamic of the speed evolution can be tuned, a total control of the speed trajectory is a great asset when the electric powertrain is coupled to the main powertrain. This would allow to reduce the mechanical constraints on the coupling belt. Other applications could benefit from this kind of controller such as actuators for aircraft technology, as described in [36], [37] and [38].

Selected control strategies that are used or could be useful for automotive applications have been presented and discussed in this section. The six-step controller, since it is a simple and robust solution, is often used when the switching frequency is a constraint and when the powertrain operates most of the time at steady state. However for applications where transient phases are the majority, a vector control strategy associated with PWM signal generation is more suitable [26], [21]. For specific applications where the speed or the excitation current's trajectories have to be rigorously controlled, a flatness-based controller could be privileged although the control laws are more complex. For the mild-hybrid powertrain studied in this thesis, a vector controller at least is necessary since the powertrain is mainly performing transient phases. The main objective of the work presented in this thesis being to control a mild-hybrid electric powertrain without any current sensor on the stator of the machine, the following section will be focused on sensorless control strategies existing in the scientific literature and that could be useful for our application.

1.4 Observation of non measured variables

This section's role is to propose a selected study of existing sensorless control solutions. The most described sensorless solution is the mechanical sensorless control, usually only referred in the literature as solely "sensorless control". If mechanical sensorless control cannot specifically be applied to the electric powertrain studied, the techniques used to control the machine without some specific sensors are interesting to investigate since the approach is the same for current sensorless control.

In the second paragraph, an existing current sensorless control in a particular system configuration will be presented. This solution is interesting to remove current sensors on the stator of the machine but requires another current sensor with a large bandwidth on the DC bus of the inverter.

To conclude with this section and this first chapter, Valeo's mild-hybrid powertrain will be presented in details in order to fully understand which sensors are removed and which are still available on the powertrain.

1.4.a Mechanical sensorless control solutions

Mechanical sensorless control solutions, usually simply referred as "sensorless control" since it is the most widespread sensorless control of electric machines, have been subject to numerous studies in the past three decades. The removal of the mechanical sensor on a rotor of a machine is indeed extremely appealing for manufacturers: it allows to reduce the manufacturing costs linked

to the purchase of mechanical sensors, to reduce the manufacturing time linked to the tuning of the offset mechanical angle between the rotor and the stator and to decrease the bulk and weight of a system. In addition, the reliability of the whole system is increased when a sensorless control is added to a system, making it resistant to sensor failures. This kind of sensorless control is thus particularly suitable for embedded solutions and more specifically for the automotive industry, where manufacturing costs and the size of the system are critical issues.

Several solutions of sensorless control exist, with different approaches, but most of them are based on the reconstruction of the mechanical state variable, the rotor speed and angular position. In the PhD work realized in [39] the author shows more explicitly this trend in his state of the art studies: mechanical sensorless control relies either on a synchronous machine's back EMF measures estimations to obtain the missing mechanical state variable or on direct estimation of the speed. The first solution will be briefly introduced in this paragraph but the back EMF cannot be used in the same conditions for state currents reconstruction. Direct speed estimation solutions will also be presented in this paragraph, since they are more likely to be reused for other state variables such as stator currents.

Back EMF estimation for speed reconstruction have been widely studied and used for mechanical sensorless control. Studies such as in [40], [41], [42] or [43] have been focused on this particular subject. The back EMF of a synchronous machine indeed carries information on its speed state variable. The principle of back EMF based sensorless current relies on the use of an extra mechanical angle φ, representing the offset angle between the real rotor angle Θ and the estimated one ν, as it is sketched on figure 1.17.

In $\delta\gamma$ frame, only the mechanical angle ν is known and corresponds to the angle shift between the $\alpha\beta$-axis and the estimated rotor angle represented by the $\delta\gamma$-axis. Due to this lack of knowledge of the real rotor position, the dq-axis cannot be known, thus all the variables that usually are written in the dq-axis are, in sensorless applications, written in the $\delta\gamma$-axis. In addition ,the state vector of the system contains the classic state variables (in the $\delta\gamma$ frame)

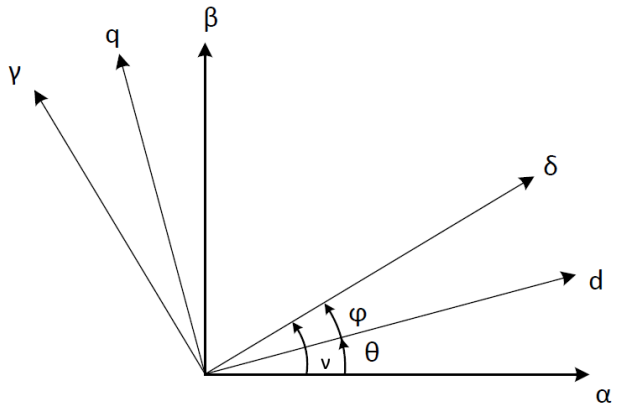

Figure 1.17. Mechanical reference frame showing the angle shifts between $\alpha\beta$-axis, dq-axis and $\delta\gamma$-axis.

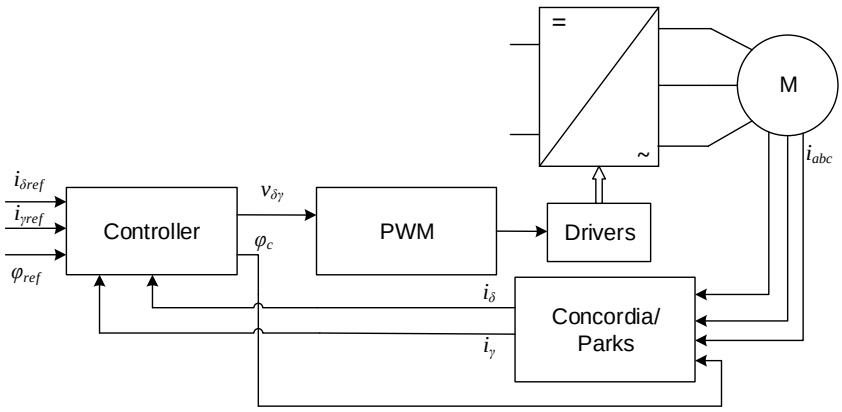

Figure 1.18. Bloc diagram showing the principle of back EMF based sensorless control.

which are the rotor speed Ω, the stator currents i_δ and i_γ, with an extra variable representing the mechanical angle shift $\frac{\varphi}{p}$, giving a state vector $X = \begin{bmatrix} \frac{\varphi}{p} & \Omega & i_\delta & i_\gamma \end{bmatrix}^T$, a command vector $U = \begin{bmatrix} \Omega_c & v_\delta & v_\gamma \end{bmatrix}^T$ with Ω_c the estimated mechanical speed of the rotor (linked to the electric speed of the $\delta\gamma$ frame) and a measured state variables vector $Y = \begin{bmatrix} i_\delta & i_\gamma \end{bmatrix}^T$. The proof of controllability and observability of the system under this form is demonstrated in [40] and the observability is guaranteed for all operating point except the mechanical standstill ($\Omega = 0rpm$). Finally by controlling the variable φ to 0 modulo $2k\pi$ it is possible to make the $\delta\gamma$-axis coincide with the dq-axis. The control strategy is summarized on figure 1.18.

The back EMF elements in the $\delta\gamma$ frame can be written, according to [41], as:

$$\begin{aligned} e_\delta &= p.\Psi_f.\Omega.sin\varphi \\ e_\gamma &= p.\Psi_f.\Omega.cos\varphi \end{aligned} \tag{1.3}$$

with Ψ_f the magnetic flux generated by the magnets of a PMSM and p the number of pairs of poles in the machine. From those equations, it is possible to retrieve an estimation of the speed Ω from e_γ and to estimate the angle ν by making e_δ converge to 0.

This method of sensorless control is easy to implement and robust for high speeds range, it is however not suitable for low speeds. Indeed at low speeds the back EMF generated by the machines are weak and difficult to estimate. In [40], an observability study for the non-salient pole PMSM is conducted, showing that the determinant of the observability matrix dO is given by:

$$det(dO) = p.\frac{K_f^2}{L_{dq}^2}.\Omega \tag{1.4}$$

With p the number of pair of poles, Ψ_f the rotor flux created by the magnets, L_{dq} the stator inductance, Ω the mechanical speed and K_f defined by $K_f = p.\Psi_f$.

The determinant is null if Ω is null and at low speed the determinant can be very small, making the system theoretically observable but in practical very subject to measurement noises. Another study on the observability of an induction machine at low speed has been performed in [44]. The state equations linked to the induction machine is slightly different from the WRSM but the principle is the same and the results are similar: the observability index, defined by the determinant of the observability matrix, is small for low speeds and null at standstill. In

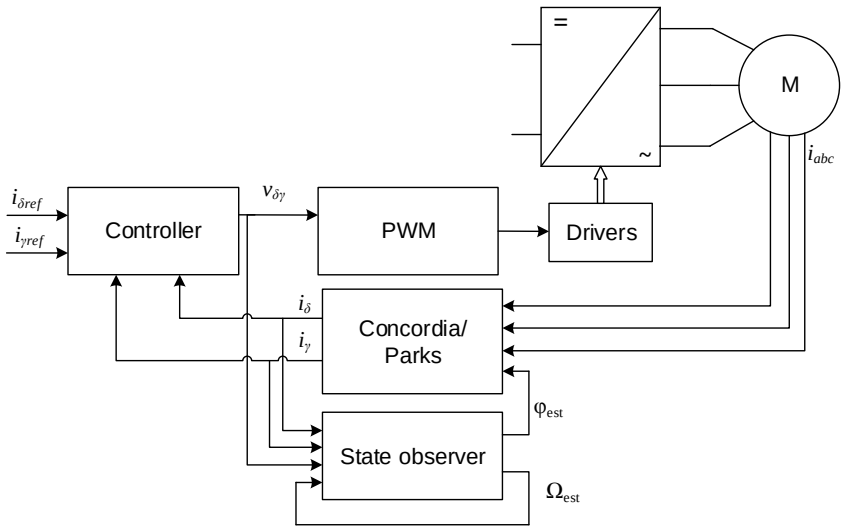

Figure 1.19. Bloc diagram showing the principle of state observer based sensorless control.

addition, the estimation of the back EMF relying on the modeling of the machine, this method is also sensitive to parameter errors. There are also a risk of multiple stable operating points for a set of state variables depending on the initial angle ν chosen, which can lead the estimator to converge towards a speed that is different from the real speed of the machine.

Another method commonly used for sensorless control of electric machines are based on the direct observation of the missing state variables. For synchronous machines applications, this requires the use of nonlinear observers. In [40], [45] and [46], an extended Kalman filter (EKF) is used to observe the missing mechanical state variables φ and Ω. The extended Kalman filter is one of the most used nonlinear state observer, due to the fact that it can be applied to any nonlinear system for state variables observation. It is also a very common tool used for noise rejection. Details on the EKF definition is given in chapter 3 of this work in section 3.2.a. Other state observers have been developed and used for mechanical sensorless applications such as the Luenberger observer. The nonlinear observers based on the model of the machine are however still dependent on the precision of the parameter used in the model, and parameter errors lead to convergence errors. The control strategy using a state observer is summarized on figure 1.19.

In order to overcome the low speed issue linked to mechanical sensorless controllers, different strategies exist, such as starting the machine in open-loop to reach high speed and switch to an observer based control. One other interesting solution that could be useful for our application is the pulse voltage injection. This methods consists in applying voltage in the stator before the start of the machine, and measuring the resulting current evolution in the stator. The higher the $\frac{di}{dt}$ the smaller the inductance in this direction. This method is well described in the work of [47] and in [48] for the low speed cases.

A different method still based on the back EMF estimation of the machine has been proposed in [49] in order to reduce the issues linked to the zero speed and the low speed range. It proposes to combine the back EMF method presented earlier with a voltage injection technique. As it has been stated and can be deduced from eaquation 1.3, back EMF at standstill is null, making the classic back EMF based sensorless control impossible to use directly. The combined method

strategy described in details in [49] is to inject a sine voltage on δ axis such as:

$$\begin{aligned} v_\delta &= A_i.cos\left(\omega_i.t\right) \\ v_\gamma &= 0 \end{aligned} \tag{1.5}$$

If there is an angular error φ between the $\delta\gamma$ axis and the dq axis, the voltage injected described in equation 1.5 is written in the dq axis:

$$\begin{aligned} v_d &= A_i.cos\left(\omega_i.t\right).cos(\varphi) \\ v_q &= A_i.cos\left(\omega_i.t\right).sin(\varphi) \end{aligned} \tag{1.6}$$

As it can be seen on equation 1.6, if $\varphi = 0$ there is no q axis voltage and thus the voltage injection has no effect on the rotor speed. However if $\varphi \neq 0$, a torque is created in the rotor with the injected voltage, leading to mechanical vibrations in the rotor. With a well chosen set of parameter for the injected voltage, the rotor can be set in motion at a sufficient speed for the back EMF to be significant for classic back EMF sensorless control or for a direct observer based method like it is described in the next paragraph.

Mechanical sensorless control strategies are interesting to study: since the spirit is similar to current sensorless, some methods can be reused. If it is not the case for the first method presented, based on the back EMF, the stategy using nonlinear observers have clearly been a source of inspiration for current sensorless control. Some methods of current sensorless already existed before the beginning of this work, but in different system configurations. One of the most usual current sensorless solution will now be presented in the next section.

1.4.b Existing current sensorless control in particular configurations

If a lot of studies concerning mechanical sensorless control, due to the fact that there are undeniable advantage to remove the mechanical sensor (listed in the previous paragraph), the literature is scarce about current sensorless control strategies. The mechanical sensors are usually expensive and difficult to mount on a rotor while a current sensor is less expensive and usually smaller, which allows it to be easily integrated on a system. On the top of that, the knowledge of the current measurements are important for the closed-loop vector control of the machine (MTPA), for safety issues (current limitations) and for machine reliability [50]. For some industrial applications however, and more specifically for embedded systems where the bulk of the powertrain, the production costs and the reliability need to be optimized, removing the current sensors become a valuable solution. This is even more true for doubly fed machines, where two stators are involved and thus at least 4 current sensors are required to measure the stator currents. In Valeo's mild-hybrid application, the removal of the stator current sensors has been justified previously. The powertrain layout is particular in this application, but even if it is uncommon, current sensorless controls have already been developed in the literature in different applications and different system layouts.

The existing current sensorless control strategy developed in literature and detailed in [51], [52], [53], [54] and [55] among others, proposes to remove the current sensors of the stator of the machine and replace it by a single current sensor on the DC link of the inverter. This solution might seem appealing since it proposes to decrease the number of sensors by at least one for a one stator machine and at least three for a doubly fed machine. From that single sensor, the authors of [51], [52], [53] and [55] propose to "reconstruct" the missing stator currents.

The principle of this current reconstruction relies on the precise measure of the inverter DC link current and on the switches states. The bloc diagram describing the principle of current sensorless control with the current reconstruction technique is displayed on figure 1.20. The denomination "current reconstruction" is not fortuitous in this case because the solution proposed is based on the evaluation of the stator currents directly from DC link current divided in the

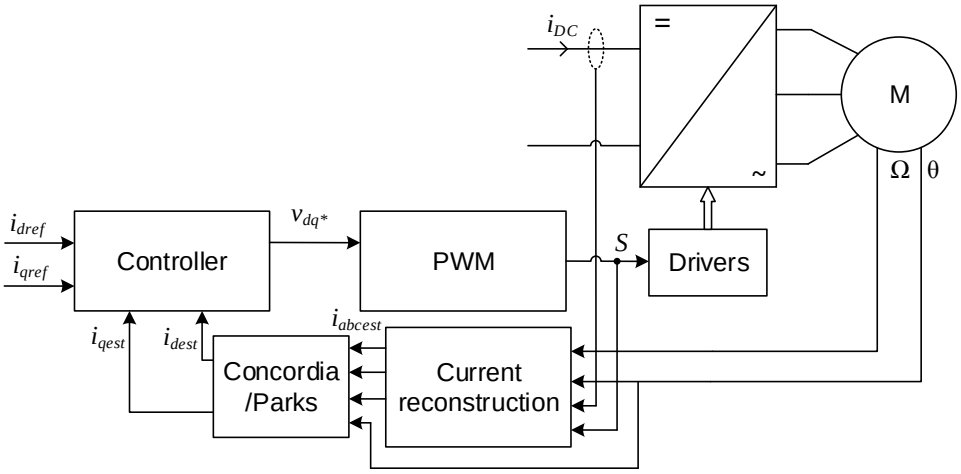

Figure 1.20. Bloc diagram showing the principle of current reconstruction based current sensorless control with DC link current measurement.

stator phases according to the semi-conductors states. Table 1.3 sums up the expected phase currents according to the switching states. In this case, the DC current has to be precisely known and the switching states are known since they are controlled. The phase currents can then be directly expressed as a function of the switching states S_a, S_b, $S_c \in \{0;1\}$ (0 if the switch is open and 1 if the switch is closed) and the DC link current I_{DC}: the DC link sensor has to be sampled at a rate high enough so that, for a given set of switch state, the DC current linked to this set can be measured (and the associated phase current deduced from table 1.3) and the former current from the previous set of switch state can still be considered the same. The current of the last phase can then be retrieved with the two others considering $i_a + i_b + i_c = 0$. This means that for a switching cycle, the DC current needs to be sampled at least twice.

This current reconstruction can be enough for motor control if the DC current I_{DC} is well known. The reconstructed currents can be used in closed-loop for control purposes. This strategy is developed in [53] and is based on the comparison of the DC current calculation from the reconstructed phase currents with the measured DC current. In this method, the phase currents are not reconstructed on the same principle than the one shown with table 1.3. They are actually

S_a	S_b	S_c	I_{DC}
0	0	0	0
0	0	1	i_c
0	1	0	i_b
0	1	1	$-i_a$
1	0	0	i_a
1	0	1	$-i_b$
1	1	0	$-i_c$
1	1	1	0

Table 1.3. Stator current outputs as a function of the DC link current i_{DC} and the switches states.

computed from the state equations of the machine, simply written as in 1.7:

$$\begin{bmatrix} v_a \\ v_b \\ v_c \end{bmatrix} = R.I_3. \begin{bmatrix} i_a \\ i_b \\ i_c \end{bmatrix} + L.I_3.\frac{d}{dt} \begin{bmatrix} i_a \\ i_b \\ i_c \end{bmatrix} + \begin{bmatrix} e_a \\ e_b \\ e_c \end{bmatrix} \tag{1.7}$$

The abc-axis voltages are calculated with the switches states and the DC voltage. The back EMF e_{abc} are computed from the electric speed and position of the machine rotor, which are both known thanks to a mechanical sensor on the rotor. Once the phase currents are calculated, the DC current is recalculated with the phase currents and the switches states, according to table 1.3. The DC current is then given by the following equation 1.8:

$$I_{DC} = i_a.S_a + i_b.S_b + i_c.S_c \tag{1.8}$$

This DC current is then compared to the measured one and a PI regulator is then used to correct the estimation of the phase voltages v_{abc} using corrected DC voltage. This correction of DC voltage estimation is used to reduce the impact of the parameter errors in the state equations 1.7. Indeed, the parameters cannot be perfectly known, leading to errors on the reconstruction of the phase currents. The whole strategy developed in Yings's work [53] is summarized through figure 1.21.

The main drawback of these methods using phase currents reconstruction is actually the use of a sensor on the DC link of the inverter. Indeed, the main asset of removing sensors on the stator of the machine is to reduce the manufacturing costs and the bulk of the system. However, if the methods presented above allows removing the phase current sensors, they both require a very precise DC current sensor on the DC link of the inverter, which means that they require the use of an expensive sensor with a large bandwidth to be able to measure all the DC current variations linked to the switches of the semiconductors. Indeed, the DC link current needs to be sampled at least twice per switching period in order to access two phase currents (see table 1.3). In addition the moments the samples are acquired need to be calculated at the beginning of every new switching period in order to be sure to sample at two different switching states. The noise due to the semiconductors switching are also source of error: if the current measurement is performed while the current is oscillating because of a resonant effect this will distort the measured value compared to the true steady state value. This actually nullify the benefits of the current sensorless strategy on the manufacturing costs and it makes the sampling pattern more complex. In addition, inverters' DC link are usually large copper bars in most embedded system

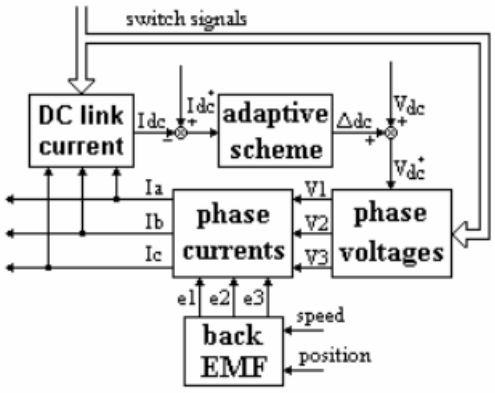

Figure 1.21. Bloc diagram showing the principle of current reconstruction from the state equations of the machine with a DC link current regulation loop [53].

layouts. A Hall effect type current sensor, necessary for a precise DC current measurement, would then have to be large enough to be mounted on this copper bar, making the DC link more bulky and oversized and reducing the benefits made on the bulk of the stator achieved by removing the stator sensors. A shunt could be used instead of the hall effect sensor in order to lower the costs, but this will lead to increased inductive effects. On the top of that, the voltage measurement on the PCB device can be impacted by other neighbor traces due to electromagnetic interference (EMI) issues [56].

The current sensorless strategies presented in this paragraph can be very interesting in some particular applications, since they propose to reconstruct the missing phase currents using a DC link current sensor and the states of the semiconductors. If the results can be very satisfying, the use of a precise DC current sensor on the DC link of an inverter reduces the benefits of a current sensorless strategy. In our particular application, the use of such a sensor would not be suitable. A more detailed presentation of the exact system layout that will be the support of the current sensorless control study will be presented in the next paragraph. From this layout and the particularities of the system studied, the global current sensorless strategy that has been chosen in this work will be introduced and explained.

1.4.c System layout for the proposed current sensorless control

This last paragraph of the first chapter of this work will be focused on the presentation of the exact layout on which this work is based. As explained earlier, this work is based on a mild-hybrid electric powertrain developed by Valeo, the i-StARS. This last section will characterize with more precision what elements are included in this powertrain.

The considered version of i-StARS mild-hybrid powertrain is powered by a 12V battery. It is actually the battery of the vehicle: the mild-hybrid solution developed by Valeo aiming to be able to be mounted on as many vehicles as possible, Valeo chose to develop the first version of its mild-hybrid system in 12V since it is the standard voltage battery of a vehicle.

The battery is then connected to an input filter in order to protect it from the voltage overshoots and from the EMI effects induced by the inverter. This input filter is made of a small inductance connected in serial from the battery and a large capacitor (6mF) in parallel. The inductance is actually the self inductance created by the connections between the battery and the inverter. This input filter is then connected to a 6-legs voltage source inverter. The switches of the inverter are MOSFETs specially designed for this application. The inverter is directly connected to the machine, it is even mounted directly on the chassis of the machine as it will be shown on photos of the i-StARS machine in the next chapter. Three of the legs are connected to a first stator and the three others are connected to a second three phase stator. Indeed as announced previously the i-StARS machine used is a doubly fed wound rotor synchronous

Figure 1.22. Photo of an example of a claw pole rotor.

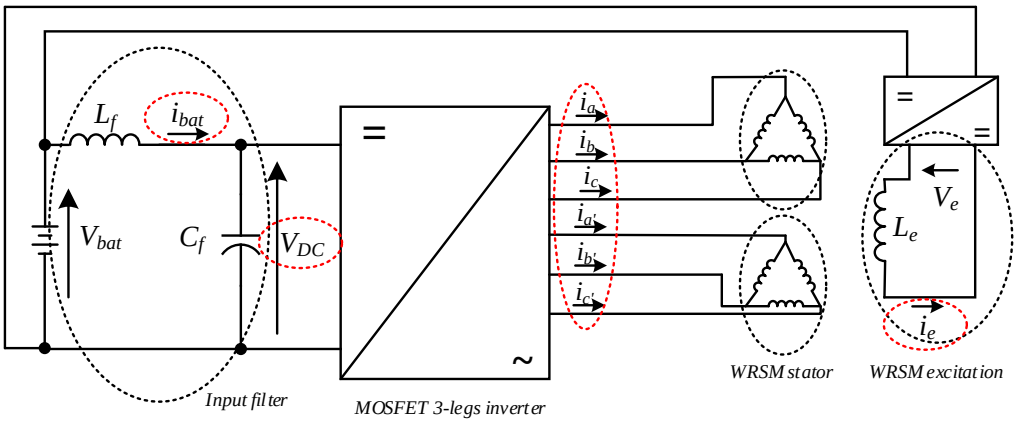

Figure 1.23. Schematized system layout of the mild-hybrid powertrain developed by Valeo.

machine. In that sense, there are two stators on the WRSM and they are both connected in delta and shifted by 30°. This angle is chosen so that the torque ripple is as small as possible [57]. The rotor of the machine is a claw pole rotor: it is divided in two parts with interlocked "teeth", as shown on figure 1.22. This machine has two sources of excitation: the main excitation is created with a DC excitation current in the wired rotor. Another minor source of excitation is induced by the magnets inserted between the teeth of the claw pole rotor. The role of these magnets is to reduce the saturation in the iron parts of the machine and limit the magnetic leakages between the rotor and the stator, but the magnetic leakage flux of the magnets impacts the back EMF of the machine. More details about the WRSM will be given in section 2.2.b of chapter 2.

The excitation current in the rotor is controlled and applied through a DC-DC converter. This DC-DC converter is a simple buck converter directly connected to the battery of the system.

The whole system as it has been described is summarized on figure 1.23. On this figure, the electric variables are circled in red. In addition of the elements presented on figure 1.23, there are sensors mounted on different part of the system. In this current sensorless application, there is obviously no current sensors on the stator of the machine, thus there is no direct access to the current in the two stators of the machine. The only sensors available on the system presented here are a mechanical sensor on the rotor, giving the mechanical speed and position of the rotor, a current sensor on the rotor winding of the machine (giving i_e) and a current and a voltage sensor on the input filter of the system (giving V_{DC} and i_{bat}).

A reasonable reflection at this point would be to question the point to remove sensors on the stators of the machine to add some other sensors on other parts of the system. Indeed the battery current sensor is important to protect the i-StARS system from excessive current peaks.

In addition it has been shown in the previous paragraph that a sensor on the DC link of the inverter is bulky and expensive. However the sensor added here is not on the inverter's DC link but directly on the output of the battery. This part is not necessarily a bus bar and since there is a capacitor between the DC current sensor and the inverter in this layout, a large bandwitdth will not be necessary because the current reconstruction introduced earlier cannot be used in that configuration.

Another debatable choice regarding the adding of sensors is the use of a wired rotor instead

of a permanent magnet rotor. The use of permanent magnets on the rotor would allow to avoid using a DC-DC converter alongside with a current and a voltage sensor and controller of the excitation current. However those elements are rather cheap and lightweight compared to permanent magnets. On the top of that, magnets are made from rare materials and Valeo have the will to avoid depending on those resources as much as possible for their products.

The system layout as it has been designed by Valeo for the mild-hybrid i-StARS powertrain has been presented in this paragraph. The choice to remove the stator sensors and to add sensors on the battery and the wired rotor is still relevant since those sensors are cheap and do not excessively increase the bulk of the system.

Conclusion

This first chapter's role was to introduce the context within which this study of current sensorless control is incorporated. A comprehensive review on the state of play of the electrification boom in the automotive field has first been proposed. Indeed, due to the application of quotas on the GHG emissions and to the increase of environmental considerations in customers choices, the automotive manufacturers are turning increasingly towards more electric vehicles. BEVs sales worldwide have grown sharply, but the price of the battery pack and the lack of infrastructures for fast charging of the batteries are still an obstacle to the expansion of this technology. Hybrid technologies as developed in parallel of BEVs. They propose to couple an electric powertrain to the ICE of a vehicle in order to reduce its fuel consumption. Several levels of hybridization exist: from the highest (PHEV, EREV) to the lowest (Stop-Start). Mild-hybrid technology is an intermediate level: it proposes to activate the electric powertrain anytime during a driving cycle when the vehicle needs a power boost, where the fuel consumption is the highest. In this framework, the LowCO2Motion+ project initiated by Valeo aims to extend an existing starter-alternator, the i-StARS, to a mild-hybrid application.

The automotive field being extremely competitive, the manufacturing costs always need to be optimized. For this reason, it could be interesting for Valeo to remove the current sensors of the stator of its i-StARS claw-pole machine to avoid their costs. An open-loop control could be considered but a vector control allows better performances of the control. The aim of the work realized in this thesis is then to propose a solution of current sensorless control of Valeo's claw-pole machine.

Sensorless control solutions exist but mainly focus on the mechanical sensor removal. Most of the existing strategies are based on the back EMF estimation of the machine to retrieve the rotor speed and position of the rotor. Some solutions also propose to inject a voltage in the stator of the machine in order to have more information for estimation at the start of the machine. Some current sensorless control strategies also exist but in a particular configuration, when the DC link current of the inverter is measured. With this measurement and the knowledge of the switches states, it is possible to retrieve the stator currents with a good precision. However in our layout this measurement is not available. Indeed, removing the stator sensors to add one sensor on the DC link shows few interest since the sensor required on the DC link needs to be precise, thus expensive: it nullifies the benefits of a current sensorless control on the cost reduction of the system.

Finally, only the measures of the excitation current, of the DC link voltage, of the battery current and of the mechanical speed are available. The following work of this thesis will focus on the stator current estimation in order to perform a current sensorless control of the WRSM. The first step, presented in the next chapter will be centered on the modeling of claw-pole wired rotor synchronous machines.

Chapter 2

Electric modeling of the Wound Rotor Synchronous Machine

Contents

Introduction

The main objective of the work realized within this study is to control the electric powertrain designed by Valeo without the current sensors on the stator of the machine. As it has been stated previously, this achievement is motivated by the potentially reduced manufacturing costs induced by the removal of the sensors.

However, removing the current sensors of a system is not without consequences. Indeed, the motor torque is closely related to the stator currents and its control requires good information on the stator current vector. Therefore, if these currents are not measured, they have to be estimated using an accurate model. However, no model perfectly represents the system, especially in the transient phases where sub-transient phenomenons difficult to model may occur. In addition, the wear of the different components of the system (in the machine or in the inverter) due to mechanical (temperature, dusts or humidity) and electrical constraints (current peaks, large voltage gradients) change their expected values. The change of temperature in the system is also responsible of modifications in the value of the resistors in the system (in the rotor and stator of the machine and on the resistor of the semiconductors in the inverter) as highlighted in [58], and the saturation of the machine induces variations of the values of the inductances.

All the phenomenon described above may induce a variation of the different parameters of the model, making it particularly difficult to accurately estimate unmeasured variables like the stator currents. The objective of this second chapter is to describe the system as a model, both simple and accurate enough, to reduce the sensitivity of the current sensorless control to mechanical and electrical constraints.

As a first step, the different parts of the electric powertrain will be described in details. For this work, only the WRSM and the load machine have been supplied by Valeo: the rest of the devices of the powertrain have been designed and assembled in the laboratory in order to emulate similar performances than the real powertrain proposed by Valeo.

An important point in the modeling of the i-StARS machine is to take into account the rotor winding and the mutual interactions between the stator and the rotor of the machine. In order to have a better understanding of the machine provided by Valeo, theoretical work undertook in the thesis of Dr. Geoffrey Devornique [59] will be explained. A characterization of the WRSM on the test bench built in the beginning of this study will then be proposed to have access to the different parameters of the machine for a nominal operating point. From these first tests, a system of state equations will be proposed to fit mathematically the real functioning of the system.

The WRSM state variables sensitivity towards errors on the parameters values in the model chosen will then be undertaken. This characterization of the machine sensitivity towards parametric variations is important to know which parameters are the most prone to induce errors in the state variables observation.

Regarding the parametric sensitivity study results, the last part of this chapter will introduce a solution of reduced map of one sensitive parameter using an online parameter estimator. Indeed, when a particular set of parameters is selected, it will be shown that a map of only one parameter can compensate for other parameter variations in such a way that the model together with the map describe the system's behavior with sufficient accuracy for the whole operational range at steady-state with a given system of state equations. The possibility of including the temperature in this reduced map of parameter will be discussed but a mapping covering the whole temperature range has not been realized. Indeed, taking into account the precise temperature in the system would be pointless in this particular case since the semiconductors and the WRSM are not assembled in the same way it is done by Valeo on the vehicles. The temperatures in the vehicle powertrain and on the one designed in this study are thus not comparable.

2.1 Description of the different elements of the studied electric powertrain

2.1.a Valeo's i-StAR starter-alternator

The latest technical solutions used by Valeo for hybridization of vehicles are based on an electric powertrain supplied by a 12V battery. In the future, Valeo is working towards the commercialization of 24V and 48V supplied powertrain. The battery uses a Li-ions technology with an intern resistor between 2 to $5m\Omega$.

The battery supplies an input filter simply composed of an inductance and a capacitor in parallel. From the data provided by Valeo the value of the inductance is small and corresponds to the wiring inductance and the value of the capacitor is large, $C_f = 6mF$ in order to protect the battery from high voltage gradients from the inverter. The input filter is connected to the inverter. This configuration is shown on the summarizing figure 2.8 at the end of this section. On the real powertrain designed by Valeo, the inverter is assembled directly on the WRSM chassis, and the two parts are interlocked with each other as shown on figure 2.1.

On this photograph, the DC positive terminal can be seen on the bottom right. The negative terminal is connected to the chassis of the machine. The black plastic device contains the inverter of the system. The control unit can be seen on the center right. This inverter is composed of six legs of power MOSFETs. The HDTMOS power technology used for these MOSFETs allows the inverter to be extremely compact. The principle of this kind of semiconductors are described with details in [60]. In this configuration, the inverter is cooled down by the air flow produced

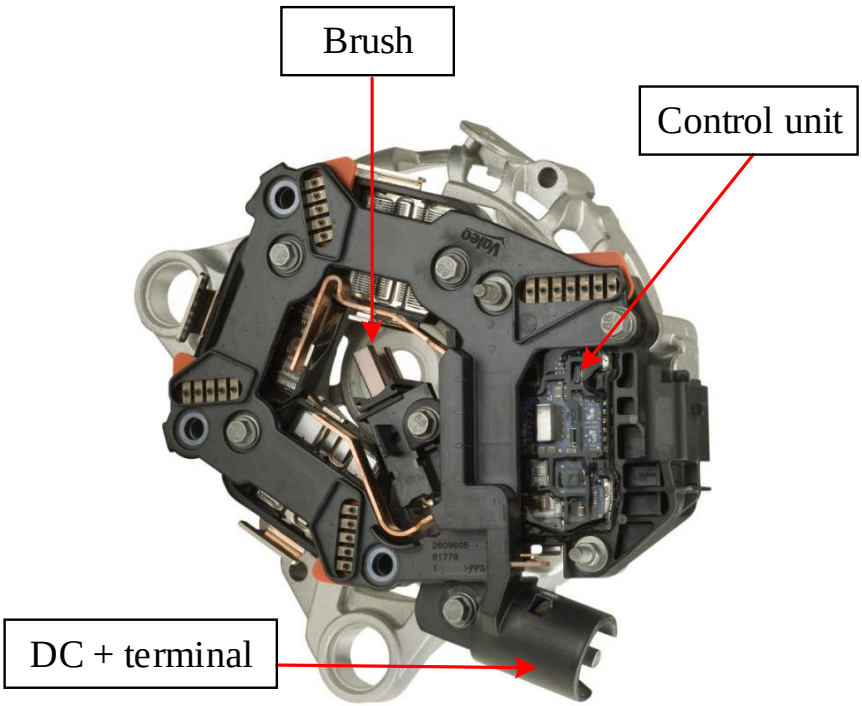

Figure 2.1. Photo of the WRSM chassis with the inverter interlocked.

by the movement of the rotor.

The MOSFETs used are specific for this application. Each power MOSFET measures less than 8mm in length and width, and its thickness is less than 0.3mm. The drain-source ON resistance $R_{DS(ON)}$ is between 0.8 and 1.3 $m\Omega$. In addition, the nominal drain current is $I_D = 500A$ with a maximum peak current to $700A$. These kind of power MOSFETs are specially designed for harsh automotive environment, with a low $R_{DS(ON)}$ and a rugged avalanche performance.

The i-StARS is a wound rotor synchronous machine with two three-phase delta stators. The delta configuration is often used for automotive application, since the torque produced in that configuration is higher than for a star connection when the supply voltage is small. In motor operation, the i-StARS nominal speed is 1500 rpm for a current of $130A_{rms}$ (with peaks up to $300A_{rms}$. The rotor is a claw-pole wired rotor. Valeo chose to use a claw-pole rotor (as it is usually used in automotive alternators) because it is robust and easy to produce on an industrial scale in foundries thanks to the fact that they are composed of one solid ferromagnetic part conversely to a laminated rotor [61]. Two teeth from each claw form a pair of pole. The i-StARS machines have 6 pairs of pole and small magnets are placed between each teeth of a claw. Their role is to desaturate the machine iron parts and limit the magnetic leakages. The other reason for this choice to use a wired rotor instead of a permanent magnet synchronous machine is motivated by several factors. First, the manufacturing costs are lower, since magnets are quite expensive compared to copper. The magnets resources are almost exclusively located in China, which makes it very vulnerable to price fluctuations [62], [63]. In addition, a wired rotor allows increasing or decreasing the excitation flux at will by controlling the excitation current, giving another degree of freedom compared to a PMSM [64].

The excitation current injected in the wired rotor is controlled with a simple buck converter directly supplied by the 12V battery. The connection between the buck converter and the wired rotor is made through a collector and the brush is easily recognizable on the photograph 2.1. The slip ring on the rotor can be seen on figure 2.2.

When mounted on a vehicle, the electric powertrain is connected to the main powertrain with a system of cam and mechanical belt and the load torque applied on the i-StARS may be highly

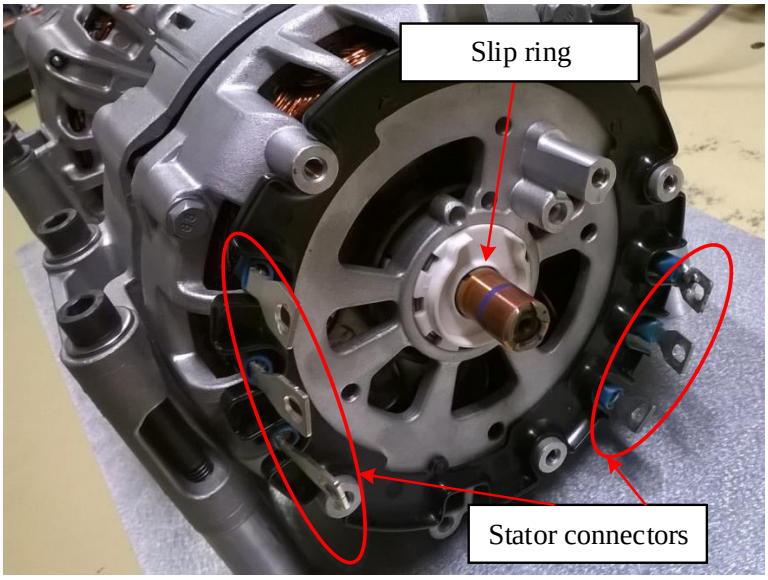

Figure 2.2. The i-StAR machine without the inverter and the brush.

variable. Indeed, since mild-hybrid application aims to activate the electric powertrain even when the vehicle is moving, the mechanical load may be difficult to characterize and depends on the connection with the ICE.

2.1.b Comparison with the experimental test bench developed for current sensorless control

The system made in the GREEN laboratory within the framework of the current sensorless control is slightly different from electric powertrain commercialized by Valeo. Indeed there was no combustion engine available to connect the electric powertrain to. Moreover, the control unit as it is done on Valeo system does not easily allow prototyping, however it is important in this study to implement rapidly different control solutions for testing. This paragraph will introduce the test bench realized in the laboratory and will explicit the differences with Valeo electric powertrain.

For our study, a battery as it is used on vehicles was not a reasonable choice to adopt. A battery has to be recharged frequently and its voltage varies with the charge level. For this reason, it has been decided to use a controllable power supply instead of a battery. The other advantage of using a power supply is the possibility to impose a saturation on the output current: this is a welcomed overall protection when testing current sensorless controllers on the WRSM.

Valeo provided for this study the WRSM, an i-StARS machine with its inverter interlocked on the stator. The inverter in this configuration was however difficult to use. Indeed, the control unit and the MOSFETs are produced industrially for the machine and the control unit was not accessible for implementing our own control laws. For this reason, it has been decided to remove the original electronic devices and only keep the machine. To replace it, a new inverter has been designed and built in a way to have characteristics as close as possible to the original one. It has been decided to order MOSFETs module with similar characteristics than the ones used by Valeo. The most adapted module for our application was Mitsubishi Electric's FM600TU-07A MOSFETs module [65]. This module is already in a 3-legs inverter configuration: it contains 6 MOSFETs assembled as sketched on diagram 2.3. These modules have a maximum drain source voltage of $V_{DSS} = 75V$ and a maximum drain current of $I_D = 300A$. The drain-source ON resistance $R_{DS(ON)}$ is between 0.5 and 0.75 $m\Omega$. Two of the modules described have been mounted on a large radiator. The radiator has been willingly over sized, since compactness and thermal issues are not a part of our study. The control of the MOSFETs is made thanks to 6 drivers SKHI 22BH4R, 3 for each modules. These drivers are convenient since one can control the two MOSFETs of one leg: it is a dual driver that drives interlocked top and bottom MOSFETs of a leg. They also feature an intern and adjustable deadtime generator.

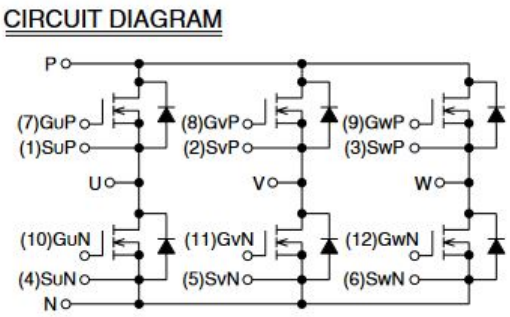

Figure 2.3. Diagram representing the connection between the MOSFETs in the FM600TU-07A module [65].

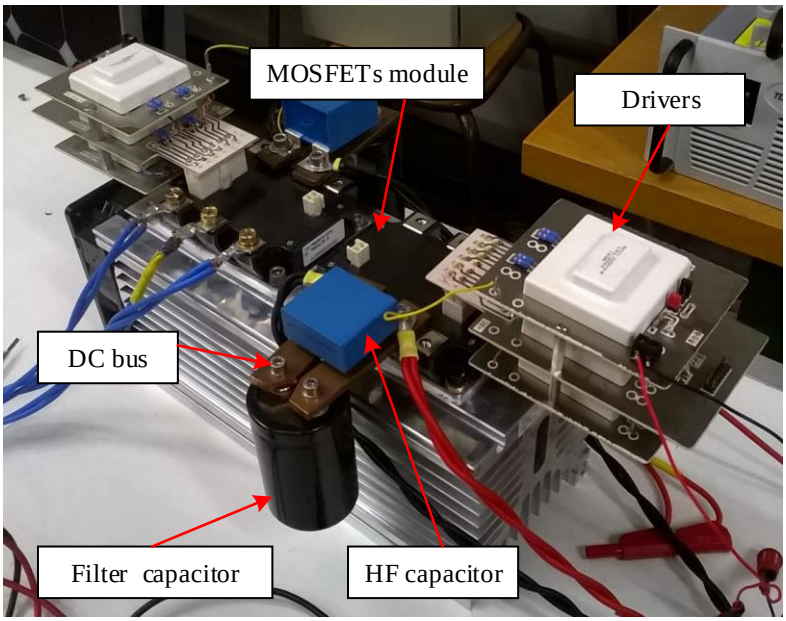

Figure 2.4. Photo of the electronic devices assembled together.

The input filter has also been included with the inverter: a large aluminum electrolytic capacitor of 6.8 mF has been wired to the DC bus of the inverter with a bus bar. In parallel with this large capacitor, a decoupling capacitor has been added in order to filter high frequency noises from the inverter. The whole device containing the MOSFETs modules, the radiator, the driver and the input filter capacitor can be seen on photo 2.4.

In order to load the i-StARS machine, another WRSM has been coupled on the same axis, as shown on figure 2.5. This load machine is a former model of Valeo alternator. The current created in this alternator flows through a rectifier which is linked to a DC active load. This is a useful configuration to easily vary the mechanical load applied to the i-StARS machine.

The i-StARS machine without its inverter interlocked lacks an important device: the brush that connects to the rotor collectors, as it can be seen on figure 2.2. An adapted brush has been fixed on the stator. A Buck converter was designed and built in order to control the excitation current as it is done on Valeo's system. Both the inverter and the Buck converter control signals are generated with a dSpace MicroLabBox.

Sensors on the test bench have been added in order to test the sensorless control and for the security of the system. Valeo has supplied the mechanical sensor, a voltage supplied hall effect sensor that gives a sine and cosine voltage in output that gives an image of the rotor position and speed after signal processing with a Phase-Locked Loop (PLL). The principle of a Hall effect speed sensor is described in [66]. It consists in a ring magnet mounted on the rotor shaft of the machine with Hall sensors placed around and shifted by 120° electric which corresponds to 120° divided by the number of pair of poles, as it is shown on figure 2.6. The ring magnet is a homogeneous piece of permanent magnet material into which a chosen number of pole have been magnetized. In the Hall effect sensor used in Valeo's system, 6 pair of poles have been magnetized so that the voltage output of the Hall effect sensors directly give the electric speed and position of the rotor.

This sensor is very robust and accurate and allows having a precise measurement of the rotor position and speed. A current clamp has been placed on the DC+ output of the power supply

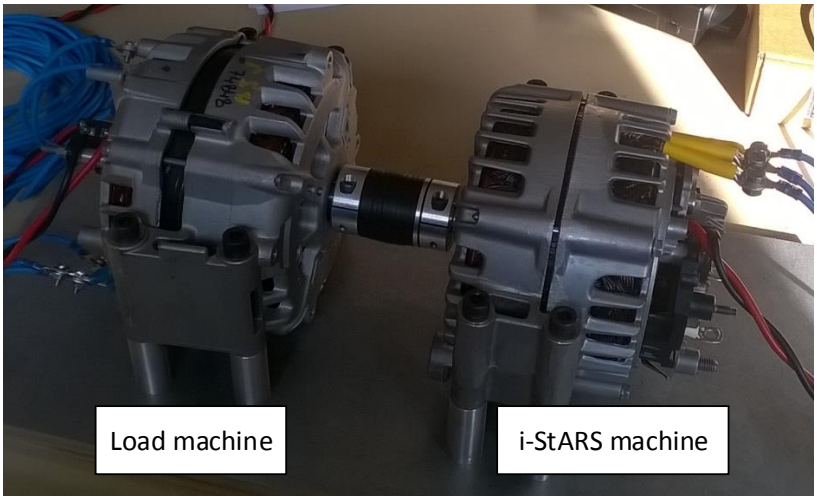

Figure 2.5. Photo i-StAR machine and the load machine coupled.

and corresponds to the battery current that is measured on Valeo's system. In the rest of this study, this current will be refereed as the battery current i_{bat} for simplification. A voltage sensor placed on the filter capacitor gives a measure of the DC voltage.

The whole system built and described in this paragraph can be seen on the photograph of figure 2.7, where the two WRSM can be seen on the bottom left. The load alternator is on the left and the i-StARS is on the right. The dSpace MicroLabBox is on the right of the picture. In the background, the power supply for the inverter (bottom) and for the rotor (top) can be seen. The electric diagram associated to this test bench is presented on figure 2.8.

With this setup, the characteristics of the electric powertrain built (WRSM, inverter and power supply) are similar to Valeo's powertrain. It is however not as compact, and the control is made in a more adapted configuration for research, with a possibility to change easily the control laws when required.

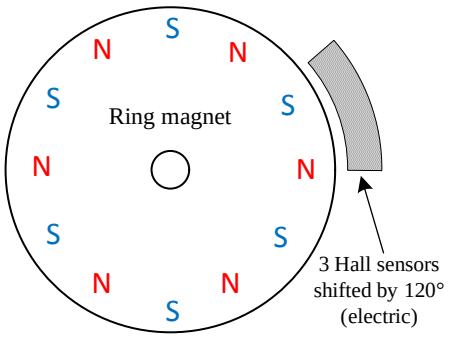

Figure 2.6. Diagram of the Hall effect based position sensor.

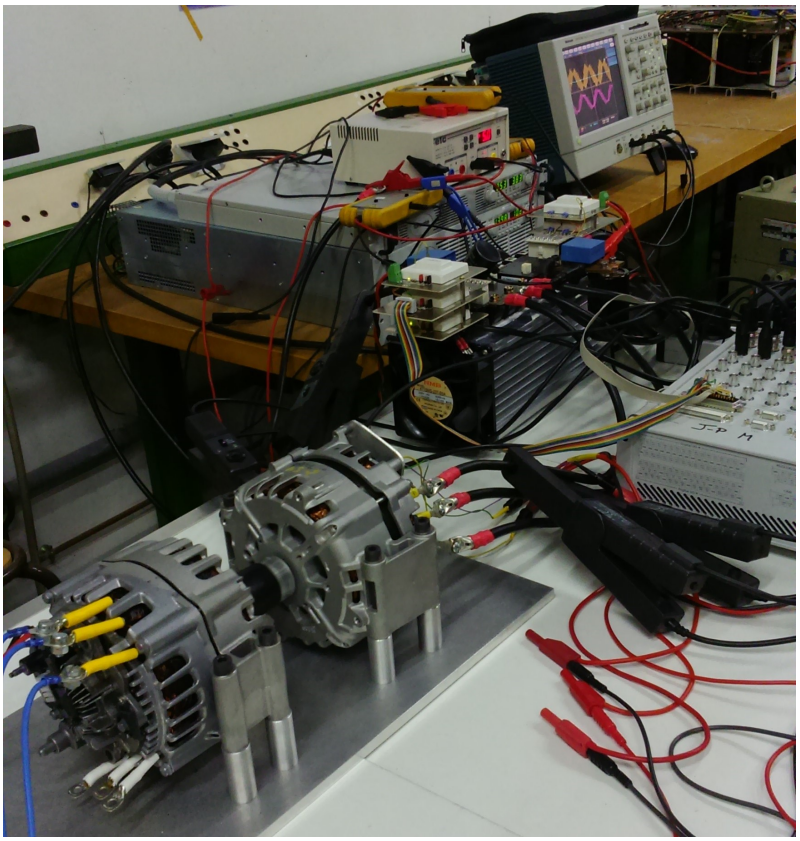

Figure 2.7. Photograph of the electric powertrain built in the laboratory.

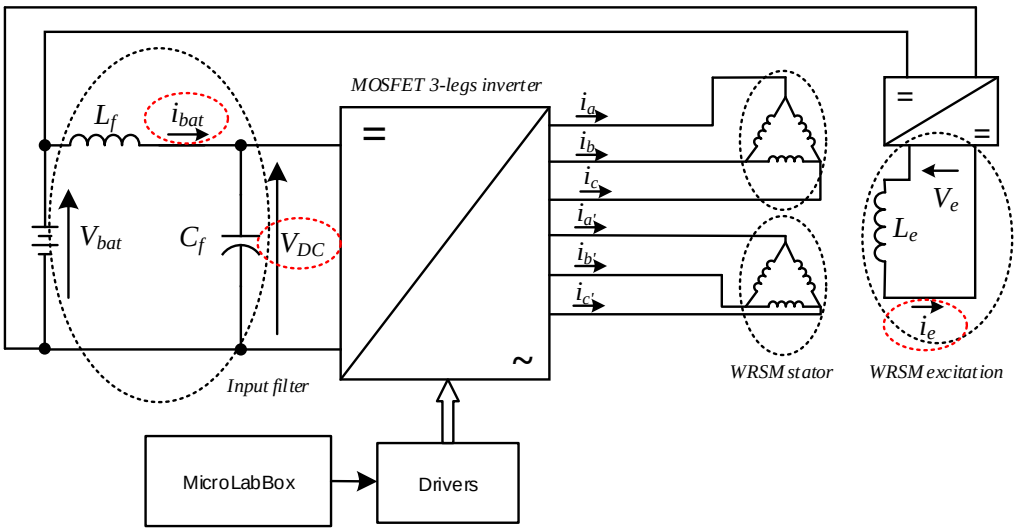

Figure 2.8. Electric diagram of the electric powertrain built.

2.2 Modeling of the machine

Before starting any experimental measurements on the system built and described in the previous section, a theoretical study of the functioning of the i-StARS machine has been conducted in the PhD study of Geoffrey Devornique in the GREEN laboratory and within the LowCO2Motion+ project [59]. A part of his work focused on the electromagnetic description of the machine. If the theoretical results are not directly usable, the interpretation of the results obtained in this study can lead to a better knowledge of the electric equations related to the machine. The theoretical modeling will then focus on the electric model that will be used for the characterization of the test bench machine and that will be usable for the observers designed and presented in chapter 3.

2.2.a Electromagnetic approach

In [59], the main objective of Dr. Devornique's study was to propose an electromagnetic modeling of a WRSM that combines robustness (or precision) of the electromagnetic fields calculated with this modeling while dividing the computation time by at least 4 with the method developed compared to classic formulations. The purpose of this modeling improvement was to be able to propose an optimization of the geometry of the i-StARS machine in order to improve the performances of the WRSM. The optimization mainly focuses on the geometry of the claw-poles of the rotor, with and without magnets between the poles. The approach used for the modeling relies on the finite element method with the free software Gmsh-GetDP. A 3D model of the i-StARS machine has been meshed based on CAD files sent by Valeo in order to obtain a mesh geometry as close as possible to the real machine. The meshing result made in [59] is shown on figure 2.9. On this figure, it is interesting to notice on the central figure representing the rotor, how the magnets are mounted between the claw-poles in a darker grey. The winding is inside the rotor in red.

It is yet proven in this work that there is a periodicity of the geometry of the machine: the stator can be divided in 6 identical parts, each one representing an angle of 60° of the full stator. The stator presents indeed a rotational 6-fold symmetry. The rotor have the same symmetric properties. It is then shown in G.Devornique's work that only $1/6^{th}$ of the full machine is enough to mesh to make calculation for the whole machine. The result of this meshing is presented on figure 2.10. This avoids making redundant calculation and saves a significant amount of time (tables of calculation times are given in [59]).

Figure 2.11 represents the calculation of the flux on a double pole pitch for a given operating point in the full meshed machine of figure 2.9 (in dashed linestyle) and in the meshed single pole of figure 2.10 (in solid linestyle). The method of calculation of the flux on the 3 phases of each

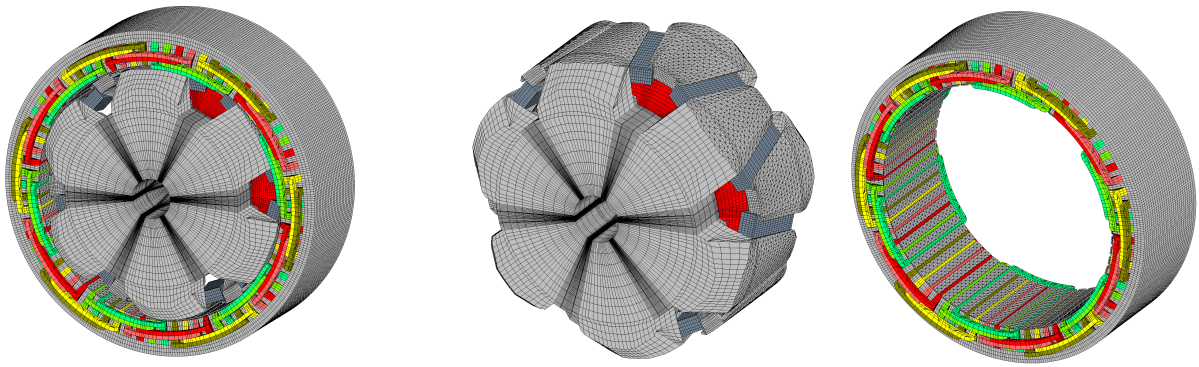

Figure 2.9. Meshing of the full i-StARS machine with Gmsh-GetDP [59].

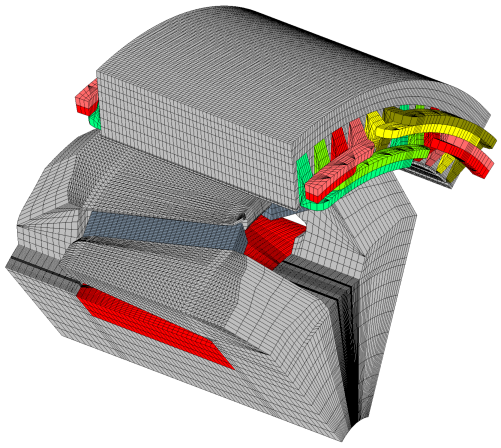

Figure 2.10. Meshing of 1 pole of the i-StARS rotor and stator with Gmsh-GetDP [59].

stator is detailed in [59]. From this figure, it can be noted that the calculation results are really close for the two different kinds of meshing, which tends to validate the single pole meshing use. Indeed the results are equivalent for a reduced computing time.

These results presented so far however only rely on a finite element analysis (FEA) model of the machine and needs to be validated with experimental tests on the real test bench. Indeed, with finite elements methods, the results strongly depend on the choice of calculation method and on the meshing of the machine. In Dr. Devornique's work are presented comparisons between different techniques of calculation of the flux and also between different meshings and the results can present more or less disparities. To validate a model, some experiments have been undertaken in collaboration with Dr. Devornique on the test bench built and presented in the previous section.

In order to validate the model of the machine presented on 2.10, it has been decided to compare the back-EMF induced in the stator at no-load operating point, when it is driven by the other machine on the test bench (see figure 2.5) at 520 rpm with the results computed using Dr. Devornique's FEA model. To do so, Valeo's former alternator has been controlled in order to reach the reference speed. The stators of the i-StARS machine are in open circuit, only voltage sensors have been connected to the stators. The i-StARS back-EMF measurements are done for an excitation current in the rotor going from 0 to 8A with a step of 0.5A between each measures.

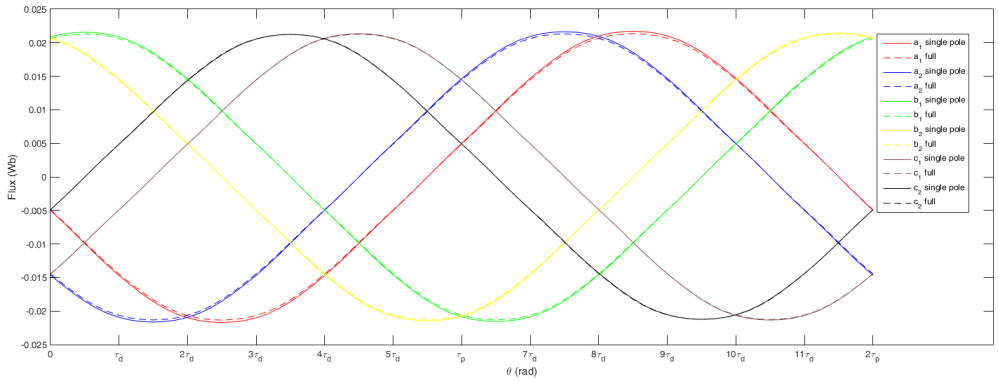

Figure 2.11. Comparison of the flux calculations in the complete meshed machine and in the periodic meshed machine.

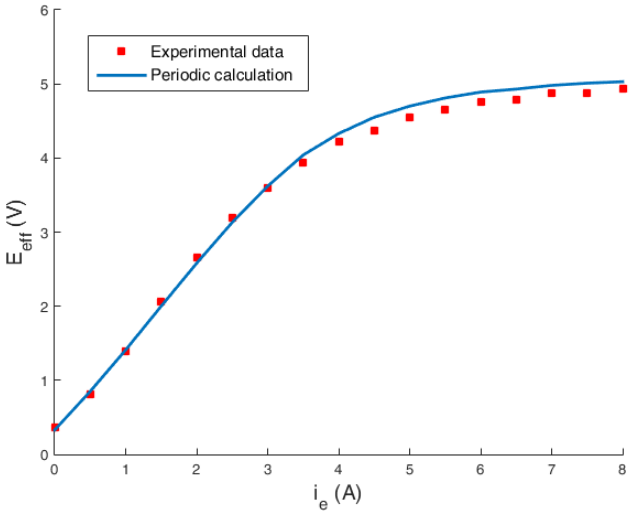

Figure 2.12. Back-EMF in the i-StARS driven at 520 rpm as a function of the excitation current.

The same test is reproduced in the finite element model of the machine. The results are combined on figure 2.12.

From figure 2.12, it is remarkable that the results from the test bench measurements and the ones from the simulations are very close to each other. These results will also give precious information for the knowledge of the electric model of the machine. Indeed from the blue curve of figure 2.12, it is possible to deduce that between 0A and 4A of excitation current, the machine works in a linear operational range. Above this current value, the machine can be considered in saturated operational range. The saturation knee is between 4A and 5A. It is interesting to notice that when the excitation current is null in the rotor, there is still a small back-EMF of $0.4V_{rms}$ induced in the machine. This is due to the effect of the magnets between the claw-poles of the rotor. Their role is to restrict the flux leakages in the rotor, but they also have a weak contribution to the back-EMF.

2.2.b Circuit-based electric model

The information brought by the electromagnetic modeling of the machine, and more particularly the relation between the back-EMF and the excitation current will be useful to build a model for control and observation purposes. This chapter will be focused on building a dq-model composed of state equations representing as accurately as possible the functioning of a WRSM fed by an inverter. For the sake of simplification, the model will be developed for a single stator.

A 3-phase synchronous machine stator can be simply represented by an inductance with an intern resistance on 3 phases a, b and c distant from each other by an angle of $\frac{2\pi}{3}$ radians. The wired rotor can be represented by an inductance with an intern resistance aligned with an axis "dr" and in quadrature with the axis "qr", shifted by an angle θ from the a-axis. This representation is summed up on figure 2.13. Note that in the developed model in this chapter, the damping effect in the machine are not taken into account, as well as all the parasitic effects that can be involved in a physical machine (parasitic capacitors between the phases in the stator, hysteresis phenomenons in the iron, eddy currents in the iron and other parasitic phenomenons).

From this representation of the WRSM, the following equations can be deduced:

$$\begin{array}{rcl} [V_s] & = & \mathbf{r_s}.[i_s] + [\frac{d\Phi s}{dt}] \\ V_r & = & r_r.i_r + \frac{d\Phi r}{dt} \end{array} \tag{2.1}$$

with $[X_s] = \begin{bmatrix} X_a \\ X_b \\ X_c \end{bmatrix}$, V_s being the stator voltages vector, i_s the stator currents vector, Φ_s the magnetic fluxes in the stator. $\mathbf{r_s}$ is the matrix of the stator resistances written $I_3.[r_s]$. The variables V_r, i_r, r_r and Φ_r are respectively the rotor voltage, the rotor current, the rotor resistance and the rotor magnetic flux. The machine is supposed balanced thus $r_a = r_b = r_c = R_s$

The sum of the currents in the stator being null, it is possible to express the 3-phase equations of the stator into a new two-phase frame of reference $\alpha\beta$. The change from the abc frame of reference to the $\alpha\beta$ frame is made through a change of basis with the Concordia matrix T_{32} such as:

$$\begin{bmatrix} V_\alpha \\ V_\beta \end{bmatrix} = R_s. \begin{bmatrix} i_\alpha \\ i_\beta \end{bmatrix} + \frac{d}{dt} \begin{bmatrix} \Phi_\alpha \\ \Phi_\beta \end{bmatrix} \tag{2.2}$$

where $\begin{bmatrix} X_\alpha \\ X_\beta \end{bmatrix} = T_{32}^t. \begin{bmatrix} X_a \\ X_b \\ X_c \end{bmatrix}$ with $T_{32} = \sqrt{\frac{2}{3}} \begin{bmatrix} 1 & 0 \\ -\frac{1}{2} & \frac{\sqrt{3}}{2} \\ -\frac{1}{2} & -\frac{\sqrt{3}}{2} \end{bmatrix}$

Now the variables linked to the stator can be described in a two-phase frame, but the system as it is still depends on the position of the rotor. Indeed, voltages, currents and fluxes are sine functions depending on the angle θ. To avoid this dependence, the $\alpha\beta$ stator variables are expressed in a rotating frame dq, linked to the rotor frame: the d-axis is the same than the dr-axis shown on 2.13, same goes for the q-axis that is the same than the qr-axis on the figure. To perform this change of basis, the Park transform is used, which is a rotation matrix $P(-\theta)$ applied to the $\alpha\beta$ variables, giving:

$$\begin{bmatrix} V_d \\ V_q \end{bmatrix} = R_s. \begin{bmatrix} i_d \\ i_q \end{bmatrix} + \frac{d}{dt} \begin{bmatrix} \Phi_d \\ \Phi_q \end{bmatrix} + \dot{\theta}.P\left(\frac{\pi}{2}\right). \begin{bmatrix} \Phi_d \\ \Phi_q \end{bmatrix} \tag{2.3}$$

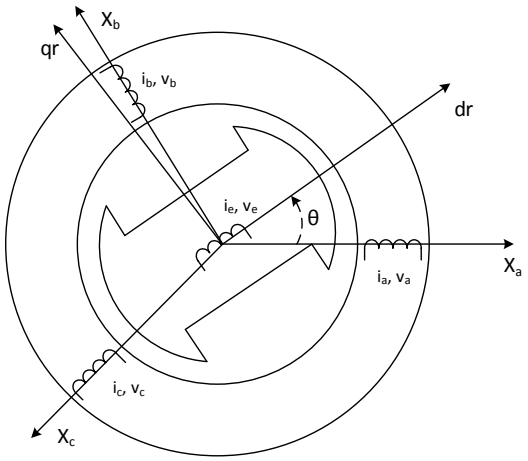

Figure 2.13. Simplified representation of the WRSM.

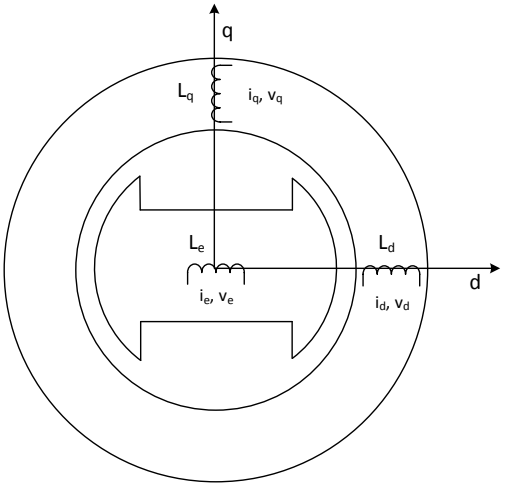

Figure 2.14. Simplified representation of the wired synchronous machine in the dq reference frame.

with: $\begin{bmatrix} X_d \\ X_q \end{bmatrix} = P(-\theta).\begin{bmatrix} X_\alpha \\ X_\beta \end{bmatrix}$ (Park's transformation)
and $P(\theta) = \begin{bmatrix} cos(\theta) & -sin(\theta) \\ sin(\theta) & cos(\theta) \end{bmatrix}$ (rotational matrix)

In this frame of reference, the figure 2.13 can be drawn again with the two-phase dq axis. The representation of the simplified WRSM in the dq reference frame is shown on figure 2.14.

The fluxes on the d and q axis can now be written:

$$\begin{array}{rcl} \Phi_d & = & L_d.i_d + \Phi_{ed} \\ \Phi_q & = & L_q.i_q \\ \Phi_r & = & L_e.i_e + \Phi_{de} \end{array} \tag{2.4}$$

For the WRSM, Φ_{ed} is created by the excitation current in the stator d-axis, which traduces in equation with:

$$\Phi_{ed} = M.i_e + \Psi_f \tag{2.5}$$

With M the mutual inductance between the rotor and the stator and Ψ_f the flux generated by the inter-pole magnets through the stator windings if the WRSM features those. Indeed it corresponds to the leakage flux of the magnets. Its impact on the torque of the machine can however be neglected compared to $M.i_e$ for the usual values of excitation current: from figure 2.12, when an excitation current of 3A is applied in the rotor and by considering Ψ_f constant, the part of the permanent magnets on the total back-EMF is only 6% and it decreases when i_e rises. For the rest of the study we will consider equation 2.6:

$$\Phi_{ed} = M.i_e \tag{2.6}$$

In the same way, Φ_{de} is the flux created by the d-axis current of the stator in the rotor, which gives equation 2.7:

$$\Phi_{de} = M.i_d - \Psi_r \tag{2.7}$$

With Ψ_r the flux generated by the rotor magnets through the rotor winding. This flux is useful to reduce the saturation of the rotor magnetic circuit. It is supposed constant. It is important to also note that, if the stator inductances depend on the position of the rotor in the 3-phase reference frame, the dq axis inductances are constant.

From equations 2.3 to 2.7, the following system of electric state equations can be formulated:

$$\begin{array}{rcl} V_d & = & R_s.i_d + \frac{d\Phi_d}{dt} - \omega.\Phi_q \\ V_q & = & R_s.i_q + \frac{d\Phi_q}{dt} + \omega.\Phi_d \\ V_e & = & R_e.i_e + \frac{d\Phi_r}{dt} \end{array} \tag{2.8}$$

And by injecting equations 2.4 to 2.7 in 2.8, this yields:

$$\begin{array}{rcl} V_d & = & R_s.i_d + L_d.\frac{d}{dt}i_d + M.\frac{d}{dt}i_e - \omega.L_q.i_q \\ V_q & = & R_s.i_q + L_q.\frac{d}{dt}i_q + \omega.(L_d.i_d + M.i_e) \\ V_e & = & R_e.i_e + L_e.\frac{d}{dt}i_e + M.\frac{d}{dt}i_d \end{array} \tag{2.9}$$

with $\omega = \dot{\theta}$ the electric angular speed of the rotor. This electric speed can be linked to the mechanical speed of the rotor Ω with the relation $\omega = p.\Omega$, p being the number of pair of poles of the machine.

When equations 2.9 are rewritten to be interpreted as a system of state equations, it gives:

$$\begin{array}{rcl} \frac{d}{dt}i_d + \frac{M}{L_d}.\frac{d}{dt}i_e & = & \frac{1}{L_d}\left(V_d - R_s.i_d + \omega.L_q.i_q\right) \\ \frac{d}{dt}i_q & = & \frac{1}{L_q}\left(V_q - R_s.i_q - \omega.(L_d.i_d + M.i_e)\right) \\ \frac{d}{dt}i_e + \frac{M}{L_e}.\frac{d}{dt}i_d & = & \frac{1}{L_e}\left(V_e - R_e.i_e\right) \end{array} \tag{2.10}$$

When replacing $\frac{d}{dt}i_e$ in the equation of i_d, and $\frac{d}{dt}i_d$ in the equation of i_e, the following system of state equations is obtained:

$$\left\{ \begin{array}{rcl} \frac{d}{dt}i_d & = & \frac{L_e}{L_d.L_e - M^2}\left(V_d - R_s.i_d + p.\Omega.L_q.i_q - \frac{M}{L_e}\left(V_e - R_e.i_e\right)\right) \\ \frac{d}{dt}i_q & = & \frac{1}{L_q}\left(V_q - R_s.i_q - p.\Omega.\left(L_d.i_d + M.i_e\right)\right) \\ \frac{d}{dt}i_e & = & \frac{L_d}{L_d.L_e - M^2}\left(V_e - R_e.i_e - \frac{M}{L_d}\left(V_d - R_s.i_d + p.\Omega.L_q.i_q\right)\right) \end{array} \right. \tag{2.11}$$

The system of equation 2.11 represents here a simplified WRSM. In that configuration, the saturation of the machine is not taken into account while it exists according to the tests done and represented on figure 2.12. The saturation can be considered by replacing the linear functions in equations 2.8 by the actual nonlinear functions derived from a finite element analysis. In this case, it is preferable to choose the fluxes as the state variables. This leads to the following model:

$$\begin{array}{rcl} \frac{d\Phi_d}{dt}(i_d, i_q, i_e) & = & V_d - R_s.i_d + \omega.\Phi_q(i_d, i_q, i_e) \\ \frac{d\Phi_q}{dt}(i_d, i_q, i_e) & = & V_q - R_s.i_q - \omega.\Phi_d(i_d, i_q, i_e) \\ \frac{d\Phi_r}{dt}(i_d, i_q, i_e) & = & V_e - R_e.i_e \end{array} \tag{2.12}$$

And equation 2.12 yields to:

$$\begin{array}{rcl} i_d & = & f_d(\Phi_d, \Phi_q, \Phi_r) \\ i_q & = & f_q(\Phi_d, \Phi_q, \Phi_r) \\ i_e & = & f_e(\Phi_d, \Phi_q, \Phi_r) \end{array} \tag{2.13}$$

with f_d, f_q and f_e nonlinear functions that can be determined through a FEA study of the WRSM.

The other important phenomenon not represented in this model is the damping effect in the machine. The damping effect phenomenon in WRSM is described in [67]. This phenomenon can

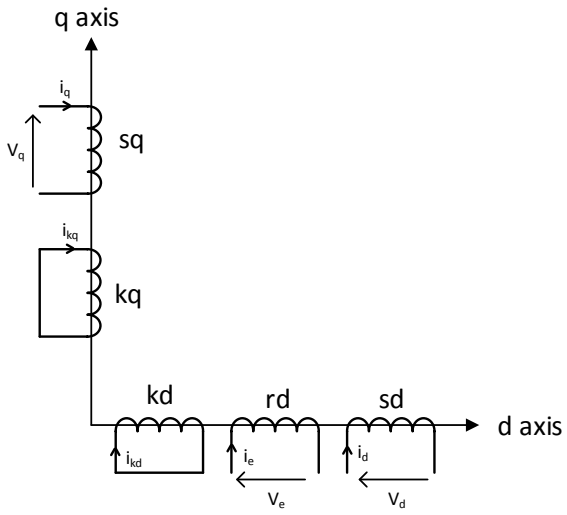

Figure 2.15. Simplified representation of the machine windings with the damping effect.

be modeled by one inductance in short circuit on both the d and the q-axis, as shown on figure 2.15.

From figure 2.15, the fluxes on the d and q axes can be written:

$$\begin{array}{rcl} \Phi_d & = & L_d.i_d + M.i_e + M_{kd}.i_{kd} \\ \Phi_q & = & L_q.i_q + M_{kq}.i_{kq} \\ \Phi_r & = & L_e.i_e + M.i_d + M_{kr}.i_{kd} \\ \Phi_{kd} & = & L_{kd}.i_{kd} + M_{kd}.i_d + M_{kr}.i_e \\ \Phi_{kq} & = & L_{kq}.i_{kq} + M_{kq}.i_q \end{array} \tag{2.14}$$

with M_{kd} the mutual inductance between the damper winding of the d axis with the d axis of the stator, M_{kr} the mutual inductance between the damper winding of the d axis with the rotor and M_{kq} the mutual inductance between the damper winding of the q axis with the q axis of the stator.

This leads to the voltage equations 2.15:

$$\begin{array}{rcl} V_d & = & R_s.i_d + L_d.\frac{d}{dt}i_d + M.\frac{d}{dt}i_e + M_{kd}.\frac{d}{dt}i_{kd} - \omega.(L_q.i_q + M_{kq}.i_{kq}) \\ V_q & = & R_s.i_q + L_q.\frac{d}{dt}i_q + M_{kq}.\frac{d}{dt}i_{kq} + \omega.(L_d.i_d + M.i_e + M_{kd}.i_{kd}) \\ V_e & = & R_e.i_e + L_e.\frac{d}{dt}i_e + M.\frac{d}{dt}i_d + M_{kr}.\frac{d}{dt}i_{kd} \\ 0 & = & R_{kd}.i_{kd} + L_{kd}.\frac{d}{dt}i_{kd} + M_{kd}.\frac{d}{dt}i_d + M_{kr}.\frac{d}{dt}i_e \\ 0 & = & R_{kq}.i_{kq} + L_{kq}.\frac{d}{dt}i_{kq} + M_{kq}.\frac{d}{dt}i_q \end{array} \tag{2.15}$$

As it can be seen from equations 2.15, the damper windings in the WRSM affect the evolution of the dq axis currents and the excitation current during transient phases. However, as it will be experimentally shown in the next section, the damper effect can be neglected and it is not needed to theoretically describe the electric variables of the i-StARS WRSM. The electric model chosen to describe the machine is the one given by equations 2.11. The next section will aim to characterize experimentally the different parameters of the studied WRSM used in those equations.

2.3 Measurements of the WRSM characteristics

The general characteristics of the WRSM have been provided by Valeo, but a knowledge as precise as possible of the machine is required to perform current sensorless control. In this section, measurements will be conducted on the test bench in order to fully characterize the electric powertrain. The aim of this procedure is to establish the system of state equations that fits our experimental setup the best. This system of equation will be useful for the simulation of the machine in Simulink, its control on the test bench and, as it will be detailed in the next chapter, for the precision of current observation for current sensorless control. For the sake of generality, the WRSM being a machine quite subject to parametric variations as it will be shown later, the measurements and the current sensorless control tests will be conducted during transitions between different operating points. This will allow considering effects of the magnetic saturation and the dampers. In order to focus on the phenomenons linked to the interactions between the wired rotor and one stator and to avoid the magnetic interactions between the two stators, it has been decided to only use one stator in the following tests.

2.3.a Characterization of the WRSM for a given operating point

The first step that has been decided to undertake is a full characterization of the machine for one operating point. This includes a set of tests to estimate the parameters of the above model. This operating point has been chosen in a way to be as close as possible to a nominal operating point of a powertrain mounted on a vehicle. When the machine reaches its thermal steady-state, measurements have been conducted in order to characterize all the parameters used in the system of equation of 2.15. To do so, the rotor is blocked so that the speed is maintained to 0 rpm. Doing this, the back-EMF is zero. The rotor excitation circuit is opened in order to remove the impact of the excitation flux on the d-axis stator current (see figure 2.15).

With this setup, a step on the voltage V_d is applied, from 0.4V to 0.8V while V_q is fixed to 0. The evolution of the d axis current due to this step of voltage is shown on figure 2.16.

In these configurations, the equations of 2.15 on the stator currents can be simply rewritten:

$$\begin{aligned} \frac{d}{dt}i_d &= \frac{1}{L_d}\left(V_d - R_s.i_d - M_{kd}.\frac{d}{dt}i_{kd}\right) \\ \frac{d}{dt}i_q &= \frac{1}{L_q}\left(V_q - R_s.i_q - M_{kq}.\frac{d}{dt}i_{kq}\right) \end{aligned} \tag{2.16}$$

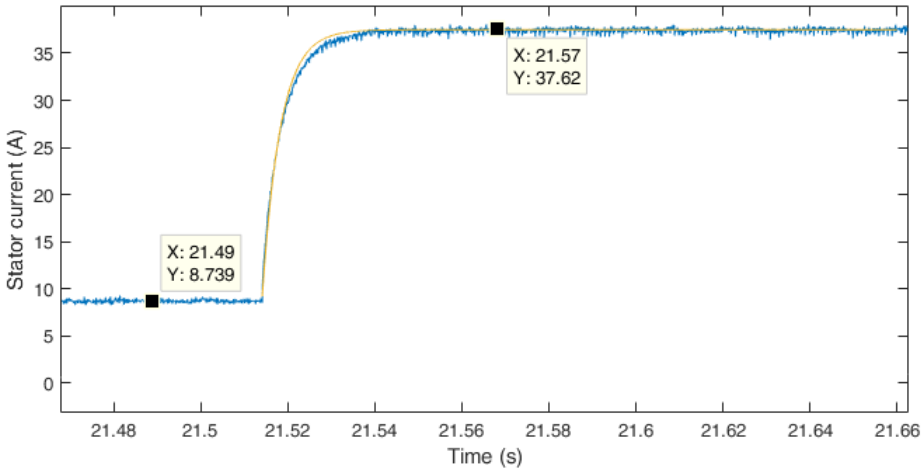

Figure 2.16. Evolution of the d-axis current (blue) and the theoretical response of a first order system (yellow) when a step on V_d is applied.

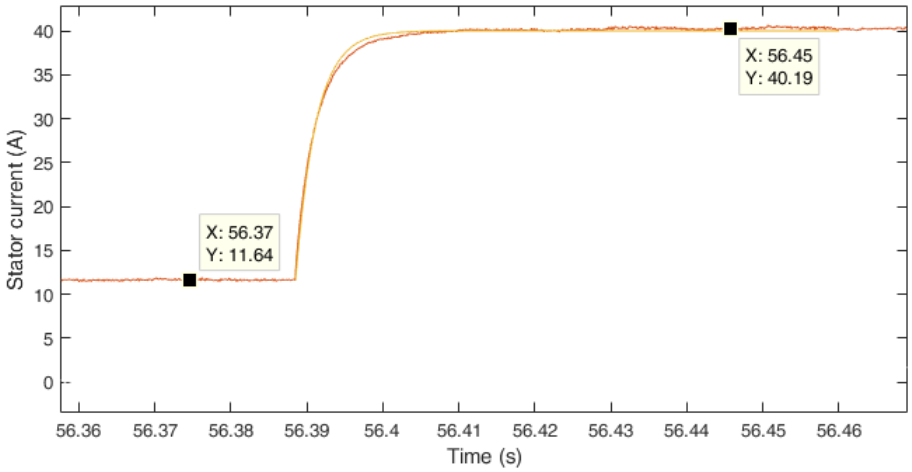

Figure 2.17. Evolution of the q-axis currents (red) and the theoretical response of a first order system (yellow) when a step on V_q is applied.

Equation 2.16 suggests that, if the damper windings impact are neglected, the stator d-axis current should behave as a response of a first-order system to a step on the voltage V_d. From figure 2.16, the evolution of the current (in blue) behaves as the theoretical response of a first-order system to a voltage step (in yellow), showing that the damper effect is negligible in the studied machine. From the curve of i_d, the parameters L_d and R_s in 2.16 can be deduced. Indeed, for a a response of a first-order system to a voltage step, the resistance R_s can be easily found on any point of the curve with an Ohm's law and the time constant leads to the inductance value.

From figure 2.16, it is possible to deduce : $R_s = 0.014\Omega$ and $\tau_d = 4.2ms$. Since $\tau_d = \frac{L_d}{R_s}$, the d-axis inductance can be retrieved and is equal to $L_d = 58.4\mu H$.

The same test has been run with a step on the voltage V_q while V_d is fixed to zero. With the same logic than for the d-axis current, the q-axis current is expected to behave as a first order response to a voltage step. The evolution of the current is presented on figure 2.17.

The same procedure for q-axis parameters identification than for the d-axis parameters has been used. In normal condition this step on the q-axis voltage would make the rotor start. In order to avoid that and keep the speed rotor null, the angle measurement from the mechanical sensor is disconnected from the Park's transformation of the voltages and currents in the control and replaced by a constant value. From figure 2.17, the following parameters have been identified : $R_s = 0.014\Omega$, $\tau_q = 2.7ms$ and $L_q = 38\mu H$. As expected, the stator resistance is the same for both d and q axes. The yellow curve on figure 2.17 is the theoretical response of a a first order system to a step on V_q, showing that on this axis the damper windings can be neglected too.

The electric parameters linked to the rotor winding has also been measured. The setup of the system is the same than for the previous tests (machine heated up, rotor blocked) but this time the stator circuit is open to guarantee that i_d and i_q are null. In this configuration, the following equation can be deduced:

$$\frac{d}{dt} i_e = \frac{1}{L_e} \left(V_e - R_e . i_e \right) \tag{2.17}$$

Note that the current i_{kd} is not included since it has been shown from figures 2.16 and 2.17 that the damper effect is negligible in the studied WRSM.

A voltage step on V_e is applied, from 2V to 5V. As for the stator currents, the expected excitation current evolution should be similar to a response of a first-order system. The excitation

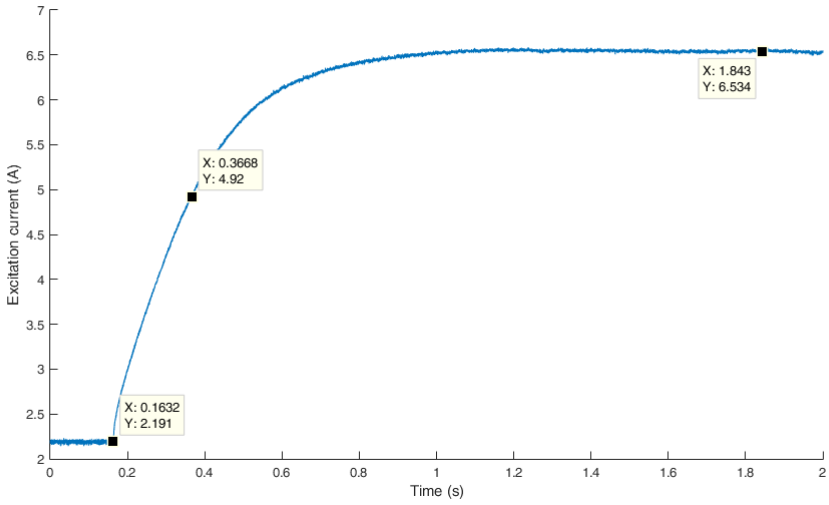

Figure 2.18. Evolution of the excitation current when a step on V_e is applied.

current evolution is shown on figure 2.18.

From figure 2.18, by assimilating the curve described by i_e to a response of a first-order system, the following electric parameters linked to the rotor are obtained: $R_e = 0.7\Omega$, $\tau_e = 0.20s$ and since $\tau_e = \frac{L_e}{R_e}$, $L_e = 0.14H$.

The parameters linked to the mechanical equation of the machine and the mutual inductance between the rotor and the stator still need to be identified. To do so, a classic PI control of the stator currents is implemented. The d-axis current is controlled to 0A ($i_d = 0$), and at a certain time, the reference for i_q is changed. The dynamics of the currents being way higher than the mechanical dynamics of the machine, the variation of i_q can be considered as a step in the mechanical time scale. In that condition, and considering that the terms $(L_d - L_q).i_d$ and Ψ_f can be neglected in the torque equation since i_d is controlled to 0A and it has been shown before that the impact of Ψ_f on the back-EMF is negligible, the equation on the speed of the machine can be written:

$$\frac{d}{dt}\Omega = \frac{1}{J}\left(p.i_q.M.i_e - f.\Omega - \Gamma_0\right) \tag{2.18}$$

with J the constant of mechanical inertia of the rotating components, f the friction coefficient of the rotor and Γ_0 the load torque applied to the rotating components.

On figure 2.19, the evolution of the rotor speed is presented. The excitation current is controlled at $i_e = 4.5A$ and it remains constant for all this measurement. At t=0.2s, a step on the q-axis current reference from 20 A to 31 A is performed. As the test was performed at no-load, $\Gamma_0 = 0$. Then from equations 2.11 and 2.18, this test allows estimating parameters M, f and J. Indeed in equation 2.11, all the parameters are known on the q-axis equation except M. The state variables are measured, so it is possible to deduce the parameter M from this equation with the measures of the rotor speed and the stator current. From figure 2.19, the two steady states operating points are:

First steady state operating point :

$V_q = 2.5V$
$i_q = 20A$
$\Omega = 230rpm - 24.1rd.s$
$i_e = 4.5A$

Second steady state operating point :

$V_q = 6.4V$
$i_q = 31A$
$\Omega = 700rpm - 73rd.s$
$i_e = 4.5A$

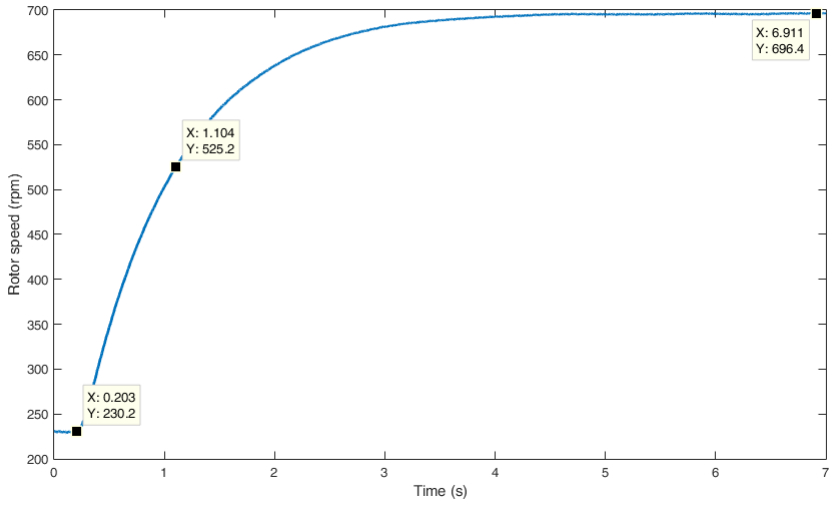

Figure 2.19. Evolution of the rotor speed when a step on i_q reference is applied.

From the q-axis equation 2.11, we have for the first steady state operating point:

$$V_{q1} - R_s.i_{q1} - p.\Omega_1.M.i_e = 0 \tag{2.19}$$

And the second operating point:

$$V_{q2} - R_s.i_{q2} - p.\Omega_2.M.i_e = 0 \tag{2.20}$$

And 2.20 minus 2.19 yields to:

$$M = \frac{\Delta V_q - R_s.\Delta i_q}{p.\Delta\Omega.i_e} \tag{2.21}$$

Equation 2.21 gives $M = 2.8mH$. It is interesting to notice that this value is coherent with the one that can be deduced from figure 2.12. The machine being driven by the load machine with no load, the back-EMF can be written $E_{rms} = p.\Omega.M.i_e = 4.3V$ and for the excitation current of 4.5 A, the associated M deduced is equal to $2.9mH$. In addition, because of leakage inductance, the condition $M^2 < L_d.L_e$ is respected.

The fluid friction coefficient can be found with the analysis of the low and high operating points of figure 2.19. From these two sets of measurements presented above and with the same method than for the calcultation of M but this time with equation 2.18, the deduced fluid friction coefficient f is $f = 0.017kg.m^2.s^{-1}$. The first order response gives the time constant $\tau_m = \frac{J}{f} = 0.9s$ which leads to the mechanical inertia J of the rotor $J = 0.0153kg.m^2$.

As it has been stated earlier, each operating point of the machine is described by a different set of electrical and mechanical parameters. The heat of the machine is responsible for electrical parameters modifications. Studies made in [68] show that the resistor of a machine can be modified by the temperature. The inductance of the phases of the stator are impacted by the saturation level of the motor [69].

The mechanical parameters also have their values changed according to the load of the machine and the wear of the mechanical components of the WRSM. Indeed, a long time use of the motor can lead to small defaults on the ball bearings, changing the frictions forces in the system as shown in [70] and [71]. In addition, the heating of the mechanical parts leads to a dilatation of the mechanical components that can induce a change in the mechanical parameters as well [72].

2.3.b Study on the parameter sensitivity for the observation

In order to characterize the sensitivity of the estimation of the state currents i_d and i_q towards parameter errors, a study based on tangent linearization of the electric state equations 2.11 around the estimated electric parameter has been conducted and will be presented in this paragraph. This linearization has been theoretically formulated in [73] and applied to an integrated PMSM (IPMSM) in [74]. Let's rewrite the first equation of 2.11 with estimated electric parameters $\hat{R_s}$, $\hat{L_d}$, $\hat{L_q}$ and $\hat{M}$ with $\hat{X} = X + \tilde{X}$, $\hat{X}$ being the estimation of a a given parameter X, $\tilde{X}$ being the error of estimation of a given parameter X. This formulation will be useful in the next chapter for the study on the nonlinear observers: errors in the parameters will be added to characterize their impact on the current estimation. It leads to equations 2.22:

$$\begin{array}{rcl} f_1 = \frac{di_d}{dt} & = & \frac{L_e}{\hat{L_d}.L_e - \hat{M}^2}\left(V_d - \hat{R_s}.i_d + p.\Omega.\hat{L_q}.i_q - \frac{\hat{M}}{L_e}\left(V_e - R_e.i_e\right)\right) \\ f_2 = \frac{di_q}{dt} & = & \frac{1}{\hat{L_q}}\left(V_q - \hat{R_s}.i_q - p.\Omega.\left(\hat{L_d}.i_d + \hat{M}.i_e\right)\right) \\ f_3 = \frac{d\Omega}{dt} & = & \frac{1}{J}\left(\hat{M}.i_e.p.i_q - f.\Omega - \Gamma_0\right) \end{array} \tag{2.22}$$

From this, the Jacobian matrix dO of the partial derivatives of f_1, f_2 and f_3 with respect to the vector of estimated electric parameters $X_p = \begin{bmatrix} \hat{R_s} & \hat{L_d} & \hat{L_q} & \hat{M} \end{bmatrix}^T$. It gives:

$$dO = \begin{bmatrix} \frac{\partial f_1}{\partial \hat{R_s}} & \frac{\partial f_1}{\partial \hat{L_d}} & \frac{\partial f_1}{\partial \hat{L_q}} & \frac{\partial f_1}{\partial \hat{M}} \\ \frac{\partial f_2}{\partial \hat{R_s}} & \frac{\partial f_2}{\partial \hat{L_d}} & \frac{\partial f_2}{\partial \hat{L_q}} & \frac{\partial f_2}{\partial \hat{M}} \\ \frac{\partial f_3}{\partial \hat{R_s}} & \frac{\partial f_3}{\partial \hat{L_d}} & \frac{\partial f_3}{\partial \hat{L_q}} & \frac{\partial f_3}{\partial \hat{M}} \end{bmatrix} \tag{2.23}$$

From equations 2.22, this leads to:

$$dO = \begin{bmatrix} \frac{-L_e}{\hat{L_d}.L_e - \hat{M}^2}.i_d & dO_{12} & \frac{L_e}{\hat{L_d}.L_e - \hat{M}^2}.p.\Omega.i_q & dO_{14} \\ \frac{-i_q}{\hat{L_q}} & \frac{-p.\Omega.i_d}{\hat{L_q}} & dO_{23} & \frac{-p.\Omega.i_e}{\hat{L_q}} \\ 0 & \frac{p.i_d.i_q}{J} & \frac{-p.i_d.i_q}{J} & \frac{p.i_e.i_q}{J} \end{bmatrix} \tag{2.24}$$

with:

$dO_{12} = \frac{-L_e^2}{(\hat{L_d}.L_e - \hat{M}^2)^2}.\left(V_d - \hat{R_s}.i_d + p.\Omega.\hat{L_q}.i_q - \frac{\hat{M}}{L_e}\left(V_e - R_e.i_e\right)\right)$

$dO_{14} = \frac{2.L_e.\hat{M}}{(\hat{L_d}.L_e - \hat{M}^2)^2}.\left(V_d - \hat{R_s}.i_d + p.\Omega.\hat{L_q}.i_q - \frac{\hat{M}}{L_e}\left(V_e - R_e.i_e\right)\right) - \frac{V_e - R_e.i_e}{\hat{L_d}.L_e - \hat{M}^2}$

$dO_{23} = \frac{-1}{\hat{L_q}^2}.\left(V_q - \hat{R_s}.i_q - p.\Omega.\left(\hat{L_d}.i_d + \hat{M}.i_e\right)\right)$

Let's consider a steady state where $i_d = 0$, $i_q = I_q \neq 0$ and $i_e = I_e \neq 0$. The matrix dO in 2.24 gives:

$$dO = \begin{bmatrix} 0 & dO_{12} & \frac{L_e}{\hat{L_d}.L_e - \hat{M}^2}.p.\Omega.I_q & dO_{14} \\ \frac{-I_q}{\hat{L_q}} & 0 & dO_{23} & \frac{-p.\Omega.I_e}{\hat{L_q}} \\ 0 & 0 & 0 & \frac{p.I_e.I_q}{J} \end{bmatrix} \tag{2.25}$$

with:

$dO_{12} = \frac{-L_e^2}{(\hat{L_d}.L_e - \hat{M}^2)^2}.\left(V_d + p.\Omega.\hat{L_q}.I_q - \frac{\hat{M}}{L_e}\left(V_e - R_e.I_e\right)\right)$

$dO_{14} = \frac{2.L_e.\hat{M}}{(\hat{L_d}.L_e - \hat{M}^2)^2}.\left(V_d + p.\Omega.\hat{L_q}.I_q - \frac{\hat{M}}{L_e}\left(V_e - R_e.I_e\right)\right) - \frac{V_e - R_e.I_e}{\hat{L_d}.L_e - \hat{M}^2}$

$dO_{23} = \frac{-1}{\hat{L_q}^2}.\left(V_q - \hat{R_s}.I_q - p.\Omega.\hat{M}.I_e\right)$

Since $\hat{X} = X + \tilde{X}$, in steady state it leads to:

$$dO = \begin{bmatrix} 0 & \frac{-L_e^2}{(\hat{L_d}.L_e - \hat{M}^2)^2}.\left(p.\Omega.\tilde{L_q}.I_q\right) & \frac{L_e}{\hat{L_d}.L_e - \hat{M}^2}.p.\Omega.I_q & \frac{2.L_e.\hat{M}}{(\hat{L_d}.L_e - \hat{M}^2)^2}.\left(p.\Omega.\tilde{L_q}.I_q\right) \\ \frac{-I_q}{\hat{L_q}} & 0 & \frac{-1}{\hat{L_q}^2}.\left(\tilde{R_s}.I_q - p.\Omega.\tilde{M}.I_e\right) & \frac{-p.\Omega.I_e}{\hat{L_q}} \\ 0 & 0 & 0 & \frac{p.I_e.I_q}{J} \end{bmatrix} \tag{2.26}$$

The matrix dO in equation 2.26 should be understood as follow: the rows correspond respectively from first to third to the sensitivity of i_d, i_q and Ω towards variations of the parameters corresponding to each columns, respectively from first to fourth to R_s, L_d, L_q and M. For example, if there is an error on the parameter L_q, meaning $\tilde{L_q} \neq 0$, i_d is sensitive towards variations of L_d (value of the element row 1 column 2 different from 0). If $\tilde{L_q} = 0$, the current i_d will not be sensitive to variation of L_d.

As it can directly be deduced from the last formulation of dO 2.26, variations on R_s do not affect the d axis current estimation when it is controlled to $0A$, as well as variations on L_d do not affect the q axis current. From matrix 2.26, it can also be noticed that when the parameters are considered well known, small variations of $\hat{L_q}$ affect current i_d and small variations of $\hat{R_s}$ and $\hat{M}$ affect current i_q.

Considering at a given instant all the parameters well known ($\tilde{X} = 0$) for a classic operating point ($\Omega = 600rpm$, $I_e = 6A$, $I_q = 35A$), the matrix numerical evaluation gives:

$$dO = \begin{bmatrix} 0 & 0 & 6.6e9 & 0 \\ -9.2e5 & 0 & 0 & -6e7 \\ 0 & 0 & 0 & 8.2e4 \end{bmatrix} \tag{2.27}$$

This shows that i_d is particularly sensitive to variations on L_q and i_q is sensitive to variations on R_s and M.

When 50% of error are added on the parameters $\hat{M}$ ($\tilde{M} = \frac{1}{2}.M$), the numerical evaluation of matrix dO for a classic operating point ($\Omega = 600rpm$, $I_e = 6A$, $I_q = 35A$) gives:

$$dO = 1.10^6 \begin{bmatrix} 0 & 0 & -298 & 0 \\ -0.92 & 0 & 5829 & -60 \\ 0 & 0 & 0 & 0.082 \end{bmatrix} \tag{2.28}$$

Similarly, when 50% of error are added on the parameters $\hat{R_s}$, the matrix dO gives:

$$dO = 1.10^6 \begin{bmatrix} 0 & 0 & 735 & 0 \\ -0.92 & 0 & -51 & -60 \\ 0 & 0 & 0 & 0.082 \end{bmatrix} \tag{2.29}$$

This shows that the both i_d and i_q are sensitive to parametric variations. However one of main issue is located on the parameter M since it is the most subject to variations according to the saturation of the machine and the excitation current used. In the next section, an introduced parameter will be mapped in order to reduce the sensitivity of the current to parametric variations. Let's characterize mathematically the impact of transferring all the parametric errors within the estimated parameter $\hat{M}$. From equations 2.22, and by considering the previously neglected Ψ_f in order to have a more more exhaustive formulation, we can write:

$$\begin{aligned} \frac{di_d}{dt} &= \frac{L_e}{(\hat{L_d} - \tilde{L_d}).L_e - (\hat{M} - \tilde{M})^2}\left(V_d - (\hat{R_s} - \tilde{R_s}).i_d + p.\Omega.(\hat{L_q} - \tilde{L_q}).i_q - \frac{(\hat{M} - \tilde{M})}{L_e}\left(V_e - R_e.i_e\right)\right) \\ \frac{di_q}{dt} &= \frac{1}{\hat{L_q} - \tilde{L_q}}\left(V_q - (\hat{R_s} - \tilde{R_s}).i_q - p.\Omega.\left((\hat{L_d} - \tilde{L_d}).i_d + (\hat{M} - \tilde{M}).i_e + \Psi_f\right)\right) \end{aligned} \tag{2.30}$$

At steady state, the errors can be expressed with $\hat{M}$ as shown in the following equations:

$$\begin{aligned} V_d - \hat{R}_s.i_d + p.\Omega.\hat{L}_q.i_q - \frac{V_e - R_e.i_e}{L_e}\left(\hat{M} - \tilde{M} - \frac{\tilde{R}_s.i_d.L_e}{V_e - R_e.i_e} + \frac{p.\Omega.\tilde{L}_q.i_q.L_e}{V_e - R_e.i_e}\right) &= 0 \\ V_q - \hat{R}_s.i_q - p.\Omega.\hat{L}_d.i_d - p.\Omega.i_e.\underbrace{(\hat{M} - \tilde{M} - \frac{\tilde{L}_d.i_d + \Psi_f}{i_e} - \frac{\tilde{R}_s.i_q}{p.\Omega.i_e})}_{=\mu_M} &= 0 \end{aligned} \tag{2.31}$$

As it can be noticed from the two equations at steady state 2.31, all the model errors can be transferred to the parameter $\hat{M}$. By considering the q axis equation, a new variable μ_M containing $\hat{M}$ and the other parametric errors can be introduced:

$$\mu_M = \hat{M} - \tilde{M} - \frac{\tilde{L}_d.i_d + \Psi_f}{i_e} - \frac{\tilde{R}_s.i_q}{p.\Omega.i_e} \tag{2.32}$$

For this reason, it has been decided to use a map of the parameter μ_M in order to reduce the sensitivity of the system towards parametric errors and variations. The following section will present the mapping strategy used.

2.4 Model precision enhancement through parameter mapping

It has been shown previously that the different parameters used in state equations 2.11 and 2.18 are subject to variations according to different factors that cannot be controlled (temperature, wear, saturation,...). In addition, the state equations from which the system is described is also a large simplification of what physically occurs in a running WRSM. This simplification is necessary in order to be able to use them in nonlinear observers and avoid their implementation to be too complex. The errors linked to parameter measurements may also lead to modeling lack of precision.

On the top of that, the sensitivity study carried out in the previous section quantifies the impact of parameter errors on the precision of modeling of the system. The electrical parameters R_s, L_d and L_q are sensitive but the most problematic parameter is the mutual inductance between the rotor and stator M.

In order to reduce this sensitivity, the most natural solution is the mapping of the sensitive parameters. Maps of parameters are widely used in the industry. In [75] for example the dq-axis fluxes of a PMSM are mapped as a function of the dq-axes current in order to enhance the PMSM modeling and to boost its performances. A similar mapping is performed in [76] with the aim to improve the control performances. A solution for our application could be a measurement of the whole set of parameters the same way it has been done in the beginning of the previous section for different operating points of the machine. This implies that a large number of operating points need to be measured in order to map the machine satisfyingly and those operating points vary according to the load of the system, the rotor speed, the excitation current and the temperature of the machine. These four levers make the system long to map since it creates four degrees of freedom for the mapping of the machine. According to the precision of the mapping required, the size of the maps and thus the time required may increase sharply. Consequently, it may become costly for a mass production application such as the i-StARS system developed by Valeo according to the tolerance of the manufacturing and the precision required on the parameters. Indeed, if the machines manufactured are not strictly the same, the whole map of parameters will have to be carried out for every machine coming out of the production line.

A strategy for a fast parameter mapping of the system in order to avoid this consequent loss of time and money has been implemented on the experimental test bench and will be presented in this section. This strategy is based on bringing all parameters uncertainties and variations to

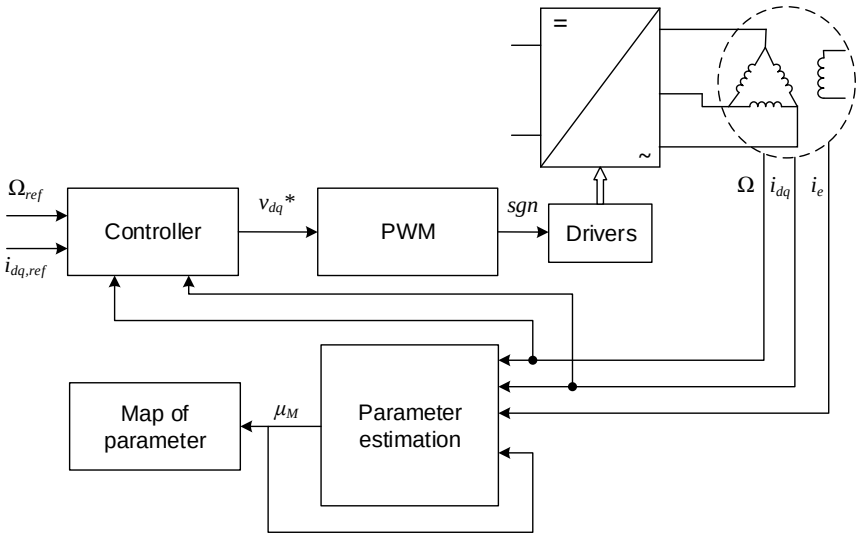

Figure 2.20. Diagram of the mapping strategy

a single, or two, parameter(s), if possible. So, all the other parameters can be supposed constant on the whole operating range and the only variable parameters have to adapt online in such a way to compensate all uncertainties. This online adaptation could be realized using either an online estimator or a map predefined offline. The online identification of parameter on which the one presented here is based is well described in the work of [74]. In this study, two parameters of a PMSM, the stator resistance R_s and the stator inductance L_s were identified online. This means these two parameters were estimated when the machine was operating and their estimation relied on the dq-axis currents measurement in the PMSM. This online parameter identification was used in this study for a PMSM mechanical sensorless control in order to improve the back-EMF estimation. A similar technique was also used for the same application in [77] with the use of a recursive least square (RLS) filter for the parameter estimation. Another possible application for online parameter identification, described in [78], is the fault detection in electric machines. Indeed, when a winding inter-turn short-circuit occurs in the stator of a synchronous machine, the stator resistance and the stator inductance values vary due to fault current in the short-circuit, as described in [79]. A fault detector based on the estimated values of the parameters may then detect a fault in the windings of the stator. The same principle is described in [78] for the detection of rotor fault in an induction machine.

As mentioned above, the second way to adapt the variable parameters is the use of an offline predefined map. According to the manufacturing tolerances and the required precision on the control, the map can be generated either on a prototype in the laboratory, or at the end of the manufacturing process. To make the generation of the map easier and faster, we propose to apply an online identification technique. Therefore, it has been decided in this study to use an online parameter estimator in order to accelerate the mapping of the parameter μ_M defined in equation 2.32. It has been shown from this equation that estimating μ_M actually means estimating M and other parametric errors included. The strategy of this fast mapping solution is based on the use of the stator currents to estimate the variable μ_M with the same estimation technique than the one used in [74]. For industrially manufactured WRSM, this preliminary work is only necessary once according to the manufacturing tolerance and the required precision on the estimation of the stator currents. A diagram summarizing the mapping strategy is shown on figure 2.20.

The online parameter identification is defined as follow: the q axis current measurement will be used for the identification of the parameter μ_M. Let's write the state equation linked to the q axis current when parameter error are included. From the equations 2.30 to 2.32, equation on i_q leads to:

$$\frac{di_q}{dt} = \frac{1}{L_q}.\left(V_q - \hat{R_s}.i_q - p.\Omega.(\hat{L_d}.i_d + \mu_M.i_e)\right) \tag{2.33}$$

The Jacobian linked to this equation regarding the parameter μ_M gives:

$$\frac{\partial \dot{i_q}}{\partial \mu_M} = -\frac{p.\Omega.i_e}{L_q} \tag{2.34}$$

And the system is observable if $\frac{\partial \dot{i_q}}{\partial \mu_M} \neq 0$ and thus from 2.34 if $\Omega \neq 0$ and $i_e \neq 0$.
Thus, the following estimation equation for the parameter μ_M can be proposed:

$$\hat{\mu_M}(t) = \hat{\mu_M}(t_0) + \int_{t_0}^{t} K_q.\tilde{i_q}(\sigma).d\sigma \tag{2.35}$$

with $\hat{\mu_M}(t)$ the estimated value of μ_M, $\hat{\mu_M}(t_0)$ the estimated value of μ_M at the initialization of the estimation, $\tilde{i_q}$ defined as $\tilde{i_q} = \hat{i_q} - i_q$ the error between the estimated $\hat{i_q}$ and the measured i_q given by the following equation:

$$\frac{d}{dt}\hat{i_q} = \frac{1}{\hat{L_q}}\left(V_q - \hat{R_s}.\hat{i_q} - p.\Omega.\left(\hat{L_d}.i_d + \hat{\mu_M}.i_e\right)\right) \tag{2.36}$$

A convergence analysis needs to be conducted in order to mathematically prove that the equation 2.35 is converging and what value should be assigned to the gain K_q.
To do so, let's consider the steady-state of the system. The equation 2.33 can be written:

$$V_q - \hat{R_s}.i_q - p.\Omega.(\hat{L_d}.i_d + \mu_M.i_e) = 0 \tag{2.37}$$

and similarly we have:

$$V_q - \hat{R_s}.\hat{i_q} - p.\Omega.(\hat{L_d}.i_d + \hat{\mu_M}.i_e) = 0 \tag{2.38}$$

i_d can be controlled to 0, which nullifies the term $\hat{L_d}.i_d$. Thus the following equation can be written:

$$\hat{R_s}.\hat{i_q} + p.\Omega.\hat{\mu_M}.i_e = \hat{R_s}.i_q + p.\Omega.\mu_M.i_e \tag{2.39}$$

which leads to:

$$\tilde{i_q} = \frac{-p.\Omega.i_e}{\hat{R_s}}.\tilde{\mu_M} \tag{2.40}$$

And from 2.35 it gives:

$$\frac{d\tilde{\mu_M}}{dt} = -K_q.\frac{p.\Omega.i_e}{\hat{R_s}}.\tilde{\mu_M} \tag{2.41}$$

From 2.41, the estimation equation presented in 2.35 is locally asymptotically stable if the term $K_q.\frac{p.\Omega.i_e}{\hat{R_s}}$ is strictly positive. Independently from the sens of rotation of the rotor, this condition is guaranteed if $K_q.\Omega > 0$.

Now that the proof of convergence has been demonstrated, this parameter identification strategy has been implemented on the test bench in order to use it for the fast identification of the parameter μ_M.

As it has been explained before, the different operating points of the system differ according to four variables: the excitation current i_e, the rotor speed Ω, the load of the machine Γ_{load} and the temperature of the system. A change in these four variables may change the values of the parameters of the WRSM. For this work, it has been decided not to include a temperature probe in the machine, due to time limitation and the fact that the thermal behavior of our protoype is quite different from that of the actual i-StARS. Therefore, the parameter mapping of the variable μ_M was performed for a nominal temperature: to reach this temperature, the machine is beforehand heated by running it to its nominal operating point for a several minutes. This preliminary step done, the online estimation of μ_M can be realized. The procedure is the following:

- First a mechanical load is chosen. For our application, three degrees of mechanical loads have been considered and applied through an active load connected to the load machine in front of the studied WRSM.
- For this selected mechanical load, the excitation current is controlled to the desired value. The excitation current range that is relevant according to the machine data provided by Valeo goes from 4A up to 12A.
- The speed of the machine is controlled from 100 rpm to 1000 rpm. The output μ_M of the parameter estimator is extracted for several steady states rotor speed of the machine.

Once the parameter μ_M has been extracted for the full speed range of the machine, the excitation current is incremented, and μ_M is extracted for the full speed range of the machine again. Once the full excitation current range has been swept, a new mechanical load is applied and the whole process starts over.

This whole process is summarized on figure 2.21. For this application, after a few preliminary tests, it has been decided to increment the excitation current by 2A for every iteration, and the rotor speed of 120 rpm. These increments can be modified according to the different needs linked to the applications.

In this study, three mechanical loads have been chosen, but this again depends on the inherent constraints of each application. The medium load has been chosen so that it corresponds to a speed of 750rpm for a q-axis current of 35A. The lowest load corresponds to a q-axis current of 25A for the same speed and the highest load a q-axis current of 45A for the same speed.

Figure 2.22 displays the graph showing the evolution of the value of μ_M as a function of the rotor speed for three different excitation currents. The colored dots on the figure represent the actual estimated value of μ_M. It should be reminded that μ_M includes not only variations of M, but also all other uncertainties. Several features can be noticed from this figure. First the influence of the excitation current is obvious from the graph: for medium and high rotor speeds, the lower the excitation current, the higher the estimated value of μ_M. This characteristic was predictable from figure 2.12 since above an excitation current of 4A, the machine saturates.

The difference between the μ_M obtained and the calculation of M made from figure 2.12 could also be expected since the estimated value μ_M is shifted by the different model errors contained in the estimator. Those model errors are described in equation 2.32, but other non predicted phenomenons may also be responsible for this difference.

On figure 2.23, the three different graphs of μ_M as a function of the rotor speed for the same excitation current $i_e = 10A$ but with three different loads (low, medium and high loads). The evolution of μ_M on those graphs are similar to the evolution displayed on figure 2.22. The fact that, the lower the mechanical load, the higher the estimated value of μ_M could have been expected. Indeed the higher the load, the higher the q axis current for a given load which increases the saturation of the machine and thus reduces the value of the real parameter M. The Joule effect should also be more important, increasing $\tilde{R}_s$ and thus μ_M.

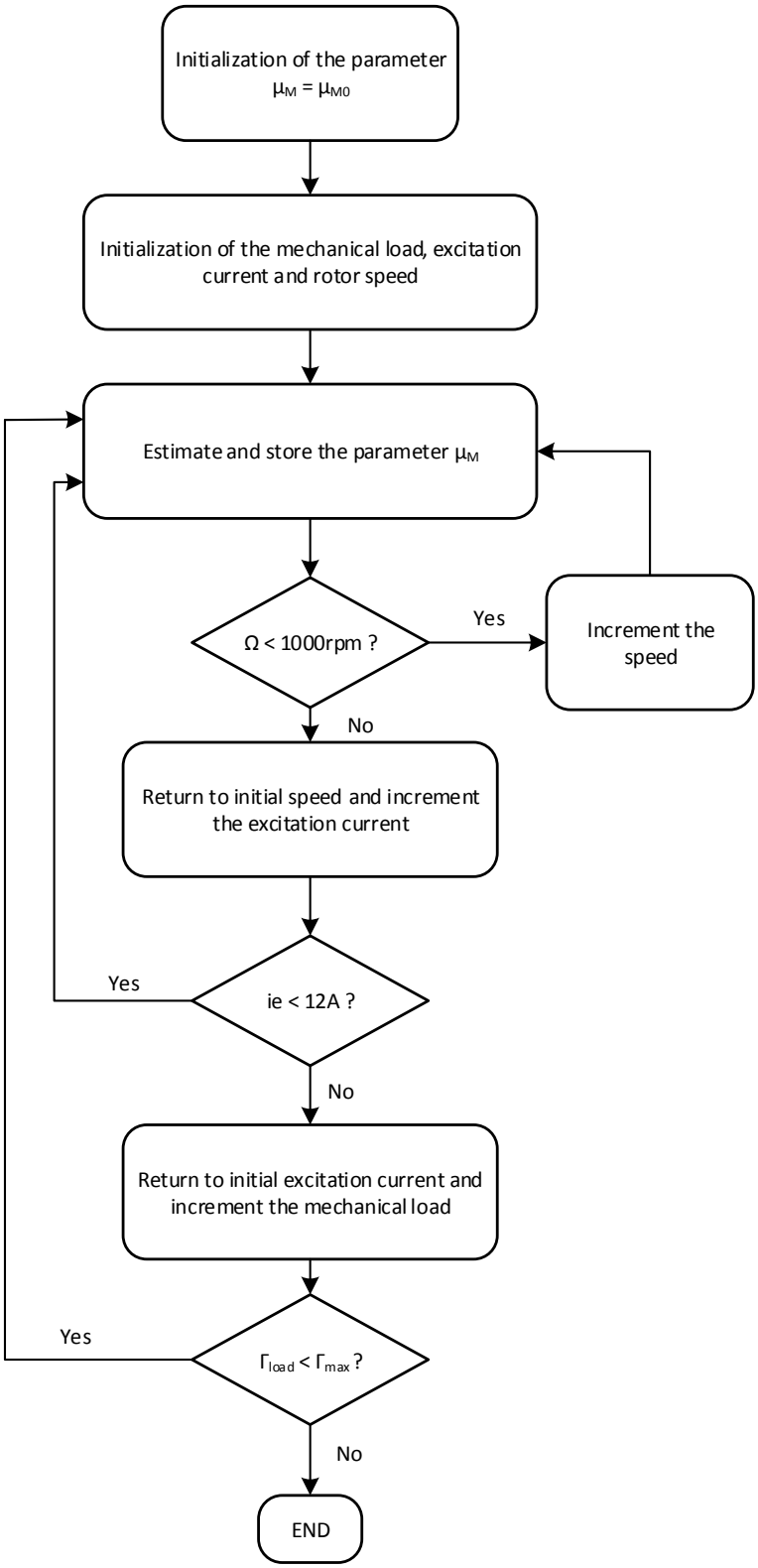

Figure 2.21. Flowchart of the mapping process.

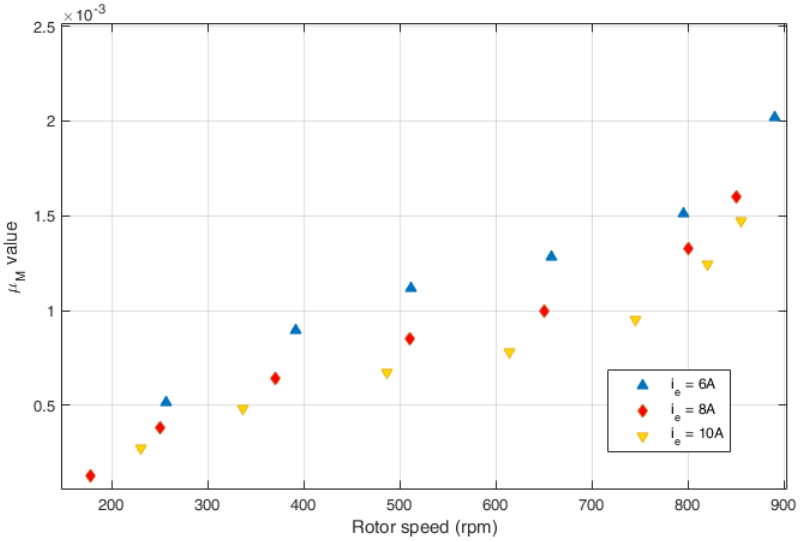

Figure 2.22. Evolution of μ_M with the rotor speed for three different values of i_e and a medium mechanical load.

The evolution of μ_M as a function of the speed as shown on figures 2.22 and 2.23 for any excitation current is not linear. For low speed, the drop of the value of μ_M can be explained by the term $-\frac{\tilde{R}_s.i_q}{p.\Omega.i_e}$ in equation 2.32: for a given $\tilde{R}_s > 0$, the lower the speed Ω the higher the absolute value of this term, decreasing the value of μ_M hence the drop. The rise at high speed is however difficult to explain with equation 2.32. This rise is probably due to one or several other neglected phenomenons that would impact the value of μ_M for large speed.

A possible strategy for the mapping of μ_M at this point is to divide the rotor speed range in sections and to attribute a value to μ_M for each sector. This solution however leads to accuracy issues: indeed when the rotor speed is on the edge of two sections, the value attributed to μ_M

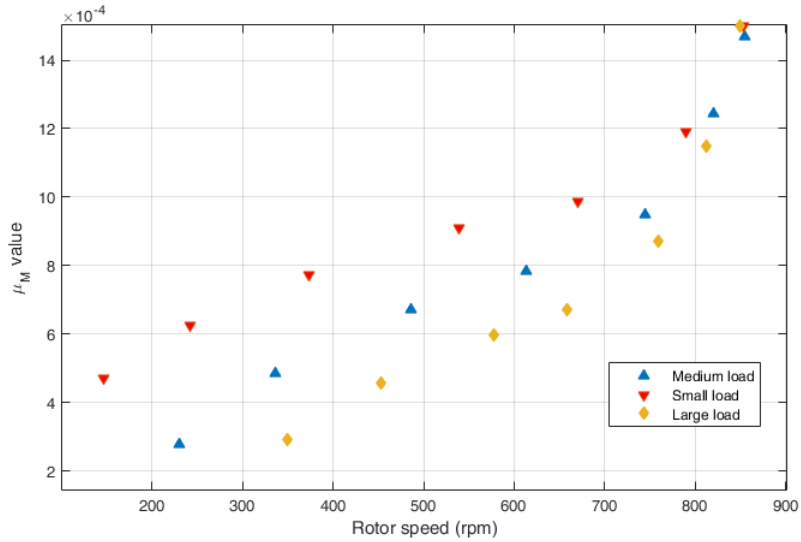

Figure 2.23. Evolution of μ_M with the rotor speed for $i_e = 10A$ and three different mechanical loads.

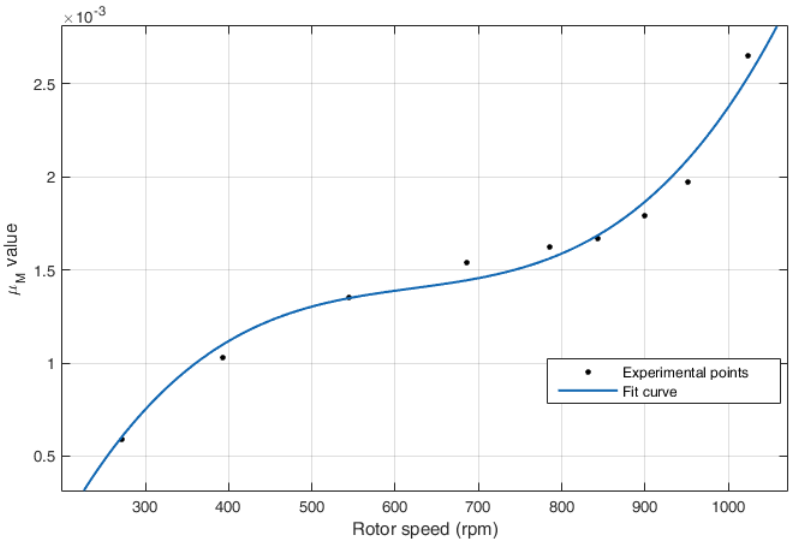

Figure 2.24. Evolution of μ_M with the rotor speed for $i_e = 4A$ and a medium mechanical load: experimental points and polynomial extrapolation.

presents an error that can be high if the number of section is low. If the number of sections is high, the precision of the map is enhanced but this requires to also increase the memory needed on the hardware of the system to store the map data.

Another solution relies on the fact that the graphs of μ_M as a function of the speed on figures 2.22 and 2.23 can be extrapolated as polynomial functions. An example of polynomial function of degree 3 is given on figure 2.24.

The polynomial extrapolation on figure 2.24 has been realized using the least squares method

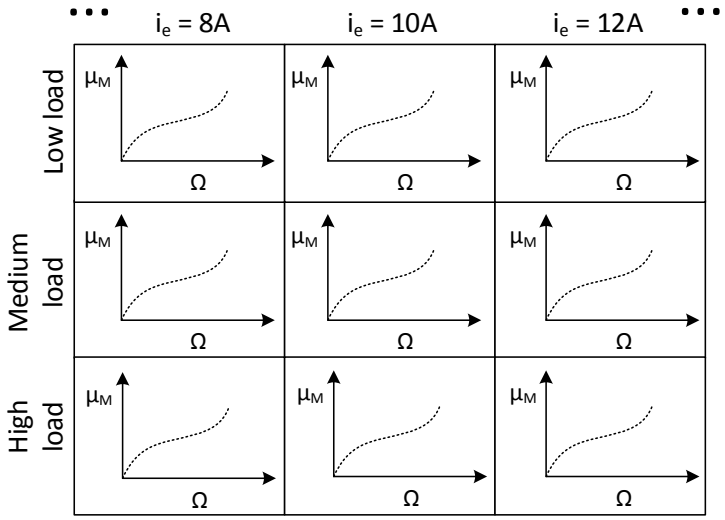

Figure 2.25. Diagram showing the mapping of μ_M using an extrapolated function on the rotor speed.

with an appropriate Matlab toolbox and the fit is described by a r-squared of 0.988 which is satisfying for this application. The polynomial extrapolation of the experimental results allows avoiding the use of discrete sections and to have a mapping of parameter μ_M for a given mechanical load and excitation current that is a function of the rotor speed only. The mapping of μ_M with the use of an extrapolated function on the rotor speed is given in figure 2.25.

The extrapolation of figure 2.24 gives a function $f_{\mu 1} : \mathbb{R} \to \mathbb{R}$. The same principle can be used to elaborate a continuous function $f_{\mu 2} : \mathbb{R}^2 \to \mathbb{R}$ to completely characterize μ_M for another variable. Figure 2.26 shows the parameter estimation results as a function of the speed and the excitation current. This function allows to extrapolate the discontinuous experimental results in a continuous $f_{\mu 2} : \mathbb{R}^2 \to \mathbb{R}$ function.

From figure 2.26, all the experimental estimations of μ_M for a medium mechanical load are displayed along two axes: the rotor speed (like it was already done on figure 2.22) and the excitation current. This allows extrapolating the data and plot a surface representing a function $f_{\mu 2} : \mathbb{R}^2 \to \mathbb{R}$. From the equation of this surface, it then possible to access to μ_M for any value of i_e and Ω in their respective operating range and thus avoid the section effect described earlier.

The graph on 2.26 is extrapolated based on 4 different excitation currents. A better extrapolation could be achieved with a lower excitation current increment or a lower rotor speed increment.

The same extrapolation $f_{\mu 2} : \mathbb{R}^2 \to \mathbb{R}$ can be realized with a fixed excitation current and by using the mechanical load as a second variable. The results are displayed on figure 2.27 for an excitation current of 10A. As for the graph displayed on figure 2.26, this $\mathbb{R}^2 \to \mathbb{R}$ extrapolation allows obtaining a continuous function for μ_M with the mechanical load and the rotor speed as variables. According to the application, one $\mathbb{R}^2 \to \mathbb{R}$ extrapolation can be preferred compared to the other. If there are few different mechanical loads applied to the system, the first $\mathbb{R}^2 \to \mathbb{R}$ extrapolation presented on figure 2.26 would be privileged, whereas if in the other hand the system is designed to run with only a few excitation current, the second $\mathbb{R}^2 \to \mathbb{R}$ extrapolation

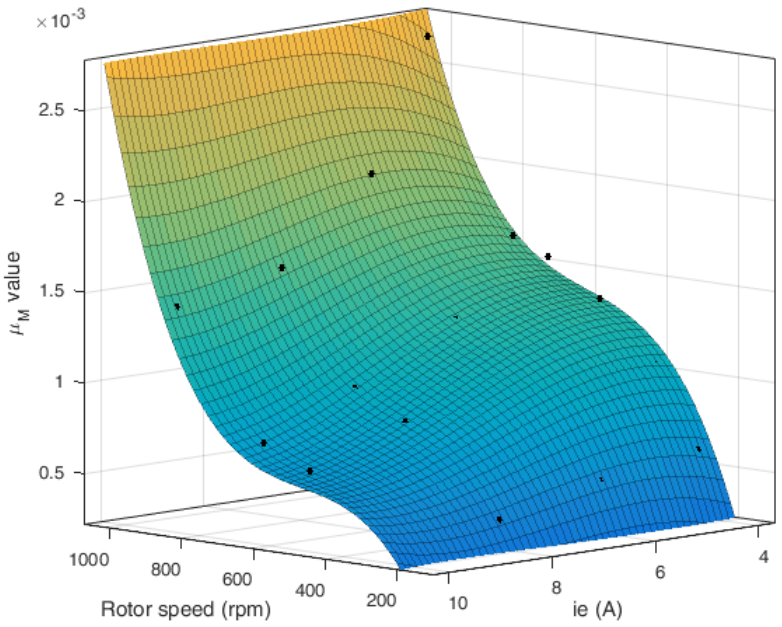

Figure 2.26. Evolution of μ_M as a function of the speed and the excitation current for a medium mechanical load: experimental points and polynomial extrapolation.

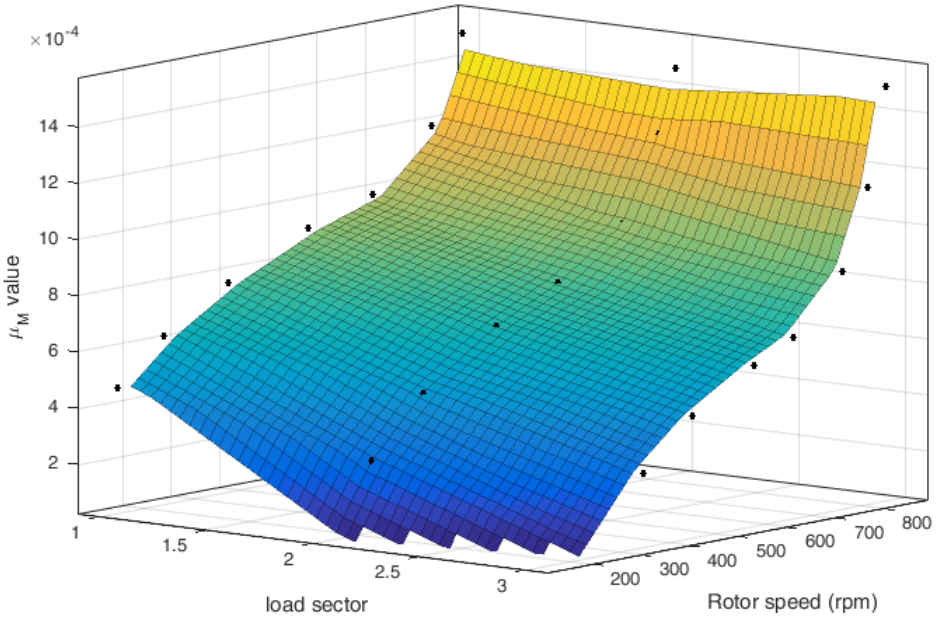

Figure 2.27. Evolution of μ_M as a function of the speed and the mechanical load for $i_e = 10A$: experimental points and polynomial extrapolation.

solution presented in figure 2.27 should be opted for. Another mean to implement the obtained map of μ_M is to use an intrapolated look-up table (LUT). Here, this leads to a $\mathbb{R}^3 \rightarrow \mathbb{R}$ LUT with 3 inputs (i_e, Ω, i_q) and 1 output (μ_M). Its use is rather easy with MATLAB-Simulink. However, its implementation on an industrial control card depends on its ability to realize this kind of LUT with interpolation integrated in.

In this section, a fast and easy to implement strategy has been developed to rapidly map a parameter of a machine. In our application, only one parameter, the variable μ_M has been mapped, due to the fact that this parameter is the most sensitive and the most subject to variations according to the operating point. As it has been explained, due to the model used, relying on state equations that includes other parameters of the system that might contain errors, the estimated parameter μ_M in output of the online parameter estimator includes the actual value of M and parameter representing the other modeling errors. According to the operating point of the system (mechanical load and excitation current), several functions of μ_M depending on the rotor speed can be extrapolated from the experimental measurements. If the application allows it, it is also possible to realize a 3D extrapolation with a function $f_{\mu 2} : \mathbb{R}^2 \rightarrow \mathbb{R}$ by making the excitation current or the mechanical load another variable of the function of μ_M alongside with the speed.

The experimental results using this parameter mapping for current sensorless control are presented in details in chapter 4. The functions describing the evolution of μ_M have been stored in different sections corresponding to one excitation current and one mechanical load. As it has been stated earlier, in our application, three different mechanical loads and five excitation currents (between 4A and 12A) have been examined and used for the mapping of μ_M and the mapping has been made using the process showing on figures 2.20 and 2.21.

If a temperature probe is available in the system setup, it could also be worth considering the mapping by adding the temperature as a new variable. To do so, the whole mapping process presented on figures 2.20 and 2.21 needs to be redone for different temperature in order to fully

cover all the operating points of the machine. The mapping process described on the flowchart 2.21 should be first done at the lowest point of the temperature range, then the temperature needs to be incremented and the process carried out again and so on until the highest point of the temperature range is reached. This can lead to a new dimension in the LUT, giving a $\mathbb{R}^4 \rightarrow \mathbb{R}$ function.

Conclusion

This was focused on the study of the i-StARS WRSM in order to obtain an exhaustive model that can be used to define the current observers. Since the experimental test bench was designed in the GREEN laboratory, the system is slightly different from the one developed by Valeo. The WRSM is the same, the i-StARS claw pole machine but the mechanical load, that is created by the connection to the ICE in the mild-hybrid application, is here induced by another claw pole alternator connected to an active load to be able to change the mechanical load level. The rest of the experimental test bench, the power electronics and the sensors used, have been designed with the aim of having the same characteristics than the industrial product.

A brief overview of the magnetic modeling of the machine realized in Dr. Devornique's work has been presented. The behavior of the model of the i-StARS developed being precise and fast to compute, this FEA-based modeling could be useful to access to a machine's parameter and simulate a current sensorless control during the development phase of a project. For the i-StARS modeling, the magnetic model is precise enough to obtain the back-EMF of one operating point of the machine but the whole spectrum of the machine could be characterize the same way. The electric model of the WRSM has then be developed in order to obtain the state equations of the dq-axis currents, the excitation current and the rotor speed. For this claw pole WRSM, the excitation current of the rotor is directly coupled with the d-axis current, and generates the excitation flux. The interpole magnets of the i-StARS also have an impact on the flux from the rotor to the stator but it is negligible. The saturation exists in the machine but in order to access the current taking in account this phenomenon, a FEA should be used for every operating point of the machine, which highly increases the complexity of the modeling. The damping effect for this kind of machine has been theoretically studied but is not significant in the i-StARS.

From the state model developed, the different parameters have been experimentally identified for one operating point. To obtain a comprehensive identification, the parameters should be identified for all the functioning range of the machine at different temperature, which is a very long process leading to a bulky map of parameters. Instead, it has been decided to identify the machine's parameters for a single operating point, and then estimate online one parameter only for the other operating points. This parameter's role is to absorb the errors of the other parameter in the model. To choose the parameter to estimate, a sensitivity study has been realized. Since the mutual inductance M is the most problematic of all the electric parameters linked to the stator currents, a new parameter μ_M has been introduced in order to absorb the error on M and other error in the model. This parameter μ_M has then be estimated online for the whole range of the machine at a given temperature along 3 variables : the rotor speed, the excitation current and the load of the WRSM. The points obtained are then extrapolated along the speed. This gives several functions of μ_M along the speed allocated in different sections of speed and load. It would also be possible to extrapolate the discontinuous $\mathbb{R} \rightarrow \mathbb{R}$ to $\mathbb{R}^2 \rightarrow \mathbb{R}$ functions or one $\mathbb{R}^3 \rightarrow \mathbb{R}$ extrapolating the estimated μ_M along all the variables, but this requires a large data storage hardware. Taking in account the temperature for this mapping process is possible with a temperature sensor but it has not been done in this study.

The next chapter will focus on nonlinear observers development for the stator current observation. The mapping results of μ_M will be used in chapter 4, where the μ_M map will be connected to the nonlinear observer developed to enhance the observation precision.

Chapter 3

Strategies of Current Sensorless Control

Contents

Introduction

In chapter 2, it has been shown that the electric modeling of the machine, as detailed as it can be, cannot take in account with precision all the physical phenomenons occurring in the machine. In addition, the change of temperature, of functioning point or the wear of the passive components induce a variation of the values of the passive components in the electric model. In that regard, relying only on the model of the system to control it does not appear as a satisfying option. On the other hand, an open loop control is not worth considering for our application, since the torque supplied by the electric powertrain needs to be controlled. Some studies, detailed in the first chapter, achieve current reconstruction based on the knowledge of the current on the DC bus of the inverter. The state of the MOSFETs being known, it is indeed possible to retrieve the phase currents with this method. However in our system configuration there is no sensor available on the DC bus of the inverter.

For those reasons the chapter 3 will be focused on the current sensorless control strategies. Usually controllers are based on the feedback of the different sensors on the system. For a regular current or torque control, the phase current sensors on the WRSM are needed because the information that they carry constitute the feedback.

Torque and current controllers are widely used for hybrid automotive applications. Indeed the electric powertrain is designed to supply a specific torque to the main powertrain. In addition, controlling the currents in the stator is important for the reliability and the safety of the system: it avoids the peak currents to become to high and potentially to become destructive for the system and accelerate the wear of the components.

On our system, the aim is to achieve a current control in order to impose the mechanical torque and avoid current overshoots, but the phase currents measurements are not available. As it will be detailed in the first part of this chapter, the choice has been made to estimate those currents with a nonlinear state observer. Indeed, with this strategy, an existing control loop doesn't necessarily have to be modified, the nonlinear observer can just be added in the loop to obtain the currents that are then injected in the existing control loop. The inherent condition in order to be able to use this strategy is to guarantee the observability of the system. The demonstration of observability will be given in the first part of this chapter.

Different kinds of nonlinear observers have been tested for the current sensorless application. Among the different existing state observers, those that will be presented in this study are the Extended Kalman Filter (EKF) and different versions of a proposed state observer based on Lyapunov candidate functions convergence. These observers and the simulation results will be introduced in a second part of this chapter. As it will be explained, those observers are useful for current estimation because they can reduce some errors that are unavoidably present in the electric model. The mechanical parameters errors in particular are well absorbed by the proposed state observer, which is a strong asset considering the fact that the mechanical parameters may vary with the weight of the vehicle or the shape of the road, and thus unknown in advance.

In a last part, another observer topology based on Lyapunov function with the control vector generation included in the same loop have been developed and tested in simulation. As it will be detailed, the control vector is integrated to the Lyapunov function, and the control vector is generated at the same time than the observation of the stator currents. This topology is useful for high speed systems, since it allows raising the control dynamic at the same level than the observation dynamic.

Other strategies that have not been investigated in details can be considered for that kind of application. Among them, strategies based on model predictive controllers (MPC) could be developed further in the context of a future work. The main issue of MPC strategies that can be immediately raised is the fact that the whole controller needs to be adapted with this strategy. Indeed, MPC controllers have a different architecture from the current loop controllers.

In addition, MPC strategies requires to predict the future states after a certain chosen number of iteration, requiring a potentially high computing power if the number of iteration is high. This could become an important drawback for industrial applications. More precisions on MPC controller applied to a WRSM are given in [80] and [81]. Model-Free Controllers (MFC) could also be investigated on current sensorless applications as an alternative that could reduce the model sensitivity towards modeling errors [82].

3.1 The current sensorless control strategy

3.1.a Choice of the strategy

In industrial applications, and particularly the automotive industry, reducing the manufacturing costs is one of the most challenging issues. Hybrid technologies for vehicles are subjected to the same constraints and one appealing solution to optimize the manufacturing costs is to spare the use of sensors in the electric powertrain and thus avoid their inherent costs. Open-loop control of the powertrain can be considered but it leads to security and reliability issues. Sensorless control however allows to remove sensors while guaranteeing the control of the system.

Current sensorless control however leads to different issues. The main difficulty is that it is impossible to directly use the common current-loop based controllers. The classic PID, the sliding-mode control described in [31] and [83] or the Flatness Based Control (FBC) are all controllers where the phase currents feedbacks are needed.

The papers [53] and [55] propose to rebuild the phase current, knowing the DC-current in the input of the inverter and the states of the switches (see 1.4.b). This is a viable solution when phase currents are not available, however this requires that there is a current sensor mounted on the DC stage of the inverter. This leads to several issues: first the DC bus of an inverter is often a bus bar, requiring a relatively bulky hall effect current sensor as shown on figure 3.1. In addition the switch of the MOSFETs may provoke current peaks with high dynamics which would impose the use of large bandwidth, and thus expensive, current sensors, canceling the

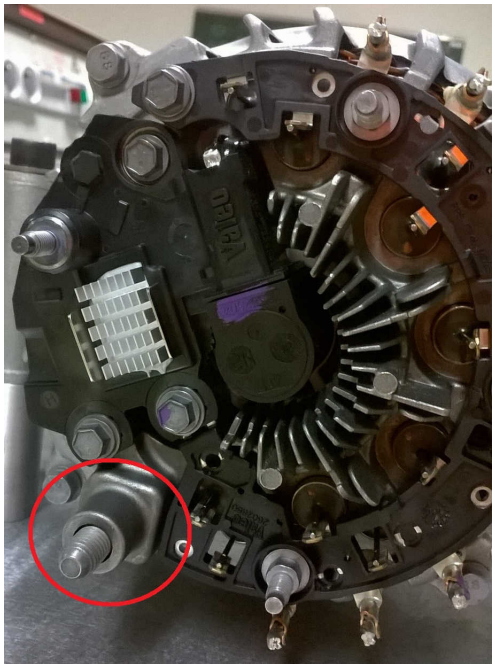

Figure 3.1. Bus bar of the i-Stars circled in red.

benefits expected by the removal of the phase current sensors on the manufacturing costs.

It is also worth considering an open-loop prediction of the future current based on a step-by-step calculation relying on the phase current equations. However this solution requires to have a strong reliable model of the system and precise knowledge of the passive components of the inverter and the machine, which is not the case most of the time, as seen in the previous chapter of this thesis.

As mentioned previously in the introduction of this chapter, the MPC strategies are also a possible solution, and they can constitute an alternative strategy for the current sensorless control. However the MPCs have an architecture that is distinct from the other current feedback controllers [80], [81]. This is a problem when the architecture of the controller is imposed, or when the current sensorless control is implemented as a backup solution to improve reliability of a system that does not use a MPC controller originally.

For these reasons, observers have been used in order to estimate the unmeasured phase currents. Indeed as shown on figure 3.2, the estimation of the phase currents with an observer can be done outside the control loop. In that way, the observer bloc can be activated or deactivated according to the operating mode. As an example, in an aircraft application, where the current sensorless control is only used as a backup solution if the current sensors are not operational, the phase currents observer can be unused during a normal operating mode and activated if needed without disrupting or modifying the main control chain.

Since the system considered is nonlinear as seen in chapter 2, mainly due to the coupling between the d-axis current i_d and the excitation current i_e (see the system of equation 2.11). In order to take in account those nonlinearities of the system, the observers' model used need to be nonlinear as well. Different kind of nonlinear observers exist. One of the most popular in the automatic field is the Kalman filter, and more particularly its nonlinear version, the Extended Kalman filter (EKF). This observer will be presented with more details in the next section of this chapter. An other method of nonlinear observation will be introduced using the convergence analysis of Lyapunov candidate functions. The principle of this observer, firstly introduced in [84] and [85] and modified to be applied to the state variables i_d and i_q, will be detailed in the next section too. An extension of this observer including the calculation of the control vector V_{dq} in the same loop has also been investigated on.

The strategy proposed using observers to retrieve the phase current is appealing and seems to be a solution presenting numerous advantages. However the system considered has to be proved

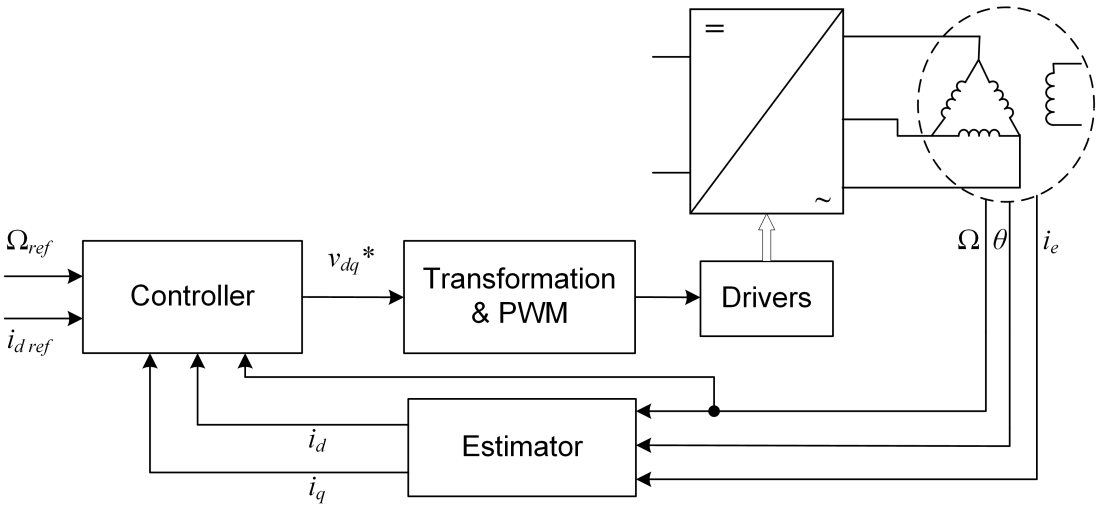

Figure 3.2. Diagram of the current sensorless control strategy with the use of an observer.

observable beforehand. The following paragraph will be dedicated to the proof of observability of the system as it has been defined in chapter 2.

3.1.b Proof of observability

Before going any further and develop the structures of each observers, the observability of the system needs to be demonstrated. By definition, a system is considered observable if the measures of its inputs and output during a finite time $[t_0; t_f]$ allows determining the initial state $x(t_0)$ and, by integration of the state equations, knowing $x(t)$ at any instant included in $[t_0; t_f]$. For a linear system, the necessary and sufficient condition of observability is guaranteed by a condition on the rank of the observability matrix, such as :

$$rank \begin{bmatrix} C \\ CA \\ \vdots \\ CA^{n-1} \end{bmatrix} = n \tag{3.1}$$

with A the state matrix and C the observation matrix, both defined by the system in its state-space representation. This criteria for observability can however only be used for linear systems, which is not the case for a WRSM where the speed of the rotor and the currents are coupled (see the system of equation 2.11 in chapter 2). This means that the feasibility of the estimation of the stator currents given some measured state variables and their derivatives have to be checked in nonlinear conditions. As seen in chapter 2, the modeling of the system with its state variables gives:

$$\begin{cases} \frac{d}{dt}i_d &= \frac{L_e}{L_d.L_e - M^2}\left(V_d - R_s.i_d + p.\Omega.L_q.i_q - \frac{M}{L_e}\left(V_e - R_e.i_e\right)\right) \\ \frac{d}{dt}i_q &= \frac{1}{L_q}\left(V_q - R_s.i_q - p.\Omega.\left(L_d.i_d + M.i_e\right)\right) \\ \frac{d}{dt}i_e &= \frac{L_d}{L_d.L_e - M^2}\left(V_e - R_e.i_e - \frac{M}{L_d}\left(V_d - R_s.i_d + p.\Omega.L_q.i_q\right)\right) \\ \frac{d}{dt}\Omega &= \frac{1}{J}\left(p.i_q.M.i_e - f.\Omega - \Gamma_0\right) \end{cases} \tag{3.2}$$

To formulate the problem in a mathematical form, let us consider in a first approach the state variables (containing the variables to estimate, the stator currents in the d-q axis) $x = \begin{bmatrix} i_d \\ i_q \\ i_e \\ \Omega \end{bmatrix}$ and the measured variables are $y = \begin{bmatrix} i_e \\ \Omega \end{bmatrix}$.

The system (3.2) is nonlinear and non autonomous. The observability demonstration that will be performed can not rely directly on the same demonstration than for a linear dynamic system. To do so, the system as to be linearized around operating points as it is well explained in [86] and [74]. As demonstrated in [86], [87] and in [88], a rank condition can be used to prove the local observability, i.e the observability around the linearized point. This is formally defined as follow. Let's consider a nonlinear system described as:

$$\begin{cases} \dot{x} &= f(x) + g(x).u \\ y &= h(x) \end{cases} \tag{3.3}$$

with $x \in \mathbb{R}^n$ the state variables, $u \in \mathbb{R}^m$ the control vector and $y \in \mathbb{R}^p$ the measured variables. The observation space O is defined by the smaller vector space containing h_1, h_2, ..., h_p and their successive Lie derivates:

$$O = span\{L_f^j h_i(x); i = 1, ..., p; j = 0, 1, 2, ...\} \tag{3.4}$$

with $L_f^j h = L_f(L_f^{j-1}h)$, $j \geq 2$ and $L_f^0 h = h$ where:

$$L_f h(x) = \sum_{i=1}^{n} f_i(x) \frac{\partial h(x)}{\partial x_i} \tag{3.5}$$

is the Lie derivates of $h(x)$ along the integral curve of $f(x)$. The system 3.3 is then locally observable in the neighborhood of $x_0 \in \mathbb{R}^n$ if the rank of the observability matrix dO is full rank:

$$rank\, dO(x_0) = n \tag{3.6}$$

In concrete terms, to study local observability, it is required to verify the rank of the observability matrix dO defined as follow:

$$dO = \frac{\partial \dot{y}}{\partial x} = \begin{bmatrix} \frac{\partial f_{ie}}{\partial i_d} & \frac{\partial f_{ie}}{\partial i_q} \\ \frac{\partial f_\Omega}{\partial i_d} & \frac{\partial f_\Omega}{\partial i_q} \end{bmatrix} \tag{3.7}$$

where f_{ie} and f_Ω, referring to 3.2, are given by:

$$f_{ie} = \frac{d}{dt} i_e, f_\Omega = \frac{d}{dt}\Omega$$

When developing 3.7, it yields:

$$dO = \begin{bmatrix} \frac{-M.R_s}{M^2 - L_d.L_e} & \frac{p.M.L_q}{M^2 - L_d.L_q} \\ 0 & \frac{p.M}{J}.i_e \end{bmatrix} \tag{3.8}$$

From 3.8 it is possible to conclude that dO is always full rank if $i_e \neq 0$, even at standstill (when $\Omega = 0$) and when $i_d = i_q = 0$. This result shows that the measured variables $y = \begin{bmatrix} i_e & \Omega \end{bmatrix}^T$ contains enough information for the estimation of $x = \begin{bmatrix} i_d & i_q & i_e & \Omega \end{bmatrix}^T$.

It is also important to notice that this system is observable for a given set of parameters. As it has been explained, the parameters of the system will vary according to different event, such as the wear of the passive components, the temperature of the system or the saturation of the machine for some operating points.

In this configuration of observability, there are two measured state variables : i_e and Ω. In theory, it is possible to use only the excitation current and its derivative form. Indeed if we write the observability matrix dO as in 3.7 with :

$$f_{ie} = \frac{d}{dt} i_e, f_{ie2} = \frac{d^2}{dt^2} i_e$$

When developing the observability matrix dO in this configuration, we obtain:

$$dO = \begin{bmatrix} \frac{-M.R_s}{M^2 - L_d.L_e} & \frac{p.M.L_q}{M^2 - L_d.L_q} \\ O_{21} & O_{22} \end{bmatrix} \tag{3.9}$$

with: $\mathrm{d}O_{21} = \frac{L_d}{L_d.L_e - M^2} . \left(\frac{-R_e.M.R_s}{L_d.L_e - M^2} - \frac{L_e.R_s^2.M}{L_d.(L_d.L_e - M^2)} - p.\Omega^2.L_d \right)$

$$dO_{22} = \frac{L_d}{L_d.L_e - M^2} . \left(\frac{R_e.M.p.\Omega.L_q}{L_d.L_e - M^2} + \frac{L_e.R_s.M.p.\Omega.L_q}{L_d.\left(L_d.L_e - M^2\right)} + p.\Omega.R_s + \frac{2.p^2.i_q.L_q.M.i_e}{J} - \frac{p.L_q.\left(f.\Omega + \Gamma_0\right)}{J} \right)$$

It can be noticed that this observability matrix dO is full rank even at the standstill of the machine. This configuration shows that in theory it is possible to avoid using the mechanical

equation of the machine as a state equation. However, this requires to have access to the measure of the derivation of the excitation current, which is difficult to realize in practice. This would indeed require a high quality, thus relatively expensive, current sensor on the excitation circuit with a bandwidth large enough. This solution would also be vulnerable to measurement noises.

In a second time, the observability of the system including two parameters will be tested. To reduce the impact of the error on the parameters values of the system, a parameter error vector x_p is introduced, with $x_p = \begin{bmatrix} I_p & \Delta\Gamma \end{bmatrix}^T$. I_p is introduced in order to absorb the errors on the electrical parameters that would not be included in μ_M (see 2.32 in chapter 2), and $\Delta\Gamma$ to absorb the errors on the mechanical parameters.

When these parameters are added in the system of equation 3.2 it gives:

$$\begin{cases} \frac{d}{dt}i_d &= \frac{L_e}{L_d.L_e - M^2}\left(V_d - R_s.i_d + p.\Omega.L_q.i_q - \frac{M}{L_e}\left(V_e - R_e.i_e\right)\right) \\ \frac{d}{dt}i_q &= \frac{1}{L_q}\left(V_q - R_s.i_q - p.\Omega.\left(L_d.i_d - M.i_e\right)\right) \\ \frac{d}{dt}i_e &= \frac{L_d}{L_d.L_e - M^2}\left(V_e - R_e.i_e - \frac{M}{L_d}\left(V_d - R_s.i_d + p.\Omega.L_q.i_q\right)\right) \\ \frac{d}{dt}\Omega &= \frac{1}{J}\left(p.i_q.M.i_e - f.\Omega - \Gamma_0 - \Delta\Gamma\right) \\ \frac{d}{dt}V_{DC} &= \frac{i_{bat}}{C_f} - \frac{V_d.i_d + V_q.i_q}{C_f.V_{DC}} - \frac{I_p}{C_f} \end{cases} \tag{3.10}$$

In this configuration, both the input filter voltage V_{DC} and the battery output current i_{bat} which were unused in the precedent observability study are now needed. For the observability demonstration, the vector of measured variables $y = \begin{bmatrix} i_e & \Omega & V_{DC} \end{bmatrix}^T$ and the vector of estimated variables $x = \begin{bmatrix} i_d & i_q & i_e & \Omega & V_{DC} & I_p & \Delta\Gamma \end{bmatrix}^T$ are introduced.

The choice of $\Delta\Gamma$ as a torque error seems logical in our application since no information is available on the load and the friction forces of the machine and it is likely to vary during a driving cycle of the vehicle. The reason why I_p has been chosen as one of the parameter error added in the system of equation in order to take advantage of the measure of the DC voltage available. Indeed I_p represents in this configuration a current error due to the losses in the DC part of the inverter. In addition, an error parameter, the parameter μ_M introduced in chapter 2, has already been used in the equation of i_q. It will however not be part of the nonlinear observer study conducted in this chapter.

This configuration of parameter error vector is a choice. Other parameters could have been introduced and added on the other equations of the system model. However this set of parameter errors have been privileged because they are located on measured variables and have different natures : $\Delta\Gamma$ is homogeneous to a mechanical torque and I_p to a current. Moreover, as it will now be demonstrated, the configuration described by 3.10 is observable.

With the same method than the one used previously, the rank of the new observability matrix dO defined bellow has to be found:

$$dO = \frac{\partial \dot{y}}{\partial x} = \begin{bmatrix} \frac{\partial f_{ie}}{\partial i_d} & \frac{\partial f_{ie}}{\partial i_q} & \frac{\partial f_{ie}}{\partial I_p} & \frac{\partial f_{ie}}{\partial \Delta\Gamma} \\ \frac{\partial f_{\Omega}}{\partial i_d} & \frac{\partial f_{\Omega}}{\partial i_q} & \frac{\partial f_{\Omega}}{\partial I_p} & \frac{\partial f_{\Omega}}{\partial \Delta\Gamma} \\ \frac{\partial f_{V}}{\partial i_d} & \frac{\partial f_{V}}{\partial i_q} & \frac{\partial f_{V}}{\partial I_p} & \frac{\partial f_{V}}{\partial \Delta\Gamma} \\ \frac{\partial f_{ie2}}{\partial i_d} & \frac{\partial f_{ie2}}{\partial i_q} & \frac{\partial f_{ie2}}{\partial I_p} & \frac{\partial f_{ie2}}{\partial \Delta\Gamma} \end{bmatrix} \tag{3.11}$$

where f_{ie}, f_{Ω}, f_V and f_{ie2}, referring to 3.10, are given by:

$$f_{ie} = \frac{d}{dt}i_e,\ f_{\Omega} = \frac{d}{dt}\Omega,\ f_V = \frac{d}{dt}V_{DC} \text{ and } f_{ie2} = \frac{d^2}{dt^2}i_e$$

When developing the new observability matrix dO from 3.11 it gets:

$$dO = \begin{bmatrix} \frac{-M.R_s}{M^2-L_d.L_e} & \frac{p.M.L_q}{M^2-L_d.L_q} & 0 & 0 \\ 0 & \frac{p.M}{J}.i_e & 0 & \frac{-1}{J} \\ \frac{-V_d}{C_f.V_{DC}} & \frac{-V_q}{C_f.V_{DC}} & \frac{-1}{C_f} & 0 \\ dO_{41} & dO_{42} & 0 & \frac{-L_d.p.L_q.i_q}{J.(L_d.L_f-M^2} \end{bmatrix} \tag{3.12}$$

with: $dO_{41} = \frac{L_d}{L_d.L_e-M^2}.\left(\frac{-R_e.M.R_s}{L_d.L_e-M^2} - \frac{L_e.R_s^2.M}{L_d.(L_d.L_e-M^2)} - p.\Omega^2.L_d\right)$

$$dO_{42} = \frac{L_d}{L_d.L_e - M^2}.\left(\frac{R_e.M.p.\Omega.L_q}{L_d.L_e - M^2} + \frac{L_e.R_s.M.p.\Omega.L_q}{L_d.\left(L_d.L_e - M^2\right)} + p.\Omega.R_s + \frac{2.p^2.i_q.L_q.M.i_e}{J} - \frac{p.L_q.\left(f.\Omega + \Gamma_0\right)}{J}\right)$$

From 3.12, it is possible to conclude that, like for 3.8, the matrix dO is always full rank if $i_e \neq 0$, hence the system is locally observable in this configuration too.

3.2 Presentation of the observers used for currents estimation

The local observability of the phase currents have been demonstrated for different configurations in the previous section. This section will now focus on the nonlinear observers that have been used for the estimation of the phase currents in the stator of the WRSM.

Logically the first nonlinear observer that has been tried for this study and that will be presented in this section is the extended Kalman Filter (EKF), since it is a widely used tool in industrial automation. Another nonlinear observer, originally from [84] but adapted here for state variables, has been used, showing good results in simulations and experimental works. Two versions of this proposed nonlinear observer will be presented, one simple estimating only the phase currents in the WRSM and an extended one including the estimation of two parameters Δ_Γ and I_p (introduced in the previous section for the demonstration of observability).

3.2.a The Extended Kalman Filter

The Kalman filter is an extremely widely used tool in the field of automation. Indeed it is a tool that can be adapted to different type of applications. Extended reviews on Kalman filter and its applications are made in [89], [90]. It can be used as a filter, as its name stands for, in order to reduce the noise or to retrieve incomplete data from a measure. It can also be used as an observer of a variable when other measures are known. The nonlinear form of the Kalman filter, the extended Kalman filter has been developed for the same applications and is based on the same principles but can be applied to nonlinear systems. This is the version that will be developed in this work since the system studied is nonlinear.

The EKF operating principle can be divided in two parts:

- First a prediction part, that calculates the next step observed variables based on the state-model of the system
- In a second time there is an update part, that calculates a prediction on the error made on the system output

Let us consider a discretized nonlinear system described by the following equations:

$$\begin{cases} X_{k+1} &= f(X_k, u_k) \\ Y_k &= h(X_k, u_k) \end{cases} \tag{3.13}$$

with: $X_k \in \mathbb{R}^n$ the state variables of the system at the k^{th} step, $u_k \in \mathbb{R}^m$ the command vector at the k^{th} step and $Y_k \in \mathbb{R}^p$ the measured variables at the k^{th} step. $f(X_{k-1}, u_k)$ and $h(X_k, u_k)$ are nonlinear functions given by the system considered.

The prediction part of the EKF gives the predicted estimated state variable given by:

$$\hat{X}_{k+1|k} = f(\hat{X}_k, u_k) \tag{3.14}$$

The update step for the state variable would then be:

$$\hat{X}_{k+1} = \hat{X}_{k+1|k} - K_{k+1}.\tilde{Y}_{k+1} \tag{3.15}$$

with K_k the near-optimal Kalman gain and $\tilde{Y}_{k+1}$ the measurement residual defined by:
$\tilde{Y}_{k+1} = h(\hat{X}_{k+1|k}, u_{k+1}) - Y_{k+1}$

The near-optimal Kalman gain has to be determined so that the EKF output is stable, i.e that the observation of $\hat{X}_{k|k}$ converges in a finite time. From the previous equation, the dynamic of estimation error $\tilde{X}_k = \hat{X}_k - X_k$ can be deduced:

$$\tilde{X}_{k+1} = f(\hat{X}_k, u_k) - f(X_k, u_k) - K_{k+1}.\left(h(\hat{X}_{k+1|k}, u_{k+1}) - h(X_{k+1|k}, u_{k+1})\right) \tag{3.16}$$

The first degree Taylor series associated to the functions f and h from 3.16 give:

$$\begin{aligned} f(\hat{X}_k, u_k) - f(X_k, u_k) &= A_k.\tilde{X}_k + R_F(X_k, \hat{X}_k, u_k) \\ h(\hat{X}_{k+1|k}, u_{k+1}) - h(X_{k+1|k}, u_{k+1}) &= C_{k+1}.\tilde{X}_{k+1|k} + R_H(X_{k+1}, \hat{X}_{k+1|k}, u_{k+1}) \end{aligned} \tag{3.17}$$

with:

$$\begin{aligned} A_k &= \frac{\partial}{\partial X} f(\hat{X}_k, u_k) \\ C_{k+1} &= \frac{\partial}{\partial X} h(\hat{X}_{k+1|k}, u_{k+1}) \end{aligned} \tag{3.18}$$

and $R_F(X_k, \hat{X}_k, u_k)$ and $R_H(X_{k+1}, \hat{X}_{k+1|k}, u_{k+1})$ are the residual terms with a degree equal or superior to 2 at the point $\tilde{X}_k$ and $\tilde{X}_{k+1|k}$ respectively.

Finally when reusing 3.17 in 3.16, it gives:

$$\tilde{X}_{k+1} = (A_k - K_{k+1}.C_{k+1}.A_k).\tilde{X}_k + \Delta_{k+1} \tag{3.19}$$

with Δ_{k+1} the linearization error given by:

$$\Delta_{k+1} = (I_n - K_{k+1}.C_{k+1}).R_F(X_k, \hat{X}_k, u_k) - K_{k+1}.R_H(X_{k+1}, \hat{X}_{k+1|k}, u_{k+1}) \tag{3.20}$$

When considering the error Δ_{k+1} negligible, the full characterization of the EKF can be summarized by the following equations:

- Prediction step:

$$\begin{aligned} \hat{X}_{k+1|k} &= f(\hat{X}_k, u_k) \\ P_{k+1|k} &= A_k.P_k.A_k^T + Q_k \end{aligned} \tag{3.21}$$

  with $P_{k+1|k}$ the predicted covariance matrix of the error of observation, P_k the covariance matrix of the error of observation and Q_k the covariance matrix of process noise.

- Update step:

$$\begin{array}{rcl} K_{k+1} & = & P_{k+1|k}.C_{k+1}^{T}.\left(C_{k+1}.P_{k+1|k}.C_{k+1}^{T}+R_k\right)^{-1} \\ P_{k+1} & = & \left(I_n - K_{k+1}.C_{k+1}\right).P_{k+1|k} \\ \hat{X}_{k+1} & = & \hat{X}_{k+1|k} - K_{k+1}.\tilde{Y}_{k+1} \end{array} \tag{3.22}$$

  with R_k the covariance matrix of measurement noise.

The performances of the EKF depend largely on the choice of the matrix R_k and Q_k. This is even more true when there are errors on the initialization of the different gains and of the observed state variables vector $\hat{X}_0$ of the system. These matrix are difficult to obtain. Some methods such as the Autocovariance Least-Square (ALS) method described in [91] can be used for linear systems, but with nonlinear systems, the linearization error might be responsible for an increased error on R_k and Q_k. This is the main drawback of the use of the EKF as a nonlinear observer. The choice of the initial state variables $\hat{X}_0$ can be deduced with a satisfying precision thanks to the modeling of the system. In our case however, as it will be seen later, the initialization of the EKF being at standstill of the machine, the initialization is not a problem, all the observed state variables being equal to zero. The initial value P_0 of $P_{k+1|k}$ also has to be determined, but it is usually enough to choose a diagonal matrix in which the values correspond to the uncertainties on the initial state variables. If the initial values are perfectly known, the P_0 chose can be a zero matrix.

The EKF observer principle has been described generically. Applied to our system described by the equations 3.2, the state variables vector X is given by $X = \begin{bmatrix} i_d & i_q & i_e & \Omega \end{bmatrix}^T$ and the measured variables vector Y is given by $Y = \begin{bmatrix} i_e \\ \Omega \end{bmatrix}$. As demonstrated the subsection "Proof of Observability", the system is locally observable in this configuration. The study on the EKF applied to the WRSM for a current sensorless application has been published in [92] and [93].

As seen in the description of the EKF, this version of the EKF observer can be applied on discretized systems. In the system considered, the discretized system of equation based on 3.2 gives the following discretized system:

$$\begin{cases} i_d(k+1) & = & i_d(k) + \Delta T.\frac{L_e}{L_d.L_e - M^2}\left(V_d - R_s.i_d(k) + p.\Omega(k).L_q.i_q(k) - \frac{M}{L_e}\left(V_e - R_e.i_q(k)\right)\right) \\ i_q(k+1) & = & i_q(k) + \Delta T.\frac{1}{L_q}\left(V_q - R_s.i_q(k) - p.\Omega(k).\left(L_d.i_d(k) - M.i_e(k)\right)\right) \\ i_e(k+1) & = & i_e(k) + \Delta T.\frac{L_d}{L_d.L_e - M^2}\left(V_e - R_e.i_e(k) - \frac{M}{L_d}\left(V_d - R_s.i_d(k) + p.\Omega(k).L_q.i_q(k)\right)\right) \\ \Omega(k+1) & = & \Omega(k) + \Delta T.\frac{1}{J}\left(p.i_q(k).M.i_e(k) - f.\Omega(k) - \Gamma_0\right) \end{cases} \tag{3.23}$$

The constant ΔT corresponds is the time step related to the sample rate of the system.

Based on the system of equation 3.23, it is possible to deduce the functions $f(X_k, u_k)$ and $h(X_k, u_k)$ from 3.13.

The system with the EKF observer has been implemented in simulation with Matlab/Simulink, in order to test the performances and the feasibility of the state currents observation with this tool. The simulation results when no parameter errors are added in the EKF model are presented on figure 3.3 to 3.5.

Figures 3.3 and 3.4 features the estimation results in output of the EKF for a simulated start of the machine at t = 0.1s from 0rpm to 500rpm and an acceleration at t = 1.5s from 500rpm to 800rpm. At the initialization of the EKF, an error of 5A is introduced on the estimated dq-axis currents.

As it can be seen from those two graphs, even with errors introduced on the initialization of the currents, the EKF outputs converge towards the real currents when no parametric errors

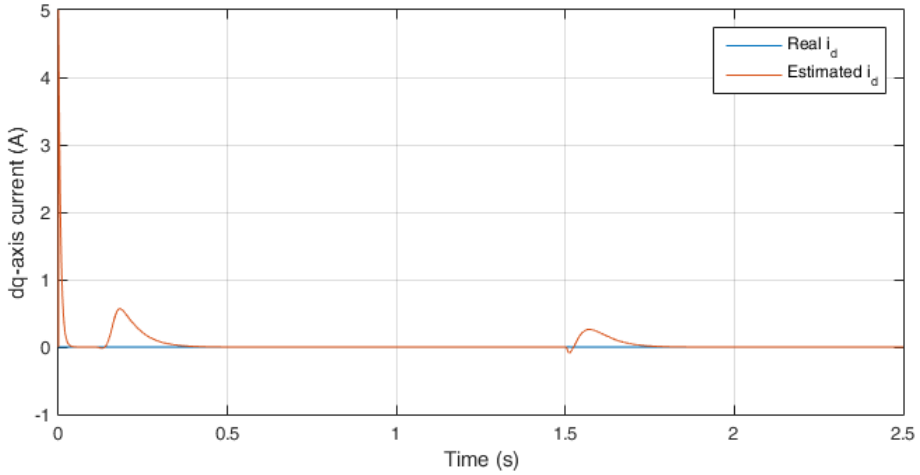

Figure 3.3. Comparison between the real d-axis current and the EKF estimation without parametric error.

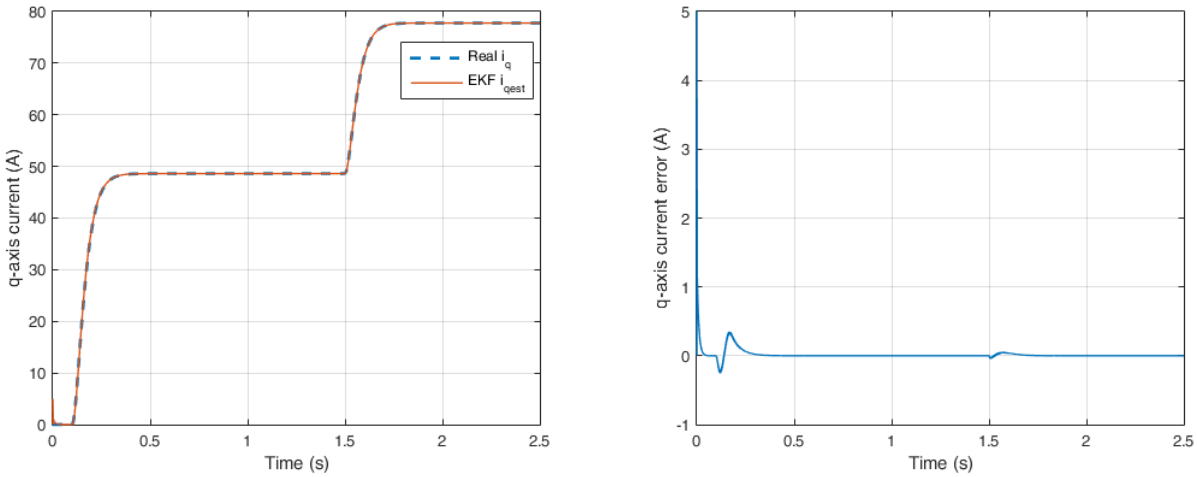

Figure 3.4. Left: real i_q and EKF estimated i_q without parametric error. Right: error between the real and the estimated i_q.

are introduced in the EKF equations. The transient phases provoke errors on the currents but they converge back towards the real currents values. In order to characterize the influence of the choice of the matrix R_k on the convergence speed of the EKF outputs, figure 3.5 show the dynamic of convergence and the noise rejection for of the estimated q-axis current towards the real current values for two different set of R_k and Q_k.

As it can be seen from figures 3.5, the value chosen for R_k and Q_k influences the convergence of the current estimation and the noise rejection. For this test, a measurement noise is added on Ω and i_e in input of the EKF. When the covariance matrix of measurement noise R_k (corresponding to the measurement uncertainties) is high compared to the covariance matrix of process noise Q_k (corresponding to the model uncertainties), the noise on the current output is reduced but the estimation take a longer time to converge. On the other hand, when R_k is small compared to Q_k, the noise effect on the estimation current is greater, but the EKF converges faster.

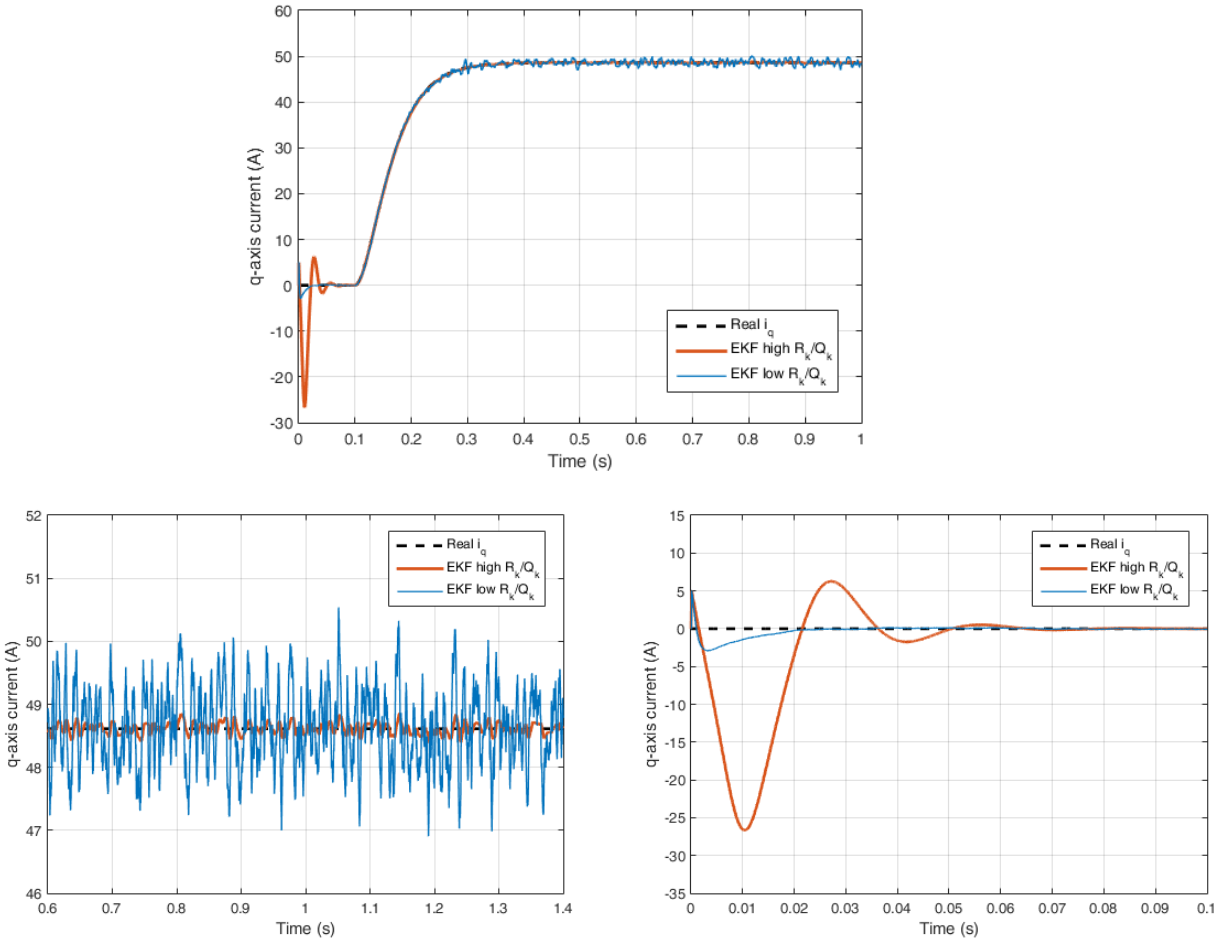

Figure 3.5. Comparison of the EKF q-axis estimation for two sets of R_k and Q_k for a simulated start of the WRSM from 0rpm to 500rpm at t=0.1s with noise on the measurements. Top: global view. Bottom left: zoom on the steady-state. Bottom right: zoom on the start.

3.2.b The proposed observer

It has been mentioned before that the first observer implemented and tested on the current sensorless control was logically the Extended Kalman filter, since it is a very common tool in automation engineering. The EKF has been described and the results associated are given in the previous subsection.

After setting up the EKF observer, it has been decided to test another kind of observer based on a different convergence principle.

In 2013, an parameter observer applied to a DC/DC converter has been developed in the GREEN laboratory in the context of the thesis of Dr. Hugues Renaudineau. This parameter observer was used to observe some parameters of the system thanks to the measures of state variables (the currents and voltages in the converter) and the convergence of the observation was based on the convergence analysis of a Lyapunov candidate function describing the energy of the system. This observer showed good results that are given with all the details needed in [84] and [85].

In the context of current sensorless control, the estimation needed are not parameters but the stator currents and thus state variables. Due to this fact, the observer proposed in Dr. Renaudineau's work has been modified to comply to the problematic of this work, and will be

detailed in the next paragraphs.

Let us consider a continuous system whose state-space model can be put under the following formulation:

$$\begin{cases} \dot{x} &= f_x(y,u) + g(y,u).x \\ \dot{y} &= f_y(y,u) + h(y,u).x \end{cases} \tag{3.24}$$

where y corresponds to the measured variables, x is the vector of the state variables to observe and u represents the control vector. The nonlinear functions $f_x(y,u)$, $f_y(y,u)$, $g(y,u)$ and $h(y,u)$ are considered continuous and derivable at least one time, and are determinable thanks to the state-space model of the system.

If a system can be put under the form presented in 3.24, the proposed observer associated is written:

$$\begin{cases} \dot{\hat{x}} &= f_x(y,u) + g(y,u).\hat{x} - \eta(y,u).\epsilon_y \\ \dot{\hat{y}} &= f_y(y,u) + h(y,u).\hat{x} - K.\epsilon_y \end{cases} \tag{3.25}$$

with $\hat{y}$ the estimation of the measured variables, $\hat{x}$ the observed unmeasured state variables. The term ϵ_y is the difference between the estimation of y and the measures of y, defined mathematically by $\epsilon_y = \hat{y} - y$. The constant matrix K and the function $\eta(y,u)$ need to be designed in a way that the convergence of the observation is guaranteed. Thus their expressions will be determined later with the demonstration of convergence of observation.

In order to demonstrate the convergence of this proposed observer, let us analyze the dynamics of estimation error. These dynamics are given the derivation of ϵ_y and ϵ_x (the difference between the estimation of x and the real x: $\epsilon_x = \hat{x} - x$). This is clearer when put through equations:

$$\begin{cases} \dot{\epsilon_x} &= \dot{\hat{x}} - \dot{x} \\ \dot{\epsilon_y} &= \dot{\hat{y}} - \dot{y} \end{cases} \tag{3.26}$$

From 3.24 and 3.25, the system of equations 3.26 leads to:

$$\begin{cases} \dot{\epsilon_x} &= g(y,u).\epsilon_x - \eta(y,u).\epsilon_y \\ \dot{\epsilon_y} &= h(y,u).\epsilon_x - K.\epsilon_y \end{cases} \tag{3.27}$$

Now, as announced in the introduction of this paragraph on the proposed observer, the convergence of this topology of observer is based on the convergence on an associate Lyapunov function.

The Lyapunov candidate function associated to this observer that has been chosen is written:

$$V = \frac{1}{2}.\begin{bmatrix} \epsilon_x^T & \epsilon_y^T \end{bmatrix} \begin{bmatrix} \epsilon_x \\ \epsilon_y \end{bmatrix} \tag{3.28}$$

To demonstrate a convergence of the system, the derivation of the Lyapunov candidate function has to be strictly negative. From 3.28, the derivation of V gives:

$$\dot{V} = \epsilon_x^T.\dot{\epsilon_x} + \epsilon_y^T.\dot{\epsilon_y} \tag{3.29}$$

From 3.27, 3.29 gives;:

$$\dot{V} = \epsilon_x^T.\left(g(y,u).\epsilon_x - \eta(y,u).\epsilon_y\right) + \epsilon_y^T.\left(h(y,u).\epsilon_x - K.\epsilon_y\right) \tag{3.30}$$

and this leads to:

$$\dot{V} = -\epsilon_y^T.K.\epsilon_y + \epsilon_x^T.g(y,u).\epsilon_x + \epsilon_y^T.\left(h(y,u) - \eta^T(y,u)\right).\epsilon_x \tag{3.31}$$

When considering 3.31, it is possible to remove the non-quadratic term by choosing:

$$\eta(y,u) = h^T(y,u) \tag{3.32}$$

In that case $\dot{V}$ can finally be written:

$$\dot{V} = -\epsilon_y^T.K.\epsilon_y + \epsilon_x^T.g(y,u).\epsilon_x \tag{3.33}$$

In order to guarantee the asymptotic convergence of the observation, according to Lyapunov stability, the condition $\dot{V} < 0$ has to be true. Looking at 3.33, it brings the following conditions:

$$\begin{cases} K & > & 0 \\ g(y,u) & < & 0 \\ \eta(y,u) & = & h^T(y,u) \end{cases} \tag{3.34}$$

To conclude, in order to guarantee the asymptotic convergence of this topology of observer, the correction matrix K has to be defined positive, the correction function $\eta(y,u)$ has to be chosen equal to $h^T(y,u)$ (given by the state model 3.24. In addition $g(y,u)$ has to be Hurwitz but this depends on the system and it cannot be modified. Let's note that, given the resulting equation on $\dot{V}$ in equation 3.33, if the matrix $g(y,u)$ can be considered defined negative and bounded and if K is strictly positive, it exists a constant λ defined positive such as:

$$\dot{V} = -\epsilon_y^T.K.\epsilon_y + \epsilon_x^T.g(y,u).\epsilon_x < -\frac{1}{2}.\lambda.(\epsilon_x^T.\epsilon_x + \epsilon_y^T.\epsilon_y) \tag{3.35}$$

Thus leading to:

$$\dot{V} < -\lambda.V \tag{3.36}$$

If the observer guarantee this formulation, then the observer can be considered exponentially convergent. The exponential convergence is stronger than the asymptotic convergence since it guarantees observability in any conditions.

Now the stability of this proposed observer has been demonstrated, let's apply it to our study. For the application of the WRSM, and regarding the state equations 3.2, the vector y of the measured state variables of the system corresponds to $y = \begin{bmatrix} i_e \\ \Omega \end{bmatrix}$ and the vector x of the state variables to observe is $x = \begin{bmatrix} i_d \\ i_q \end{bmatrix}$. When the state model 3.2 is put under the form of the proposed observer 3.24, it gives for the measured state variables y:

$$\begin{cases} \frac{d}{dt}i_e & = & \frac{L_d}{L_d.L_e - M^2}\left(V_e - R_e.i_e - \frac{M}{L_d}.V_d\right) + \frac{M}{L_d.L_e - M^2}\left(R_s.i_d - p.\Omega.L_q.i_q\right) \\ \frac{d}{dt}\Omega & = & \frac{1}{J}\left(-f.\Omega - \Gamma_0\right) + \frac{1}{J}.p.i_q.M.i_e \end{cases} \tag{3.37}$$

This leads to, in a more explicit form:

$$\begin{bmatrix} \dot{i_e} \\ \dot{\Omega} \end{bmatrix} = \begin{bmatrix} \frac{L_d}{L_d.L_e - M^2}\left(V_e - R_e.i_e - \frac{M}{L_d}.V_d\right) \\ \frac{1}{J}\left(-f.\Omega - \Gamma_0\right) \end{bmatrix} + \begin{bmatrix} \frac{M.R_s}{L_d.L_e - M^2} & \frac{-M.p.\Omega.L_q}{L_d.L_e - M^2} \\ 0 & \frac{M.p.i_e}{J} \end{bmatrix} \cdot \begin{bmatrix} i_d \\ i_q \end{bmatrix} \tag{3.38}$$

By identification, the functions $f_y(y,u)$ and $h(y,u)$ from 3.24 can be deduced:

$$f_y(y,u) = \begin{bmatrix} \frac{L_d}{L_d.L_e - M^2}\left(V_e - R_e.i_e - \frac{M}{L_d}.V_d\right) \\ \frac{1}{J}\left(-f.\Omega - \Gamma_0\right) \end{bmatrix} \tag{3.39}$$

$$h(y,u) = \begin{bmatrix} \frac{M.R_s}{L_d.L_e - M^2} & \frac{-M.p.\Omega.L_q}{L_d.L_e - M^2} \\ 0 & \frac{M.p.i_e}{J} \end{bmatrix} \tag{3.40}$$

The same procedure can be used for the state equations linked to the vector x:

$$\begin{cases} \frac{d}{dt}i_d &= \frac{L_d}{L_d.L_e - M^2}\left(V_d - \frac{M}{L_d}.(V_e - R_e.i_e\right) + \frac{L_e}{L_d.L_e - M^2}\left(-R_s.i_d + p.\Omega.L_q.i_q\right) \\ \frac{d}{dt}i_q &= \frac{1}{L_q}\left(V_q + p.\Omega.M.i_e\right) + \frac{1}{L_q}.\left(-R_s.i_q - p.\Omega.L_d.i_d\right) \end{cases} \tag{3.41}$$

By simplifying 3.41, the following form is obtained:

$$\begin{bmatrix} \dot{i}_d \\ \dot{i}_q \end{bmatrix} = \begin{bmatrix} \frac{L_d}{L_d.L_e - M^2}\left(V_d - \frac{M}{L_d}.(V_e - R_e.i_e\right) \\ \frac{1}{L_q}\left(V_q + p.\Omega.M.i_e\right) \end{bmatrix} + \begin{bmatrix} \frac{-L_e.R_s}{L_d.L_e - M^2} & \frac{L_e.p.\Omega.L_q}{L_d.L_e - M^2} \\ \frac{-p.\Omega.L_d}{L_q} & \frac{-R_s}{L_q} \end{bmatrix} . \begin{bmatrix} i_d \\ i_q \end{bmatrix} \tag{3.42}$$

By identification, the functions $f_x(y,u)$ and $g(y)$ from 3.24 can be deduced:

$$f_x(y,u) = \begin{bmatrix} \frac{L_d}{L_d.L_e - M^2}\left(V_d - \frac{M}{L_d}.(V_e - R_e.i_e\right) \\ \frac{1}{L_q}\left(V_q + p.\Omega.M.i_e\right) \end{bmatrix} \tag{3.43}$$

$$g(y,u) = \begin{bmatrix} \frac{-L_e.R_s}{L_d.L_e - M^2} & \frac{L_e.p.\Omega.L_q}{L_d.L_e - M^2} \\ \frac{-p.\Omega.L_d}{L_q} & \frac{-R_s}{L_q} \end{bmatrix} \tag{3.44}$$

Now the system of equation has been modulated to fit the suitable form of 3.24, it is important to check that the matrix $g(y,u)$ is Hurwitz, which means that the eigenvalues of the matrix are negatives.

In the case where $\Omega = 0$, from 3.44 is a negative diagonal matrix so it can be immediately concluded that $g(y,u)$ is negative and the condition given in 3.34 is guaranteed. In order to check that the matrix $g(y,u)$ is Hurwitz for all the spectrum of operating point of the WRSM, the eigenvalues of $g(y,u)$ have been calculated for a speed varying from $0 rad.s^{-1}$ to $150 rad.s^{-1}$ in both rotating directions. The real part of the eigenvalues of $g(y,u)$ for $-150 < \Omega < 150$ are plotted on figure 3.6.

The matrix K, as seen in the demonstration of the proposed observer, has to be defined positive to have an exponential convergence of the observation. This is the only necessary

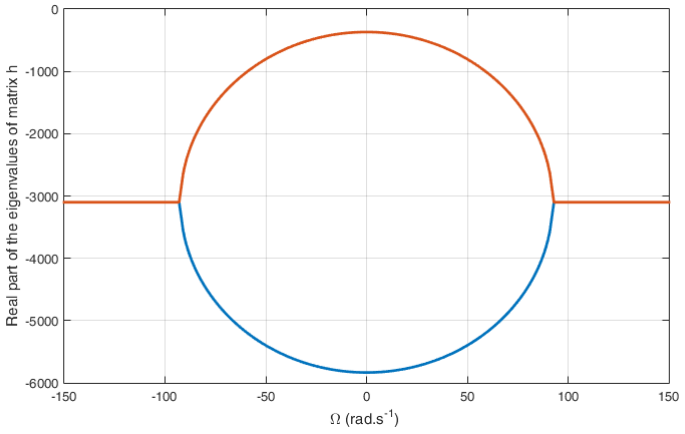

Figure 3.6. Real part of the eigenvalues of $g(y,u)$ as a function of the rotor speed.

condition, the elements of K can be chosen by the user. As a first choice, a diagonal matrix is used. The elements of the diagonal will determine the dynamics of convergence of the state variable associated. Indeed, the correction term $K.\epsilon_y$ can be written:

$$K.\epsilon_y = \begin{bmatrix} k_1 & 0 \\ 0 & k_2 \end{bmatrix} . \begin{bmatrix} \hat{i_e} - i_e \\ \hat{\Omega} - \Omega \end{bmatrix} \tag{3.45}$$

The element k_1 will determine the dynamic of convergence of the excitation current and the element k_2 will determine the dynamic of convergence of the rotor speed. Therefore, the elements k_1 and k_2 need to be weighted according to the user's needs and the characteristics of the system studied.

In our system, the condition $\eta(y,u) = h^T(y,u)$ that is required to remove the non quadratic term of the derivation of the Lyapunov function (see demonstration) brings the following $\eta(y,u)$:

$$\eta(y,u) = \begin{bmatrix} \frac{M.R_s}{L_d.L_e - M^2} & 0 \\ \frac{-M.p.\Omega.L_q}{L_d.L_e - M^2} & \frac{M.p.i_e}{J} \end{bmatrix} \tag{3.46}$$

At this point, all the elements needed to define the proposed observer are made explicit for the WRSM system. In order to check that the performances and stability of this proposed observer, some simulation with the software Matlab/Simulink have been conducted. To do so, the proposed observer's equations given before from equation 3.37 to equation 3.46 have been implemented in a matlab function in the form given in 3.25.

This matlab function describing the proposed observer is then integrated to the main Simulink file containing the whole description of the WRSM with its environment (battery, inverter and input filter) and the main control chain, and are connected with each other as shown on figure 3.2.

For the first simulations of this paragraph, the system begins at the standstill of the WRSM, at 0.1s there is a first reference step to a rotor speed of 500rpm and at 1.5s there is a second step from 500rpm to 800rpm. In order to check the stability and the dynamic performances of this observer, the model of the machine will be considered well known, which translates into the fact that there are no differences between the equations describing the model of the WRSM in the main simulink and in the matlab function describing the observer. In other simulations shown later in this section, errors will be added to test the robustness of the proposed observer.

The figure 3.7 compares, in the conditions of simulations described above, the real d-q axis currents with the observed dq-axis currents given in output of the proposed observer.

The first important remark that can be done from this figure is that, when the parameters used in the model of the proposed observer to describe the system are well known, the observed dq-axis currents converge towards the real stator currents. In addition, the dynamics of convergence are fast in comparison with the control dynamics. A zoom at 1.5s is given in the figure 3.8. Here the convergence of the estimated state variable after a perturbation (in this case a step in the reference of the speed of the machine) shows that the proposed observer is stable. The observation of the currents converges fast enough not to be noticeable on figure 3.7.

Figure 3.7 shows also the exponential convergence of this proposed observer to variations on the state variables, here on the speed of the rotor. Indeed, the estimator converges at standstill, then at 500rpm from $t = 0.1s$ to $t = 1.5s$ and 800rpm from $t = 1.5s$ to $t = 3s$. It is important to note that the estimated currents are controlled in this simulation and the actual ones are plotted for comparison purposes.

When errors of initialization on the state variables are added, it is possible to characterize the speed of convergence of ϵ_y as a function of the constant matrix K, as it has been pointed out with equation 3.45. Figure 3.9 shows the difference of convergence speed for ϵ_y with a K given

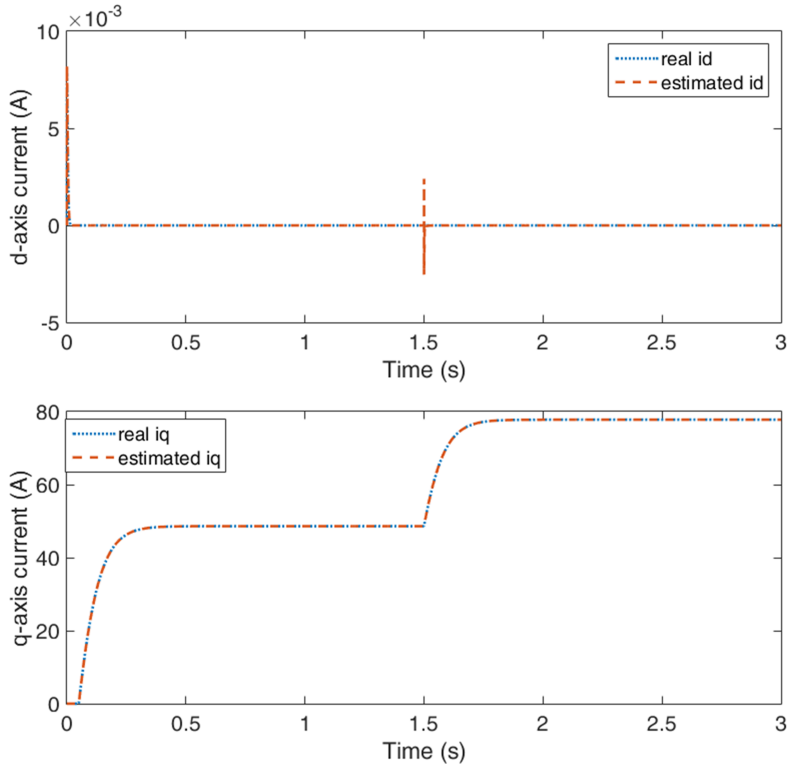

Figure 3.7. Estimated d-q axis currents in the WRSM with the proposed observer with no parameter error.

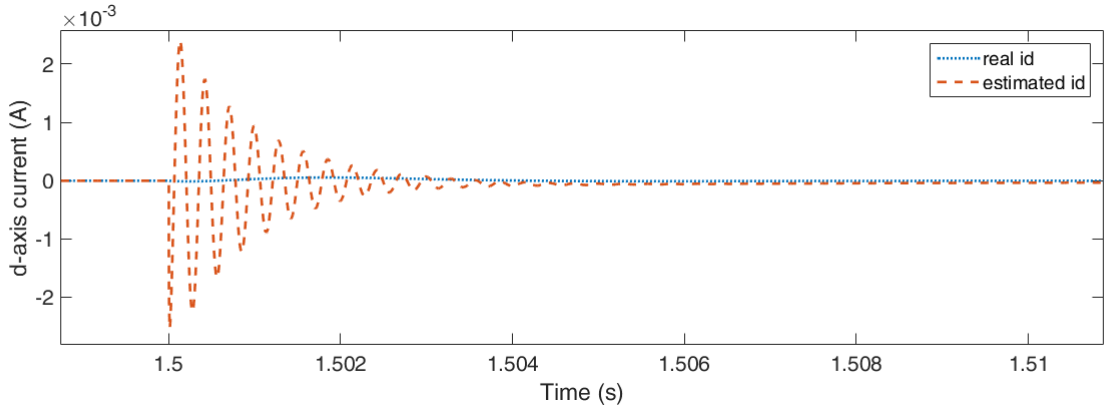

Figure 3.8. Zoom at 1.5s of 3.7 .

by $K = \begin{bmatrix} 20 & 0 \\ 0 & 20 \end{bmatrix}$ on the left and a K ten times larger on the right. From these two simulation, the impact of the constant K on the dynamic of convergence of ϵ_y is clear, and the larger the values on the diagonals of K, the higher the dynamic of convergence of i_e and Ω.

The tests presented up to this point were presented in the case were there is no error on the parameters in the model of the observer. However, as it has been shown in the chapter 2, this is impossible to guarantee on a real WRSM drive. Indeed, the parameters values are modified with the temperature of the system, with the saturation of the machine or the wear of the components. For this reason, the proposed observer's robustness to parameter errors in the model has also

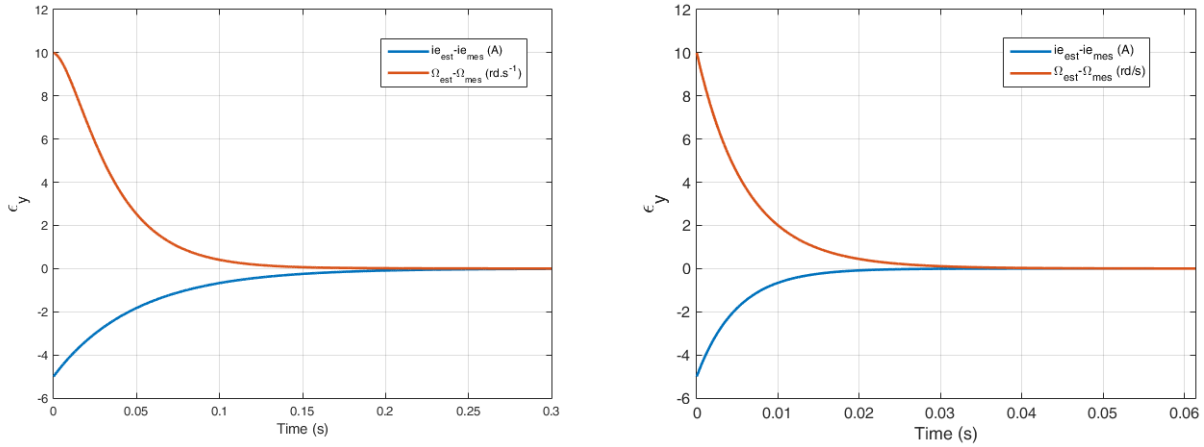

Figure 3.9. Comparison of the dynamics of evolution of ϵ_y with two different K.

been tested.

In order to simulate parameter errors, it has been decided to add an error value to all the parameters that are likely to have their value modified by the causes listed above. Those parameters are the stator resistor R_s, the mutual inductance M and the stator inductances L_d and L_q for the electric parameters and the rotor inertia J and the friction forces coefficient f for the mechanical parameters. The error terms are then added to the standard values to simulate errors on the parameters in the observer. The parameter values of the proposed observer are then written:

$$\begin{cases} \hat{R_s} = R_s + \tilde{R_s} \\ \hat{M} = M + \tilde{M} \\ \hat{L_{dq}} = L_{dq} + \tilde{L_{dq}} \\ \hat{J} = J + \tilde{J} \\ \hat{f} = f + \tilde{f} \end{cases} \tag{3.47}$$

The following simulation results shows the comparison between the robustness towards electrical parameters errors of the proposed observer and the EKF. Figure 3.10 shows the results of the currents estimations with the proposed observer and the EKF with 50% error on the electrical parameters R_s, L_d and L_q and with noise added on the measures of the speed and the excitation current. The test performed features a first speed step from $0rpm$ to $500rpm$ at $t = 0.1s$ and a step from $500rpm$ to $800rpm$ at $t = 1.5s$.

The two top graphs of this figure show that the estimations converge to wrong values for both observers. On the top figure, corresponding to the q-axis current, the EKF and the proposed estimator have the same behavior: the estimated i_q for both of the observers converge towards the same value, $32A$ after the first step and $65A$ after the second step, while the real current reaches respectively $52A$ and $78A$. The fact that both of the observers converge to the same values was expected. Indeed, the system modeling and the errors added are the same for the two observers. In this test, the d-axis current is well estimated, both the EKF and the proposed observer converging towards a value close to $0A$ like the real current. The parameter errors added in this test lead for the two observers to an relative error of 45% after the first step and 33% on the second step. These errors are large, but the errors added are great and their values do not reflect the real errors occurring in a machine.

On the two top graphs of figure 3.10, a small $R_k.Q_k^{-1}$ has been used for the EKF. With this set of covariance matrix, the measurement noises impact the EKF and the proposed observer in the same proportion, the ripple due to the noise being the same for the two observers. On

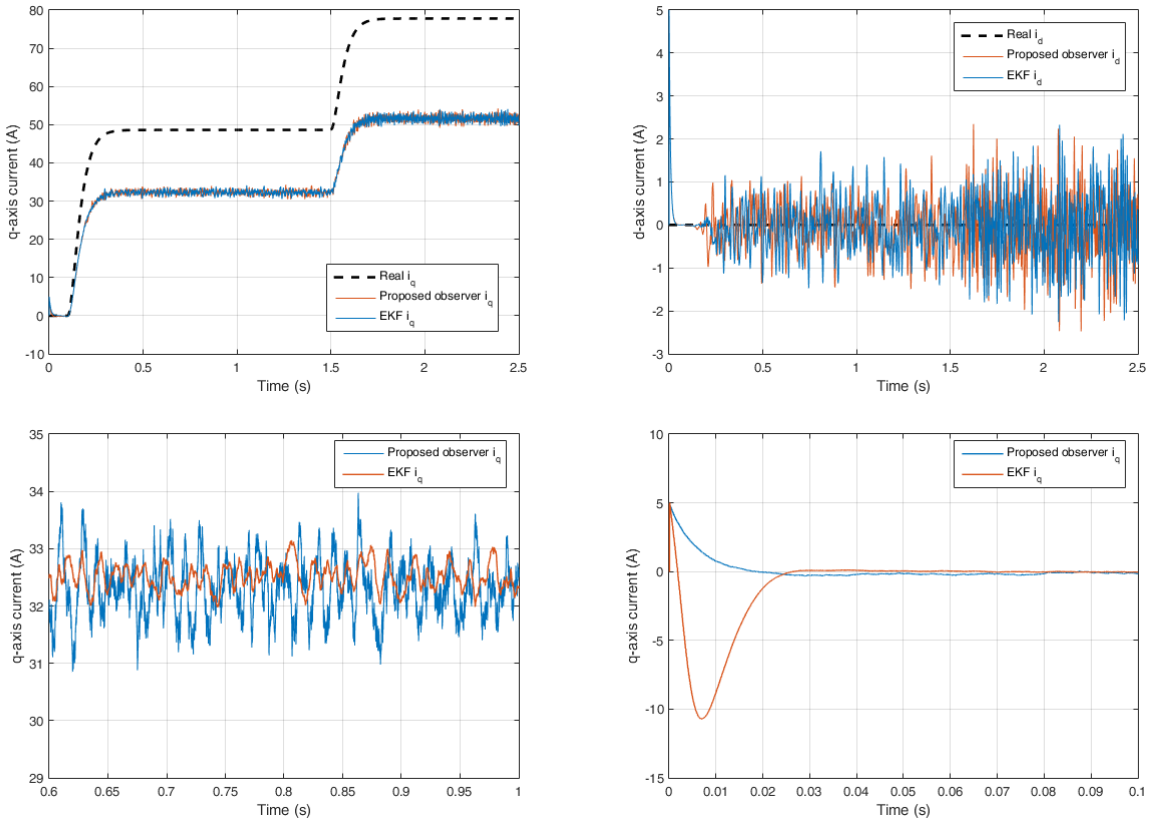

Figure 3.10. Comparison between the proposed state observer and the EKF when 50% error are added on the electric parameters. Top left: q-axis currents with low $R_k.Q_k^{-1}$ for the EKF. Top right: d-axis currents with low $R_k.Q_k^{-1}$ for the EKF. Bottom left: Zoom on q-axis currents at steady-state with high $R_k.Q_k^{-1}$ for the EKF. Bottom right: Zoom on q-axis currents at the start with high $R_k.Q_k^{-1}$ for the EKF.

the two bottom graphs, the same test is realized but with a large $R_k.Q_k^{-1}$ for the EKF. The bottom left graph is a zoom of the estimated q-axis current. It shows that the EKF rejects the measurement noise more effectively than the proposed observer. However, as it has been seen in the previous section on the EKF, the bottom right graph shows that the dynamic of convergence is reduced with the large $R_k.Q_k^{-1}$ compared to the dynamic of the proposed observer.

When focusing on the proposed observer parameter sensitivity separately, it is clear that the impact of the parameter L_d is negligible. The figure 3.11 shows the evolution of ϵ_x when there is an error of 50% on the parameter L_d. A step on the d-axis current is imposed at $t = 0.6s$ from 0 A to 10 A. As it can be noticed on figure 3.11, when the current is null in the WRSM stator, the impact of the error on L_d is not significant, but when i_d is different from 0, an error on the estimation appears. This test is coherent with the parameter sensitivity study realized in section 2.3.b.

This is a positive result since for the steady-state operating points, there is no need to have a fluw weakening on the WRSM and the current is usually controlled to be equal to 0 A. However in some applications, for the starting phase of the system, a flux weakening can be applied to reach the operating point wanted faster. In those field weakening phases, an error on L_d can lead to estimation errors.

Since the torque of the machine is caused by the q-axis current of the machine, i_q is not null on steady state operating point of the machine, and thus the observation of the currents is a lot more sensitive to an error on the q-axis current. Figure 3.12 presents the variable ϵ_x when there

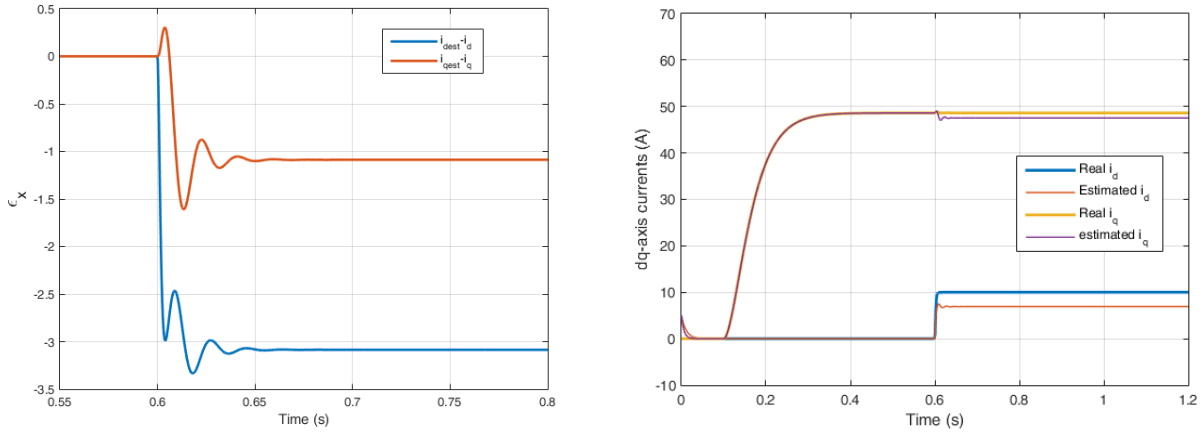

Figure 3.11. Left: ϵ_x with the proposed observer with 50% errors on L_d with a step of 10A on the d-axis current reference at t=0.6s. Right: real and estimated dq-axis currents for the same test.

is a 50% error on parameter L_q in the observer compared to the real q-axis inductance in the machine. At $t = 0.05s$ and $t = 1.5s$ there is a step up from respectively $0rpm$ to $500rpm$ and $500rpm$ to $800rpm$ on the speed reference of the machine. On this figure, it can be noticed that the error on estimation on both d-axis and q-axis current is quite substantial. Indeed the error reaches up to respectively 45% of the total current $I_{tot} = \sqrt{i_d^2 + i_q^2}$ for the first step and 33% for the second step.

The parameter R_s corresponding to the stator restistance also induces sensitivity on the observers. The following simulation presented in figure 3.13 shows the error of observation when errors on R_s are added. From this simulation, the impact of the error of R_s on the observation is obvious and, the same way than when there is an error on the inductances, the observation is flawed. To be precise, the proposed observer errors ϵ_x and ϵ_y still converge towards 0, but because of the error of parameters, the ϵ_x in the observer is different from the real one, hence the error of observation.

However, the most sensitive parameter among the electrical parameters is the mutual inductance M. Figure 3.14 shows the error on the observed currents when a 50% error is added on M

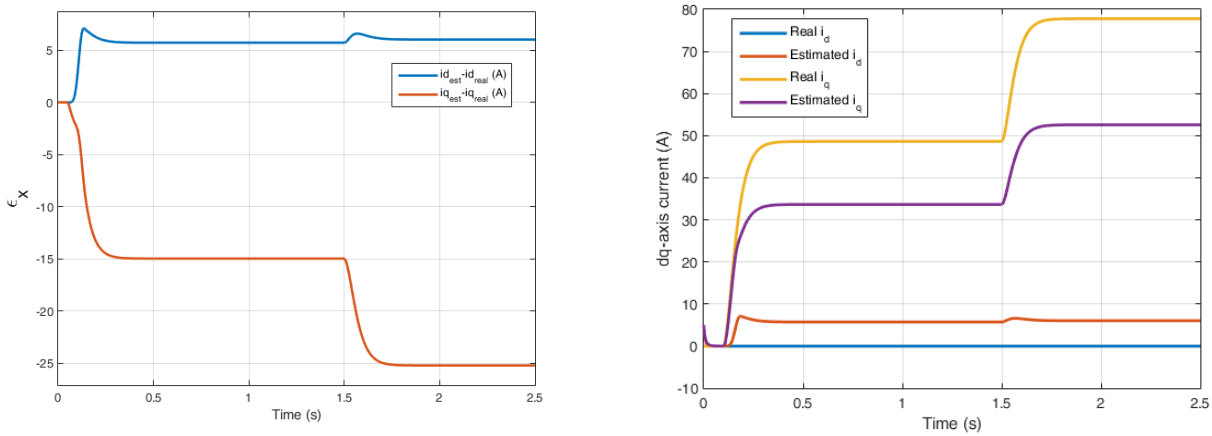

Figure 3.12. Left: ϵ_x with the proposed observer with 50% errors on L_q with a step on the d-axis current reference at $t = 0.05s$ and $t = 1.5s$. Right: real and estimated dq-axis currents for the same test

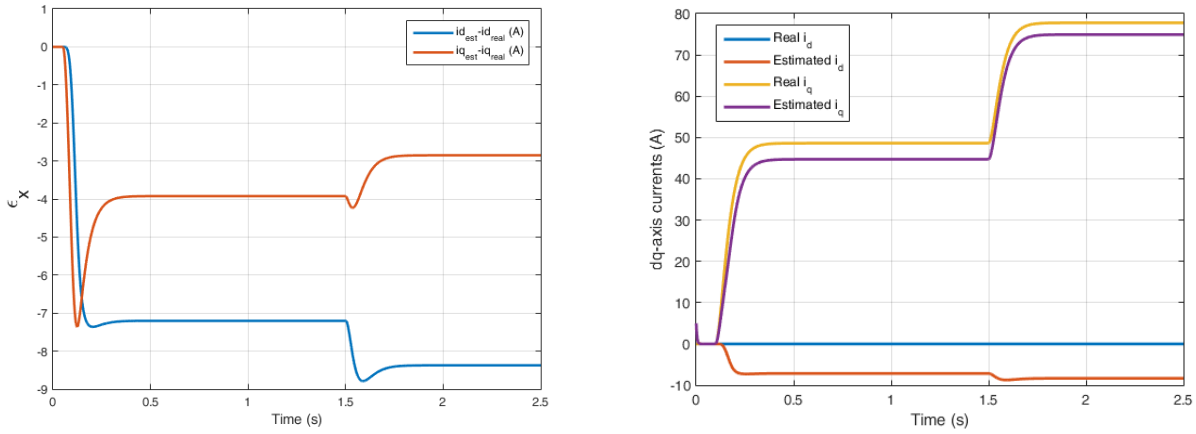

Figure 3.13. Left: ϵ_x with the proposed observer with 50% errors on R_s with a step on the q-axis current reference at $t = 0.05s$ and $t = 1.5s$. Right: same test with the real and estimated dq-axis currents displayed

in the observer state model. The errors indicated on this figure are very high compared to the errors induced by the other electrical parameters. The mutual inductance M is indeed extremely sensitive and errors on this parameter should be avoided as much as possible.

The errors located on the most sensitive electrical parameters have been presented and shown on simulation figures. However the errors on the mechanical parameters also need to be characterize. Indeed, the mechanical parameters f, corresponding to the fluid friction forces on the WRSM, and J corresponding to the mechanical inertia of the WRSM, are usually not known with precision. Moreover, if electrical parameters can be mapped (see chapter 2), the mechanical parameters are difficult to map since it depends on the weight of the vehicle the WRSM is mounted on (and thus depends on the number of passengers or the presence or not of luggage for example).

The following simulations will focus on the mechanical parameter errors. On the next simulation presented on figure 3.15, an error of 100% on the parameters f and J have been added. This large error can be justified by the fact that, as stated in the paragraph above, the mechanical parameters are poorly known and may vary a lot according to how the vehicle is used.

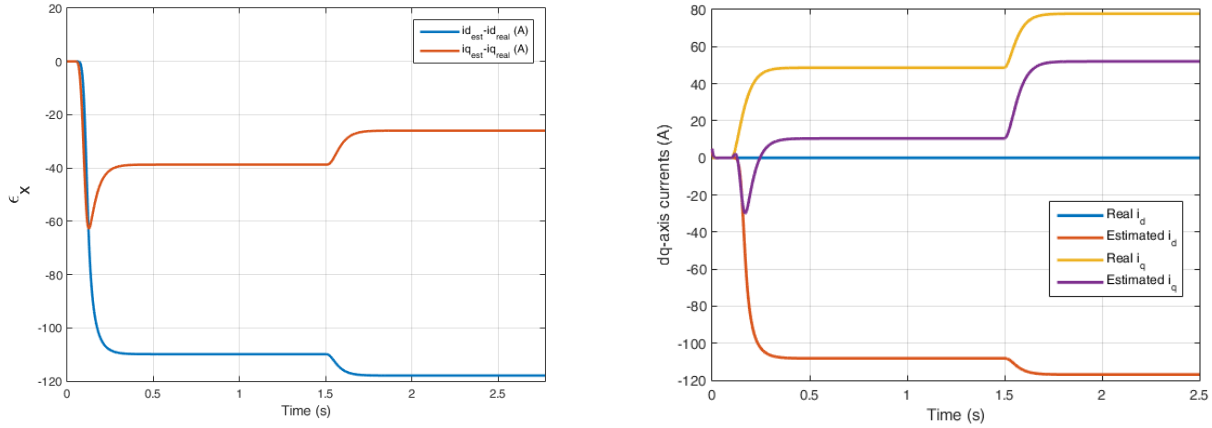

Figure 3.14. Left: ϵ_x with the proposed observer with 50% errors on M with a step on the q-axis current reference at $t = 0.05s$ and $t = 1.5s$. Right: same test with the real and estimated dq-axis currents displayed

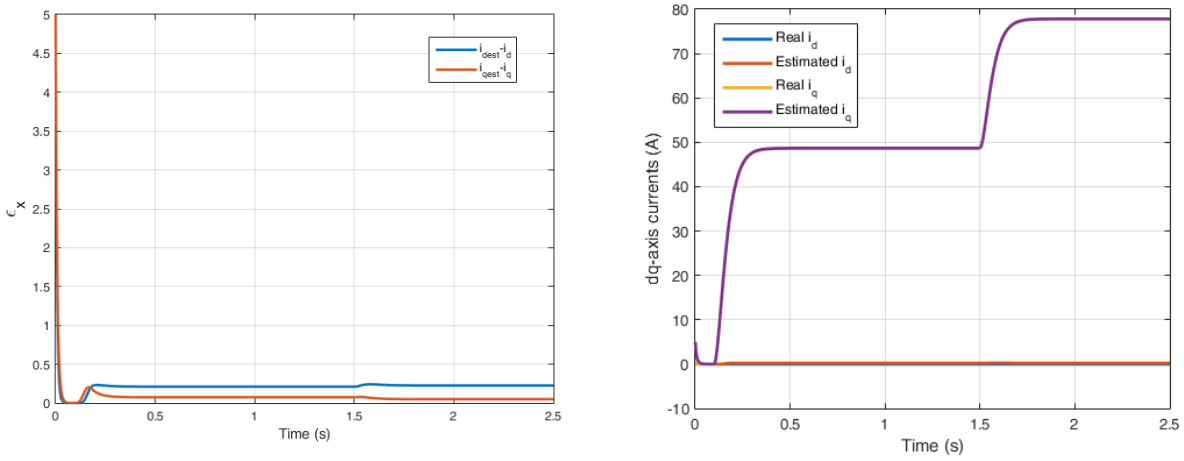

Figure 3.15. Left: ϵ_x with the proposed observer with 100% errors on the mechanical parameters J and f with a step on the q-axis current reference at $t = 0.05s$ and $t = 1.5s$. Right: same test with the real and estimated dq-axis currents displayed

From this simulation results, it can be concluded that the errors on the mechanical parameters induces a disparity between the real and the observed stator current, although this error is small: less than $0.1A$ for i_q and around $0.5A$ for i_d, which is small compared to the real currents in the stator of the WRSM.

The simulations made to test the proposed observer in optimal conditions (no error on the parameters) and in degraded conditions (errors on different parameters) showed that the errors on electrical parameters have a significant impact on the quality of the current estimation. The proposed observer on the other hand is less sensitive to errors on mechanical parameters.

These errors on estimation are obviously unwanted and must be avoided. In order to reduce the sensitivity induced by the parameter errors, an extension of this proposed observer has been developed and will be introduced in the next paragraph.

3.2.c The Extended Proposed Observer

With the proposed observer and the EKF observer, it has been shown in the previous chapters that both these observers are sensitive to parameter errors. In order to increase the robustness towards parameter errors in the system, an extension of the proposed observer introduced in the previous chapter has been developed and will be presented in this paragraph.

The principle of the extended observer is the same than the proposed observer, and its functioning is based on the analysis of a Lyapunov candidate function convergence. The difference with the proposed observer is that, instead of observing solely state variables (in our system the two stator currents), the extended observer is designed to observe also a set of parameters chosen in a way to absorb the parameter errors that exist between the real system and the state model used in the observer. This work has been published in [94]

The set of parameters chosen is the one described in the paragraph of the demonstration of observability in the equations 3.10 to 3.12. This set of parameter $x_p = \begin{bmatrix} I_p & \Delta\Gamma \end{bmatrix}^T$ has been designed in order to absorb the electrical parameters errors with I_p and the mechanical parameter errors with $\Delta\Gamma$.

The topology of this extended proposed observer is described by the following equations. If

the system can be put under the form:

$$\begin{cases} \dot{x} &= f_x(y,u) + g_1(y,u).x \\ \dot{y} &= f_y(y,u) + h_1(y,u).x + h_2(y,u).x_p \end{cases} \tag{3.48}$$

where y corresponds to the measured variables, x is the vector of the state variables to observe, x_p is the vector of parameters to observe and u represents the control vector. The nonlinear functions $f_x(y,u)$, $f_y(y,u)$, $g_1(y,u)$ and $h_1(y,u)$ are considered continuous and derivable at least one time, and are determinable thanks to the state-space model of the system.

Then the extended proposed observer is described by the following system of equations:

$$\begin{cases} \dot{\hat{x}} &= f_x(y,u) + g_1(y,u).\hat{x} - \eta_1(y,u).\epsilon_y \\ \dot{\hat{y}} &= f_y(y,u) + h_1(y,u).\hat{x} + h_2(y,u).\hat{x_p} - K.\epsilon_y \\ \dot{\hat{x_p}} &= -\eta_2(y,u).\epsilon_y \end{cases} \tag{3.49}$$

with $\hat{y}$ the estimation of the measured variables, $\hat{x}$ the observed unmeasured state variables and $\hat{x_p}$ the observed parameters. The term ϵ_y is the difference between the estimation of y and the measures of y, defined mathematically by $\epsilon_y = \hat{y} - y$. This variable is known. ϵ_x is the estimation of the error of observation of the state variables x. Similarly ϵ_p is introduced and represent the error of estimation of x_p. The constant matrix K and the functions $\eta_1(y,u)$ and $\eta_2(y,u)$ need to be designed in a way that the convergence of the observation is guaranteed.

The demonstration of convergence of this extended proposed observer relies on the same principles than for the standard proposed observer. The Lyapunov function V is introduced and is defined by:

$$V = \frac{1}{2}.\begin{bmatrix}\epsilon_x^T & \epsilon_y^T & \epsilon_p^T\end{bmatrix}.\begin{bmatrix}\epsilon_x \\ \epsilon_y \\ \epsilon_p\end{bmatrix} \tag{3.50}$$

Derivating V gives:

$$\dot{V} = \epsilon_x^T.\dot{\epsilon_x} + \epsilon_y^T.\dot{\epsilon_y} + \epsilon_p^T.\dot{\epsilon_p} \tag{3.51}$$

The error terms dynamics are written:

$$\begin{cases} \dot{\epsilon_x} &= \dot{\hat{x}} - \dot{x} \\ \dot{\epsilon_y} &= \dot{\hat{y}} - \dot{y} \\ \dot{\epsilon_p} &= \dot{\hat{x_p}} - \dot{x_p} \end{cases} \tag{3.52}$$

And from 3.48 and 3.49 it brings:

$$\begin{cases} \dot{\epsilon_x} &= g_1(y,u).\epsilon_x - \eta_1(y,u).\epsilon_y \\ \dot{\epsilon_y} &= h_1(y,u).\epsilon_x + h_2(y,u).\epsilon_p - K.\epsilon_y \\ \dot{\epsilon_p} &= -\eta_2(y,u).\epsilon_y \end{cases} \tag{3.53}$$

When replacing 3.53 in 3.51, we obtain:

$$\begin{aligned} \dot{V} &= \epsilon_x^T.(g_1(y,u).\epsilon_x - \eta_1(y,u).\epsilon_y) \\ &\quad +\epsilon_y^T.(h_1(y,u).\epsilon_x + h_2(y,u).\epsilon_p - K.\epsilon_y) \\ &\quad -\epsilon_p^T.\eta_2(y,u).\epsilon_y \end{aligned} \tag{3.54}$$

In a more intelligible form, 3.54 gives:

$$\begin{aligned} \dot{V} &= -\epsilon_y^T.K.\epsilon_y + \epsilon_x^T.g_1(y,u).\epsilon_x \\ &\quad +\epsilon_x^T.(-\eta_1(y,u).\epsilon_y) \\ &\quad +\epsilon_y^T.(h_1(y,u).\epsilon_x + h_2(y,u).\epsilon_p) \\ &\quad -\epsilon_p^T.\eta_2(y,u).\epsilon_y \end{aligned} \tag{3.55}$$

Finally, by choosing:

$$\begin{cases} \eta_1(y,u) &= h_1^T(y,u) \\ \eta_2(y,u) &= h_2^T(y,u) \end{cases} \tag{3.56}$$

Then $\dot{V}$ can be simply written:

$$\dot{V} = -\epsilon_y^T.K.\epsilon_y + \epsilon_x^T.g_1(y,u).\epsilon_x \tag{3.57}$$

From 3.57, and if the functions $\eta_1(y,u)$ and $\eta_2(y,u)$ are chosen as in 3.56, then the extended proposed observer converges exponentially if $\dot{V}$ is strictly negative, which means if K is defined positive and if $g_1(y,u)$ is Hurwitz. As for the standard proposed observer, K is chosen according to the dynamics of convergence needed, while $g_1(y,u)$ depends on the system.

Now that the stability of the extended proposed observer has been demonstrated, it can be applied to our system.

As stated in the beginning of this paragraph, the measured state variables corresponds now to $y = \begin{bmatrix} i_e \\ \Omega \\ V_{DC} \end{bmatrix}$, the observed state variables vector in output is $x = \begin{bmatrix} i_d \\ i_q \end{bmatrix}$ and the observed parameters vector is written $x_p = \begin{bmatrix} I_p \\ \Delta\Gamma \end{bmatrix}$.

Put under the form of 3.48, the model 3.10 can be written for the measured state variables vector y:

$$\begin{cases} \frac{d}{dt}i_e &= \frac{L_d}{L_d.L_e-M^2}\left(V_e - R_e.i_e - \frac{M}{L_d}.V_d\right) + \frac{M}{L_d.L_e-M^2}\left(R_s.i_d - p.\Omega.L_q.i_q\right) \\ \frac{d}{dt}\Omega &= \frac{1}{J}\left(-f.\Omega - \Gamma_0\right) + \frac{1}{J}.p.i_q.M.i_e - \frac{\Delta\Gamma}{J} \\ \frac{d}{dt}V_{DC} &= \frac{i_{bat}}{C_f} - \frac{V_d.i_d+V_q.i_q}{C_f.V_{DC}} - \frac{I_p}{C_f} \end{cases} \tag{3.58}$$

This gives:

$$\begin{bmatrix} \dot{i_e} \\ \dot{\Omega} \\ \dot{V_{DC}} \end{bmatrix} = \begin{bmatrix} \frac{L_d}{L_d.L_e-M^2}\left(V_e - R_e.i_e - \frac{M}{L_d}.V_d\right) \\ \frac{1}{J}\left(-f.\Omega - \Gamma_0\right) \\ \frac{i_{bat}}{C_f} \end{bmatrix} + \begin{bmatrix} \frac{M.R_s}{L_d.L_e-M^2} & \frac{M.p.\Omega.L_q}{L_d.L_e-M^2} \\ 0 & \frac{M.p.i_e}{J} \\ \frac{-V_d}{C_f.V_{DC}} & \frac{-V_q}{C_f.V_{DC}} \end{bmatrix} \cdot \begin{bmatrix} i_d \\ i_q \end{bmatrix} + \begin{bmatrix} 0 & 0 \\ 0 & \frac{-1}{J} \\ \frac{-1}{C_f} & 0 \end{bmatrix} \cdot \begin{bmatrix} I_p \\ \Delta\Gamma \end{bmatrix} \tag{3.59}$$

From 3.59, the functions $f_y(y,u)$, $h_1(y,u)$ and $h_2(y,u)$ can be deduced:

$$f_y(y,u) = \begin{bmatrix} \frac{L_d}{L_d.L_e-M^2}\left(V_e - R_e.i_e - \frac{M}{L_d}.V_d\right) \\ \frac{1}{J}\left(-f.\Omega - \Gamma_0\right) \\ \frac{i_{bat}}{C_f} \end{bmatrix} \tag{3.60}$$

$$h_1(y,u) = \begin{bmatrix} \frac{M.R_s}{L_d.L_e-M^2} & \frac{M.p.\Omega.L_q}{L_d.L_e-M^2} \\ 0 & \frac{M.p.i_e}{J} \\ \frac{-V_d}{C_f.V_{DC}} & \frac{-V_q}{C_f.V_{DC}} \end{bmatrix} \tag{3.61}$$

$$h_2(y,u) = \begin{bmatrix} 0 & 0 \\ 0 & \frac{-1}{J} \\ \frac{-1}{C_f} & 0 \end{bmatrix} \tag{3.62}$$

Proceeding the same way for the vector x gives:

$$\begin{bmatrix} \dot{i_d} \\ \dot{i_q} \end{bmatrix} = \begin{bmatrix} \frac{L_d}{L_d.L_e - M^2} \left(V_d - \frac{M}{L_d}.(V_e - R_e.i_e) \right) \\ \frac{1}{L_q} \left(V_q + p.\Omega.M.i_e \right) \end{bmatrix} + \begin{bmatrix} \frac{-L_e.R_s}{L_d.L_e - M^2} & \frac{L_e.p.\Omega.L_q}{L_d.L_e - M^2} \\ \frac{-p.\Omega.L_d}{L_q} & \frac{-R_s}{L_q} \end{bmatrix} . \begin{bmatrix} i_d \\ i_q \end{bmatrix} \tag{3.63}$$

And the functions $f_x(y,u)$, $g_1(y,u)$ can be deduced:

$$f_x(y,u) = \begin{bmatrix} \frac{L_d}{L_d.L_e - M^2} \left(V_d - \frac{M}{L_d}.(V_e - R_e.i_e) \right) \\ \frac{1}{L_q} \left(V_q + p.\Omega.M.i_e \right) \end{bmatrix} \tag{3.64}$$

$$g_1(y,u) = \begin{bmatrix} \frac{-L_e.R_s}{L_d.L_e - M^2} & \frac{L_e.p.\Omega.L_q}{L_d.L_e - M^2} \\ \frac{-p.\Omega.L_d}{L_q} & \frac{-R_s}{L_q} \end{bmatrix} \tag{3.65}$$

It can be noted that, in this particular configuration and due to how the parameters to observe have been chosen, the functions $f_x(y,u)$ and $g_1(y,u)$ are the same than for the standard proposed observer. The demonstration of $g_1(y,u)$ being Hurwitz is then the same than the demonstration done in the previous paragraph for $g(y,u)$.

This extended proposed observer has been tested in simulation too and compared to its "standard" version presented in the previous paragraph. The first simulations have been done with no error on the parameter in order to verify the convergence of observation of this extended observer. Similarly to the results of the simple proposed observer, the observation shows no error compared to the real currents.

A simulation has been conducted to test the convergence of observation of the two observed parameters Δ_Γ and I_p. To test this convergence these two parameters have been added in the model of the WRSM. At a given time, a step with a low-pass filter of Δ_Γ and I_p are imposed in the WRSM. The results shown in 3.16 prove that the observed vector x_p composed of Δ_Γ and I_p converges to the expected values. Indeed, in this simulation, a step from 0 to 5 N.m for Δ_Γ and from 0 to 3 A for I_p are added in the WRSM at $t = 0.4s$, and the observation of x_p converges to these values exactly.

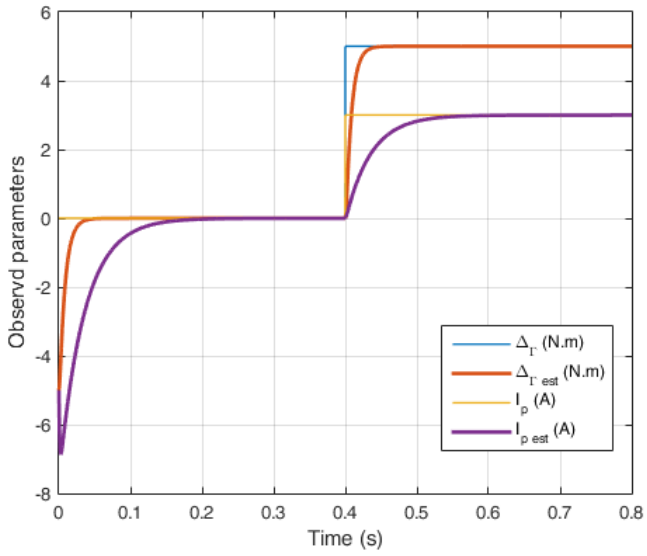

Figure 3.16. Evolution of y_p when a step on Δ_Γ and I_p are added in the WRSM at $t = 0.4s$

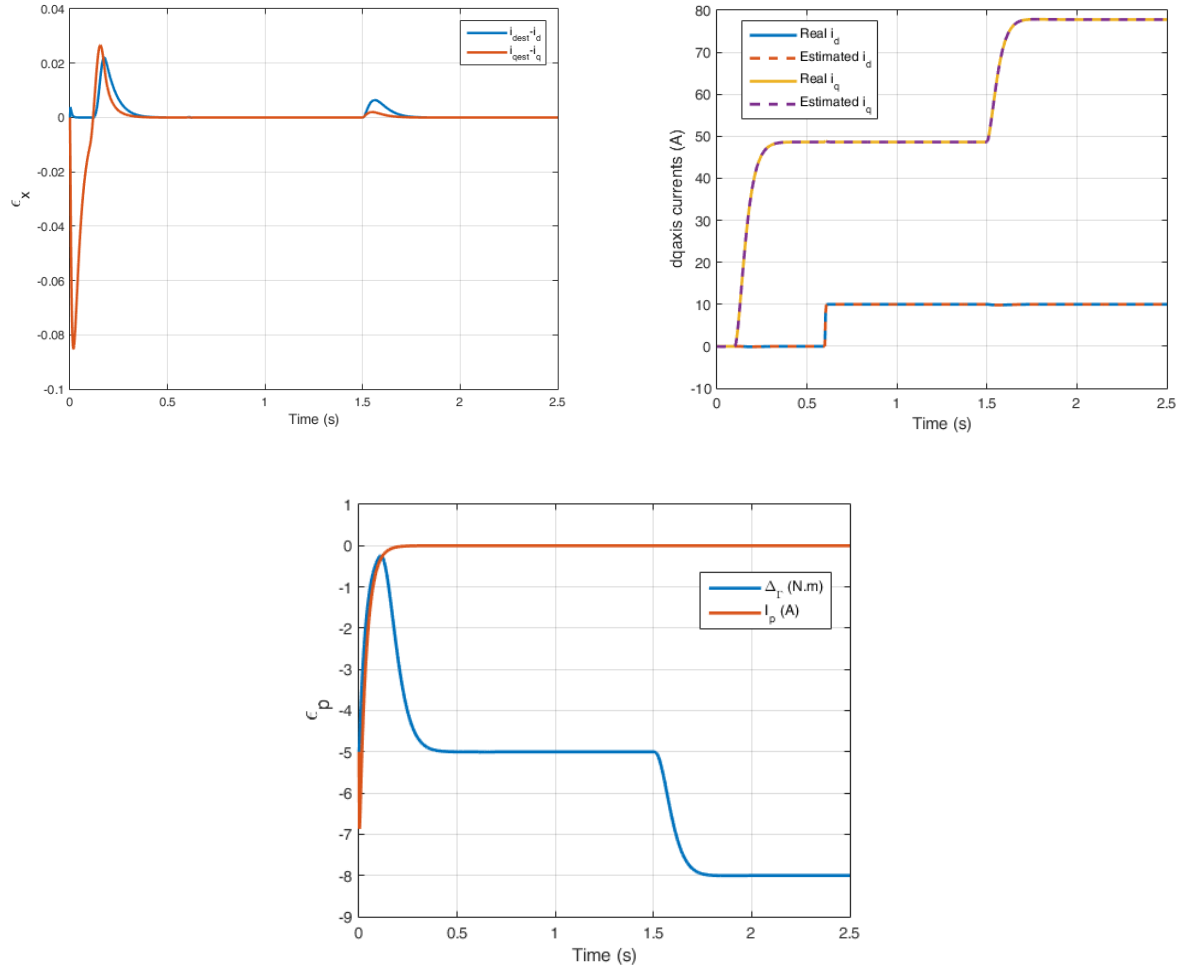

Figure 3.17. Top left: ϵ_x with the proposed observer with 100% errors on mechanical parameters with a step on the q-axis current reference at $t = 0.1s$ and $t = 1.5s$ and a step of 10A on the d-axis reference at $t = 0.6s$. Top right: same test with the real and estimated dq-axis currents displayed. Bottom: Evolution of ϵ_p during this test

Now we have checked that, with no error on the parameters, both the vector x and x_p converges to the expected values, the next simulation will focus on the observation with errors on the parameters included. Since the observed parameters of vector x_p are added to reduce the sensitivity of the errors of parameters, the observation of the stator currents is expected to be more precise.

When 100% errors are added on the mechanical parameters J and f, the errors are actually fully absorbed with the extended version of the proposed observer. The figure on the left of 3.17 shows the difference between the estimated and the real stator currents i_d and i_q. As for the previous simulations of the standard observer, at $t = 0.05s$ and $t = 1.5s$ there are steps on the reference of i_q in the controller. As it can be noted, the errors converges to 0 and the estimation gives precisely the values of the real currents. The bottom figure of 3.17 shows the evolution of x_p in the same simulation. As expected, only the parameter $\Delta\Gamma$ converges towards a value different from 0 since it is the parameter located on the mechanical equation of the system.

As for the proposed nonlinear observer, some errors on the electrical parameters have been added. The errors added are the same than for the proposed observer (50% on R_s, L_d and L_q). The results are shown on 3.18. As it can be noticed from this figure on the graph on the

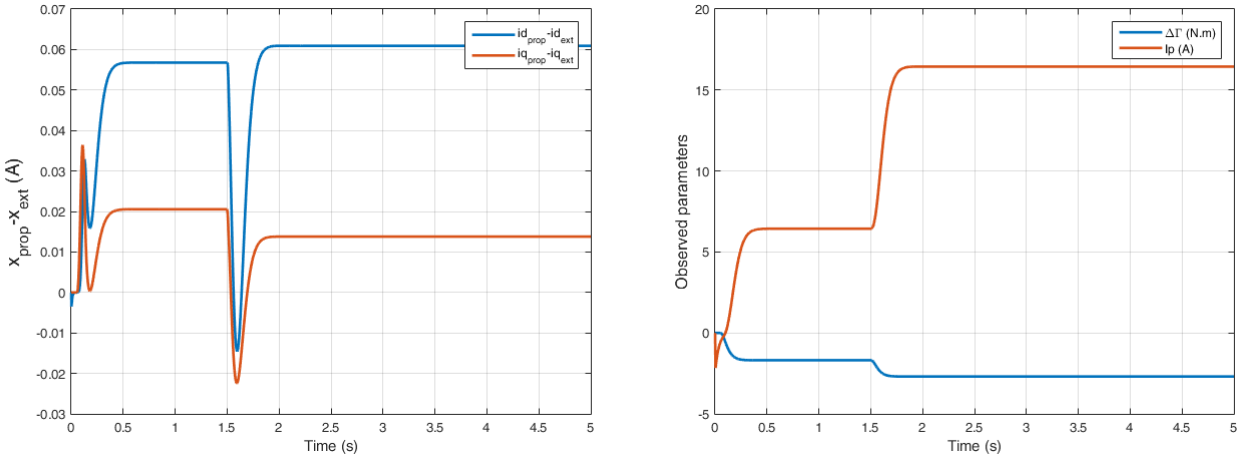

Figure 3.18. Left: Estimated currents differences between the extended and standard versions of the proposed observer with 50% errors on electric parameters with a step on the q-axis current reference at $t = 0.05s$ and $t = 1.5s$. Right: Evolution of the extended proposed observer estimation x_p for this test.

right, when errors are added on the electric parameters R_s, L_d and L_q, the estimated parameters $\Delta\Gamma$ and I_p change their value and converge towards a point different from 0. However, those two parameters are not sufficient and do not contain enough information to estimate the dq-axis currents without error. Indeed, as it can be seen on the graph on the left, the difference of estimation between the classic proposed observer and the extended one is extremely small and not significant when there are errors on the electric parameters, even with the added set of estimated parameters.

The extended proposed observer presented in this paragraph shows a slightly modified version of the classic proposed observer introduced earlier, with the adding of a vector of two parameters to estimate in order to reduce the sensitivity of the proposed observer towards parameter errors. The parameter $\Delta\Gamma$ added in the mechanical equation allows to suppress the sensitivity of the estimation towards mechanical parameter errors which is a great assert on a system where those parameters are not well known and may vary a lot, as it is occurring for a hybrid vehicle application. It remains however sensitive towards electric parameter errors, the parameter I_p added on the excitation current equation having a negligible impact on the estimation.

A timer has also been used in order to quantify the time needed to compute the estimation with the EKF and with the extended proposed state observer. Matlab's tool "tic" and "toc" is used to access the computation time with the EKF, and the average value obtained is compared to the average value obtained with the proposed observer in the same conditions. As it could have been expected because of the matrix inversions, it appears that the computation time of the EKF is two times larger than the computation time of the proposed observer. For this reason, and because the mechanical parameter errors are absorbed with the extended proposed state observer, this observer is the one that will be used in the experimental tests detailed in chapter 4.

3.3 A unified design of the current sensorless controller and the extended proposed observer (CSC-EO)

In the first section of this chapter, the reasons why nonlinear observers that can be integrated in an existing controller has been listed and justified. However, within the framework of this

study, other strategies of current sensorless control have been examined.

Indeed in some applications, it can be interesting to design the controller and the observer in the same time. In this section, a different control strategy from the ones described in the previous section will be presented and detailed. This strategy, unifying a current sensorless controller by including the extended proposed observer (CSC-EO), is similar to the proposed observer and its extended version, except it proposes to generate the control voltages V_d and V_q and to observe the currents simultaneously.

One of the main drawbacks concerning the EKF observer and two versions of the proposed observer described in the previous section, is that the control dynamics have to be slower than the dynamics of estimations, otherwise the observed currents feedback might not have been converging when compared for regulation. This results in a non optimal control of the state variables or even in a divergence of the controlled variables.

Taking this fact in account, it has been decided to extend once again the principle introduced with the proposed observer. In the current sensorless controller with included observer (CSC-EO), the principle of Lyapunov candidate function convergence analysis is still used as for the extended proposed observer with the addition of an output vector corresponding to the state variables that need to be controlled. The control vector u is then calculated, in the same calculus step than the observation. The aim of this strategy is to be able to raise the dynamics of the control. This work on this observer and controller topology has been presented in [95].

Let's consider a system described by a state model that can be written under the following form:

$$\begin{cases} \dot{x} &= g_0(y) + g_1(y).x + \sum_{j=1}^{n} \left(g_{3j}(y).x + g_{4j}(y)\right).u_j \\ \dot{y} &= h_0(y) + h_1(y).x + h_2(y).x_p + \sum_{j=1}^{n} \left(h_{3j}(y).x + h_{4j}(y)\right).u_j \end{cases} \tag{3.66}$$

with y the measured state variables, x the observed state variables, x_p the observed parameters and u_j ($1 \leq j \leq n$ with $n \subset \mathbb{N}^*$ corresponding to the number of controlled state variables). The functions $g_k(y)$ and $h_k(y)$ ($0 \leq k \leq 2$) and g_{3j}, g_{4j}, h_{3j} and h_{4j} ($0 < j \leq n$) are derivable and defined by the system considered.

The vector y_{out} is also introduced. It corresponds to the controlled state variables of the system and it is defined by $y_{out} = f(x, y, x_p)$, the function $f(x, y, x_p)$ being given by the state model equations of the system.

Then the CSC-EO can be defined by the following system of equation:

$$\begin{cases} \dot{\hat{x}} &= g_0(y) + g_1(y).\hat{x} + \sum_{j=1}^{n} \left(g_{3j}(y).\hat{x} + g_{4j}(y)\right).u_j - \eta_1(y).\epsilon_y - \eta_x \\ \dot{\hat{y}} &= h_0(y) + h_1(y).\hat{x} + h_2(y).\hat{x_p} + \sum_{j=1}^{n} \left(h_{3j}(y).\hat{x} + h_{4j}(y)\right).u_j - K.\epsilon_y - \eta_y \\ \dot{\hat{x_p}} &= -\eta_2(y).\epsilon_y \end{cases} \tag{3.67}$$

with $\hat{y}$ the estimation of the measured variables, $\hat{x}$ the observed unmeasured state variables and $\hat{x_p}$ the observed parameters. The term ϵ_y is the difference between the estimation of y and the measures of y, defined mathematically by $\epsilon_y = \hat{y} - y$. This variable is known. ϵ_x is the estimation of the error of observation of the state variables x. Similarly ϵ_p is introduced and represent the error of estimation of x_p. The constant matrix K and the functions $\eta_1(y)$, $\eta_2(y)$, η_x and η_y need to be designed in a way that the convergence of the observation is guaranteed.

In addition, the observation of y_{out} is written $\hat{y_{out}} = f(\hat{x}, \hat{y}, \hat{x_p})$ and thus leads to:

$$\dot{\hat{y_{out}}} = \frac{\partial f}{\partial \hat{x}}.\dot{\hat{x}} + \frac{\partial f}{\partial \hat{y}}.\dot{\hat{y}} + \frac{\partial f}{\partial \hat{x_p}}.\dot{\hat{x_p}} \tag{3.68}$$

Before going any further, let's also introduce $\epsilon_{out} = \hat{y_{out}} - y_{out}$ the estimation of the error on the controlled state variables. It will be needed for the demonstration of Lyapunov convergence.

As for the standard and extended proposed observers, the CSC-EO's convergence is based on a Lyapunov function. The Lyapunov function that has been chosen is written:

$$V = \frac{1}{2}.\begin{bmatrix}\epsilon_x^T & \epsilon_y^T & \epsilon_p^T & \epsilon_{out}^T\end{bmatrix}.\begin{bmatrix}\epsilon_x \\ \epsilon_y \\ \epsilon_p \\ \epsilon_{out}\end{bmatrix} \tag{3.69}$$

By derivating 3.69 we obtain:

$$\dot{V} = \epsilon_x^T.\dot{\epsilon_x} + \epsilon_y^T.\dot{\epsilon_y} + \epsilon_p^T.\dot{\epsilon_p} + \epsilon_{out}^T.\dot{\epsilon_{out}} \tag{3.70}$$

The error terms dynamics are written:

$$\begin{cases} \dot{\epsilon_x} = \dot{\hat{x}} - \dot{x} & = & g_1(y).\epsilon_x + \sum_{j=1}^{n} g_{3j}.\epsilon_x.u_j - \eta_1(y).\epsilon_y - \eta_x \\ \dot{\epsilon_y} = \dot{\hat{y}} - \dot{y} & = & h_1(y).\epsilon_x + h_2(y).\epsilon_p + \sum_{j=1}^{n} h_{3j}.\epsilon_x.u_j - K.\epsilon_y - \eta_y \\ \dot{\epsilon_p} = \dot{\hat{x_p}} - \dot{x_p} & = & -\eta_2(y).\epsilon_y \\ \dot{\epsilon_{out}} = \dot{y_{out}} - \dot{y_{out}} & = & \dot{y_{out}} \end{cases} \tag{3.71}$$

When replacing 3.71 in 3.70, we obtain:

$$\begin{aligned} \dot{V} \;=\; & \epsilon_x^T.\left(g_1(y).\epsilon_x + \sum_{j=1}^{n} g_{3j}.\epsilon_x.u_j - \eta_1(y).\epsilon_y - \eta_x\right) \\ & +\epsilon_y^T.\left(h_1(y).\epsilon_x + h_2(y).\epsilon_p + \sum_{j=1}^{n} h_{3j}.\epsilon_x.u_j - K.\epsilon_y - \eta_y\right) \\ & +\epsilon_p^T.(-\eta_2(y).\epsilon_y) \\ & +\epsilon_{out}^T.\dot{y_{out}} \end{aligned} \tag{3.72}$$

Finally when putting the quadratic terms together, the following form is obtained:

$$\begin{aligned} \dot{V} \;=\; & -\epsilon_y^T.K.\epsilon_y + \epsilon_x^T.g_1(y).\epsilon_x + \epsilon_{out}^T.\dot{y_{out}} \\ & +\epsilon_x^T.\left(-\eta_1(y).\epsilon_y + \sum_{j=1}^{n} g_{3j}.\epsilon_x.u_j - \eta_x\right) \\ & +\epsilon_y^T.\left(h_1(y).\epsilon_x + h_2(y).\epsilon_p + \sum_{j=1}^{n} h_{3j}.\epsilon_x.u_j - \eta_y\right) \\ & +\epsilon_p^T.(-\eta_2(y).\epsilon_y) \end{aligned} \tag{3.73}$$

With the same methodology than for the previous proposed observers, it is possible to obtain only quadratic terms by choosing:

$$\begin{cases} \eta_1(y) & = & h_1^T(y) \\ \eta_2(y) & = & h_2^T(y) \\ \eta_x & = & \sum_{j=1}^{n} g_{3j}.\epsilon_x.u_j \\ \eta_y & = & \sum_{j=1}^{n} h_{3j}.\epsilon_x.u_j \\ \dot{y_{out}} & = & -K_2.\epsilon_{out} \end{cases} \tag{3.74}$$

If the conditions of 3.74 are respected, then:

$$\dot{V} = -\epsilon_y^T.K.\epsilon_y + \epsilon_x^T.g_1(y).\epsilon_x - \epsilon_{out}^T.K_2.\epsilon_{out} \tag{3.75}$$

From 3.75, it can be concluded that if K and K_2 are strictly positive matrix and if $g_1(y)$ is Hurwitz, then the observation is stable in the sens of Lyapunov and converges asymptotically.

Now that the convergence of the observation has been demonstrated, the last step of calculation of the CSC-EO is to define the control vector $u = \begin{bmatrix}u_1 & u_2 & ... & u_n\end{bmatrix}^T$. If we take a look at

3.74, we see that we chose $\dot{y_{out}} = -K_2.\epsilon_{out}$ in order to keep a quadratic form for the controlled variables. If 3.74 is injected in 3.68, it brings:

$$-K_2.\epsilon_{out} = \frac{\partial f}{\partial \hat{x}}.\dot{\hat{x}} + \frac{\partial f}{\partial \hat{y}}.\dot{\hat{y}} + \frac{\partial f}{\partial \hat{x_p}}.\dot{\hat{x_p}} \tag{3.76}$$

Let's replace the terms $\dot{\hat{x}}$, $\dot{\hat{y}}$ and $\dot{\hat{x_p}}$ in 3.76 by the ones in 3.67. This leads to the following equation:

$$\begin{array}{rcl} -K_2.\epsilon_{out} & = & \frac{\partial f}{\partial \hat{x}}.\left(g_0(y) + g_1(y).\hat{x} + \sum_{j=1}^{n}\left(g_{3j}(y).\hat{x} + g_{4j}(y)\right).u_j - \eta_1(y).\epsilon_y - \eta_x\right) \\ & & + \frac{\partial f}{\partial \hat{y}}.\left(h_0(y) + h_1(y).\hat{x} + h_2(y).\hat{x_p} + \sum_{j=1}^{n}\left(h_{3j}(y).\hat{x} + h_{4j}(y)\right).u_j - K.\epsilon_y - \eta_y\right) \\ & & + \frac{\partial f}{\partial \hat{x_p}}.\left(-\eta_2(y).\epsilon_y\right) \end{array} \tag{3.77}$$

When isolating the terms with the u_j in it, it gives:

$$\begin{array}{l} \frac{\partial f}{\partial \hat{x}}.\sum_{j=1}^{n}\left(g_{3j}(y).(\hat{x} - \epsilon_x) + g_{4j}(y)\right).u_j + \frac{\partial f}{\partial \hat{y}}.\sum_{j=1}^{n}\left(h_{3j}(y).(\hat{x} - \epsilon_x) + h_{4j}(y)\right).u_j \\ = -K_2.\epsilon_{out} + \frac{\partial f}{\partial \hat{x}}.\left(g_0(y) + g_1(y).\hat{x} - \eta_1(y).\epsilon_y\right) \\ + \frac{\partial f}{\partial \hat{y}}.\left(h_0(y) + h_1(y).\hat{x} + h_2(y).\hat{x_p} - K.\epsilon_y\right) \\ + \frac{\partial f}{\partial \hat{x_p}}.\left(-\eta_2(y).\epsilon_y\right) \end{array} \tag{3.78}$$

From 3.78, it is possible to simplify greatly this equation and write directly:

$$E.u = U \tag{3.79}$$

With E a non-singular matrix deduced from 3.78 and U the right term of equation 3.78 made explicit in the following equation:

$$\begin{array}{rcl} U & = & -K_2.\epsilon_{out} + \frac{\partial f}{\partial \hat{x}}.\left(g_0(y) + g_1(y).\hat{x} - \eta_1(y).\epsilon_y\right) \\ & & + \frac{\partial f}{\partial \hat{y}}.\left(h_0(y) + h_1(y).\hat{x} + h_2(y).\hat{x_p} - K.\epsilon_y\right) \\ & & + \frac{\partial f}{\partial \hat{x_p}}.\left(-\eta_2(y).\epsilon_y\right) \end{array} \tag{3.80}$$

Finally the control vector u is obtained by solving the equation $u = E^{-1}.U$.

It is important to notice that, at this point, the exponential convergence of the observation in the sens of Lyapunov has been demonstrated as well as the stability of the control of the system with the state variables of y_{out}. Logically, the following paragraphs will focus on the application of this new controller with included observer on the system with the WRSM described in 3.10.

In our application, the vectors x, y, y_p are the same than for the extended proposed observer and correspond to $y = \begin{bmatrix} i_e \\ \Omega \\ V_{DC} \end{bmatrix}$, $x = \begin{bmatrix} i_d \\ i_q \end{bmatrix}$ and $x_p = \begin{bmatrix} I_p \\ \Delta\Gamma \end{bmatrix}$. Concerning the controlled variables, it has been chosen for the study of this controller with observer included to control the two stator currents i_d and i_q (that are also the observed state variables) and the excitation current in the rotor i_e.This gives: $y_{out} = \begin{bmatrix} i_d \\ i_q \\ i_e \end{bmatrix}$. Consequently, the control vector u corresponds to $u = \begin{bmatrix} V_d \\ V_q \\ V_e \end{bmatrix}$

If we put the system of equation 3.10 into the same form than 3.66, this brings for the vector y:

$$\begin{cases} \frac{d}{dt}i_e & = & \frac{-L_d.R_e}{L_d.L_e-M^2}.i_e + \frac{M}{L_d.L_e-M^2}\left(R_s.i_d - p.\Omega.L_q.i_q\right) + \frac{-M}{L_d.L_e-M^2}.V_d + \frac{L_d}{L_d.L_e-M^2}.V_e \\ \frac{d}{dt}\Omega & = & \frac{1}{J}\left(-f.\Omega - \Gamma_0\right) + \frac{1}{J}.p.i_q\left(\left(L_d - L_q\right).i_d + M.i_e\right) - \frac{\Delta\Gamma}{J} \\ \frac{d}{dt}V_{DC} & = & \frac{i_{bat}}{C_f} - \frac{I_p}{C_f} - \frac{i_d}{C_f.V_{DC}}.V_d - \frac{i_q}{C_f.V_{DC}}.V_q \end{cases} \tag{3.81}$$

By considering the term $\left(\left(L_d - L_q\right).i_d\right.$ negligible, 3.81 leads to:

$$\begin{bmatrix} \dot{i}_e \\ \dot{\Omega} \\ \dot{V}_{DC} \end{bmatrix} = \begin{bmatrix} \frac{-L_d.R_e}{L_d.L_e-M^2} \\ \frac{1}{J}\left(-f.\Omega - \Gamma_0\right) \\ \frac{i_{bat}}{C_f} \end{bmatrix} + \begin{bmatrix} \frac{M.R_s}{L_d.L_e-M^2} & \frac{M.p.\Omega.L_q}{L_d.L_e-M^2} \\ 0 & \frac{M.p.i_e}{J} \\ 0 & 0 \end{bmatrix} \cdot \begin{bmatrix} i_d \\ i_q \end{bmatrix} + \begin{bmatrix} 0 & 0 \\ 0 & \frac{-1}{J} \\ \frac{-1}{C_f} & 0 \end{bmatrix} \cdot \begin{bmatrix} I_p \\ \Delta\Gamma \end{bmatrix}$$
$$+ \left(\begin{bmatrix} \frac{-M}{L_d.L_e-M^2} \\ 0 \\ 0 \end{bmatrix} + \begin{bmatrix} 0 & 0 \\ 0 & 0 \\ \frac{-1}{C_f.V_{DC}} & 0 \end{bmatrix} \cdot \begin{bmatrix} i_d \\ i_q \end{bmatrix} \right).V_d + \begin{bmatrix} 0 & 0 \\ 0 & 0 \\ 0 & \frac{-1}{C_f.V_{DC}} \end{bmatrix} \cdot \begin{bmatrix} i_d \\ i_q \end{bmatrix}.V_q + \begin{bmatrix} \frac{L_d}{L_d.L_e-M^2} \\ 0 \\ 0 \end{bmatrix}.V_e \tag{3.82}$$

With 3.82, the formulation seen in 3.66 is more easily recognizable. The same procedure is applied to the vector x:

$$\begin{bmatrix} \dot{i}_d \\ \dot{i}_q \end{bmatrix} = \begin{bmatrix} \frac{M.R_e}{L_d.L_e-M^2}.i_e \\ \frac{p.\Omega.M.i_e}{L_q} \end{bmatrix} + \begin{bmatrix} \frac{-L_e.R_s}{L_d.L_e-M^2} & \frac{L_e.p.\Omega.L_q}{L_d.L_e-M^2} \\ \frac{-p.\Omega.L_d}{L_q} & \frac{-R_s}{L_q} \end{bmatrix} \cdot \begin{bmatrix} i_d \\ i_q \end{bmatrix}$$
$$+ \begin{bmatrix} \frac{L_d}{L_d.L_e-M^2} \\ 0 \end{bmatrix}.V_d + \begin{bmatrix} 0 \\ \frac{1}{L_q} \end{bmatrix}.V_q + \begin{bmatrix} \frac{M}{L_d.L_e-M^2} \\ 0 \end{bmatrix}.V_e \tag{3.83}$$

From equations 3.82 and 3.83, it is possible to identify the functions of the canonical form of the CSC-EO given in 3.67. For the functions linked to the vector of measured state variables y, the identification gives:

$$h_0(y) = \begin{bmatrix} \frac{-L_d.R_e}{L_d.L_e-M^2} \\ \frac{1}{J}\left(-f.\Omega - \Gamma_0\right) \\ \frac{i_{bat}}{C_f} \end{bmatrix} \qquad h_1(y) = \begin{bmatrix} \frac{M.R_s}{L_d.L_e-M^2} & \frac{M.p.\Omega.L_q}{L_d.L_e-M^2} \\ 0 & \frac{M.p.i_e}{J} \\ 0 & 0 \end{bmatrix} \qquad h_2(y) = \begin{bmatrix} 0 & 0 \\ 0 & \frac{-1}{J} \\ \frac{-1}{C_f} & 0 \end{bmatrix}$$

$$h_{31}(y) = \begin{bmatrix} 0 & 0 \\ 0 & 0 \\ \frac{-1}{C_f.V_{DC}} & 0 \end{bmatrix} \quad h_{41}(y) = \begin{bmatrix} \frac{-M}{L_d.L_e-M^2} \\ 0 \\ 0 \end{bmatrix} \quad h_{32}(y) = \begin{bmatrix} 0 & 0 \\ 0 & 0 \\ 0 & \frac{-1}{C_f.V_{DC}} \end{bmatrix} \quad h_{43} = \begin{bmatrix} \frac{L_d}{L_d.L_e-M^2} \\ 0 \\ 0 \end{bmatrix}$$

For the identification of the functions linked to the unmeasured observed state variables x, the procedure is the same than for y and the following equations give the results of identification:

$$g_0(y) = \begin{bmatrix} \frac{M.R_e}{L_d.L_e-M^2}.i_e \\ \frac{p.\Omega.M.i_e}{L_q} \end{bmatrix} \qquad g_1(y) = \begin{bmatrix} \frac{-L_e.R_s}{L_d.L_e-M^2} & \frac{L_e.p.\Omega.L_q}{L_d.L_e-M^2} \\ \frac{-p.\Omega.L_d}{L_q} & \frac{-R_s}{L_q} \end{bmatrix}$$

$$g_{41}(y) = \begin{bmatrix} \frac{L_d}{L_d.L_e-M^2} \\ 0 \end{bmatrix} \qquad g_{42}(y) = \begin{bmatrix} 0 \\ \frac{1}{L_q} \end{bmatrix} \qquad g_{43}(y) = \begin{bmatrix} \frac{M}{L_d.L_e-M^2} \\ 0 \end{bmatrix}$$

The last identification to conduct in order to complete the application of the CSC-EO to our system is the equation describing y_{out} given its theoretical form in 3.68. We saw that

$\hat{y_{out}} = f(\hat{x}, \hat{y}, \hat{x_p})$ so here it simply leads to:

$$\hat{y_{out}} = \begin{bmatrix} 0 & 0 & 0 \\ 0 & 0 & 0 \\ 1 & 0 & 0 \end{bmatrix} .\hat{y} + \begin{bmatrix} 1 & 0 \\ 0 & 1 \\ 0 & 0 \end{bmatrix} .\hat{x} \tag{3.84}$$

And then for the equation 3.68 the identification gives:

$$\frac{\partial f}{\partial \hat{y}} = \begin{bmatrix} 0 & 0 & 0 \\ 0 & 0 & 0 \\ 1 & 0 & 0 \end{bmatrix} \qquad \frac{\partial f}{\partial \hat{x}} = \begin{bmatrix} 1 & 0 \\ 0 & 1 \\ 0 & 0 \end{bmatrix} \qquad \frac{\partial f}{\partial \hat{x_p}} = 0$$

It is now possible to characterize all the terms needed in the system of equation 3.74 that are involved in the observer part of the CSC-EO described in the system 3.67, and also to retrieve the terms E and U from equation 3.79 for the control of the vector y_{out}.

All the correction terms for the observation added in the definition of the CSC-EO in the system of equation 3.67 are set by the equations of the system as stated in the conditions of 3.74. The constants K and K_2 are set by the user according to the specifications needed. K will fix the dynamics of convergence of the measured state variables in the observation part of the CSC-EO, and K_2 will set the dynamics of convergence of the controlled variables towards their reference values. The rest of the dynamics are dependent on the nature of the system. Indeed it can be seen on equation 3.75, the dynamics of convergence of the observed variables x is set by the matrix $g_1(y)$ which depends on the system equations.

As for the proposed observer and its extension the matrix K can be chosen diagonal, and the diagonal terms can be weighted if a different dynamic of convergence for the measured state

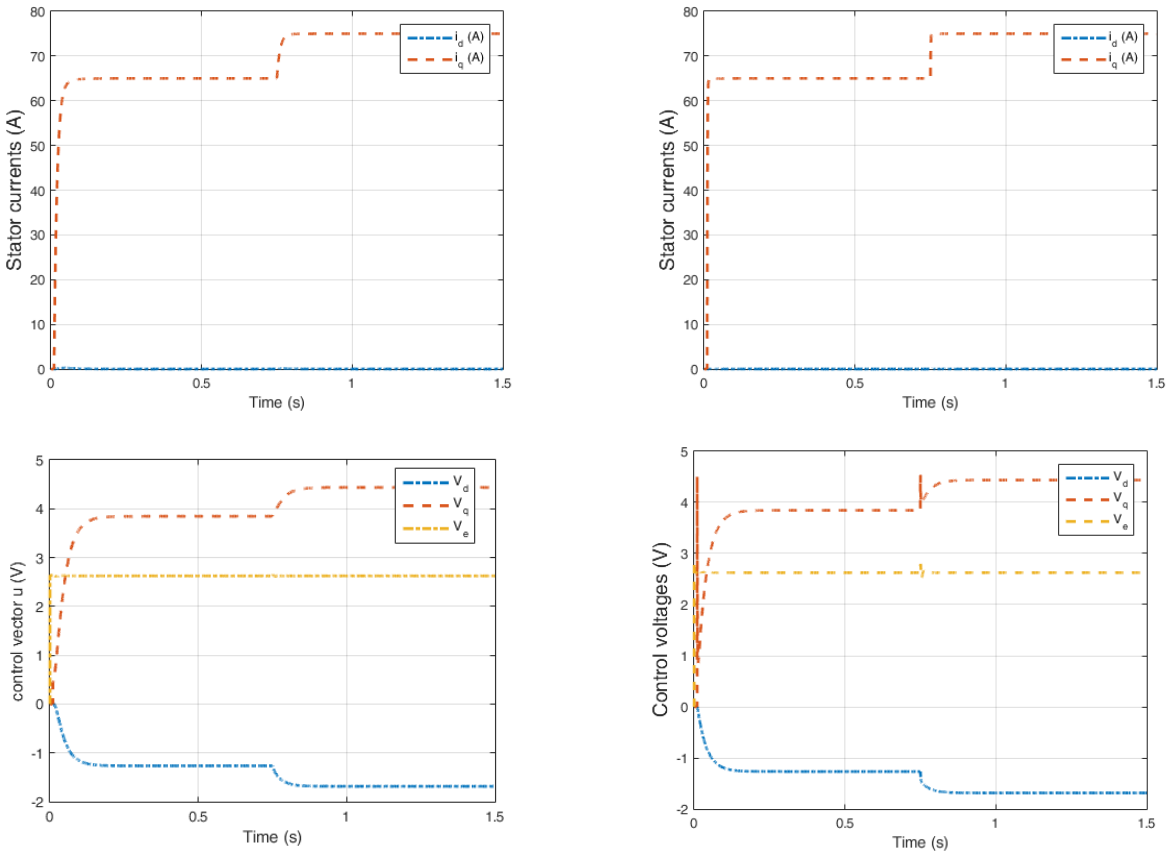

Figure 3.19. Estimated currents evolution (top) and computed voltages (bottom) with $K_2 = 100.I_3$ on the left and $K_2 = 1000.I_3$ on the right with no parameter error.

variables is wanted. The way to choose K_2 is similar: a diagonal matrix with the diagonal terms weighted according to the speed of convergence of the variables of the vector y_{out} towards the reference set by user. A simulation without parameter errors have been run for two different values of K_2. The results are displayed on figure 3.19.

On figure 3.19, two similar tests are run with two different values for the diagonal matrix K_2. The first test shows a reference step on the q axis current from 0A to 65A and a second one from 65A to 75A. The d-axis current reference is kept at 0A. The matrix K_2 chosen for this test is diagonal such as $K_2 = 100.I_3$ with I_3 the identity matrix of order 3. The second test is the same but with $K_2 = 1000.I_3$.

From those two tests, the influence of the value of K_2 can easily be noticed. Indeed, in the second test where K_2 is ten times higher than in the first one, the converging time of the state vector x is shorter. According to the application and the needs imposed by the specifications, this controller is extremely useful regarding the possibility to easily increase or decrease the dynamics of estimation by changing the matrix K_2.

It can be seen from the previous tests that the CSC-EO converges towards the reference values when no errors are added on the parameter of the system. On figure 3.20, a test with 100% error on the mechanical parameters J and f is performed. On the top figure the dq-axis currents are displayed. At the start of the simulation, a step on the q-axis reference current is imposed from 0A to 65A. A second step from 65A to 125A occurs at 0.8s. As it can be seen, the currents are precisely estimated and are the same than the real currents. On the bottom graph of figure 3.20, the evolution on the estimated parameters $\Delta\Gamma$ and I_p are displayed. Their evolution are similar than for the extended proposed observer presented earlier and they absorb the mechanical parameter errors added in the model of the system.

However, as it is the case for every observer presented in this work, the CSC-EO is still sensitive to errors on the electric parameters. Figure 3.21 displays the evolution of the estimated and the real dq-axis currents in the same conditions than for figure 3.20 but with 50% error

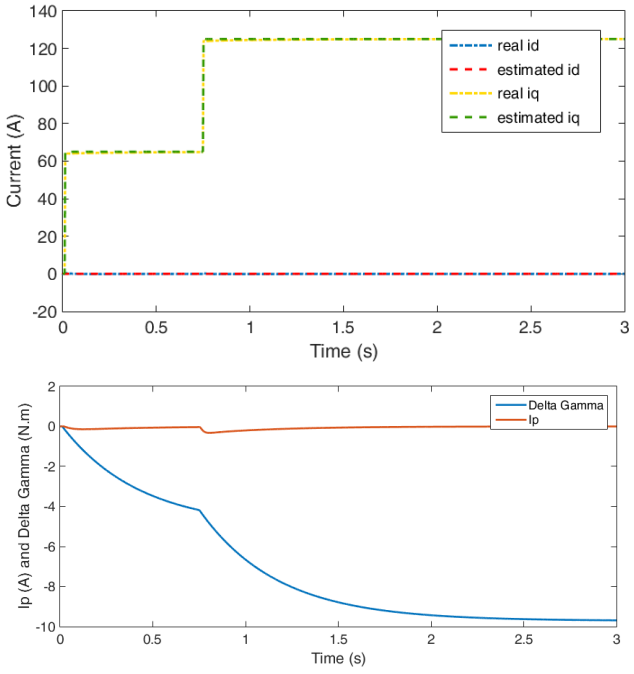

Figure 3.20. Evolution of the vector y (top) and y_p (bottom) for two reference i_q steps with 100% error added on the mechanical parameters J and f.

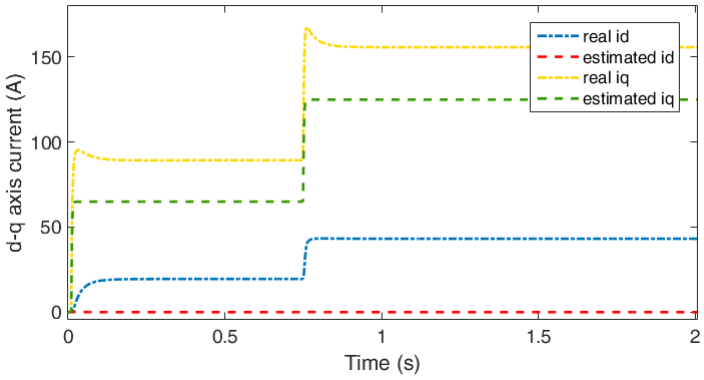

Figure 3.21. Evolution of the vector y for two reference i_q steps with 50% error added on the electrical parameters

added on the electric parameters R_s, L_d and L_q.

A comparison study has been run between the CSC-EO and a solution combining an observation of state variables with the EKF and a control of those state variables with a PI controller. In order to perform a proper comparison, both the dynamics of the CSC-EO and the EKF + PI solution have been optimized so that the convergence towards the steady state is as fast as possible. Figure 3.22 show the evolution of i_d and i_q for both strategy when a reference step from 0A to 50A is imposed at $t = 0.01s$ and from 50A to 80A at $t = 0.75s$. In this test, no parameter errors are added. Both current sensorless solutions converge towards the expected values which could be expected since there is no error in the model of the machine. However, the CSC-EO converges much faster than the EKF + PI solution. Indeed from the two graphs, it can be measured that the CSC-EO reaches 90% of the final value in less than 1ms while it takes 20ms for the EKF + PI for the q-axis current and the d-axis current. In addition, the EKF + PI features overshoots on the two currents that are not present for the CSC-EO.

Another similar comparison has been run when 100% of error are added on the mechanical parameters. The results are displayed on figure 3.23. Since the EKF does not includes the observation of the parameter vector $x_p = \begin{bmatrix} \Delta\Gamma \\ I_p \end{bmatrix}$, this solution converges but towards a different

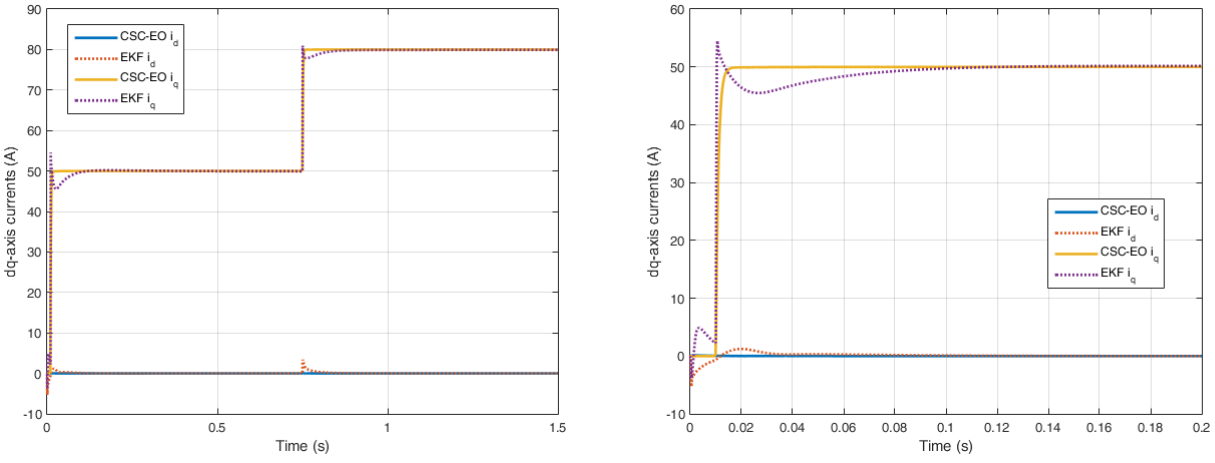

Figure 3.22. Performance comparison between the CSC-EO and the EKF + PI solution with no parameter error

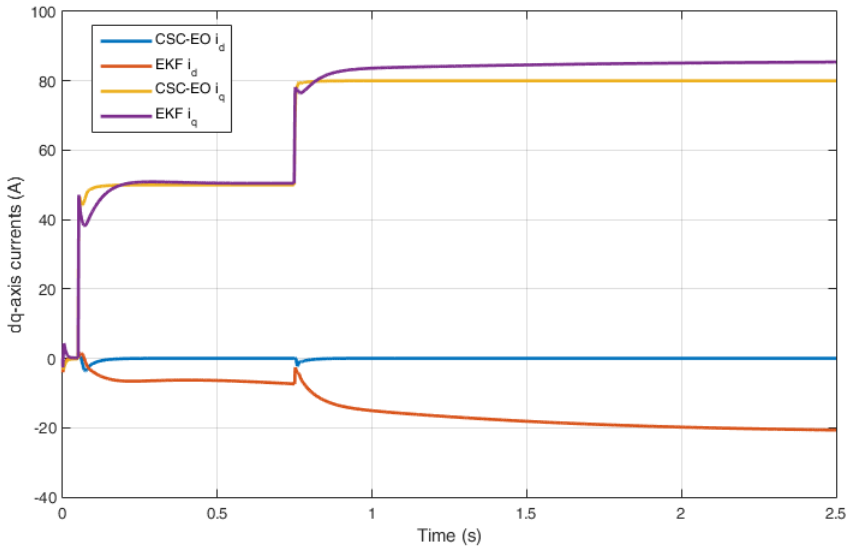

Figure 3.23. Performance comparison between the CSC-EO and the EKF + PI solution with 100% error on the mechanical parameters

value than the currents in the machine, while the CSC-EO converges towards the proper values as it was already the case on figure 3.20.

The CSC-EO is a very interesting tool since it allows to generate the control voltages in the same loop than the observation of the state variables. The observer topology of the CSC-EO being the same than for the proposed observer and the extended proposed observer, the results of observation are similar. However, including the control voltages in the observation loop allows to accelerate the time required for the state variables to converge, as it can be seen from the comparison between the CSC-EO and a PI controller combined with the EKF for the current observation. The CSC-EO, despite its different topology, remains sensitive to the same parameters than the extended proposed observer, most precisely the electric parameters R_s, L_d, L_q and the mutual inductance M.

Conclusion

The study realized in this chapter focused on developing state observers for the stator currents estimation. Indeed, one of the main decision made in this thesis concerning the different possible paths to achieve current sensorless control of the WRSM was to privilege the dq-currents estimation in order to use them in a vector control such as a MTPA controller. Since vector control requires the currents feedback for their regulation, an state observer is needed to retrieve the currents in a current sensorless application. However, before starting developing state observers, the proof of observability needed to be demonstrated. The observability study showed that the stator currents i_d and i_q are observable using the measurements of i_e, Ω and their derivates.

The first state observer that has been developed is the Extended Kalman Filter. The EKF was a natural first choice since it is a commonly used tool in the automation field for state variable observation and measurement noises rejection. The EKF principle relies on two steps: first a prediction step, relying on the model of the system and secondly an update step, using the error between the values of i_e and Ω obtained in the prediction step and their measurements. The simulation results shows that without parameter errors in the observer model, the current

estimation is precise. According to the values of the covariance matrix, the convergence can be fast but the measurement noise is not rejected, or the noise is rejected but but the observation takes a longer time to reach the real values.

Another kind of observer has been tested on the current estimation. Relying on the system model, it is based on a convergence analysis using a Lyapunov candidate function. With this state observer, the dynamic of convergence of the estimation towards the real values are induced by the system modeling. Only the speed of convergence of the measured variables can be chosen. The convergence of the currents is however proven to converge exponentially as long as i_e is non null. The results with and without parameter errors in the model are similar with the results of the EKF, showing a lot of sensitivity towards errors on the mutual inductance M. In order to reduce the parameter error sensitivity, an extension of this observer has been developed, adding the input DC voltage as a state variable and two observed parameters Δ_Γ and I_p in the state equations with the aim of reducing the parametric sensitivity of the current estimation. This extended version shows good results towards errors on the mechanical parameters, nullifying the estimated currents errors, but does not improve the estimation when errors on the electric parameters are added.

Finally a last extension of the proposed state observer has been developed. This version proposed to couple the control vector generation with the state currents observation. The observer topology is the same than in the previous versions, except the Lyapunov candidate function used for the convergence analysis features an element corresponding to the error between the estimated controlled variable output and the output references. The convergence analysis leads to the extraction of the control vector to apply on the system to converge toward the reference values. This observer containing the control generation can be useful since the control vector is generated in the same loop than the observation. For this reason, there is no need to reduce the dynamic of the control compared to the dynamic of observation, allowing a faster control.

Other state observer exist in the scientific literature and could be used for the current sensorless application, yet the one developed show good simulation results, except when there are too large errors on the electric parameters, and they are proven exponentially convergent. In the following chapter, concerning the experimental results when connecting the parameter mapping realized in chapter 3 with a state observer, only the second version of the proposed observer will be used, since it was not sensitive to mechanical parameters error. Different strategies could also be considered in future work: model-free controllers for example could be a alternative to the model-based observers and reduce the sensitivity of the current estimation towards parameter errors.

Chapter 4

Experimental Results and Energy Performances Comparison

Contents

Introduction

The two previous chapters each presented a different part of the study realized to achieve current sensorless vector control. The second chapter was focused on the improvement of the understanding of the wired rotor synchronous machine in a way that could be useful for sensorless control. The third chapter introduced different topologies of nonlinear observers to retrieve the stator currents from a given electric state model of a WRSM when the current sensors are absent on the system.

The study made to improve the modeling of the machine and the development of nonlinear current observers were however realized independently. It was shown in the third chapter that, as any model based observer, the state observers developed were sensitive towards parameter errors in the state model of the system. The study made in the second chapter proposed to establish an electric model that fits the WRSM for any operating point by mapping one sensitive parameter, μ_M, absorbing the errors on the mutual inductance and other electric parameter errors of the modeling (see equation 2.32).

The aim of this chapter is then to make the connection between the modeling of the system presented in chapter two, with the extended proposed observers developed in chapter three. The state equations structures are not modified during the observation but the parameters in the equations of the observers may vary as a function of the operating point in order to have a behavior as precise as possible for every steady-state operating point possible and studied.

In this chapter, a current sensorless control of the powertrain presented in chapter 2 will be performed. The observed currents will be the one used as a feedback for the controller, achieving the main objective of this study, removing the current sensors of the stator while keeping closed loop controller. The observed state currents will be compared to measured currents in order to check the precision of the observation.

Another important comparison that will be detailed in this chapter is the comparison between the current sensorless control and the classic control with measurement feedbacks regarding the energy consumption for a given operating point. Indeed, the observation of the current still features imprecision on the estimated d and q axis currents. Nevertheless, as it will be shown, the errors on the estimated currents do not lead to a significant extra energy use that would worsen the overall power use from the battery compared to a classic control with current measurement. Of course, this conclusion depends on the usage profile of the electric powertrain.

The first part of this chapter will explain with more details the connection made between the modeling of the WRSM and the observers through the variation of some sensitive parameters in order to maximize the reduction of observation errors on the estimated state currents. This hybrid control method will then be applied experimentally and a successful current sensorless control will be performed. Different operating points will be tested, as well as transient phases and load steps in order to test the dynamics of this controller and its robustness. A last part in this chapter will focus on the energetic comparison between the current sensorless control and a classic control in order to characterize the impact of the removal of the current sensors on the efficiency of the whole system.

4.1 Synthesis and connection between the machine enhanced modeling and the state observers

As stated in the introduction, this first section will present the connection of the parameter mapping realized in chapter 2 with the extended version of the proposed observers studied in chapter 3. Indeed, the third chapter was focused on the estimation of the stator currents from a state model and using other available measures on the system as feedbacks with state observers and the model used in the nonlinear observers had fixed parameters. Observations results with

state observers are precise without model errors, but they are sensitive to errors in the parameters of the model used as a support for the observers. A state observer including parameters errors estimation has shown better robustness towards some parameter errors, however large parameters variation, especially on the mutual inductance M between the rotor and the stator winding, still induce errors on the estimated currents compared to the real ones.

This fourth chapter's aim is to perform a synthesis of the two previous chapters in order to combine their assets. There was already a connection between the two chapters, because the state model used as a support for the observers was elaborated and discussed in chapter 2. However in this chapter, the parameter mapping made previously will be included and used in the nonlinear observers. This means that the parameters used in the prediction step of the observers will no longer be a fixed set of parameters for every operating points of the machine, but a varying set of parameters depending on the excitation current value, on the speed of the rotor and on the load of the machine in steady-state. The diagram on figure 4.1 sums up the connection between the mapping of the machine and the nonlinear observer.

Indeed the diagram of figure 4.1 shows that the control strategy is the same than for figure 3.2 in chapter 3, yet the mapping of parameter is added to adjust the parameters in the state model according to the static operating point of the machine.

It was seen in chapter 2, that the mapping of parameters could be reduced to a single parameter μ_M, defined with the equation 2.32 determined in chapter 2. The map made in chapter 2 is a three-dimensional table in the way that there are three input variables, the excitation current i_e and the load indicator, which is obtained and calibrated from the battery current measure i_{bat} and the speed of the machine Ω. The output of this 3D table is the estimated parameter μ_M as a function of the rotor speed Ω as it was shown on figures 2.22 to 2.27.

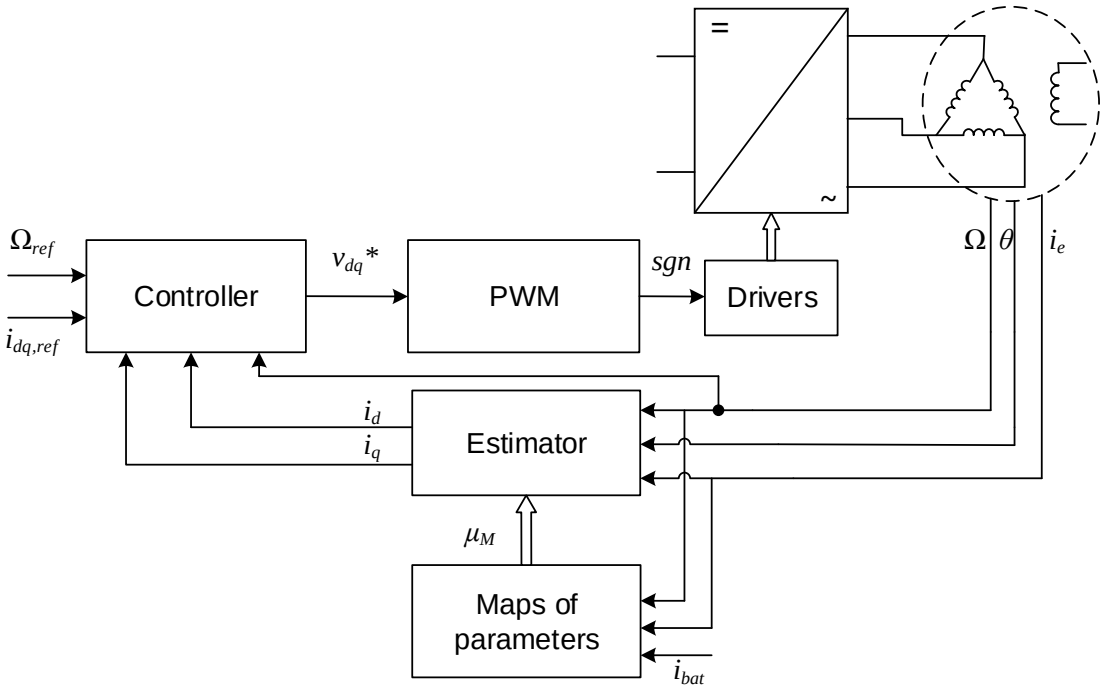

Figure 4.1. Diagram of the control chain with nonlinear observer and map of parameters connected.

The description on how the variable μ_M is measured is made in the flowchart 2.21 chapter 2. In order to use the table of μ_M on the experimental test bench, the table has been completed by first calculating μ_M for a fixed excitation current. μ_M is then calculated for different loads for this i_e. Then i_e is increased by a chosen value and the same process is reproduced until the excitation current reaches a limit value, in our case $15A$. The step value of the excitation current can be modified according to the precision wanted on the table of parameter and according to the available memory space in the system. In the tests made that will be presented and discussed later, a step of current excitation of 2A has been chosen to fill the table of parameter. For each excitation currents, it has been decided to measure μ_M for 3 different loads. As it will be discussed in the next section, 3 different loads for each excitation current brings a satisfying precision on the parameter μ_M for our study. Again, this however depends on the degree of precision needed, and a higher amount of loads could be used to have a larger table of parameter.

In order to access the values of the table, the operating points of the machines are divided in different sections. There are 6 sections for the excitation current (from 4A to 14A) and 3 sections for the load of the machine (low, mid or high load). A selection vector has been implemented in Matlab in order to select the rights sections for each operating point of the machine. This select vector is then used in the table of parameter, which outputs is the suitable value of μ_M. Figure 4.2 sums up the functioning of the map of μ_M used.

This table has been implemented in Matlab/Simulink and integrated in the file with the extended proposed observer developed in chapter 3. μ_M is no longer a fixed parameter in the script of the observer, but an input that is modified, as explained before, according to the sections where the machine operates.

The main drawback of the use of a table of parameter like the one developed in this study is the inherent problem of the section: when the operating point is close to the bounds of a section, the μ_M selected is not nominal. For example, if the excitation current is under 5A, the section

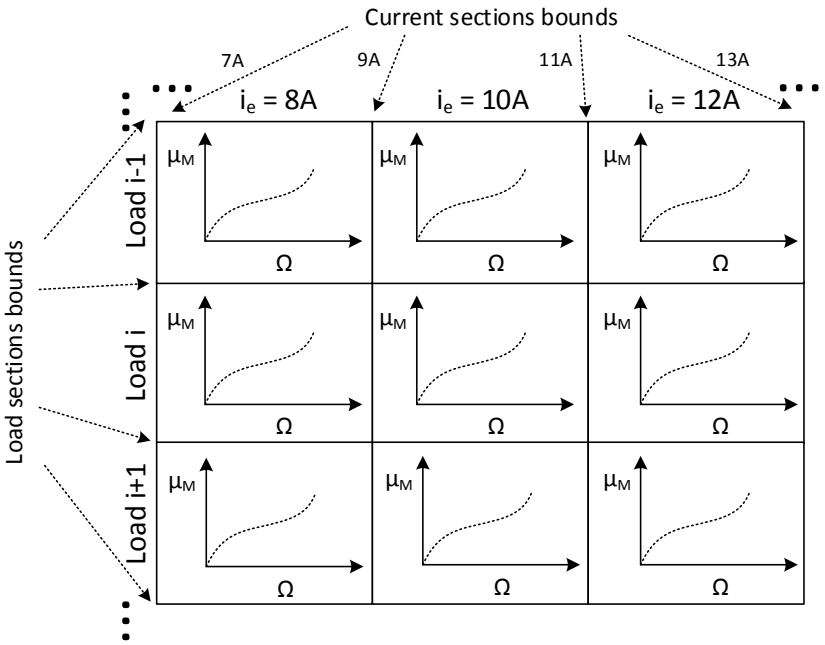

Figure 4.2. Explicit drawing of the functioning of the mapping of μ_M implemented.

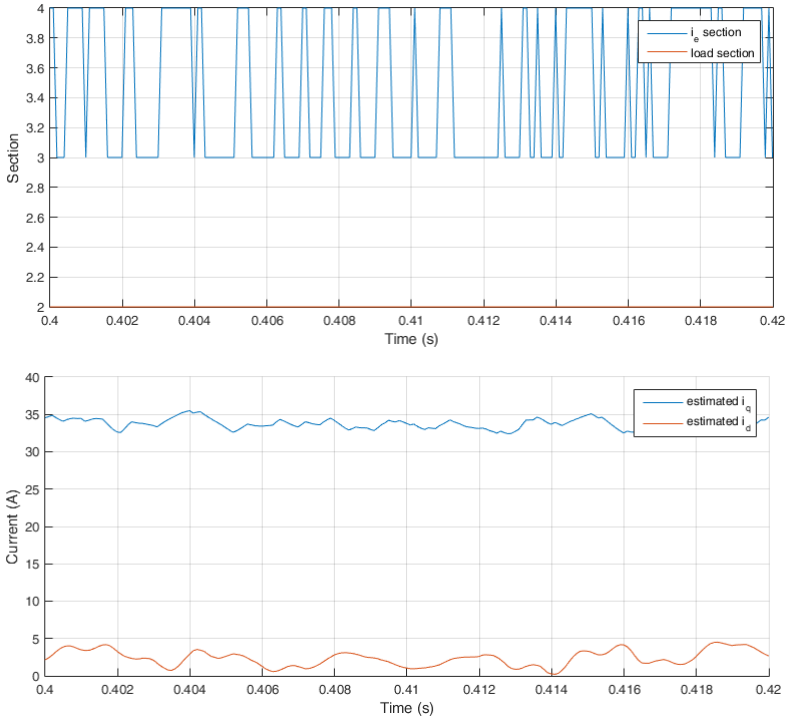

Figure 4.3. Section switching due to the excitation current (top) and impact on the estimated dq-axis currents (bottom).

related to excitation current selected is the number 2, and if the current is above the section is the number 3. With the ripple of the current, the selector oscillates between two sections and the value of μ_M keeps changing in the observer. This induces a ripple on the estimation current.

On figure 4.3, it is possible to observe this switching phenomenon. The excitation current is regulated at 9A, which is on the bounds of the excitation current section 3 (between 7A and 9A) and 4 (between 9A and 11A). Because of the current ripple, the uncontrolled switching between two sections can easily be seen on this figure. This causes the estimation of the stator currents to present some discontinuities. The same phenomenon goes for the switching between load sections, as it can be seen on the middle graph of figure 4.6. These undesired effects can be reduced by increasing the number of sections: the gap between sections will be smaller and as a result the gap in the estimation will be less noticeable. Another solution to avoid this ripple due to the section switching would be to use an interpolated 3D LUT such as the ones presented in the end of chapter 2 (2.26 and 2.27). This solution however requires a significantly higher calculus power in order to be properly implemented.

The mapping of the parameter μ_M as it has been presented in chapter 2 and in this first section has been tested experimentally when connected to the extended proposed nonlinear observer. The next section will present experimental results associated to the configuration schematized by figure 4.1.

4.2 Experimental results of the current sensorless control with a dynamic set of parameter

The first part of this paragraph will present and discuss results of estimation realized outside the current control loop (off-loop estimation). The second part will show results with the

estimated current in the current control loop (in-loop estimation). This means that the stator currents used as feedback in the controllers are no longer the measured currents but the observed ones. The measures of the stator currents in this part will only be used for the comparison with the estimation. This is actually current sensorless control results, the objective that was fixed at the beginning of this study. Both off-loop and in-loop estimations are realized using the mapping of parameter μ_M.

4.2.a Off-loop estimation of the stator currents

The off-loop estimation is an important step in the achievement of current sensorless control. Its role is to ensure that the current observation is effective in terms of precision of the current estimation and to verify the relevance of the map of μ_M.

For the tests realized and presented in this chapter, the controller used is a classic PI controller on the dq axis currents. A pole-zero compensation study is applied in order to obtain the the controller parameters. The estimation of the currents is made through the extended proposed observer. On the following figures, the measured i_q curves will be shown in blue, the measured i_d in yellow, and the estimated i_q and i_d in respectively red and purple.

The first experiments presented here, on figure 4.4, features steady states operating points. For all the graphs of this figure the excitation current injected in the rotor of the WRSM was $i_e = 6A$. On the top graph of 4.4, the measured d-axis current is controlled to $0A$ and the measured q-axis current is controlled to $35A$. The rotor speed is $600rpm$. This steady state operating point corresponds to a machine functioning at a medium load in the load section.

The top graph shows that, for a medium load and speed, the proposed nonlinear observer combined with the parameter table shows that the estimation is precise. Indeed, the estimated and measured i_q are overlapping, and the estimated i_d has less than 1A of difference with the measure. The norm of the estimated vector gives $I_{Test} = \sqrt{\hat{i_d}^2 + \hat{i_q}^2}$ and the real current vector is written $I_T = \sqrt{i_d^2 + i_q^2}$. The comparison of these two norms $\frac{I_{Test} - I_T}{I_T}$ gives an error inferior to 0.1%, so negligible.

The graph in the middle of the figure shows the estimation results for another steady state operating point, for a low load and a medium speed ($700rpm$). The q axis current is regulated at $30A$. Compared to the previous graph, the excitation current section used for the parameter table is the same but the load section is different (mid load section previously and low load section for this graph).

Again the estimation results are extremely satisfying: there is no error between the estimation of i_q and the actual measured value, and as for the previous graph the estimated i_d has less than $1A$ of error.

The last steady state operating point presented in figure 4.4 corresponds to a high load operating point and a medium speed ($530rpm$). i_q is controlled at $45A$ and the estimator gives an estimation of i_q of $41A$, leading to an error of estimation of $4A$. The estimated i_d has an error of $3A$. There are errors in this configuration but they need to be put in perspective considering the total current I_T. In this case the combined error values on i_d and i_q do not exceed 9% of the total current in the stator, which can be considered acceptable depending on the requirements of the specifications.

The principal reason why the last operating point shows more error than the other is that it is close to the bounds of a section. This is due to the fact that in a section, the function of μ_M used is fixed. Thus at a border of a section, the values of μ_M given by the function may not be the same than in the neighborhood of where μ_M has been calculated. If the load sections were more numerous, the table of parameter would be more precise and consequently the quality of steady state observation would improve.

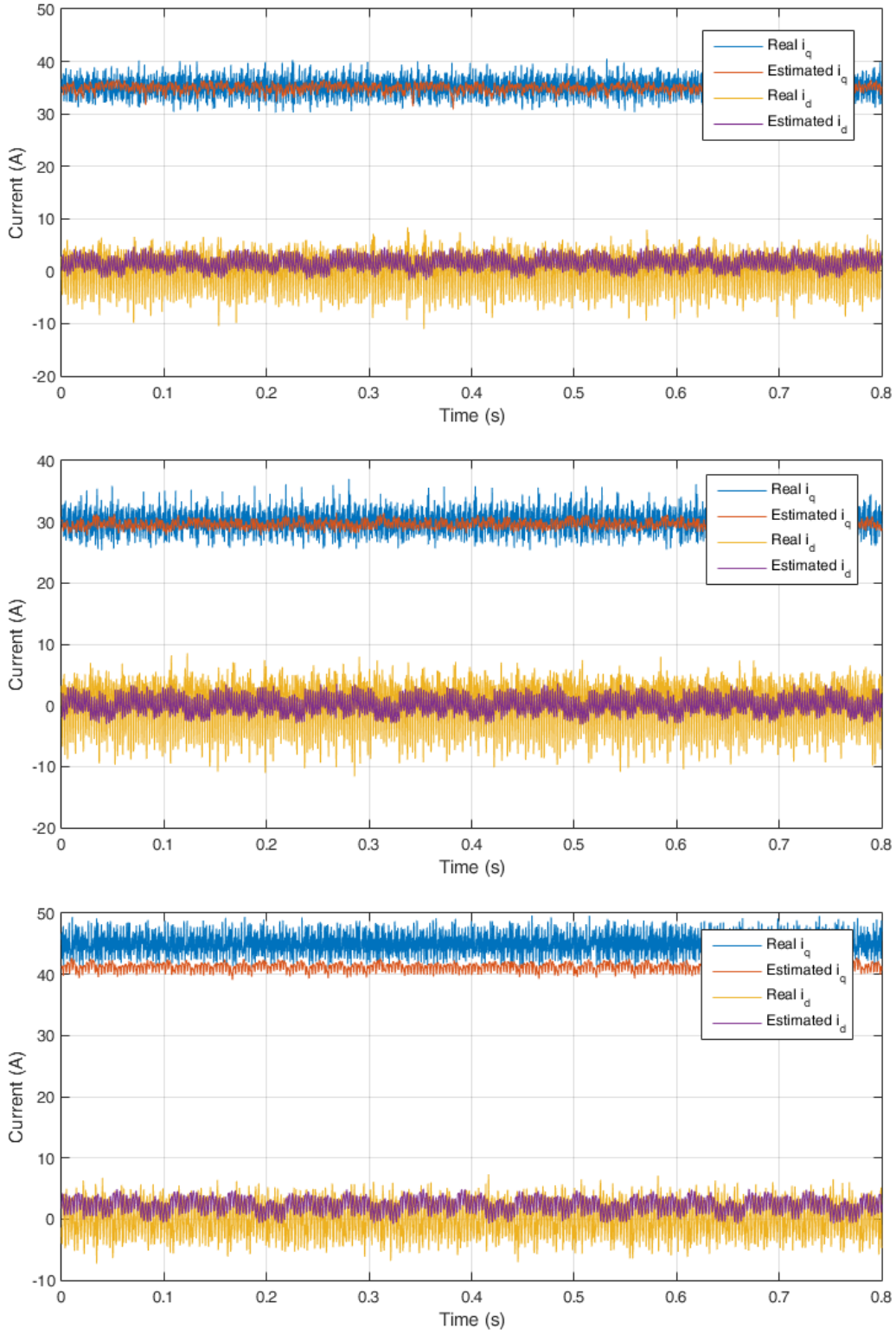

Figure 4.4. Current observation for a steady state operating point with a mid load (top), low load (middle) and high load (bottom) for $i_e = 6A$.

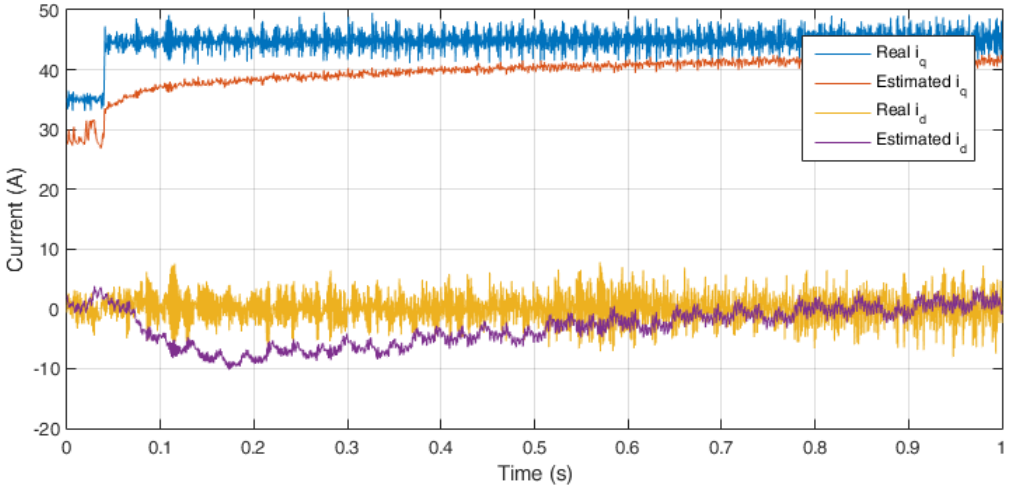

Figure 4.5. Current observation for a step on i_q from $35A$ to $45A$ for a high load and $i_e = 10A$.

The results presented on figure 4.4 featured results of steady state operating points. Figure 4.5 shows a step on the reference of the q axis current when the machine is already operating, from $35A$ to $45A$ for an excitation current of $10A$ and for a high load.

The first important thing to notice is that the estimated currents reach their steady-state in a longer time than the controlled currents. Furthermore, a step variation on i_q introduces an error on the estimated i_d. Meanwhile, it can be noticed that the steady-state error is close to zero. In fact, this dynamic is related to the speed variation as we will see in figure 4.6.

Another test has been run in order to characterize the estimation of currents for a start of the machine. On figure 4.6, the machine is initially stopped ($i_d = i_q = 0A$ and $\Omega = 0rpm$), then a step on the q axis current is applied from 0 to $35A$ for an excitation current $i_e = 6A$.

Figure 4.6 shows that at standstill of the machine, the current are well estimated and are both equal to $0A$. After the step of q-axis current, the estimations converge with no error compared to the measures of the currents. The estimated i_q reaches 90% of the final value in $0.3s$. The d axis current estimation takes a longer time to converge, about $1.1s$. The time of convergence of the estimation is actually linked to the evolution of the dq voltage references presented on the two bottom graphs of figure 4.6. With the graph at the top of the figure representing the evolution of the voltages in the stator, the link between the two dynamics of the estimated currents and the voltages are more clear. This evolution of the voltages is clearly due to the increasing of the speed of the rotor (bottom graph), which consequently increases the back-EMF according to the equations: $e_d = -p.\Omega.L_q.i_q$ and $e_q = p.\Omega.(L_d.i_d + M.i_e)$. Since the measurements of the parameter μ_M has been realized only for the WRSM steady-states, there might be transient phase phenomenons that make μ_M vary, resulting in estimation errors during the acceleration and deceleration of the machine.

The second graph of figure 4.6 displays the switch of the load section with the change of operating point. As it can be noticed on the graph, the switch between two sections is not neat, and between 0.4s and 0.7s, the section used for the parameter table switches between section 1 and 2. During this time the estimated q axis current has a largest ripple and the mean value of i_q decreases, due to the use of another value for μ_M than in section 1. In addition, the evolution of the speed also modifies the value of μ_M according to the equation associated to each section.

Figure 4.6 is useful to notice the link between the evolution of the estimated currents and the switch of section. It also allows characterizing the dynamic of convergence to a steady state.

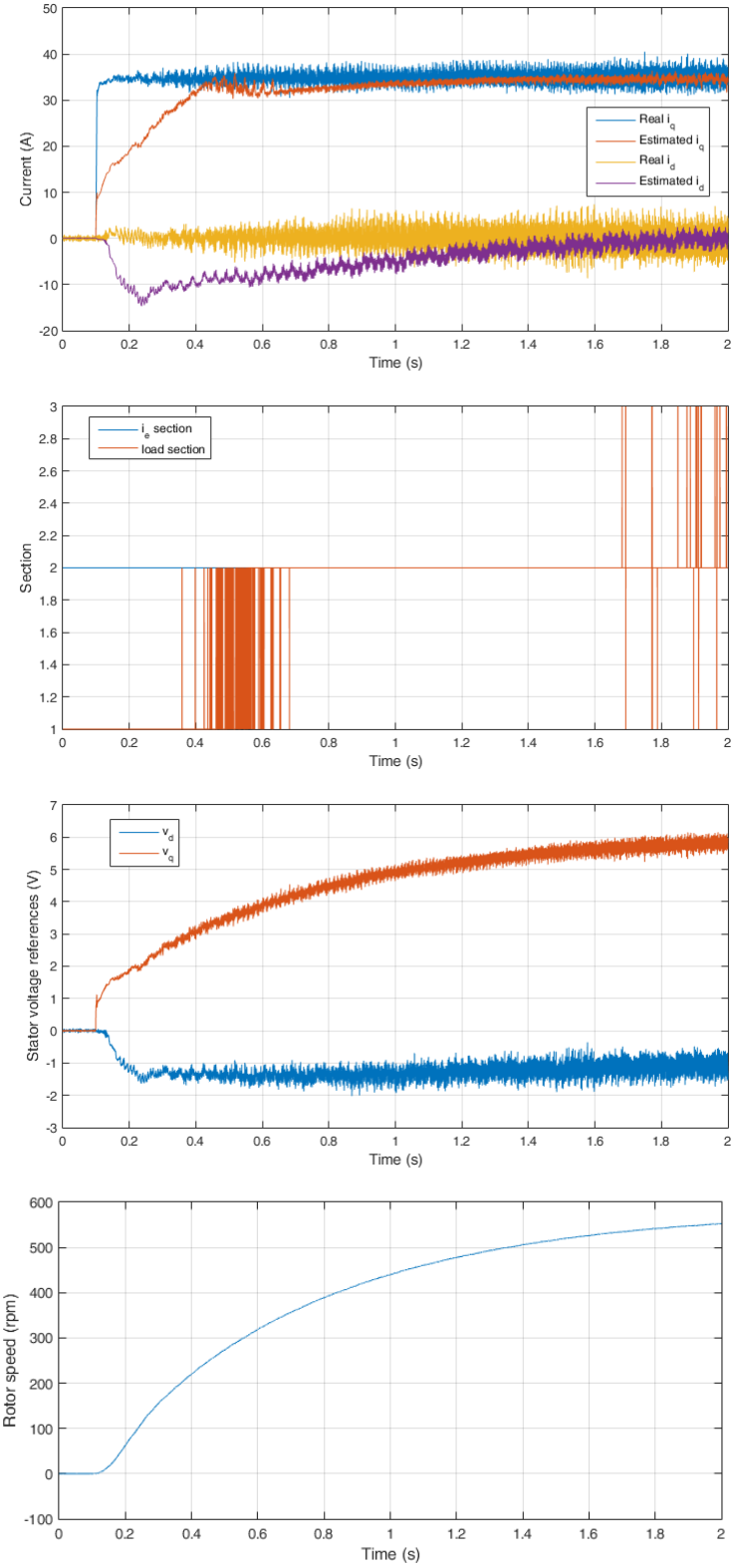

Figure 4.6. Current observation (top), load and excitation current sections (second graph), reference voltages (third graph) and rotor speed evolution (bottom) for a step on i_q from $0A$ to $35A$ for a medium load and $i_e = 6A$.

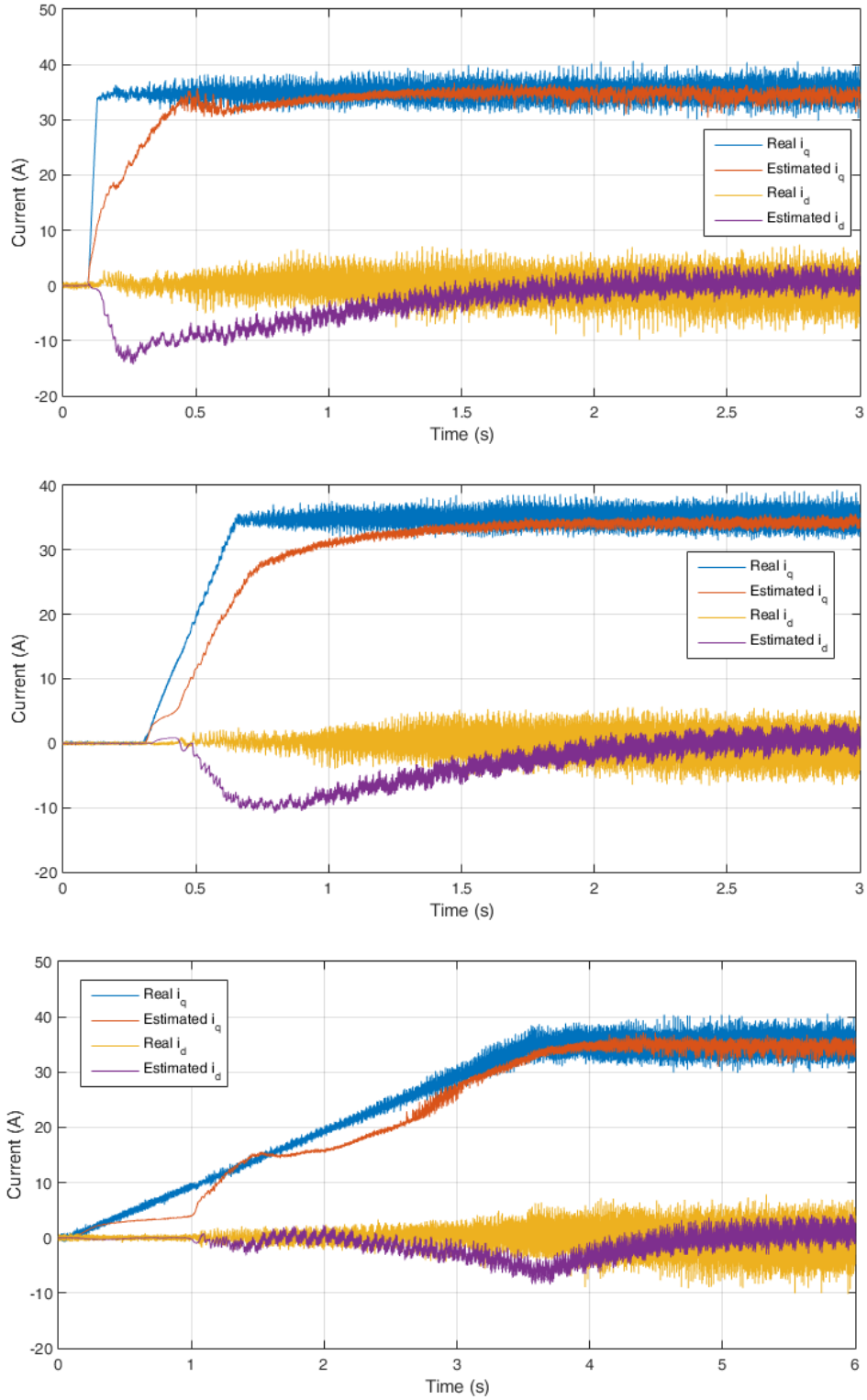

Figure 4.7. Current observation with a ramp of $1000A.s^{-1}$ on the current references (top), a ramp of $100A.s^{-1}$ (middle) and a ramp of $10A.s^{-1}$ (bottom) for a step on i_q from $0A$ to $35A$, medium load and $i_e = 6A$.

Figure 4.7 shows three graphs representing the evolution of the measured and observed stator currents when a ramp replace the reference step. On the top graph, the reference ramp on the q axis current is $1000A.s^{-1}$, on the middle graph the ramp is $100A.s^{-1}$ and the bottom graph has a ramp of $10A.s^{-1}$. From this figure it can be noted that the instantaneous error between the measures and the estimations is smaller when the controller dynamics current are slowed down. Indeed the instantaneous maximum error when a ramp of $100A.s^{-1}$ is imposed does not exceed $10A$ on both d and q axis current, while it reaches $14A$ on the d axis current for a ramp of $1000A.s^{-1}$ and up to $20A$ on the q axis current. With the $10A.s^{-1}$ ramp, the error never exceed $6A$.

Since figure 4.6 showed that the transient phase induced error on the estimation, it has been decided to add a ramp on the q-axis current reference in order to reduce the dynamics of evolution of the transient phase in order to lower the impact of the transient phenomenons on the WRSM model and thus on the estimations. The adding of a ramp indeed reduces the error between the controlled and the observed currents but it slows the dynamics of the system. Indeed figure 4.7, the time needed to reach 90% of the final value for the estimated q axus current is $0.7s$ with the ramp of $100A.s^{-1}$ while it was $0.3s$ without ramp on the reference. However, the effect on the dynamic of the rotor speed is lower and has to be put in perspective. Figure 4.8 shows the evolution of the rotor speed of the machine with a ramp of $100A.s^{-1}$ and $1000A.s^{-1}$ on the q axis reference current. From 4.8 delay of the speed link to the ramp of $100A.s^{-1}$ compared to the ramp of $1000A.s^{-1}$ does not exceed $0.2s$ for a 90% response time of $1.2s$.

Ramps lower than $100A.s^{-1}$ may however be unsuitable regarding the mechanical dynamics of the system. A ramp of $10A.s^{-1}$ reduces considerably the error of estimation on the currents but it also slows the evolution of the rotor speed to unacceptable response time for hybrid vehicles applications.

Another important test to perform in order to validate the nonlinear observer with the parameter table, is the application of a load step on the motor in order to check the robustness of the system. To do so, a sudden variation of the resistance of the active load is applied. This changes the mechanical torque on the load machine and thus provokes a load step on the studied machine. Figure 4.9 shows a sudden increase and figure 4.10 a sudden decrease of the mechanical load applied to the rotor of the machine.

From the two figures 4.9 and 4.10, it can be noticed that the observation converges when both a sudden load increase and a sudden load drop is applied on the system. The load steps

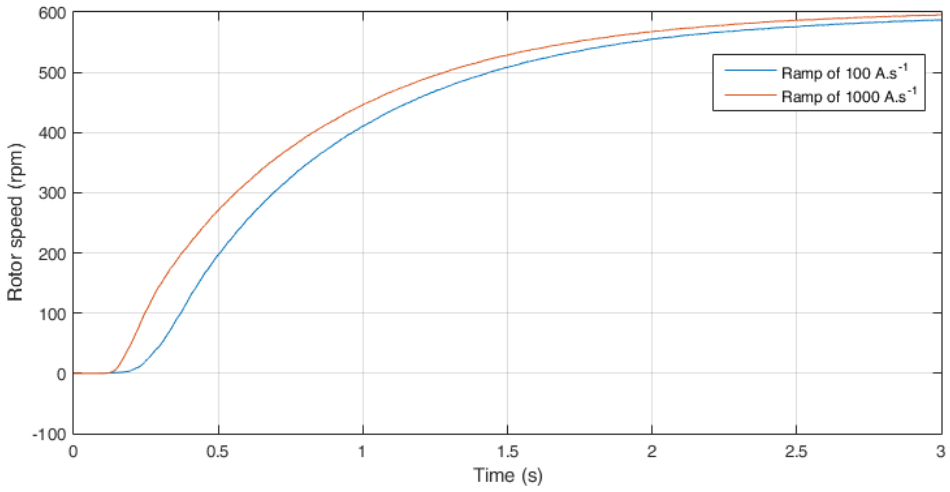

Figure 4.8. Rotor speeds associated to the currents of figure 4.7.

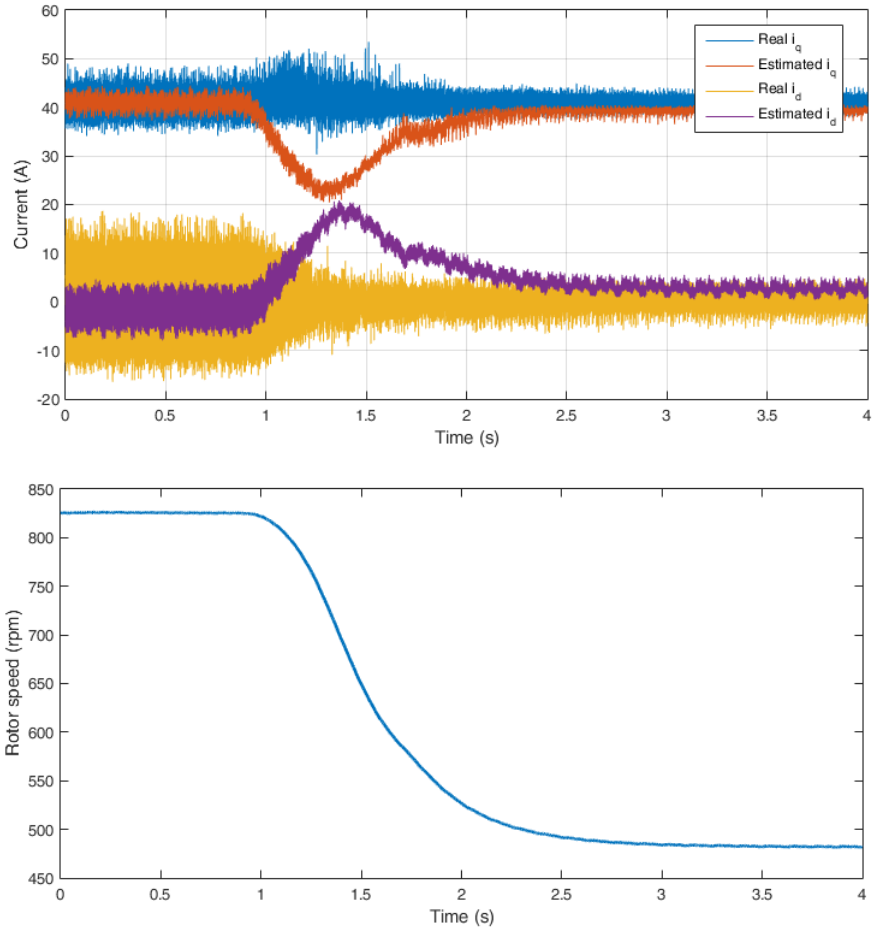

Figure 4.9. Currents (top) and speed (bottom) evolution for a sudden mechanical load increase applied on the machine.

are significant and the rotor speed changes from 830rpm to 470rpm in 1 second (time to reach 90% of the final speed) when the load step up is applied and from 470rpm to 790rpm in 2.3 seconds when the load step down is applied. From these two figures, it can also be noted that the load step up induces higher errors on the observations of both stator currents during the transient phases. Indeed the error on the d and q axis current reaches 18 A for the load step up, and only 5 A on i_q and 8A on i_d for the load step down. This can be explained by the fact that the rotor speed varies faster during the load step up than during the load step down. This lead to a greater transient phase dynamic and as it could be noticed on figure 4.7, the higher the $\frac{di}{dt}$ during a transient phase, the higher the error on the estimation.

The observer coupled with the parameter table is robust towards load variations and gives satisfying results thanks to the use of different load sections in the parameter table. However, since there also are several sections for the excitation current, the robustness of the estimation towards sudden excitation current variations has been verified as well.

Figure 4.11 features two graphs. The top one presents the evolution of measured and estimated stator currents when an excitation current step up from 4 A to 10 A is controlled. The bottom one displays the same currents but for an excitation current step down from 10 A to 4 A.

From the two graphs of figure 4.11, the change of excitation current impacts the stator currents observation, but the change of excitation current sections allows the observer's model

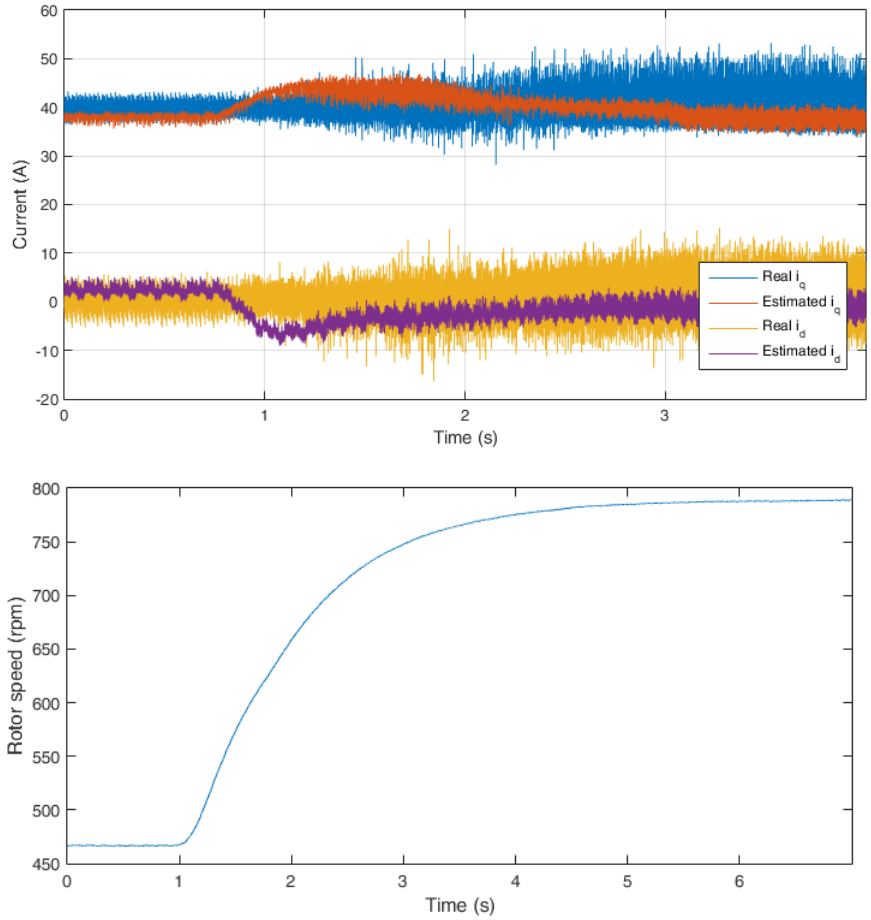

Figure 4.10. Currents (top) and speed (bottom) evolution for a sudden mechanical drop increase applied on the machine.

to have the most suitable parameters for the estimation. The change of section can easily be spotted on the graphs at 0.3s, 0.5s and 1.1s on the top graph and 0.4s, 0.55s and 1.1s on the bottom one.

This figure also shows that the switch between excitation current sections is working as expected and it also demonstrates that the observer is robust to a sudden excitation current variation, whether it is a step up or a step down. This is a useful asset mostly for the fact that during the start of the machine the excitation current is usually controlled to high values (up to 15 A) in order to accelerate the start of the machine by increasing the starting torque. When the nominal speed is reached, the excitation current is reduced to 5 A in the knee saturation point of the machine (see figure 2.12).

It has now been shown that the solution of nonlinear observer coupled with the parameter table based on sections switching is robust in steady-state towards both load and excitation steps when the estimation of stator currents is performed off-loop. The next section will be focused on the actual current sensorless control, with the current estimations in-loop.

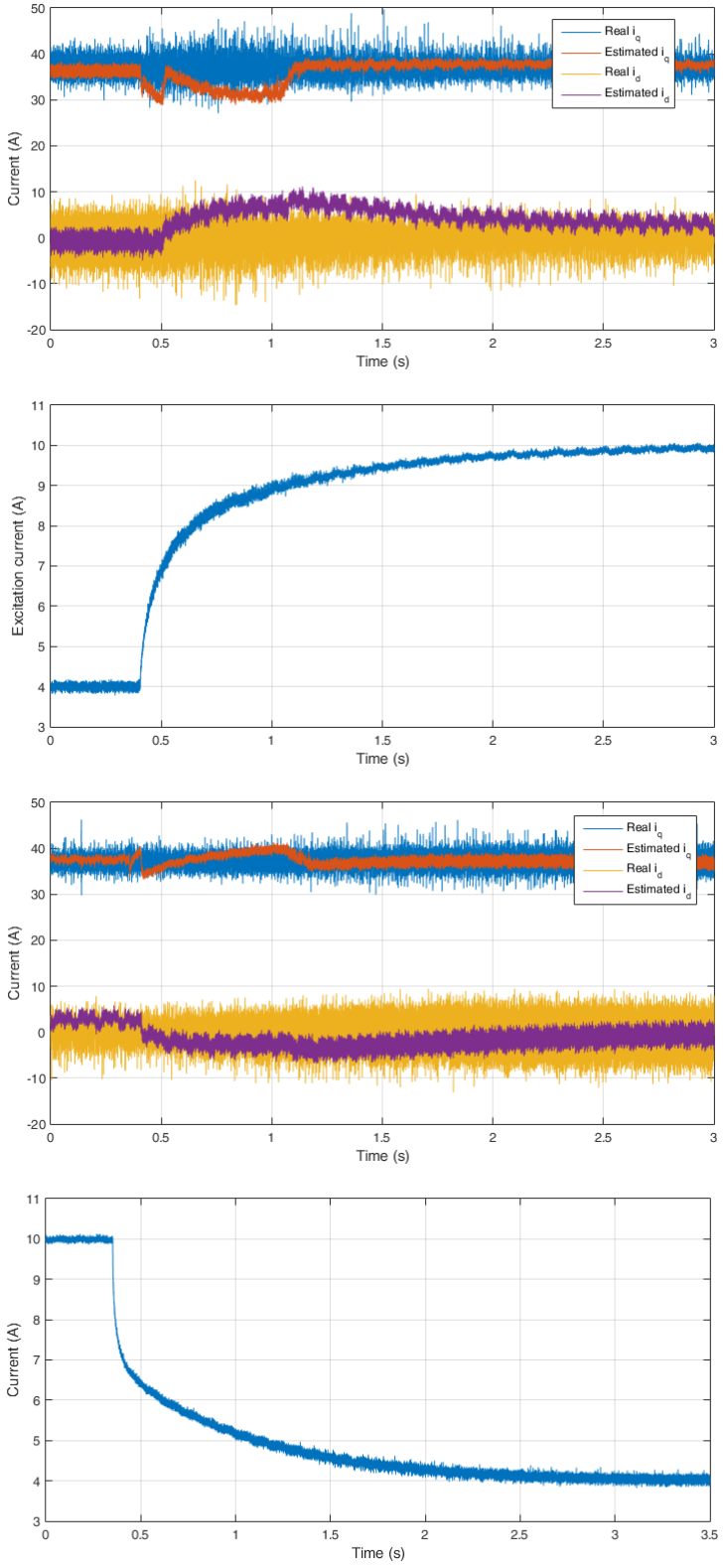

Figure 4.11. Currents evolution for a sudden excitation current increase from 4A to 10A (top) and a sudden excitation current drop from 10A to 4A (bottom) applied on the machine.

4.2.b In-loop estimation: characteristics and performances of the developed current sensorless control

The previous paragraph focused and presented results of the current estimation when it is performed outside the control loop. The off-loop estimation's role was to test the precision of the solution proposed, for steady-states operating points and transient phases. In fact, the previous paragraph's off-loop experiments showed that the estimation is precise in steady states phases thanks to the table of a parameter included in the nonlinear observer. The transient responses lead to errors on the estimation because of the rotor speed lower dynamics, but this error is less if ramp current references are applied. Finally, the observation has been proved robust to excitation current steps and the load changes in steady-state.

In this paragraph, the experiments that will be introduced all features actual current sensorless control. This means that the controlled stator current are not the measured currents anymore but the estimated ones. As it was stated before, the control of the currents without using the measurements in order to remove the sensors was the main objective to reach in this study. As for the off-line estimation, the current sensorless control has to be tested for several environment. Different steady-state operating points will first be tested within the range of functioning of the machine.

The set of experiment that will follow is realized in the same conditions than for the previous paragraph: the controller used is a PI controller, the first tests will feature a current control and a speed control of the machine will also be implemented.

The following figures will present the first results of current sensorless control for different steady state points. The first point depicted on figure 4.12 is for a low mechanical load, an excitation current of 8 A and a q axis current reference of 25 A. The machine speed for this test is constant at 550 rpm.

This first figure representing current sensorless control results are interesting: from the graph, the estimated currents are perfectly controlled, showing no ripple. This could be expected, since the output currents of the nonlinear proposed observer are now the controlled variables, the ripple existing on the real currents does not impact the estimation since the model used in the observer does not take the ripple in account. There was however a ripple on the off loop estimation for the reason that the ripple of the real current impacted the voltage references of the controller (since the real current were controlled). The dq voltage references thus propagated the ripple to

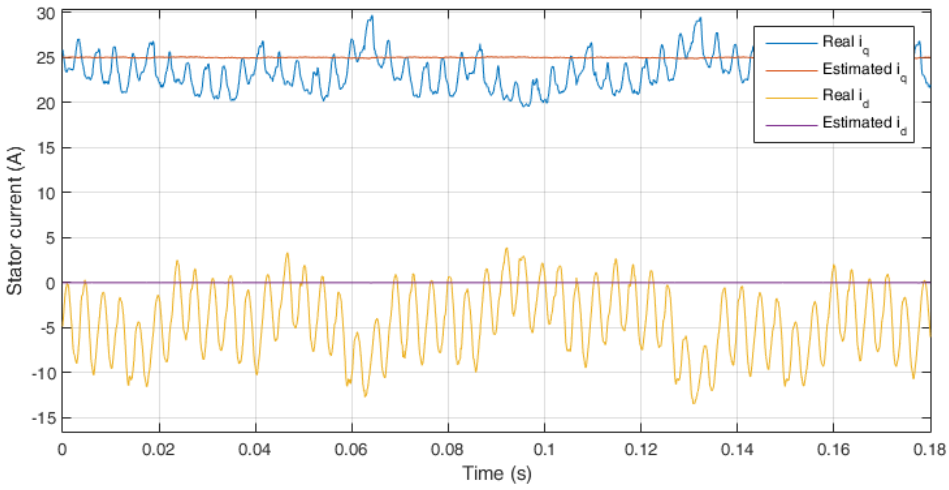

Figure 4.12. Current sensorless control for a low load and a q-axis current reference of 25 A.

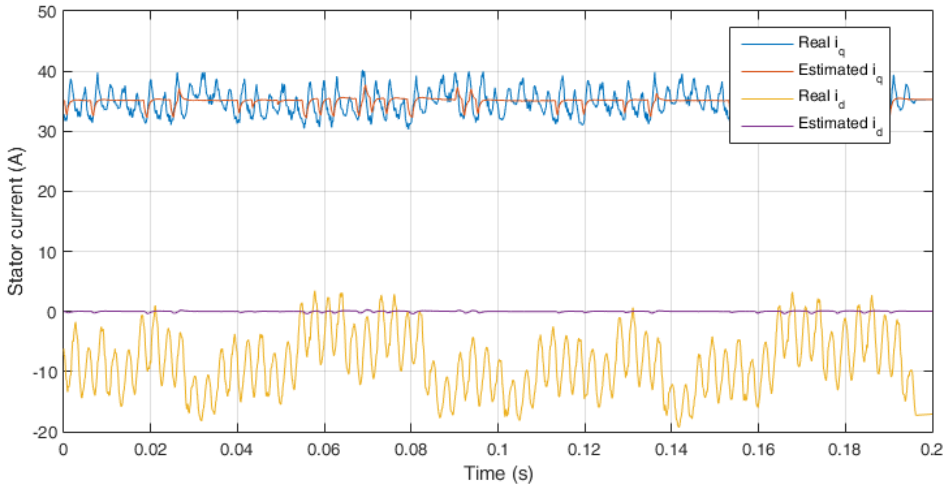

Figure 4.13. Current sensorless control for a medium load and a q-axis current reference of 35 A.

the estimations. This is not the case for in-loop current sensorless configuration.

Moreover, figure 4.12 shows that the estimation is accurate: indeed the measurements of the currents show that there is less than 1A of error for the q-axis and an average of 5 A for the d-axis current which corresponds to an overall error of 2% when considering $\frac{I_{Test}-I_T}{I_T}$.

However the estimated currents can contain a ripple in some circumstances. Figure 4.13 displays current sensorless results for a different operating point. For this test, the q-axis current reference is 35 A for a medium load and an excitation current of 8 A.

On figure 4.13, the precision of the q axis current estimation is optimal and there is no error comparing to the measured current. There is however an average error of 7 A on i_d, leading to an overall error of 2%. The important thing to notice on this test is that the estimated and controlled currents are not constant as it was for the operating point of figure 4.12. Indeed from the graph of 4.13, some ripples can be noticed on the estimated currents. This is in fact not linked to the ripple on the measured currents but on the section switching. This operating point

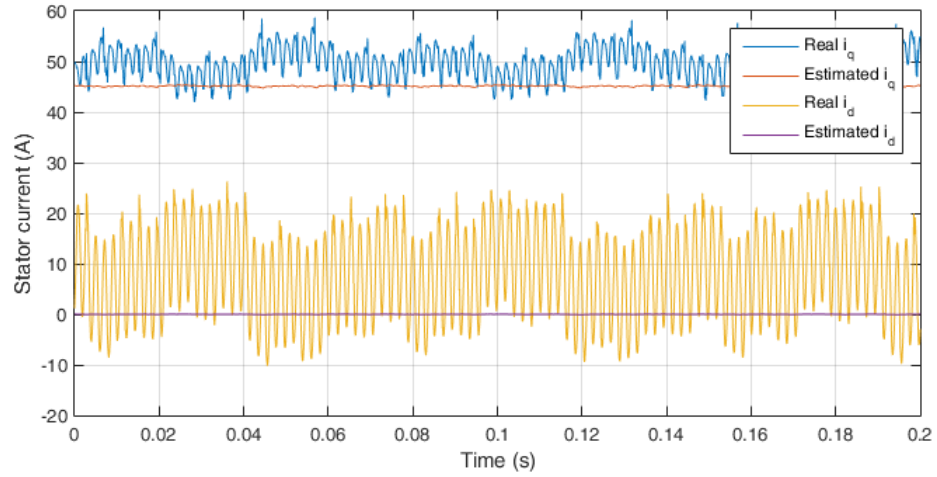

Figure 4.14. Current sensorless control for a high load and a q-axis current reference of 45 A.

is close to the edge of a load section, and the table of parameter switches when the load section changes, hence the ripple on the estimated currents. It can be noticed that the q-axis current is more impacted by the sections switching, because as seen before, the variation of the parameter μ_M has a lower impact on the d-axis current because this current is closed to 0A.

Figure 4.14 shows a last steady-state operating point for another excitation current, $i_e = 10A$ for a high load and a q-axis current of 45A. Here there is an error of 4A on the estimated q-axis current and 9A for the istimated i_d, leading to an overall error of 8%.

Around the operating points that have been considered for the mapping of parameters, the steady-state estimations give satisfying results and do not exceed 10% of error between the estimations and the measures. A map of μ_M with more sections would reduce this steady-state error, but this would increase the memory use of the control as it has been explained in the beginning of this chapter.

4.2.c In-loop estimation: speed control of the WRSM

In some applications, it is required to reach a target speed whatever the current is under physical constraints of the drive. In this case, we have to use a speed controller. Therefore, another control loop on the speed of the rotor is then implemented above the current loop. As seen in the previous chapters, the dynamics linked to the electric variables in the machine are at least one decades faster than the dynamics of the mechanical variables. That way, an external PI controller of the speed of the machine can be added without changing the PI controller for the current, the behavior of the mechanical speed of the machine on the current being approximated as a first order (see chapter 2).

The PI controller on the speed of the machine has been tuned beforehand using the measures of the stator currents. Once the speed of the machine was controlled in satisfying conditions with the measures, the same controlled has been tested with the estimated currents as feedbacks for the inner control loop, performing current sensorless control of the speed of the machine. The results of this current sensorless control configuration will now be presented and detailed.

The first tests that have been realized to validate the current sensorless control of the mechanical speed of the machine are, as for the current control, steady-states operating point. The graph displayed on figure 4.15 presents the operating point corresponding to a speed controlled to the reference of $\Omega_{ref} = 500rpm$ for a high mechanical load and a excitation current of 8 A.

The speed of the machine has not been displayed here because it is controlled at a constant point at 500 rpm. However this figure show that the speed controller is stable and makes the speed converge towards the wanted value even without the current measures, using only the estimation from the proposed nonlinear observer coupled with the dynamic table of parameter.

The evolution of real and estimated stator currents of figure 4.15 shows that, apart from the fact that the speed is successfully controlled, the results are similar to the ones obtain when the currents were directly controlled. Indeed for this operating point, the real q-axis current presents an average error of 4 A compared to the estimated one, and an average error of 11 A on the d-axis current, leading to an overall error between the estimated current vector and the real one of 12%. As for the control of the current, the estimated current is perfectly flat, meaning that there is no section switching in the table of parameter at this operating point. The operating point presented on figure 4.16 on the other hand stands on the border of two load sections.

Indeed, figure 4.16 features a q axis estimated current showing frequently current peaks, consequence of a change of the parameter μ_M used in the nonlinear observer. The same way than for figure 4.13 featuring a steady-state point for the sensorless control of the current, the impact of the section switching is negligible on the d axis current. For this operating point, there is an overall eror of 8%.

The different steady-state operating points obtained with the current sensorless control of

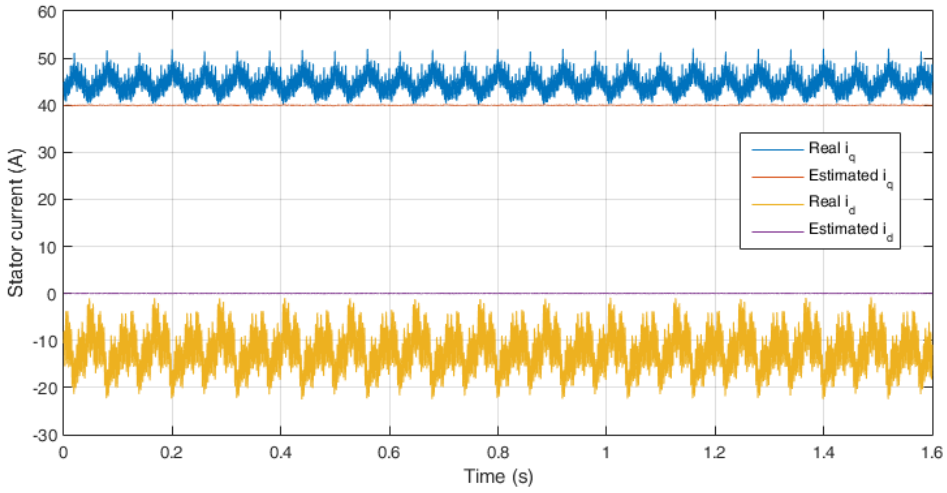

Figure 4.15. Current sensorless control of the speed for a steady-state operating point: $\Omega_{ref} = 500rpm$, $i_e = 8A$, high load.

the rotor speed give markedly similar results for the real and estimated currents than with the current sensorless control of the dq axis currents.

An inevitable drawback inherent to this proposed solution of current sensorless control is the error of estimation during the transient phases of the machine. Indeed in this section introducing the experimental results of current sensorless control (of the speed as well as the current), peaks of error could be noted. This is due to the low dynamic of the mechanical speed of the machine which implies a slow evolution of the back emf produced in the stator, which leads to a large voltage gap between the reference voltage and the back emf, hence inducing a high $\frac{di_{dq}}{dt}$. In addition, transient phenomenons that are not taken in account in the modeling of the machine and that are not included in the parameter μ_M (the mapping of μ_M being realized during steady-states) may lead to errors of estimation. The steady-states of the machine on the other hand are

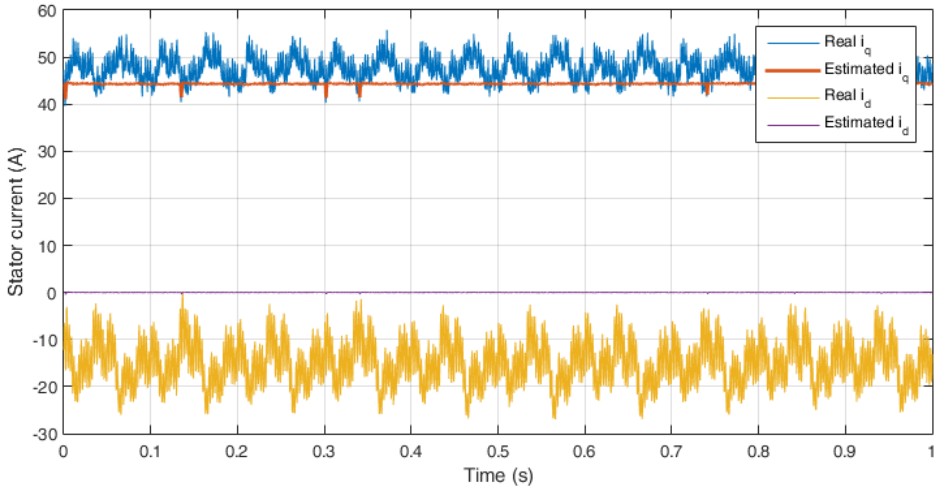

Figure 4.16. Current sensorless control of the speed for a steady-state operating point: $\Omega_{ref} = 600rpm$, $i_e = 8A$, high load.

very well estimated for all the operating point tested.

These error peaks are leading to an energy loss during the transient phases of the machine. This energy additional loss will be discussed in the following section. An energetic comparison between a classic control of the machine and a current sensorless control will be performed during transient and steady-state phases.

4.3 Comparison of energetic consumption with and without current sensors

As it has been showed in the previous section, the proposed current sensorless control cannot entirely suppress estimation errors on the stator currents. These errors on the estimation of the dq-axis currents can be responsible for an energy overconsumption of the battery. In this last section, an appraisal based on the energy comparison of the current sensorless control with a classic current feedback control will be conducted. This is an important last step: if the removal of the current sensors are a clear benefit for the manufacturing costs and the reliability of the system, and even if the estimator has been shown precise in steady-state, excessive losses due to error of estimation can be a serious drawback on the overall system and could be a reason to avoid choosing current sensorless solution for particular applications.

This comparison will be conducted by looking at the battery current in both situations for similar operating points. Indeed, the DC voltage being constant and equal to 12V, the difference

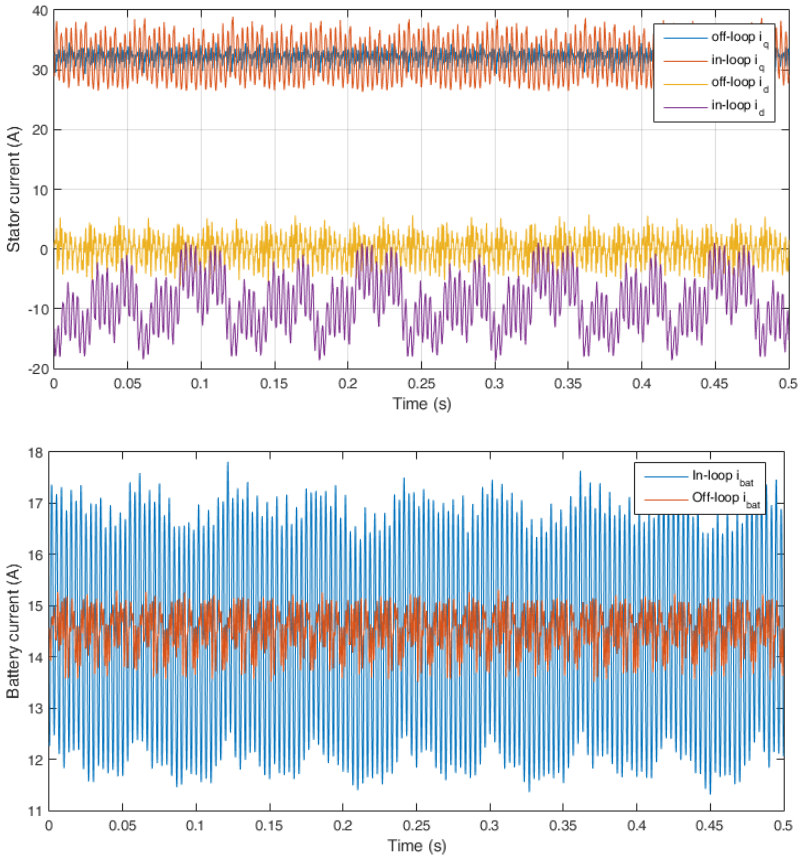

Figure 4.17. Steady-state comparison of real dq-axis currents (top) and battery current (bottom) in-loop (blue) and off-loop (red) at 500rpm with $i_e = 10A$ and at medium load.

of energy consumption on the DC level of the system will be characterized thanks to the battery current. Thus for an identical operating point, a higher battery current consumption indicates that a higher electric input power is necessary for the same mechanical power in output of the powertrain. The first experimental results will be shown for different steady-states, then for transient phases.

The results displayed on 4.17 show on the top graph the comparison between the real dq-axis currents for a classic control strategy (with current sensors or off-loop) and current sensorless control strategy (in-loop), for a medium load, an excitation current of 10A and a rotor speed of 500rpm.

It is interesting to notice from these two graphs that, even if the in-loop d-axis current is shifted from 0A with an error of 10A, the battery current is, in average the same than for a classic controller. The main difference between the two battery currents is the ripple which is higher for the current sensorless control (5A of ripple current while it does not exceed 1A for the classic control). As a side note for these experiments, the top graph of 4.17 shows that the q-axis currents are identical in average. This is a logical result, since the currents displayed here are the real currents and not the estimated ones, and the load and speed being identical for the two cases, the q-axis currents are expected to be the same.

On a steady-state, even with significant error of estimation on the currents for the sensorless control, the energy consumption on the DC branch of the system is not significantly impacted. The same experiment has been run for the same operating point but with a higher mechanical load, and is shown on 4.18.

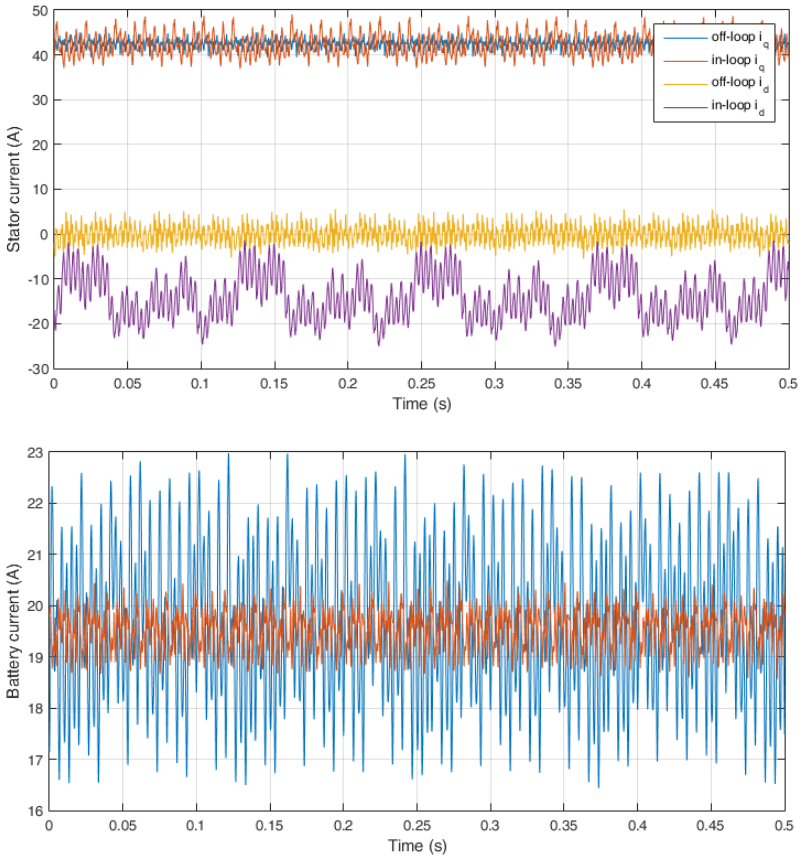

Figure 4.18. steady-state comparison of real dq-axis currents (top) and battery current (bottom) in-loop (blue) and off-loop (red) at 500rpm with $i_e = 10A$ and at high load.

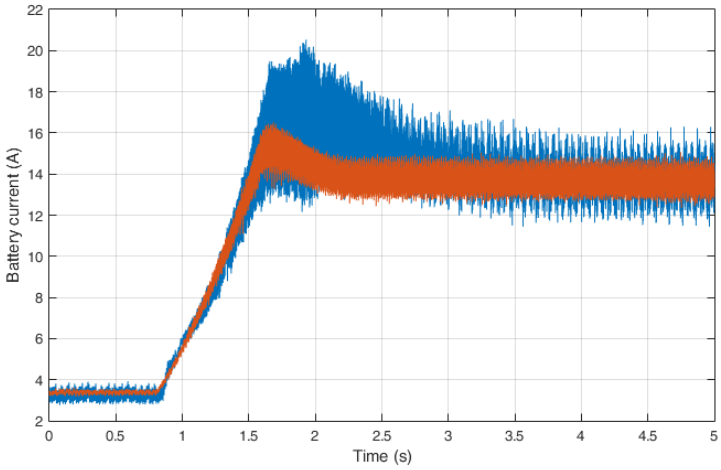

Figure 4.19. Comparison of the battery current in-loop (blue) and off-loop (red) from 200rpm to 600rpm with $i_e = 10A$ and at low load.

The results for this other operating point is significantly the same, and the current in output of the 12V battery is identical in average for the two control strategies. The ripple is also higher for the current battery associated to the current sensorless controller.

It has however been said in the previous section that transient phases, such as a change in the speed reference or a sudden load variation, induces consequent estimation error. With the ramps, it could be notice that the slower the evolution of the currents, the smaller the estimation errors. The next experiments for the energy comparison study undertaken in this section will thus be focused on transient phases of the system.

The graphics shown on figure 4.19 represents evolution of the battery currents for a classic and a current sensorless controller. The experiment associated to this figure corresponds to an acceleration of the machine from 200 to 600rpm with an excitation current $i_e = 10A$ and a low load.

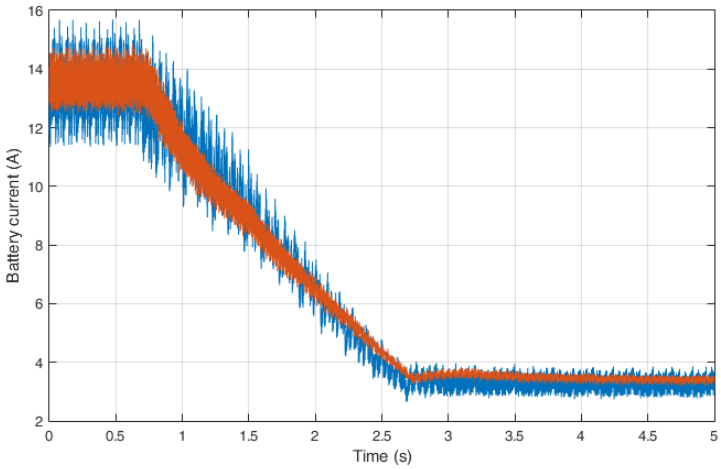

Figure 4.20. Comparison of the battery current in-loop (blue) and off-loop (red) from 600rpm to 200rpm with $i_e = 10A$ and at low load.

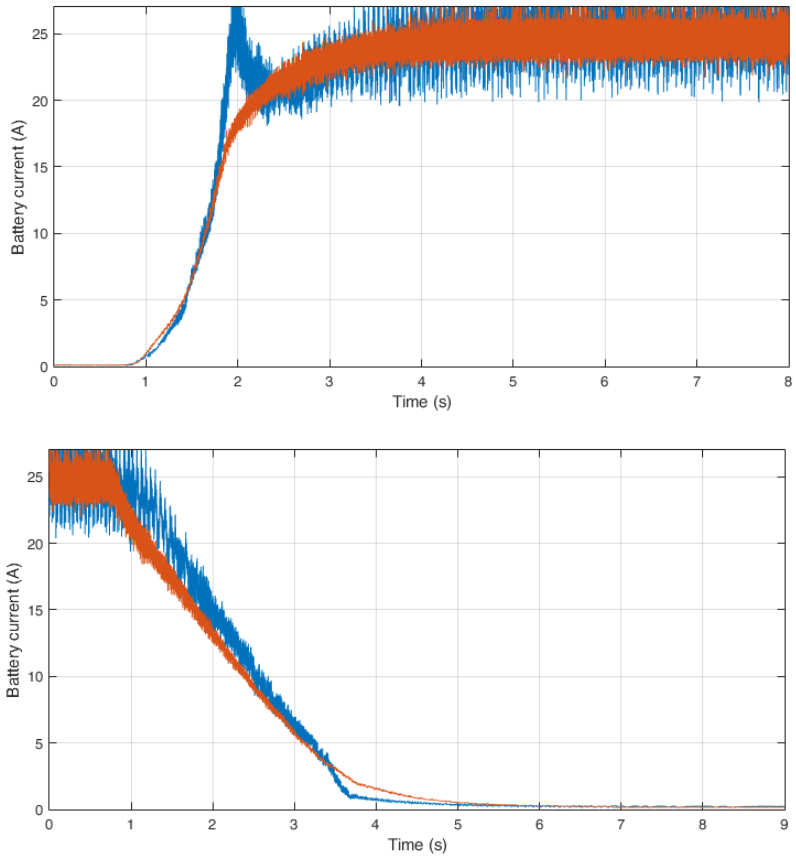

Figure 4.21. Comparison of the battery currents evolution for a start (top) and a stop (bottom) of the WRSM in-loop (blue) and off-loop (red) with $i_e = 10A$ and at high load.

The graph of figure 4.19 shows the battery currents during the acceleration of the machine. An overshoot on the in-loop battery current can be noticed at the same time than the overshoots of the stator currents, with a peak at 1.7s. This overshoot rises up to 16A in average, for a final average value at steady-state of 14A. This overshoot on the battery current is however low compared to the overshoots corresponding to the stator current and corresponds to 14% of the final value. In comparison, the battery current of the classic controller presents a similar overshoot. In this graph, it can be noted that the battery current for the in-loop current sensorless control and the classic off-loop controller are almost the same in average. This means that the errors between the estimated currents and the real ones do not lead to an excessive energy loss between compared to the control of the real currents.

Another transient phase test has been run for a deceleration of the machine, from 600rpm to 200rpm. The results are shown on figure 4.20 display a stop of the machine with an excitation current of 10A and with a low mechanical load.

Again for this test, the errors between the real and estimated currents are negligible in regard of the battery current: indeed no peak can be notices on the battery current linked to the sensorless control and the average profile is the same than the battery current of a control of the measured currents.

The last figure 4.21 features the battery current comparison between in-loop and off-loop control for a start (standstill to 600rpm) and a stop (600rpm to standstill) of the machine for a high mechanical load and $i_e = 10A$.

Here the differences are more noticeable. On the top graph corresponding to a start of the

machine, an peak on the in-loop battery current can be noticed, leading to a current 7A higher than for the off-loop battery. The battery current is however higher for a short time, less than 0.5s. The steady-states are identical. This means that, for a short amount of time during the start of the machine, the current sensorless control consumes more energy than the classic off-loop control. For the stop of the machine, the in-loop battery current is slightly higher during the deceleration but no significant peak can be noticed.

From the different tests that have been made in order to compare the energy consumption between the electric powertrain with the current sensorless control and the electric powertrain with a classic controller, it can be noticed that in steady-state, the average energy consumption is the same even with errors of estimation on the d-axis current. During the transient phases, the errors on the dq-axis currents for the current sensorless tests lead to a slightly higher consumption of the battery current during the overshoots. This energy over-consumption is however very small and only occurs during start phases of the machine. These results are very encouraging, since the main drawback of estimation errors on the dq-axis stator currents is the energy issue, which is particularly problematic in embedded systems like hybrid vehicles technologies.

Conclusion

In its construction, this chapter is the experimental combination of the studies on the modeling of the machine made in chapter 2 and the studies on the observer of state variables realized in the chapter 3. Indeed the results obtained in those two chapters are complimentary: a better understanding of the machine, and a sharp mapping of the parameters of the system allow to obtain enhanced results of the nonlinear state observers developed in the chapter 3, mainly because those observers are sensitive to parameter errors.

In a first part of this chapter, the map of parameter μ_M realized in chapter 2 has been implemented and tested. According to the operating point of the system (excitation current, speed of the rotor and load of the machine), the map switches the parameter μ_M used in the proposed state observer developed in chapter 3. The results of the switching displayed in the first section of this chapter show that the map switches according to the operating point satisfactorily.

In a second section, experimental results of the chosen solution outside of the control loop (referred as off-loop estimation) have been displayed. Different steady-state operating points have been tested: several mechanical loads, speeds and excitation currents in order to see the impact of the parameter switching on the current observation. For steady-state tests, the results are extremely positive: according to the operating point, the error of estimation of the stator currents does not exceed 10%. During transient phases, the variation of speed provokes a change of section as expected, but there are also overshoots on the estimated currents due to dynamic phenomenons that are difficult to take in account in the state equations of the machine used in the observer. In addition with the overshoots, there is also a delay on the evolution of the estimated currents due to the fact that the estimation is linked to the evolution of the rotor speed which as a slower dynamic than the dynamic of the currents.

In order to reduce the dynamic phenomenons that lead to estimation errors, a ramp on the current reference can be added in order to slower the rise of the current and thus lower the delay on the currents estimation. The value of this ramp depends on the specifications of the system. Some more experiments have been conducted in order to check the robustness of the estimation: sudden mechanical load variation have been applied on the rotor and change of the excitation current have been controlled. The results of estimation are good with a rapid return to steady-state. These tests allows to notice the switching of parameter μ_M on the estimations.

After checking the precision and robustness of the current estimation off-loop, the next crucial step was to test the current sensorless solution on real conditions, without current sensors in the control loop (referred as in-loop estimation). First, steady-states tests with current sensorless

controller have shown similar results than for the off-loop estimation, with a good precision of estimation according to the operating point, with a maximum accumulated error of 12%. The same tests have been run with a speed control this time. The current sensorless control is still robust and precise except during the steady-states. However the main drawback of the current sensorless control as it has been developed so far is the estimation during transient phases. Indeed, the same way there were estimation errors during the off-loop experiments, the in-loop estimated currents present error during the transient phases, due to transient and sub-transients phenomenons that have not been taken in account in the model and that are not absorbed by the map of μ_M since this parameter has been mapped for steady-states. The improvement of transient phases should be the subject further studies in the future. A possible approach could be to add to the map of μ_M another parameter estimated during transient phases. Another possibility could be to use FEA modeling results to elaborate an electric model of the machine for all steady-states and transient phases of the operating range of the machine.

Finally the last part of this chapter focused on an important issue concerning sensorless control: the energy consumption comparison between the powertrain using the proposed current sensorless solution and the powertrain using a classic controller. Indeed, even if the current sensorless controller benefits from the removal of currents sensors in regard of the manufacturing costs and the reliability of the system, it can suffers from an excessive energy consumption due to the errors of current observation. The experimental results however show that it is not the case: in steady-states, the energy consumption, represented directly by the battery current absorption, is the same for the classic controller and the current sensorless controller. In transient phases, and more particularly the start of the machine, the real currents estimation errors provoke a small overshoot on the battery current absorption. The peak on the battery current is however small and the duration of this overshoot is very not significant.

This chapter has shown successful current sensorless control by combining a state observer with a mapping of a sensitive parameter, the mutual inductance between the rotor and the stator of the WRSM. The results obtained on the precision and robustness of the current sensorless controller in steady-state are extremely encouraging and further work on this subject could enhance the performances of the current sensorless control especially for the transient phases of the machine. A study taking in account the temperature variations impact on the current estimation could also be interesting to improve the precision of the observed currents.

Conclusion

The aim of this work was to propose a current sensorless control of a WRSM. Indeed, the part of electricity in vehicles tends to increase due to the increase of quotas on gas emissions of the vehicles and the environmental marketing impact of more electric vehicles on the customers. In the first chapter, a comprehensive review of vehicle electrification has been proposed. Among the different technologies existing, mild-hybrid solutions are extensively developing: the possibility to install an electric powertrain on an existing vehicle is an appealing and rapid way to redesign a classic vehicle into a hybrid one. Since the automotive industry is an extremely competitive sector, the reduction of production costs is one of the manufacturers' main objective. Removing the stator current sensors of the electric machine is one way to achieve this cost reduction, but in order to use an efficient vector control such as MTPA, the stator current feedback is necessary. For this reason, it has been decided to estimate the missing stator currents and use them as feedback for a vector controller. In the scientific literature, different sensorless control strategies exist. The most commonly found is the mechanical sensorless control, since mechanical sensors can be expensive, bulky and difficult to install on a machine. Current sensorless control also exist but mostly in a particular configuration, when a precise current sensor is available on the DC link of the inverter, which is not possible in our application since adding an expensive sensor would nullify the benefits of the current sensorless mild hybrid application. In the end of the first chapter, the available measurements of the system studied have been listed: the excitation current of the WRSM's rotor through a low cost current sensor, the rotor speed with a precise Hall effect sensor and the DC voltage with a voltage sensor in input of the inverter.

In chapter 2, a description of Valeo's i-StARS system has been presented with details and compared to the one realized in the GREEN laboratory. The test bench has been designed to have elements as close as possible to the ones of Valeo's system. Then, a study of the modeling of the machine have been proposed. Indeed, with the aim of estimating the stator currents it is important to have a reliable modeling of the electric powertrain. First an overview of the magnetic modeling performed by Dr. Devornique has been proposed. Indeed the FEA-based model developed could be interesting to access to information on the machine behavior for every operating point without having to test them experimentally. Then an electric modeling of the system has been proposed and the state equations of the machine (with the dq-axis current stator, the excitation current and the rotor speed as state variables) have been defined. From this modeling, the different parameters have been experimentally identified. However, the procedure to identify all the model parameters for one steady-state operating point is long. In addition, the parameters may vary significantly according to the operating point (due the saturation of the machine, the excitation current change or the temperature variations), reducing the precision of the model developed. A study of sensitivity of the model towards parametric variations has been conducted in order to characterize the impact of errors on the parameters in the model. It results from this study that the most problematic parameter is the mutual inductance between the rotor and the stator. For this reason it has been decided to realize a map of an introduced parameter μ_M, with the aim of absorbing the error on the mutual inductance and other errors in

the model that may be not predicted in steady-state. A fast mapping solution has been proposed to obtain the map of μ_M, using an online estimator. μ_M has then be characterized for several values of current excitation, rotor speed and mechanical load. An interpolation of the values of μ_M for every rotor speed for a given excitation current and mechanical load. Several functions of μ_M along the speed has thus been obtained for each value of excitation current and mechanical load.

Chapter 3 was focused on the state observer design for current estimation. First an observability study has been conducted. Indeed, the proof that the currents can be observed using the available measures needs to be demonstrated. It has been shown that with the excitation current measure, the rotor speed measure and their respective derivative functions, the state currents are locally observable if the excitation current is non null. The first state observer developed for the current sensorless application was the Extended Kalman filter. This well-known tool is often used for state variables observation or noise rejection. The EKF showed good results in simulation with no error on the parameter, estimating precisely the currents in the simulated machine. When measurement noise were added, when the covariance matrix are well chosen, the EKF estimation rejected the noise but the convergence speed of the estimation was reduced. After the EKF, another state observer was proposed. This observer was based on the convergence analysis of Lyapunov candidate functions. It has been proven with this observer that the estimation is exponentially converging. Simulation results were conducted with and without parameter errors. Without parameter error, the estimation of the current is precise, but with parameter errors, estimation errors appear. In order to reduce those errors, an extension of this observer has been proposed by adding two parameters in the estimated vector, Δ_Γ and I_p. This extended version improves the estimation of the currents when error on the mechanical parameters are added but remains sensitive to electric parameter errors. A last version of this observer was tested in simulation with the control vector included in the Lyapunov candidate function so that the control vector is generated in the same loop than the observation. This could be useful for application where the control needs to be rapid compared to the observation. It has been chosen in this work to use state observers to retrieve the dq-axis currents but other strategies could be interesting to test. Model-free controllers for example might be more precise in presence of parametric errors.

Finally, the fourth chapter made the connection between the second and the third chapter. Indeed, the extended version of the proposed state observer was used with the map of parameter μ_M connected. The results off-loop showed that the steady-states tested feature almost no error of estimation. In transient phases, errors appear because of transient phenomenons that are not taken into account in the model used for the observer design. When ramps on the references are added to slow down the evolution of the currents, the errors are reduced. A true current sensorless control has then be performed, with the estimated currents in-loop. Again the steady-states are well estimated and controlled. The transient phases are however still problematic and further work should focus on the reduction of transient phases estimation errors. This could be done by adding a map of dynamic parameter that would absorb the errors induced by the transient phases phenomenons. Another possible solution would be to extend the electric model of the machine, by adding in the electric modeling information brought by a FEA-based model on the saturation of the machine and on other sub-dynamic phenomenons. A last series of tests has been conducted to characterize the energy consumption of the current sensorless control solution proposed. It has been shown through those tests that the strategy presented in this thesis does not affect significantly the energy consumption, which is an important asset considering the system is embedded and connected to a battery.

This work presented a successful current sensorless control of a WRSM which was a topic on

which the scientific literature is scarce. The main objective of controlling the i-StARS WRSM without current sensors in the stator, which was the milestone of this PhD work, has been successfully reached. Some important improvements could however be the subject of further work linked to the current sensorless control topic.

Further work

If the main objective of this study has been reached, a lot of related further work could propose enhancement of the current sensorless control strategy presented in this work. Indeed, the literature on this subject is scarce, and the different possible paths to achieve current sensorless control are numerous. Some could be more favorable according to the application. Whatever the means, further work should focus on reducing the estimation errors in transient phases. This is indeed the main issue encountered in this study. To do so, an extended dynamic mapping of parameters taking into account some usual transient phases could be considered. It could be also possible to add one or several other parameters in the mapping of the machine in order to determine if this can enhance the estimation of the currents in transient phases. Model-Free controllers could also be tested in order to test the benefits of not relying on a model of the machine.

A thermal study should also be undertaken in the future in order to take into account the temperature variations on the model and to increase the precision of the estimation for all the possible operating range of the system. The $\mathbb{R}^4 \rightarrow \mathbb{R}$ extrapolation could be tested to check if it can improve the precision of the estimation. The strategy proposed in this thesis could also be tested on other types of electric machine with different behaviors.

It could be interesting to test the solution proposed in this thesis to other electric machines than the WRSM for the sake of generality. Indeed, similar solution could be tested for a PMSM, an induction machine or a reluctance motor which are all potentially suitable for HEV application.

On a different application, the proposed current sensorless control could be used in aircraft engineering in order to improve the reliability of on electric powertrain. Indeed, the possibility to switch from a classic controller to a current sensorless controller in case of a current sensor failure could benefit the reliability of the whole electric system. Further work could focus on quantifying this reliability improvement.

Appendix: Flatness based control of a WRSM

In this annex, the mathematical proof that the WRSM state equations are flat according to the definition given in chapter 1 will be performed. First let's remind the state equations linked to the WRSM:

$$\begin{cases} \frac{d}{dt}i_d &= \frac{L_e}{L_d.L_e-M^2}\left(V_d - R_s.i_d + p.\Omega.L_q.i_q - \frac{M}{L_e}\left(V_e - R_e.i_e\right)\right) \\ \frac{d}{dt}i_q &= \frac{1}{L_q}\left(V_q - R_s.i_q - p.\Omega.\left(L_d.i_d + M.i_e\right)\right) \\ \frac{d}{dt}i_e &= \frac{L_d}{L_d.L_e-M^2}\left(V_e - R_e.i_e - \frac{M}{L_d}\left(V_d - R_s.i_d + p.\Omega.L_q.i_q\right)\right) \\ \frac{d}{dt}\Omega &= \frac{1}{J}\left(p.i_q.M.i_e - f.\Omega - \Gamma_0\right) \end{cases} \tag{4.1}$$

The state vector is then $x = \begin{bmatrix} i_d & i_q & i_e & \Omega \end{bmatrix}^T$. Here, for a speed control of the machine, the output vector is $y = \begin{bmatrix} i_d \\ i_e \\ \Omega \end{bmatrix}$ and the input vector is $u = \begin{bmatrix} V_d \\ V_q \\ V_e \end{bmatrix}$. The output vector y can be considered flat if it can be written $y = g(x, u, \dot{u}, \ddot{u}, ..., u^{(q)})$ and if x and u can be written as function of solely the flat output y and its derivatives, such as $x = h_1(y, \dot{y}, ..., y^{(r)})$ and $u = h_2(y, \dot{y}, ..., y^{(r+1)})$, where the functions g, h_1 and h_2 are regular functions.

Since the output vector y is directly composed of state variables, the function g is immediate and it gives:

$$y = \begin{bmatrix} 1 & 0 & 0 & 0 \\ 0 & 0 & 1 & 0 \\ 0 & 0 & 0 & 1 \end{bmatrix}.x \tag{4.2}$$

For the function h_1, the expressions of i_d, i_e and Ω come directly. The expression of i_q as a function of y can be written:

$$i_q = \frac{1}{p.M.i_e}.(J.\dot{\Omega} + f.\Omega + \Gamma_0) = h_{1q}(i_e, \Omega, \dot{\Omega}) \tag{4.3}$$

Finally, the expression of the input vector u as a function of the flat output vector and its derivates needs to be written. As it has been shown in chapter 2, the voltage in the machine can be written:

$$\begin{aligned} V_d &= R_s.i_d + L_d.\frac{d}{dt}i_d + M.\frac{d}{dt}i_e - \omega.L_q.i_q \\ V_q &= R_s.i_q + L_q.\frac{d}{dt}i_q + \omega.(L_d.i_d + M.i_e) \\ V_e &= R_e.i_e + L_e.\frac{d}{dt}i_e + M.\frac{d}{dt}i_d \end{aligned} \tag{4.4}$$

Which leads to:

$$\begin{aligned} V_d &= R_s.i_d + L_d.\dot{i_d} + M.\dot{i_e} - p.\Omega.L_q.h_{1q}(i_e, \Omega, \dot{\Omega}) \\ V_q &= R_s.h_{1q}(i_e, \Omega, \dot{\Omega}) + L_q.\dot{h_{1q}}(i_e, \Omega, \dot{\Omega}) + p.\Omega.(L_d.i_d + M.i_e) \\ V_e &= R_e.i_e + L_e.\dot{i_e} + M.\dot{i_d} \end{aligned} \tag{4.5}$$

It has been proven that with the model of the WRSM defined in the beginning of this appendix, both the state variables and the input voltages can be defined as functions of the flat outputs and their derivates. According to the mathematical definition of flatness, this system can be considered flat and a flatness-based controller can be used.

Glossary

Chapter 1

Symbol	Unit	Description
P_{em}	W	Power of the electric powertrain
P_{ICE}	W	Power of the ICE
$p(t)$	W	Instantaneous power linked to switching
V_{CE}	V	IGBT voltage
I_c	A	IGBT current
E	J	Energy dissipation linked to switching
T_{em}	N.m	Electromagnetic torque
p	-	Number of pair of poles
M	H	Mutual inductance between the rotor and the stator
L_d	H	d-axis inductance
L_q	H	q-axis inductance
L_e	H	Rotor wire inductance
i_d	A	d-axis current
i_q	A	q-axis current
i_e	A	Excitation current
V_d	V	d-axis voltage
V_q	V	q-axis voltage
V_e	V	rotor voltage
Ω	rad.s^{-1}	Rotor mechanical speed
ω	rad.s^{-1}	Rotor electric speed
θ	rad	Rotor electric angle
φ	rad	Angle shift between $\delta\gamma$-axis and dq-axis
ν	rad	Angle shift between $\delta\gamma$-axis and $\alpha\beta$-axis
Ω_c	rad.s^{-1}	Estimated mechanical speed
ψ_f	Wb	Magnetic flux between the rotor and the stator
e_d	V	d-axis back EMF
e_q	V	q-axis back EMF
I_{DC}	A	Inverter DC-link current
i_{abc}	A	abc-axis currents
S_{abc}	-	Inverter's switch state
V_{bat}	V	Battery voltage
i_{bat}	A	Battery current
L_f	H	Input filter inductance
C_f	F	Input filter capacitor

Chapter 2

Symbol	Unit	Description
C_f	F	Input filter capacitor
$R_{DS(ON)}$	Ω	Drain-source ON resistance
I_D	A	MOSFET current
V_{DSS}	V	Maximum drain-source voltage
i_{bat}	A	DC source current
θ	rad	Rotor electric angle
V_s	V	Stator voltages vector
Φ_s	Wb	Magnetic fluxes in the stator
R_s	Ω	Stator resistance
R_e	Ω	Rotor wire resistance
Φ_d	Wb	d-axis magnetic flux
Φ_q	Wb	q-axis magnetic flux
Φ_r	Wb	Rotor magnetic flux
i_d	A	d-axis current
i_q	A	q-axis current
i_e	A	Excitation current
L_d	H	d-axis inductance
L_q	H	q-axis inductance
L_e	H	Rotor wire inductance
Φ_{ed}	Wb	d-axis magnetic flux from the rotor
Φ_{de}	Wb	Rotor magnetic flux from the d-axis
M	H	Mutual inductance between the rotor and the stator
Ψ_f	Wb	Magnetic flux from the magnets in the stator
Ψ_r	Wb	Magnetic flux from the magnets in the rotor
Ω	rad.s^{-1}	Rotor mechanical speed
ω	rad.s^{-1}	Rotor electric speed
p	-	Number of pair of poles
Φ_{kd}	Wb	d-axis magnetic flux due to damper winding
Φ_{kq}	Wb	q-axis magnetic flux due to damper winding
M_{kd}	H	Mutual inductance between d-axis damper winding and stator
M_{kq}	H	Mutual inductance between q-axis damper winding and stator
i_{kd}	A	d-axis damper winding current
i_{kq}	A	q-axis damper winding current
J	kg.m^2	Rotor mechanical constant of inertia
f	$\text{kg.m}^2\text{.s}^{-1}$	Fluid friction coefficient
Γ_0	N.m	Dry friction torque
E_{rms}	V	Machine phase back EMF
$\hat{X}$	-	Estimated value of X
$\tilde{X}$	-	Error between estimated and real value of X
μ_M	H	Introduced parameter for modeling errors reduction

Chapter 3

Symbol	Unit	Description
i_d	A	d-axis current
i_q	A	q-axis current
i_e	A	Excitation current
L_d	H	d-axis inductance
L_q	H	q-axis inductance
L_e	H	Rotor wire inductance
R_s	Ω	Stator resistance
R_e	Ω	Rotor wire resistance
M	H	Mutual inductance between the rotor and the stator
V_d	V	d-axis voltage
V_q	V	q-axis voltage
V_e	V	rotor voltage
Ω	rad.s^{-1}	Rotor mechanical speed
θ	rad	Rotor electric angle
p	-	Number of pair of poles
J	kg.m^2	Rotor mechanical constant of inertia
f	kg.m^2.s^{-1}	Fluid friction coefficient
Γ_0	N.m	Dry friction torque
C_f	F	Input filter capacitor
i_{bat}	A	DC source current
V_{DC}	V	Inverter's DC link voltage
Δ_Γ	N.m	Estimated mechanical parameter
I_p	A	Estimated electric parameter
R_k	-	Covariance matrix of measurement noise
Q_k	-	Covariance matrix of process noise
$\hat{X}$	-	Estimated value of X
$\tilde{X}$	-	Error between estimated and real value of X
μ_M	H	Introduced parameter for modeling errors reduction
I_{tot}	A	Overall error between estimated and real current vector
K	-	Gain matrix of the measured variables
K_2	-	Gain matrix of the controlled variables

Chapter 4

Symbol	Unit	Description
i_d	A	d-axis current
i_q	A	q-axis current
i_e	A	Excitation current
L_d	H	d-axis inductance
L_q	H	q-axis inductance
Ω	rad.s^{-1}	Rotor mechanical speed
θ	rad	Rotor electric angle
V_d	V	d-axis voltage
V_q	V	q-axis voltage

Symbol	Unit	Description
R_s	Ω	Stator resistance
i_{bat}	A	DC source current
μ_M	H	Introduced parameter for modeling errors reduction
p	-	Number of pair of poles
I_T	A	Total stator current vector
I_{Test}	A	Total estimated stator current vector

Abbreviations

BEV	Battery electric vehicle
CAD	Computer assisted design
CSC-EO	Current sensorless controller with extended proposed observer
EESM	Electrically excited synchronous machine
EKF	Extended Kalman Filter
EMC	Electromagnetic compatibility
EMF	Electromotive force
EMI	Electromagnetic interference
EREV	Extended range electric vehicle
FBC	Flatness based controller
FEA	Finite element analysis
GHG	Greenhouse gas
HEV	Hybrid electric vehicle
ICE	Internal combustion engine
i-StARS	Intergrated stator alternator reversible system
LCV	Light commercial vehicle
LUT	Look-up table
MFC	Model-free controller
MPC	Model predictive controller
MTPA	Maximum torque per ampere
NEDC	New european driving cycle
PBC	Passivity-based controller
PCB	Printed circuit board
PHEV	Plug-in hybrid electric vehicle
PLDV	Passenger light duty vehicle
PLL	Phase-locked loop
PMSM	Permanent magnet synchronous machine
PWM	Pulse width modulation
SVPWM	Space-vector pulse width modulation
THG	Total harmonic distortion
WLTP	Worldwide harmonized light vehicles test procedures
WRSM	Wired rotor synchronous machine

List of Tables

List of Figures

Bibliography

[1] Eurostat. Energy, transport and environment indicators, 2016. 6, 139

[2] Global ev outlook 2018 - international energy agency. PDF, May 2018. pp. 111-117. 6, 10, 139

[3] F. Badin, J. Scordia, R. Trigui, E. Vinot, and B. Jeanneret. Hybrid electric vehicles energy consumption decrease according to drive train architecture, energy management and vehicle use. In *IET Hybrid Vehicle Conference 2006*. IEE, 2006. 6

[4] Z. Yang and A. Bandivadekar. Light-duty vehicle greenhouse gas and fuel economy standards. *International Council on Clean Transportation (ICCT)*, July 2017. 7, 139

[5] D. Tsokolis, S. Tsiakmakis, A. Dimaratos, G. Fontaras, P. Pistikopoulos, B. Ciuffo, and Z. Samaras. Fuel consumption and CO2 emissions of passenger cars over the new worldwide harmonized test protocol. *Applied Energy*, 179:1152–1165, oct 2016. 7, 139

[6] Krishna Veer Singh, Hari Om Bansal, and Dheerendra Singh. A comprehensive review on hybrid electric vehicles: architectures and components. *Journal of Modern Transportation*, 27(2):77–107, mar 2019. 7, 8, 10, 13, 14, 139

[7] Hybrid4all program. https://www.valeo.com/fr/hybrid4all/. 8

[8] Motorisation des véhicules légers neufs, émissions de CO2 et bonus écologique. https://www.statistiques.developpement-durable.gouv.fr/publicationweb/187, August 2018. 9, 139

[9] C. D. Anderson and J. Anderson. *Electric and Hybrid Cars: A History*. McFarland & Company, 2005. 9

[10] IEA (2019). Global EV outlook 2019, 2019. 10, 139

[11] Mahammad A. Hannan, Md. Murshadul Hoque, Aini Hussain, Yushaizad Yusof, and Pin Jern Ker. State-of-the-art and energy management system of lithium-ion batteries in electric vehicle applications: Issues and recommendations. *IEEE Access*, 6:19362–19378, 2018. 11

[12] M. Moragues, F. Parisot, and M. Delamarche. La voiture électrique au défi de l'autonomie. *L'Usine Nouvelle*, https://www.usinenouvelle.com/article/la-voiture-electrique-au-defi-de-l-autonomie.N435997, September 2016. 11

[13] Claire Curry. Lithium-ion battery costs and market. Bloomberg New Energy Finance, July 2017. 11, 139

[14] I. Tsiropoulos, D. Tarvidas, and N. Lebedeva. Li-ion batteries for mobility and stationary storage applications – Scenarios for costs and market growth. *Publications Office of the European Union*, 2018. 11, 12, 139

[15] Niall McCarthy. Netherlands top for electric vehicle charger density. Forbes Magazine, October 2018. 11

[16] C.C. Chan, A. Bouscayrol, and K. Chen. Electric, hybrid, and fuel-cell vehicles: Architectures and modeling. *IEEE Transactions on Vehicular Technology*, 59(2):589–598, feb 2010. 13

[17] Daniel Richard and Yannick Dubel. Valeo StARS technology: A competitive solution for hybridization. In *2007 Power Conversion Conference - Nagoya*. IEEE, apr 2007. 14

[18] Aditya Kumar Kumawat and Amrit Kumar Thakur. A comprehensive study of automotive 48V technology. *SSRG International Journal of Mechanical Engineering*, 4, May 2017. 14

[19] S.M. Lukic and A. Emadi. Effects of drivetrain hybridization on fuel economy and dynamic performance of parallel hybrid electric vehicles. *IEEE Transactions on Vehicular Technology*, 53(2):385–389, mar 2004. 14, 16

[20] Hongrui Ma, Felix Balthasar, Nigel Tait, Xavier Riera-Palou, and Andrew Harrison. A new comparison between the life cycle greenhouse gas emissions of battery electric vehicles and internal combustion vehicles. *Energy Policy*, 44:160–173, may 2012. 15, 16

[21] J.-P. Louis and C. Bergmann. Commande numérique des machines - systèmes triphasés : régime permanent. *Techniques de l'ingénieur*, November 1996. 17, 22, 139

[22] Jaeyong Park, Sungho Jung, and Jung-Ik Ha. Variable time step control for six-step operation in surface-mounted permanent magnet machine drives. *IEEE Transactions on Power Electronics*, 33(2):1501–1513, feb 2018. 17

[23] Ming-Shi Huang, Kuan-Cheng Chen, Chin-Hao Chen, Zheng-Feng Li, and Shih-Wei Hung. Torque control in constant power region for IPMSM under six-step voltage operation. *IET Electric Power Applications*, 13(2):181–189, feb 2019. 17

[24] J.-M. Retif. *Commandes vectorielles des machines asynchrones et synchrones*. INSA Lyon, 2008. 18, 20

[25] Nicolas Patin. Auxiliary converter circuits. In *Power Electronics Applied to Industrial Systems and Transports, Volume 1*, pages 51–74. Elsevier, 2015. 19

[26] J.-P. Louis and C. Bergmann. Commande numérique - régimes intermédiaires et transitoires. *Techniques de l'ingénieur*, 1997. 19, 22

[27] Eric Monmasson, editor. *Power Electronic Converters: PWM Strategies and Current Control Techniques*. Wiley-ISTE, 2013. 19

[28] Hamid Khan. *Optimised space vector modulation for variable speed drives*. PhD thesis, UNiversité Blaise Pascal - Clermont II, 2012. 19

[29] Infineon Technologies AG. *Application Note on Industrial IGBT Modules Explanation of Technical Information*, November 2015. 20, 139

[30] Hyun-Soo Seol, Je-Myung Jeong, Ju Lee, and Chang-Sung Jin. Current control of WRSM considering magnetic saturation phenomenon. *IEEE Transactions on Magnetics*, 52(7):1–4, jul 2016. 20

[31] Xiaoguang Zhang, Lizhi Sun, Ke Zhao, and Li Sun. Nonlinear speed control for PMSM system using sliding-mode control and disturbance compensation techniques. *IEEE Transactions on Power Electronics*, 28(3):1358–1365, mar 2013. 21, 67

[32] P.J. Nicklasson, R. Ortega, G. Espinosa-Perez, and C.G.J. Jacobi. Passivity-based control of a class of blondel-park transformable electric machines. *IEEE Transactions on Automatic Control*, 42(5):629–647, may 1997. 21

[33] Razvan Mocanu and Alexandru Onea. Passivity based torque control of PMSM used in electrical vehicles. In *2015 19th International Conference on System Theory, Control and Computing (ICSTCC)*. IEEE, oct 2015. 21

[34] M. Fliess, J. Lévine, P. Martin, and P. Rouchon. On differentially flat nonlinear system. *NOLCOS*, 1992. 21

[35] M. Van Nieuwstadt, M. Rathinam, and R. M. Murray. Differential flatness and absolute equivalence. *Proceedings of the 33rd Conference on decision and control*, December 1994. 21

[36] Alexandre Battiston. *Modélisation, commande, stabilité et mise en oeuvre des onduleurs à source impédante - Application aux systèmes embarqués*. PhD thesis, Université de Lorraine, 2014. 21, 22

[37] A. Battiston, E.-H. Miliani, J.-P. Martin, S. Pierfederici, and F. Meibody-Tabar. High bandwidth flatness-based control of a PM-motor with protection system in case of saturation. *European Journal of Electrical Engineering*, 2014. 21, 22

[38] Jérémy Cuenot. *Architectures d'alimentation et de commande des actionneurs haute-vitesse connectés aux réseaux avioniques à tension variable*. PhD thesis, Université de Lorraine, 2017. 21, 22

[39] Yingguang Sun. *Unified position sensorless solution with wide speed range capabilities for IPM synchronous motor drives*. PhD thesis, McMaster University, 2016. 23

[40] B. Nahid-Mobarakeh. *Commande vectorielle sans capteur mécanique des machines synchrones à aimants : méthodes, convergence, robustesse, identificatation "en ligne" des paramètres*. PhD thesis, INPL Nancy, 2001. 23, 24, 25

[41] B. Nahid-Mobarakeh, F. Meibody-Tabar, and F.-M. Sargos. Mechanical sensorless control of PMSM with online estimation of stator resistance. *IEEE Transactions on industry applications*, 2004. 23, 24

[42] J. S. Kim and S. K. Sul. New approach for high-performance PMSM drives without rotational position sensors. *IEEE Transactions on Power Electronics*, 12:904–911, September 1997. 23

[43] N. Matsui and N. Shigyo. Brushless DC motor without position and speed sensors. *IEEE Transactions on industry applications*, 1992. 23

[44] Gaetan Lefebvre, Jean-Yves Gauthier, Alaa Hijazi, Xuefang Lin-Shi, and Vincent Le Digarcher. Observability-index-based control strategy for induction machine sensorless drive at low speed. *IEEE Transactions on Industrial Electronics*, 64(3):1929–1938, mar 2017. 24

[45] S. Bolognani, M. Zigliotto, and M. Zordan. Sensorless full-digital PMSM drive with EKF estimation of speed and rotor position. *IEEE Transactions on Industry Electronics*, 46(1), February 1999. 25

[46] B.-G. Park, J.-M. Kim, Ji.-W. Kim, K.-C. Lee, D.-H. Koo, and D.-S. Hyun. New approach to EKF-based sensorless control using parallel structure for non-salient pole permanent magnet synchronous motors. In *ICEMS Busan*, October 2013. 25

[47] Riccardo Antonello, Fabio Tinazzi, and Mauro Zigliotto. Benefits of direct phase voltage measurement in the rotor initial position detection for permanent-magnet motor drives. *IEEE Transactions on Industrial Electronics*, 62(11):6719–6726, nov 2015. 25

[48] Sami Zaim. *Contribution à la commande sans capteur mécanique d' actionneurs électriques motorisés par des machines synchrones à aimants permanents.* PhD thesis, Université de Lorraine, 2013. 25

[49] F. Abry, A. Zgorski, X. Lin-Shi, and J.-M. Retif. Sensorless position control for SPMSM at zero speed and acceleration. In *Proceedings of the 2011 14th European Conference on Power Electronics and Applications*, 2011. 25, 26

[50] T. Boileau, B. Nahid-Mobarakeh, and F. Meibody-Tabar. Back-EMF based detection of stator winding inter-turn fault for PM synchronous motor drives. *IEEE Vehicle Power and Propulsion Conference*, 2007. 26

[51] H. Kim and T. M. Jahns. Phase current reconstruction for AC motor drives using a DC link single current sensor and measurement voltage vectors. *IEEE Transactions on Power Electronics*, 2006. 26

[52] F. Blaabjerg, J. K. Pedersen, U. Jaeger, and P. Thoegersen. Single current sensor technique in the DC link of three-phase PWM-VS inverters: a review and a novel solution. *IEEE TRansactions on Industry Applications*, 33(5):1241–1253, September 1997. 26

[53] L. Ying and N. Ertugrul. An observer-based three-phase current reconstruction using DC link measurement in PMAC motors. *IPEMC*, 2006. 26, 27, 28, 67, 139

[54] Y. Gu, F. Ni, D. Yang, and H. Liu. Switching-state phase shift method for three-phase-current reconstruction with a single dc-link current sensor. *IEEE Transactions on Industrial Electronics*, 58(11):5186–5194, November 2011. 26

[55] N. Ansari, N. Khan, and S. Rewatkar. Reconstruction of phase current of induction motor drive based on DC link measurement. In *ICAET*, 2014. 26, 67

[56] A. Bhargava, D. Pommerenke, K. W. Kam, F. Centola, and C. W. Lam. DC-DC buck converter EMI reduction using PCB layout modification. *IEEE Transactions on Electromagnetic Compatibility*, 53:806–813, August 2011. 29

[57] M. A. Shamsi. *Architecture d'alimentation et de commande d'actionneurs tolérants aux défauts - Régulateur de courant non linéaire à large bande passante.* PhD thesis, INPL Nancy, 2007. 30

[58] Kan Liu, Qiao Zhang, Jintao Chen, Z. Q. Zhu, and Jing Zhang. Online multiparameter estimation of nonsalient-pole PM synchronous machines with temperature variation tracking. *IEEE Transactions on Industrial Electronics*, 58(5):1776–1788, may 2011. 34

[59] G. Devornique. *Modélisation et optimisation d'un alterno-démarreur synchrone à griffes pour l'application mild-hybrid.* PhD thesis, IAEM - GREEN Université de Lorraine, 2017. 34, 41, 42, 140

[60] Beatrice Bernoux. *Caractérisation de MOSFETs de puissance cyclés en avalanche pour des applications automobile micro-hybrides.* PhD thesis, INSA Toulouse, 2010. 35

[61] Laurent Albert. *Modélisation et optimisation des alternateurs à griffes - Application au domaine automobile.* PhD thesis, Institut National Polytechnique de Grenoble, 2004. 36

[62] Jason C.K. Lee and Zongguo Wen. Rare earths from mines to metals: Comparing environmental impacts from china's main production pathways. *Journal of Industrial Ecology*, 21(5):1277–1290, sep 2016. 36

[63] U.S Department of Energy. Critical material strategy, December 2011. 36

[64] L. Vido, Y. Amara, and M. Gabsi. Machines synchrones à double excitation MSDE. *Techniques de l'Ingénieur*, February 2011. 36

[65] Mitsubishi Electric. FM600TU-07A. Technical report, Mitsubishi Electric, 2006. 37, 140

[66] Edward Ramsden. *Hall-Effect Sensors: Theory and Application*. Newnes, 2006. 38

[67] Abdelmounaim Tounzi. *Contribution à l'étude de la commande vectorielle de machines à reluctance variable : prise en compte de l'amortissement et de la saturation*. PhD thesis, Institut National Polytechnique de Lorraine, 1993. 46

[68] Nikola Z. Popov, Slobodan N. Vukosavic, and Emil Levi. Motor temperature monitoring based on impedance estimation at PWM frequencies. *IEEE Transactions on Energy Conversion*, 29(1):215–223, mar 2014. 51

[69] H. Rehaoulia, H. Henao, and G.A. Capolino. Modeling of synchronous machines with magnetic saturation. *Electric Power Systems Research*, 77(5-6):652–659, apr 2007. 51

[70] N. Praveen Kumar, C. Vinothraj, and T. B. Isha. Effect of wear and tear bearing fault in induction motor drives using FEM. In *IEEE International Conference on Power Electronics, Drives and Energy Systems (PEDES)*, 2018. 51

[71] Chao Zhang and Shaoping Wang. Experimental analysis of performance degradation of solid lubricated bearings with vibration and friction torque signal. In *IEEE 10th International Conference on Industrial Informatics*. IEEE, jul 2012. 51

[72] Jun-Woo Chin, Sung-Woo Hwang, Hyeon-Jin Park, and Jung-Pyo Hong. Thermal analysis and verification of PMSM using LPTN considering mechanical components and losses. In *2018 XIII International Conference on Electrical Machines (ICEM)*. IEEE, sep 2018. 51

[73] S. Diop and M. Fliess. Nonlinear observability, identifiability, and persistent trajectories. In *Proceedings of the 30th IEEE Conference on Decision and Control*. IEEE, 1991. 52

[74] Thierry Boileau, Nicolas Leboeuf, Babak Nahid-Mobarakeh, and Farid Meibody-Tabar. Online identification of PMSM parameters: Parameter identifiability and estimator comparative study. *IEEE Transactions on Industry Applications*, 47(4):1944–1957, jul 2011. 52, 55, 69

[75] Hao Ge, James Weisheng Jiang, Jin Ye, and Ali Emadi. Behavior study of permanent magnet synchronous machines based on a new normalized model. *IEEE Transactions on Industrial Electronics*, 66(10):7539–7550, oct 2019. 54

[76] Kan Liu, Jianghua Feng, Shuying Guo, Lei Xiao, and Zi-Qiang Zhu. Identification of flux linkage map of permanent magnet synchronous machines under uncertain circuit resistance and inverter nonlinearity. *IEEE Transactions on Industrial Informatics*, 14(2):556–568, feb 2018. 54

[77] S. Morimoto, M. Sanada, and Y. Takeda. Mechanical sensorless drives of IPMSM with online parameter identification. *IEEE Transactions on Industry Applications*, 42(5):1241–1248, sep 2006. 55

[78] S. Bachir, S. Tnani, J.-C. Trigeassou, and G. Champenois. Diagnosis by parameter estimation of stator and rotor faults occurring in induction machines. *IEEE Transactions on Industrial Electronics*, 53(3):963–973, jun 2006. 55

[79] Thierry Boileau, Nicolas Leboeuf, Babak Nahid-Mobarakeh, and Farid Meibody-Tabar. Synchronous demodulation of control voltages for stator interturn fault detection in PMSM. *IEEE Transactions on Power Electronics*, 28(12):5647–5654, dec 2013. 55

[80] Nanfang Yang, Babak Nahid-Mobarakeh, Adrien Corne, and Jean-Philippe Martin. Robust predictive current control with total disturbance observer for a synchronous motor drive. In *2016 International Conference on Electrical Systems for Aircraft, Railway, Ship Propulsion and Road Vehicles & International Transportation Electrification Conference (ESARS-ITEC)*. IEEE, nov 2016. 67, 68

[81] Nanfang Yang, Babak Nahid-Mobarakeh, Adrien Corne, and Jean-Phillippe Martin. Multiple-vector-based predictive direct current control for a wound rotor synchronous machine drive. In *2016 IEEE Industry Applications Society Annual Meeting*. IEEE, oct 2016. 67, 68

[82] Yanan Zhou, Hongmei Li, Rundong Liu, and Jingkui Mao. Continuous voltage vector model-free predictive current control of surface mounted permanent magnet synchronous motor. *IEEE Transactions on Energy Conversion*, 34(2):899–908, jun 2019. 67

[83] Raúl Santiago Munoz-Aguilar, Arnau Doria-Cerezo, Enric Fossas, and Rafel Cardoner. Sliding mode control of a stand-alone wound rotor synchronous generator. *IEEE Transactions on Industrial Electronics*, 58(10):4888–4897, oct 2011. 67

[84] Hugues Renaudineau, Jean-Philippe Martin, Babak Nahid-Mobarakeh, and Serge Pierfederici. DC–DC converters dynamic modeling with state observer-based parameter estimation. *IEEE Transactions on Power Electronics*, 30(6):3356–3363, jun 2015. 68, 72, 76

[85] H. Renaudineau. *Hybid renewable energy sourced system energy management and self-diagnosis*. PhD thesis, Université de Lorraine, 2013. 68, 76

[86] Gildas Besançon. *Nonlinear Observers and Applications*. Springer Berlin Heidelberg, 2007. 69

[87] Monia Oueder. *Synthèse d'observateur pour les systèmes non linéaires*. PhD thesis, Université de Caen Basse-Normandie, 2012. 69

[88] Pierre Rouchon and Frédéric Bonnans. *Commande et optimisation de systèmes dynamiques*. Ecole Polytechnique, 2006. 69

[89] Paul Zarchan and Howard Musoff. *Fundamentals of Kalman Filtering: A Practical Approach (Progress in Astronautics & Aeronautics)*. American Institute of Aeronautics & Astronautics, 2001. 72

[90] C.K. Chui and G. CHen. *Kalman Filtering with Real-Time Applications*. Springer Berlin Heidelberg, 2009. 72

[91] Bernt M. Åkesson, John Bagterp Jørgensen, Niels Kjølstad Poulsen, and Sten Bay Jørgensen. A generalized autocovariance least-squares method for kalman filter tuning. *Journal of Process Control*, 18(7-8):769–779, aug 2008. 74

[92] A. Corne, N. Yang, J.-P. Martin, B. Nahid-Mobarakeh, and S. Pierfederici. Nonlinear estimations of stator currents in a wound rotor synchronous machine. In *Electrical Systems for Aircraft, Railway, Ship Propulsion and Road Vehicles & International Transportation Electrification Conference (ESARS-ITEC)*, 2016. 74

[93] Adrien Corne, Nanfang Yang, Jean-Philippe Martin, Babak Nahid-Mobarakeh, and Serge Pierfederici. Nonlinear estimation of stator currents in a wound rotor synchronous machine. *IEEE Transactions on Industry Applications*, 54(4):3858–3867, jul 2018. 74

[94] A. Corne, J.-P. Martin, B. Nahid-Mobarakeh, and S. Pierfederici. Current sensorless control using a nonlinear observer applied to a wound rotor synchronous machine. In *Transportation Electrification Conference and Expo (ITEC)*, 2017. 86

[95] A. Corne, J.-P. Martin, B. Nahid-Mobarakeh, and S. Pierfederici. Robust sensorless control strategy with enhanced dynamics. In *IEEE Industry Applications Society Annual Meeting*, 2017. 92

Scientific production

International journal

A. Corne, N. Yang, J.-P. Martin, B. Nahid-Mobarakeh and S. Pierfederici. Nonlinear estimations of stator currents in a wound rotor synchronous machine. IEEE Transactions on Industry Applications, 54(4):3858-3867, jul 2018

International conferences

A. Corne, N. Yang, J.-P. Martin, B. Nahid-Mobarakeh and S. Pierfederici. Nonlinear estimations of stator currents in a wound rotor synchronous machine. In Electrical Systems for Aircraft, Railway, Ship Propulsion and Road Vehicles and International Transportation Electrification Conference (ESARS-ITEC), 2016

A. Corne, J.-P. Martin, B. Nahid-Mobarakeh and S. Pierfederici. Current sensorless control using a nonlinear observer applied to a wound rotor synchronous machine. In International Transportation Electrification Conference (ITEC), 2017

A. Corne, J.-P. Martin, B. Nahid-Mobarakeh and S. Pierfederici. Robust sensorless control strategy with enhanced dynamics. In IEEE Industry Applications Society Annual Meeting, 2017

Résumé

Stratégies de commande sans capteur de courant d'une chaîne de traction appliquée à l'automobile

L'application de quotas d'émissions de gaz à effet de serre a amené les constructeurs automobiles à augmenter le niveau d'électrification de leurs véhicules. En parallèle des véhicules tout électrique, se sont développées les solutions hybrides, tel le *mild-hybrid* autorisant l'association d'une chaîne de traction électrique avec le moteur à combustion dans le but d'absorber les pics de consommation de carburant. Afin de rester compétitif, les coûts de production d'un véhicule doivent être optimisés autant que possible, ainsi l'étude réalisée de commande de machine synchrone à griffes sans capteur de courant permet la suppression des capteurs du stator de la machine et donc de s'affranchir de leur coût.

Une commande vectorielle de la machine est nécessaire afin d'optimiser les courants statoriques pour un couple donné. L'utilisation d'observateurs d'état permettant l'estimation des courants manquants a donc été privilégiée. Ainsi différentes topologies d'observateurs ont été développées : le filtre de Kalman étendu ainsi qu'un observateur d'état et deux déclinaisons dont la conception est basée sur une analyse de convergence à l'aide de fonctions de Lyapunov. Afin d'améliorer la précision de l'observation des courants statoriques, une étude approfondie du modèle électrique de la machine a été réalisée. Elle permet de minimiser les erreurs dues aux variations paramétriques, liées notamment à la saturation magnétique de la machine et des incertitudes liées aux phénomènes non modélisés de la chaîne de conversion électromécanique. Une méthode de cartographie de la machine a ainsi été proposée à l'aide d'un estimateur paramétrique. Les résultats expérimentaux, obtenus sur un banc de test réalisé en laboratoire, sont concluants en régime établi : les courants non mesurés sont estimés avec une précision satisfaisante pour une application automobile et permettent le contrôle sans capteur de courant de la machine.

Mots clés : Moteur électrique, commande sans capteur, observateur d'état, modèle électrique, sensibilité paramétrique

Abstract

Current Sensorless Control Strategies for an Automotive Electric Powertrain

The application of greenhouse gases quotas has led the automotive manufacturers to increase the electrification level of their vehicles. In parallel with Battery Electric Vehicles (BEV), hybridization solutions have been developed. Among them, mild-hybrid technology allows the connection of an electric powertrain with an Internal Combustion Engine (ICE) with the aim of absorbing peaks of fuel consumption. In order to remain competitive, the manufacturing costs of a vehicle need to be optimized. In that regard, removing the stator currents sensors allows avoiding their inherent costs.

However, within the vector control framework, a feedback on these currents is required to optimize their value for a given torque. For this reason, it has been decided to use state observers to estimate the missing currents. Different state observer solutions have thus been developed: the Extended Kalman Filter (EKF) and a state observer with two extensions whose design is based on a convergence analysis using Lyapunov functions. With the aim of improving the precision of the stator currents estimation, an in-depth study of the machine's electrical model was carried out. It allows minimizing errors due to parametric variations, related in particular to the magnetic saturation of the machine and uncertainties due to unmodeled phenomena in the whole drive. A method for mapping the machine was proposed using a parametric estimator. The experimental results, obtained on a test bench built in the laboratory, are conclusive in steady-state: the real currents are estimated with a satisfying precision for an automotive application and allow performing a current sensorless control of the machine.

Keywords : Electric machine, sensorless control, state observer, electric modeling, parametric sensitivity